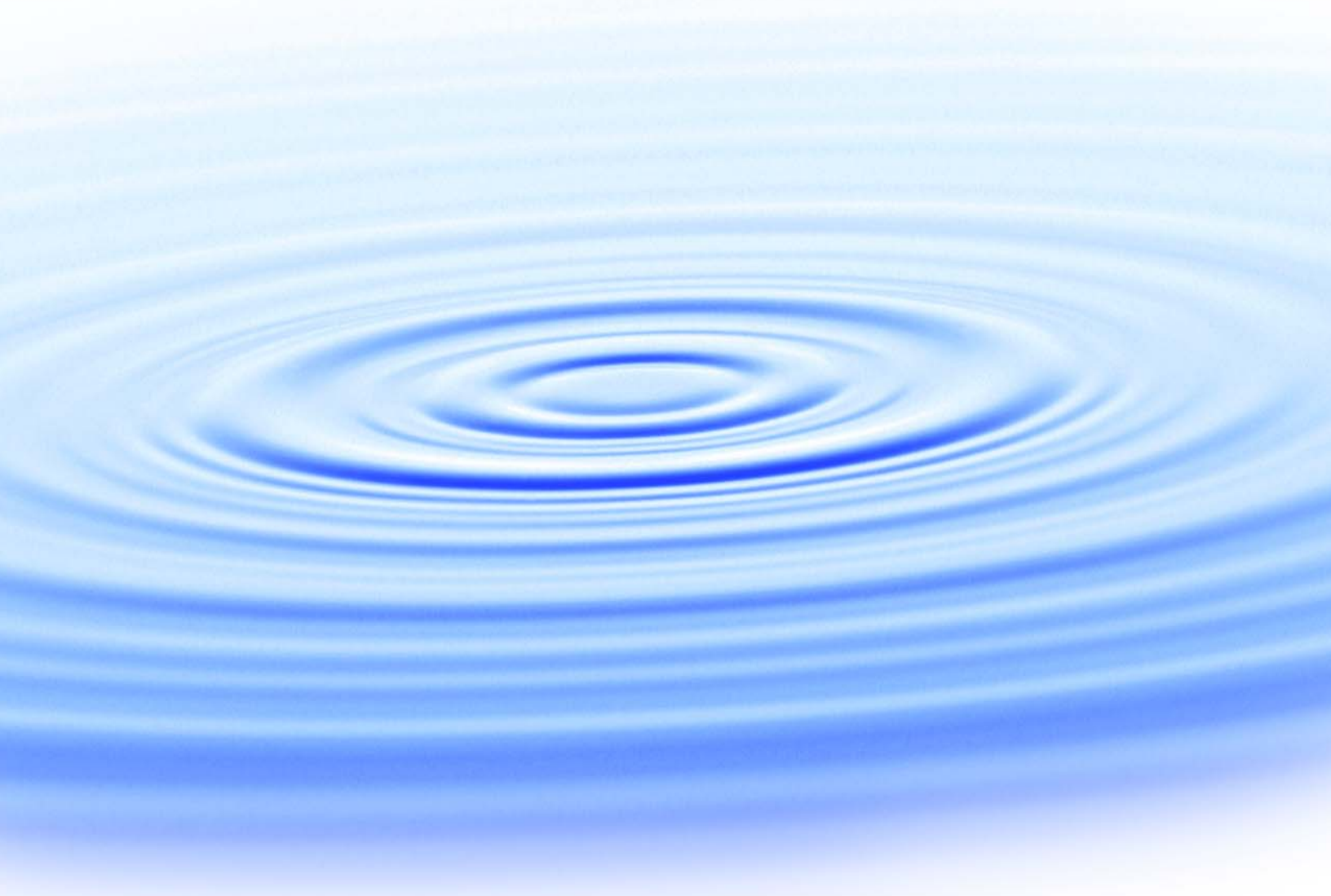




WATERREUSE

**Regulated and Emerging Disinfection
By-Products During the Production of
High Quality Recycled Water**



WaterReuse Research Foundation

Regulated and Emerging Disinfection
By-Products During the Production of
High Quality Recycled Water

About the WateReuse Research Foundation

The mission of the WateReuse Research Foundation is to build support for water reuse through research and education. The Foundation's research advances the science of water reuse and supports communities across the United States and abroad in their efforts to create new sources of high quality water for various uses through reclamation, recycling, reuse, and desalination while protecting public health and the environment.

The Foundation sponsors research on all aspects of water reuse, including emerging chemical contaminants, microbiological agents, treatment technologies, reduction of energy requirements, concentrate management and desalination, public perception and acceptance, economics, and marketing. The Foundation's research informs the public of the safety of reclaimed water and provides water professionals with the tools and knowledge to meet their commitment of providing a reliable, safe product for its intended use.

The Foundation's funding partners include the supporters of the California Direct Potable Reuse Initiative, Water Services Association of Australia, Pentair Foundation, and Bureau of Reclamation. Funding is also provided by the Foundation's members, water and wastewater agencies, and other interested organizations.

Regulated and Emerging Disinfection By-Products During the Production of High Quality Recycled Water

Maria José Farré
*Catalan Institute for Water Research
The University of Queensland (Australia)*

Howard S. Weinberg
University of North Carolina at Chapel Hill (USA)

Katrin Doederer
The University of Queensland (Australia)

Ariel Atkinson
University of North Carolina at Chapel Hill (USA)

Wolfgang Gernjak
The University of Queensland (Australia)

Cosponsors

Seqwater
Veolia Water Australia



WaterReuse Research Foundation
Alexandria, VA

Disclaimer

This report was sponsored by the WateReuse Research Foundation and cosponsored by Seqwater and Veolia Water Australia. The Foundation, its Board Members, and the project cosponsors assume no responsibility for the content of this publication or for the opinions or statements of facts expressed in the report. The mention of trade names of commercial products does not represent or imply the approval or endorsement of the WateReuse Research Foundation, its Board Members, or the cosponsors. This report is published solely for informational purposes.

For more information, contact:

WateReuse Research Foundation
1199 North Fairfax Street, Suite 410
Alexandria, VA 22314
703-548-0880
703-548-5085 (fax)
www.WateReuse.org/Foundation

© Copyright 2015 by the WateReuse Research Foundation. All rights reserved. Permission to reproduce must be obtained from the WateReuse Research Foundation.

WateReuse Research Foundation Project Number: 10-18

ISBN: 978-1-941242-31-5

Contents

List of Figures	ix
List of Tables	xiii
List of Acronyms	xv
Foreword	xix
Acknowledgments	xx
Executive Summary	xxi
Chapter 1. Introduction.....	1
1.1 Background	1
1.2 DBP Occurrence and Fate During High-Pressure Membrane Treatment in Water Reuse Applications.....	2
1.2.1 Water Reuse—Advanced Water Treatment	2
1.2.2 Disinfection By-Products.....	3
1.2.3 Disinfectants	5
1.2.4 DBP Formation.....	7
1.3 Membrane Technology in Water Reuse Applications	10
1.3.1 Membrane Chemistry	10
1.3.2 Practical Application of High-Pressure Membranes.....	12
1.4 Solute Rejection In High-Pressure Membranes	13
1.4.1 Rejection Mechanisms.....	13
1.5 Summary	18
1.6 Objectives.....	19
Chapter 2. Materials and Methods.....	21
2.1 Chemicals and Reagents	21
2.2 Analytical Techniques.....	23
2.2.1 Halogenated Volatiles.....	23
2.2.2 Haloacetic Acids.....	24
2.2.3 Cyanogen Halide Analysis	25
2.2.4 N-Nitrosamines.....	26

2.2.5	Free and Total Chlorine Analysis	26
2.2.6	Secondary Effluent Characterization	27
2.3	Sampling	28
2.3.1	WWTP Secondary Effluent	28
2.3.2	AWTP Sampling Campaigns.....	31
2.4	DBP Formation Kinetic Studies in Sampled Secondary Effluent	33
2.4.1	Disinfectant Preparation	33
2.4.2	Secondary Effluent Stability Tests.....	33
2.4.3	Gibson Island Secondary Effluent—72-Hour Kinetic Studies	36
2.4.4	Bundamba Secondary Effluent—24-Hour Kinetic Studies	36
2.5	Tools for Modeling and Experimental Design	37
2.5.1	Experimental Design.....	37
2.5.2	Statistical Analysis.....	37
2.6	Filtration Equipment and Protocols.....	38
2.6.1	Background Solution for Filtration Experiments.....	38
2.6.2	RO/NF Membrane Characterization	38
2.6.3	RO/NF Crossflow Filtration	39
2.6.4	RO Pilot-Scale Filtration at The University of Wollongong	42
Chapter 3. DBP Formation During the Treatment of Secondary Effluent.....		45
3.1	DBP Occurrence and Fate across Two AWTPs	45
3.2	DBP Occurrence and Fate across the Treatment Train	49
3.3	Effect of Operational Parameters on DBP Formation in Secondary Effluent.....	52
3.3.1	pH and Time Dependent Formation	53
3.3.2	Formation of DBPs during Pre-Formed Versus Inline- Formed Chloramination	58
3.3.3	Impact of Temperature.....	59
3.3.4	Response Surface Analysis for Chlorination and Chloramination	60
3.4	Investigation of Bromine Substitution during Chlorination and Chloramination of Secondary Effluent.....	66
3.4.1	Impact of Disinfection Strategy and Reaction Time.....	68
3.4.2	Impact of pH	71
3.4.3	Impact of Temperature.....	72
3.4.4	Evaluation of Impact of Operational Parameters on BIF with RSM	2

Chapter 4. DBP Removal by RO and NF Membranes— Influence of Operational Parameters, Solute, and Solution Properties.....	77
4.1 Preliminary Experiments	77
4.1.1 Volatilization, Hydrolysis, and Adsorption of DBPs	77
4.1.2 Time Required to Achieve Steady State DBP Removal	81
4.1.3 Feed Concentration	82
4.1.4 Sample Collection	82
4.2 DBP Rejection by RO and NF Membranes	82
4.2.1 Rejection by Different RO and NF Membranes.....	82
4.2.2 Reverse Osmosis	86
4.2.3 Nanofiltration	88
4.2.4 Multiple Linear Regression	89
4.3 Impact of Operational Parameters on the Rejection of DBPs.....	92
4.3.1 Transmembrane Flux.....	92
4.3.2 Crossflow Velocity.....	95
4.4 Impact of Feed Solution.....	96
4.4.1 Temperature	96
4.4.2 pH.....	98
4.4.3 Ionic Strength	102
4.4.4 Modeling DBP Rejection	103
4.5 DBP Rejection at Pilot-Scale (RO).....	105
4.5.1 Rejection of DBPs and N-Nitrosamines with Spiral Wound Elements.....	105
4.5.2 DBP Rejection: Coupon Versus Single Spiral Wound Element	107
4.5.3 Temperature, pH and Flux Effects between Pilot and Bench-Scale.....	108
4.5.4 Impact of Recovery	111
4.5.5 Model Application to Pilot-Scale Data.....	112
Chapter 5. Rejection of DBPs by RO and NF Membrane—Modeling Bench-, Pilot- and Full-Scale.....	113
5.1 Transport Model Description.....	113
5.1.1 Spiegler-Kedem (S-K) Model	113
5.1.2 Steric Hindrance Pore (SHP) Model	114
5.1.3 Real Rejection Obtained by Concentration Polarization Model	114
5.2 DBP Rejection Description by S-K Transport Models.....	115

5.2.1	NF Membrane—S-K—SHP Model.....	115
5.2.2	RO Membrane—S-K Model.....	118
5.3	DBP-Membrane Interaction—Adsorption.....	122
5.4	Modeling DBP Rejection at Pilot- and Full-Scale.....	123
5.4.1	Model for Spiral Wound Element.....	125
5.4.2	Model Validation.....	128
5.4.3	Model Application.....	130
Chapter 6. Conclusions and Perspectives.....		135
6.1	Conclusions.....	135
6.1.1	DBP Occurrence in Full-Scale Advanced Water Treatment Plants.....	135
6.1.2	DBP Formation and Bromine Incorporation.....	135
6.1.3	The Influence of Molecular Properties on Rejection by Dense Membranes.....	136
6.1.4	DBP Rejection—Operational Parameters.....	136
6.1.5	Prediction of DBP Removal in Bench-, Pilot- and Full-Scale RO Processes.....	137
6.1.6	Water Quality Management.....	137
6.2	Recommendations for Future Research.....	138
References.....		141
Appendix A.....		155
Appendix B.....		171
Appendix C.....		181

Figures

1.1	Unit CHO cell cytotoxicity and genotoxicity for different DBP groups.....	5
1.2	Cross section of a TFC membrane by scanning electron microscope and a typical chemical structure of the cross-linked polyamide polymer of the active surface layer.....	11
1.3	Two by one (2:1), two-stage RO train with two pressure vessels in Stage 1 and one pressure vessel in Stage 2.....	13
1.4	Visualization of the three solute removal mechanisms by high-pressure membranes.....	13
2.1	Scheme of the AWTPs studied.....	33
2.2	Photographs and flow diagram of the crossflow system.....	40
2.3	Flow diagram of the pilot-scale plant.....	42
3.1	(a) DBP formation at full-scale from reaction of secondary effluent with monochloramine at Bundamba (B) and Gibson Island (GI) AWTP; (b) DBP formation after bench-scale disinfection of secondary effluent sampled at Bundamba and Gibson Island with pre-formed monochloramine 10 mg/L as Cl ₂ for 24 hours at pH 7.....	47
3.2	Average DBP formation during pre-formed chloramination with source water of Gibson Island at pH 7 and 10 mg/L as Cl ₂	48
3.3	Scheme of the AWTPs studied.....	49
3.4	Fate of the DBPs formed across the treatment train at Bundamba AWTP: (a) disinfection strategy at the time of sampling was the application of pre-formed monochloramine to the treatment train; (b) disinfection strategy at the time of sampling was forming chloramines inline during the treatment train ..	51
3.5	DBP formation after 24 hours (a) pH 5.5, (b) pH 7, and (c) pH 8.5 for each disinfection strategy (25 mg/L Cl ₂) at 23° C.....	54
3.6	DBP formation kinetics during 24 hours for each disinfection strategy (pH 7, 25 mg/L as Cl ₂) at 23° C.....	56
3.7	TCNM and CH formation kinetics in secondary effluent during each of the disinfection strategies, 24 hours of reaction time at 23° C and pH 5.5, 7, and 8.5 and 25 mg/L as Cl ₂	57
3.8	Comparison of (a) time dependent disinfectant residuals at pH 7 during chlorination, inline and pre-formed chloramination, (b) DBPs formed after 30 minutes of reaction time during inline- and pre-formed chloramination.....	58
3.9	DCAN, CH, 1,1-DCP, and 1,1,1-TCP formation kinetics during inline-formed and pre-formed chloramination (25 mg/L Cl ₂) at 35°C and pH 8.5.....	59
3.10	Comparison of normalized linear regression coefficients pH, time, and temperature during chlorination.....	63

3.11	Comparison of normalized linear regression coefficients pH, time, and temperature during pre-formed chloramination	64
3.12	Comparison of normalized linear regression coefficients pH, time, and temperature during inline-formed chloramination	65
3.13	THM and DHAN formation during chlorination, pre- and inline-formed chloramination at pH 7 and 23° C	69
3.14	THM and DHAN BIF during (a) chlorination, (b) pre-formed chloramination, and (c) inline-formed chloramination in relation to contact time.....	70
3.15	Effect of pH and temperature on THM and DHAN BIF during chlorination, pre- and inline-formed chloramination.....	73
3.16	Comparison of standardized linear, quadratic, and interaction regression coefficients for (a) THM BIF and (b) DHAN BIF during chlorination, pre- and inline-formed chloramination	74
4.1	Percentage of DBP loss from hydrolysis within feed solution mix (white bars), percentage of DBP loss from hydrolysis during batch tests for THM4, I-THM+CH, HKs+HANs+ TCNM, and HAcAms (black bars), and losses from volatilization and adsorption (grey bars)	78
4.2	DBP rejection over time by RO (a and b) and NF (c and d)	81
4.3	(a) DBP rejection by NF versus RO and (b) the ratio of DBP passage between RO and NF in relation to their molecular volume	83
4.4	DBP rejection by NF 90 (NF) versus SW 30 (RO)	83
4.5	Comparative HAA rejection by three membranes	84
4.6	Comparison of CNX rejection by three membranes	84
4.7	DBP rejection by RO as a function of DBP properties (a) molecular width, (b) molecular volume, (c) log K_{ow} , and (d) dipole moment	87
4.8	HAA rejection by SW 30 (top row) and ESPA 2 (bottom) as a function of properties: (a) molecular volume, (b) Log K_{ow} , and (c) pKa	88
4.9	DBP rejection by NF as a function of DBP properties: (a) molecular width, (b) molecular volume, (c) log K_{ow} , and (d) dipole moment	89
4.10	Multiple linear regression prediction by (a) RO and (b) NF	92
4.11	Rejection of BCAN, DCAcAm, 1,1,1-TCP, and TIM as a function of transmembrane flux	93
4.12	Rejection of CNXs by ESPA2 as a function of transmembrane flux	94
4.13	Rejection of HAAs by ESPA2 as a function of transmembrane flux.....	95
4.14	Rejection of BCAN, DCAcAm, 1,1,1-TCP, and TIM as a function of crossflow velocity.	95
4.15	(a) Rejection of BCAN, DCAcAm, 1,1,1-TCP, and TIM as a function of temperature; (b) DBP rejection as inverse ratio (1-35°C to 23°C) in relation to molecular volume by RO, with 0 meaning no impact caused by the temperature change.....	97
4.16	Effect of temperature on salt rejection and permeability of RO and NF membranes	97
4.17	Rejection of CNXs by ESPA2 as a function of temperature	98
4.18	Rejection of HAAs by ESPA2 as a function of temperature.....	99
4.19	Effect of pH on salt rejection and permeability of RO and NF membranes.....	99

4.20	Rejection of BCAN, DCACAm, 1,1,1-TCP, and TIM as a function of pH	100
4.21	Rejection of CNXs by ESPA2 as a function of pH.....	101
4.22	Rejection of HAAs by ESPA2 as a function of pH	101
4.23	Rejection of HAcAms by NF as a function of ionic strength	102
4.24	Multiple linear regression of DBP rejection by RO: (a) calibration model and (b) validation model	103
4.25	Comparison of the application of rejection data obtained with the developed MLR and measured N-Nitrosamine rejection data	105
4.26	DBP rejection by RO at pilot-scale as a function of DBP properties (a) molecular width, (b) molecular volume, (c) log K_{ow} , and (d) dipole moment.....	106
4.27	DBP rejection in the crossflow system at bench-scale in relation to a spiral wound module at pilot-scale	108
4.28	Impact on BDCM, DBAN, 1,1-DCP, and DCACAm rejection at pilot- and bench-scale by (a) transmembrane flux, (b) pH, and (c) temperature	109
4.29	Inverse DBP rejection ratio 35° C versus 23° C as a function of molecular volume, with 0 meaning no difference in rejection between 35° C and 23° C.....	110
4.30	Impact of recovery on rejection of (a) DBAN, (b) 1,1-DCP, (c) BDCM, and (d) DCACAm at various transmembrane flux, pH, and temperature	111
4.31	Comparison of the application of rejection data obtained with the developed MLR with (a) pilot-scale and (b) bench-scale data and measured N-Nitrosamine rejection data during pilot-scale trials.....	112
5.1	(a) Real and observed rejection of DCAN, TIM, and glycerol as a function of transmembrane flux; (b) DBP rejection versus $\bar{\epsilon}$	116
5.2	(a) Spiegler-Kedem best fits of DBP real rejection data for BCAN, CH, TCNM, 1,1,1-TCP, and TCACAm, (b) obtained permeability coefficient P in relation to solute molecular width.....	117
5.3	(a) Spiegler-Kedem best fit for DCAN observed and real rejection, (b) model parameters P and σ obtained for Spiegler-Kedem best fit with real rejection (grey-filled symbols) and observed rejection.....	118
5.4	Spiegler-Kedem best fits (solid line) of experimental DBP rejection data by RO: (a) TCM, DCIM, CDIM, BDIM, TIM, and CH, (b) BDCM, DBAN, DCACAm, 1,1-DCP, and TBNM.....	120
5.5	(a) Model parameters P and σ in relation to each other; (b) P in relation to molecular volume.	121
5.6	(a) Amount of DBP mass adsorbed on active surface layer after filtration experiments divided by the initial DBP concentration spiked at the beginning of the filtration experiments; (b) DBP mass adsorbed in relation to the ratio of DBP width to log K_{ow}	123
5.7	DBP rejection during full-scale RO filtration at Gibson Island AWTP (ESPA2), Bundamba AWTP (TFC-HR), and at pilot-scale (ESPA2)	124
5.8	Single leaf of unwound spiral wound module divided into grid segments represented by index numbers i and j along the x-axis and y-axis, respectively	125
5.9	(a) Observed and modeled feed pressure along three spiral wound modules in series, (b) observed and modeled transmembrane flux as a function of the feed pressure at one spiral wound module.....	129

5.10	Modeled and observed rejection of BDCM, DCAN, 1,1-DCP, and DCACAm as a function of transmembrane flux	130
5.11	Impact of recovery on the rejection of BDCM, DCAN, 1,1-DCP, and DCACAm (18 L/m ² h)	131
5.12	Development of BDCM, DCAN, 1,1-DCP, and DCACAm along Stage 1, Stage 2, and Stage 3 with one pressure vessel holding six membrane elements.....	132
5.13	DBP rejection during full-scale RO filtration at Gibson Island AWTP (ESPA2), Bundamba AWTP (TFC-HR), modeled DBP rejection after Stage 3 and modeled cumulative rejection after Stage 3.....	133
6.1	DCAN rejection in relation to salt rejection across the RO membrane at varying crossflow velocities (0.04–0.16 m/s), flux range (3–55 L/m ² h), temperatures (23–36° C), pH (4.5–8.5), and ionic strength (7–70 mM)	140

Tables

1.1	Australian Guidelines for DBPs in Drinking Water and their Regulation in Recycled Water Compared to the U.S. Regulated Levels in Drinking Water	4
1.2	Chloramine Reactions.....	6
1.3	Rate Constants for Iodide and Bromide Oxidation by Chlorine and Chloramine	9
1.4	Summary of Impact of Operational Parameters on DBP Formation, Investigated During Chlorination or Chloramination.....	10
2.1	Chemical Structure of DBPs Analyzed.....	22
2.2	Characteristics of the Bundamba Wastewater Centre.....	29
2.3	Characteristics of the Oxley Creek Wastewater Centre.....	29
2.4	Characteristics of the Goodna Wastewater Centre	30
2.5	Characteristics of the Wacol Wastewater Centre.....	30
2.6	Characteristics of the Gibson Island Wastewater Centre.....	31
2.7	Characteristics of Secondary Effluent in Sampling Campaigns at Bundamba (B) and Gibson Island (GI) AWTP, and Freshly Sampled Secondary Effluent at Bundamba and Gibson Island WWTP for Kinetic Studies.....	32
2.8	Stability of DBPs Formed during Chlorination of Secondary Effluent and after Subsequent Storage.....	35
2.9	Stability of DBPs Formedduring Chloramination of Secondary Effluent and after Subsequent Storage	36
2.10	Characteristics of the RO and NF Membrane Used in this Study.....	39
3.1	Water Characterization for Bundamba (B) AWTP and Gibson Island (GI) AWTP	46
3.2	Experimental Factors for Each Disinfection Strategy and Corresponding Levels Investigated.....	61
3.3	Obtained Explained (R^2) and Predicted (Q^2) Variation of the Models for Chlorination, Pre- and Inline-Formed Chloramination, and their Respective Degrees of Freedom (DF)	62
3.4	Bromide–Chlorine–Chloramine Reactions Relevant during Water Treatment Conditions.....	67
3.5	Explained (R^2) and Predicted (Q^2) Variation of the Models for Chlorination, Pre- and Inline-Formed Chloramination, and their Respective Degrees of Freedom (DF)	74
4.1	DBP Properties	79
4.2	MLR Regression Statistics—RO Membranes	90
4.3	MLR Regression Statistics—NF Membranes.....	90
4.4	Calibration Model Statistics (Data Normalized).....	104

4.5	Nitrosamine Properties	105
4.6	MLR Statistics for RO—Pilot-Scale	107
5.1	Fitted Transport Parameters for NF Membrane.	117
5.2	Fitted Transport Parameters for RO Membrane.....	119

Acronyms

ANOVA	analysis of variance
AOP	advanced oxidation process
AWMC	Advanced Water Management Centre
AWTP	advanced water treatment plant
BCAA	bromochloroacetic acid
BCAcAm	bromochloroacetamide
BCAN	bromochloroacetonitrile
BCIM	bromochloroiodomethane
BDCAA	bromodichloroacetic acid
BDCAcAm	bromodichloroacetamide
BDCM	bromodichloromethane
BDIM	bromodiiodomethane
BIAcAm	bromoiodoacetamide
BIF	bromine incorporation factor
BNR	biological nutrient removal
Br-DBP	bromine-containing DBP
Br-HAN	bromine-containing HAN
C-DBP	carbon based disinfection by-product
CDIM	chlorodiiodomethane
CH	chloral hydrate
CIAA	chloroacetic acid
CIAcAm	chloroiodoacetamide
Cl-HAN	chlorine-containing haloacetonitriles
CNBr	cyanogen bromide
CNCl	cyanogen chloride
CNX	cyanogen halides
CP	concentration polarization
CT	product of concentration and contact time
DBAA	dibromoacetic acid
DBAcAm	dibromoacetamide
DBAN	dibromoacetonitrile
DBCAA	dibromochloroacetic acid
DBCACAm	dibromochloroacetamide
DBCM	dibromochloromethane
DBIM	dibromoiodomethane
DBP	disinfection by-product
DCAA	dichloroacetic acid

DCAcAm	dichloroacetamide
DCAN	dichloroacetonitrile
DCIM	dichloriodomethane
1,1-DCP	1,1-dichloropropanone
DHAN	dihalogenated acetonitriles
DHAN-Br	bromine-containing DHAN
DIACAm	diiodoacetamide
DM	dipole moment
DOC	dissolved organic carbon
DON	dissolved organic nitrogen
DPD	N,N-diethyl-p-phenylenediamine
DPR	direct potable reuse
EEM	excitation emission matrix
EfOM	effluent organic matter
GC-ECD	gas chromatography-electron capture detector
GC-MS	gas chromatography-mass spectrometry
GI	Gibson Island
HAA	haloacetic acids
HAcAm	haloacetamides
H-Acc	H-bond acceptor
HAN	haloacetonitriles
HAN4	sum of the concentrations of TCAN, DBAN, BCAN, and DCAN.
HK	halo ketones (halopropanones)
HNM	halonitromethanes
HOBr	hypobromous acid
HOCl	aqueous chlorine
HOI	hypoiodous acid
HQRW	high-quality recycled water
IC	ion chromatograph
IO ₃	iodate
IPR	indirect potable reuse
I-THM	iodinated trihalomethane
LC	liquid chromatograph
LLE	liquid/liquid extraction
LMH	liter per square metre per hour
MBAA	monobromoacetic acid
MCAA	monochloroacetic acid
MCL	maximum contaminant level
MF	microfiltration
MLR	multiple linear regression
MtBE	methyl tertiary-butyl ether
MV	molecular volume

MW	molecular weight
MWCO	molecular weight cut-off
MWidth	molecular width
N-DBP	nitrogenous disinfection by-product
NDBA	N-nitrosodibutylamine
NDEA	N-nitrosodiethylamine
NDMA	N-nitrosodimethylamine
NDPM	N-nitrosodi-n-propylamine
NF	nanofiltration
NH ₂ Br	monobromamine
NHBrCl	bromochloramine
NH ₂ Cl	monochloramine
NH ₃ Cl ⁺	monochlorammonium
NMEA	N-nitrosomethylethylamine
N-mor	N-nitrosomorpholine
NOM	natural organic matter
NPip	N-nitrosopiperidine
NPOC	nonpurgable organic carbon
NPYR	1-nitrosopyrrolidine
OBr ⁻	hypobromite
PA	polyamide
PSA	polar surface area
Q ²	predicted variation
QC	quality control
QHFSS	Queensland Health, Forensic and Scientific Services
R ²	explained variation
RO	reverse osmosis
ROC	reverse osmosis concentrate
RPD	relative percent difference
RSM	response surface modeling
SBS	sodium bisulphite
SD	solution-diffusion
S-K	Spiegler-Kedem model
SHP	steric hindrance pore model
SPE	solid-phase extraction
SUVA	specific ultraviolet absorbance
TBAA	tribromoacetic acid
TBAcAm	tribromoacetamide
TBM	tribromomethane
TBNM	tribromonitromethane
TCAA	trichloroacetic acid
TCAcAm	trichloroacetamide

TCAN	trichloroacetonitrile
TCM	trichloromethane
TCNM	trichloronitromethane
1,1,1-TCP	1,1,1-trichloropropanone
TFC	thin film composite
THM	trihalomethanes
THM-Br	bromine-containing THM
THM4	sum of the concentrations of the four regulated trihalomethanes (TCM, BDCM, DCBM and TBM)
TIM	triiodomethane
TKN	total Kjeldahl nitrogen
TN	total nitrogen
TOC	total organic carbon
UNC	University of North Carolina
UQ	The University of Queensland
U.S. EPA	United States Environmental Protection Agency
UV	ultraviolet
VDW	van der Waals
VIF	variance inflation factor
WDOC	wastewater-derived organic compounds
WWTP	wastewater treatment plant

Foreword

The WateReuse Research Foundation, a nonprofit corporation, sponsors research that advances the science of water reclamation, recycling, reuse, and desalination. The Foundation funds projects that meet the water reuse and desalination research needs of water and wastewater agencies and the public. The goal of the Foundation's research is to ensure that water reuse and desalination projects provide sustainable sources of high-quality water, protect public health, and improve the environment.

An operating plan guides the Foundation's research program. Under the plan, a research agenda of high-priority topics is maintained. The agenda is developed in cooperation with the water reuse and desalination communities including water professionals, academics, and Foundation members. The Foundation's research focuses on a broad range of water reuse and desalination research topics including

- Defining and addressing emerging contaminants, including chemicals and pathogens
- Determining effective and efficient treatment technologies to create 'fit for purpose' water
- Understanding public perceptions and increasing acceptance of water reuse
- Enhancing management practices related to direct and indirect potable reuse
- Managing concentrate resulting from desalination and potable reuse operations
- Demonstrating the feasibility and safety of direct potable reuse

The Operating Plan outlines the role of the Foundation's Research Advisory Committee (RAC), Project Advisory Committees (PACs), and Foundation staff. The RAC sets priorities, recommends projects for funding, and provides advice and recommendations on the Foundation's research agenda and other related efforts. PACs are convened for each project to provide technical review and oversight. The Foundation's RAC and PACs consist of experts in their fields and provide the Foundation with an independent review, which ensures the credibility of the Foundation's research results. The Foundation's project managers facilitate the efforts of the RAC and PACs and provide overall management of projects.

This project investigated the impact of operational conditions including different disinfectants on the occurrence, fate, and mechanisms of formation and removal of regulated and emerging nonregulated disinfection byproducts (DBPs) generated during the production of high-quality recycled water at advanced water treatment plants. DBP formation was affected by pH and temperature but was lowest when applying pre-formed monochloramine for membrane biofouling control as opposed to in situ-formed monochloramine. Similarly, excessive disinfectant contact time beyond the exposure required to inactivate microorganisms should be avoided to limit DBP formation. The processes were evaluated with the Spiegler-Kedem model and multivariate linear regression with the latter showing that besides molecular volume, polarity was an important descriptor for DBP rejection. Furthermore, changes in temperature and transmembrane flux led to the widest variations in rejection. Overall, the research identified a number of operational factors that can lead to increased DBP concentrations in the product water through increased formation, decreased rejection through high-pressure membranes or both.

Doug Owen
Chair
WateReuse Research Foundation

Melissa Meeker
Executive Director
WateReuse Research Foundation

Acknowledgments

The authors gratefully acknowledge the funding for this project by the WaterReuse Research Foundation in cooperation with Veolia Water Australia and Seqwater.

Our thanks go to Cedric Robillot, Annalie Roux (both of Seqwater) and Yvan Poussade (Veolia Water, Australia) for their assistance and guidance throughout the planning and execution of the project. We also thank Veolia Water Australia staff (in particular Bradley Rhodes and Kersval Naidoo) for assistance with sampling at the Advanced Water Treatment Plants. Long Nghiem and Takahiro Fujioka (both from University of Wollongong) are acknowledged for allowing and supporting our use of the University of Wollongong's reverse osmosis pilot plant for DBP rejection experiments.

We thank Beatrice Keller-Lehmann for assistance with chemical analysis at the Advanced Water Management Centre and Marc Pidou for assistance with the development of the laboratory set-up at the Advanced Water Management Centre and insightful discussions.

The project team thanks the Project Advisory Committee of Stuart Khan, Christopher Bellona, Daniel Gerrity, and Stuart Krasner for valuable feedback and ideas.

Principal Investigators

Maria José Farré, *The University of Queensland (Australia)*
Howard S. Weinberg, *University of North Carolina at Chapel Hill (USA)*

Project Team

Wolfgang Gernjak, *The University of Queensland (Australia)*
Katrín Doederer, *The University of Queensland (Australia)*
Ariel Atkinson, *University of North Carolina at Chapel Hill (U.S.A)*
Cedric Robillot, *WaterSecure/Seqwater (Australia)*

Participating Agencies

Seqwater
Veolia Water, Australia

Project Advisory Committee

Stuart Khan, *University of New South Wales*
Christopher Bellona, *Colorado School of Mines*
Daniel Gerrity, *University of Nevada*
Stuart Krasner, *Metropolitan Water District of Southern California*

Executive Summary

Reuse of high-quality recycled water (HQRW) is an increasingly important strategy for meeting current and future demand for potable water, whereby highly treated secondary effluent is used to augment existing water supplies. Reverse osmosis (RO) membranes are commonly used to generate HQRW from secondary effluent but require the application of disinfectants during the pretreatment stages to limit biofouling on their surface and to avoid loss of performance. As an unintentional consequence of this treatment, disinfection by-products (DBPs) are formed. Because of their potential adverse effects on human health, the understanding and control of DBP formation and fate during HQRW production at advanced water treatment plants (AWTPs) is vital.

In this project researchers undertook to understand the fundamentals of the formation and fate of individual DBPs within the groups of trihalomethanes (THMs), iodinated trihalomethanes (I-THMs), haloacetonitriles, halonitromethanes, halo ketones, haloacetamides and haloacetaldehydes across high-pressure membranes at bench-, pilot- and full-scale testing.

In order to understand and control DBP formation during full-scale HQRW production, the effect of operational parameters such as reaction time (0.5–24 hours), pH (5.5–8.5), temperature (23°C–35°C), and disinfection strategy (chlorination, pre- and inline-formed chloramines) was first investigated under controlled conditions at bench-scale. The results revealed that DBP formation in secondary effluent was affected by the various operational parameters in a manner similar to that in drinking water matrices. In particular, the concentrations of halogenated DBPs formed during the first 24 hours of reaction with the different disinfectants followed the order chlorination >> inline-formed monochloramine > pre-formed monochloramine. Depending on the group of DBPs and the disinfection strategy, either pH or reaction time was found to be the most influential parameter. Bromine-containing DBPs (Br-DBPs) were consistently found in treated secondary effluents. Because these species are generally considered to be more toxic than their chlorine counterparts, understanding and quantifying the extent of bromine substitution was undertaken. In the case of Br-DBPs, time was revealed to be the dominant parameter during chlorination although increasing reaction time decreased the amount of bromine incorporation. On the other hand, pH and time were almost equally important during chloramination, but inversely correlated.

DBP rejection by RO membranes at the AWTPs ranged from almost complete for the trichlorinated species to as low as 10% for the dihaloacetonitriles. In order to fundamentally understand the DBP rejection mechanisms by RO and nanofiltration (NF) membranes, an investigation at both bench- and pilot-scale was performed under controlled conditions. In agreement with the observations at full-scale, DBP rejection by RO and NF membranes varied widely from negligible to complete (based on analyte detection limits). In general, the RO membrane achieved higher rejection values than the NF membrane, although the four regulated THMs and three of the I-THMs were not rejected by NF. It was also observed that the intrinsic physicochemical properties of the uncharged DBPs included in the study could substantially affect their removal by the membranes. Multivariate linear regression was performed to further elucidate the influence of various DBP properties on membrane rejection and showed that besides their size, polarity was an important descriptor for DBP rejection. Furthermore, temperature and transmembrane flux led to the strongest variations in rejection although increased transmembrane flux also led to an increase in rejection, except for the I-THMs with intermediate hydrophobicity.

Finally, predictive models were used to elucidate factors and transport mechanisms that determine the rejection of DBPs by the membranes. Model predictions applying the phenomenological (Spiegler Kedem) approach were in good agreement with the experimental data. Experiments performed with a pilot system (4 inch spiral wound modules in series) were used to adapt a mechanistic predictive model to simulate DBP rejection in pilot- and full-scale RO processes. The higher membrane area at pilot-scale resulted in higher rejection of small DBPs with the tendency to interact with the membrane material, whereas increased recovery led to overall decreased rejection.

The results of this study will allow water practitioners to predict DBP formation in recycled water and their behavior in high-pressure membrane processes, which, in turn, will lead to better management and safer production of HQRW.

Chapter 1

Introduction

1.1 Background

Disinfection is an important practice for controlling biological contamination in water. As an unintentional consequence of this treatment, disinfection by-products (DBPs) are formed by the reaction between organic/inorganic matter and disinfectants such as chlorine or chloramines. Although fully acknowledging the importance and benefits of disinfection processes, minimizing DBP formation is part of an overall public health strategy because toxicological studies have associated elevated concentrations of certain DBPs with possible health risks through routes of ingestion, inhalation, and dermal adsorption (Richardson et al., 2007; Sedlak and von Gunten, 2011). An increase in risk of cancer of the liver, kidney, and the large intestine has been shown when laboratory animals are fed high single doses of some DBPs (McDonald and Komulainen, 2005; Rudel et al., 2007), whereas epidemiology studies by Nieuwenhuijsen et al. (2000) identified a relation between the consumption of chlorinated drinking water and adverse birth outcomes. With regard to their individual toxicity, bromine- and iodine-substituted DBPs were found to be more toxic than their corresponding chlorine-containing counterparts (Plewa et al., 2004). Many countries regulate some DBPs in drinking water, particularly trihalomethanes (THMs) and haloacetic acids. However, a large number of other potentially harmful DBPs have been detected after chlorination or chloramination of drinking and surface waters, as well as in secondary effluents (Richardson et al., 2007).

In response to population growth and increasing uncertainty surrounding future rainfall patterns, wastewater reclamation utilizing secondary effluent has been recognized as one of the most effective ways to reduce the demand for limited freshwater. Recycled water can be used for irrigation, industrial application, dual pipe reticulation systems in households, environmental allocation, and direct or indirect potable reuse (DPR/IPR). For all these applications, the water must be treated to a level where it is considered fit-for-purpose. Indirect potable reuse requires an environmental buffer—for example, storage dams or aquifers. However, considerable water losses in storage dams and aquifers through evaporation and ground seepage could be avoided by direct potable reuse (DPR). In terms of sustainability, system efficiency, and the high level of treatment and water quality achieved, DPR appears to be a reasonable option to consider for meeting future potable water needs.

To produce recycled water that meets the quality of drinking water, secondary effluent has to pass several barriers in an advanced water treatment plant (AWTP). A typical configuration of AWTPs to generate high-quality recycled water (HQRW) consists of the pretreatment of secondary effluent through coagulation, which is followed by micro- or ultra-filtration, reverse osmosis (RO), advanced oxidation, stabilization, and final disinfection. In this configuration the RO membranes are the last physical and key barrier for the removal of salt, organics, and pathogens. To maintain their performance, the RO membranes require disinfection during the pretreatment stages to limit biofouling on their surface. The formation of DBPs during the production of HQRW is, therefore, of critical concern because secondary effluent holds a high concentration of DBP precursors contained in the dissolved organic carbon content that is generally in the range of 5 to 15 mgC/L (Farré et al., 2011). Research on DBPs in water treatment processes has been performed almost exclusively in the domain of drinking water, but because those production processes rarely incorporate RO membranes, little data is

available on the RO performance and its potential as a barrier for DBPs. A small number of studies have shown that RO rejection of chloroform, bromoform, and N-nitrosodimethylamine (NDMA) can be negligible (Drewes et al., 2005; Fujioka et al., 2013a); whereas others such as Plumlee et al. (2008) show higher levels of NDMA removal. Besides RO, NF membranes are widely used in water purification processes and are of interest because of their larger pore size compared to RO, which allows higher permeability with resulting lower energy consumption. As a result, the control of DBP formation prior to membrane treatment, as well as the understanding of the key parameters controlling DBP removal during membrane treatment is vital. Also, because of the poor rejection of some of the DBPs, it is crucial to be able to predict their removal not only at bench- but also at full-scale operation. In this context, secondary effluents are of concern because of their high total organic carbon content that can act as DBP precursors. Effluent organic matter may form different DBPs to those formed from natural organic matter during conventional drinking water treatment, either in quantity, identity, or simply in the abundance of different DBPs relative to each other. Hence, it cannot be assumed with certainty that DBP formation will be affected in the same way by operational changes as in drinking water production. Effective control strategies can only be implemented if the key drivers for DBP formation from secondary effluents and removal by high-pressure membranes are well understood.

1.2 DBP Occurrence and Fate During High-Pressure Membrane Treatment in Water Reuse Applications

Development and use of advanced wastewater treatment technologies have greatly improved water quality of receiving waters over the past four decades. However, advances in analytical chemistry and molecular biology in the past decade have also indicated effects of trace level wastewater-derived organic compounds (WDOCs) on biota. Although multiple factors have been identified that may contribute to the observed WDOC effects on wildlife, potential for adverse ecological effects in effluent-dominated receiving waters raise questions about treated effluent used for augmentation of aquatic habitats and the safety of intentional and unintentional indirect potable water reuse.

1.2.1 Water Reuse—Advanced Water Treatment

Historically, high-pressure membranes were designed and used for water softening and desalination purposes. In addition to desalination, membranes also found wide application in industrial separations, environmental protection, and water reuse that has become an important approach to meet growing water demands (Rodriguez et al., 2009). Whether for irrigation, industrial applications, dual pipe reticulation systems in households, or environmental allocation, indirect or direct potable reuse (IPR or DPR) is in use around the globe. If the water is destined for IPR or DPR, the quality of the final water has to meet drinking water standards. The production of high-quality recycled water (HQRW) can be performed in AWTPs based on the treatment of secondary effluent through coagulation, micro- or ultra-filtration, RO followed by advanced oxidation, stabilization, and final disinfection. Combined membrane treatment is often a preferred treatment step during HQRW production because of its high removal efficiency of viruses, pathogens, total dissolved solids, effluent organic matter, and some trace contaminants.

One limitation of the membranes is their performance loss caused by various types of fouling, such as scaling, colloidal, organic, and biofouling. In order to specifically limit biofouling on the membrane surface, disinfectants such as chlorine or chloramines are applied to the source

waters, but their use has a negative side effect because of the formation of DBPs of potential health concern. The occurrence, toxicity, and formation of DBPs are discussed in the following chapter. Once formed, the high-pressure membranes are the last barrier for the DBPs in the treatment train. Hence, membrane technology and separation processes are discussed further in this chapter.

1.2.2 Disinfection By-Products

1.2.2.1 Regulation

The introduction of chlorine for drinking water disinfection at the beginning of the 20th century was an important step in the containment of waterborne diseases. In the United States, the implementation of drinking water disinfection resulted in a reduction of cholera incidences by 90%, typhoid by 80%, and amoebic dysentery by 50% (Ohanian et al., 1989). Besides the obvious public health benefits, the implementation of disinfection during water treatment leads to the formation of DBPs, which result from the reaction of organic matter, bromide, and iodide with the disinfectant. DBP formation during water treatment is an undesirable side effect as it has been associated with adverse health effects (Nieuwenhuijsen et al., 2000; Villanueva et al., 2006).

The first DBPs discovered by Rook (1974) in chlorinated drinking water were THMs, and they subsequently were found ubiquitously in most chlorinated waters. Health concerns associated with THMs led to the adoption of drinking water guidelines and regulation. After Canada suggested a guideline value for THMs in 1978, the U.S. Environmental Protection Agency (US EPA) was the first to regulate the sum of the four chlorine- and bromine-containing THMs (THM4) in 1979. Many developed countries subsequently introduced guidelines and regulation limits for THM4. To date more than 600 DBPs have been identified, although the actual number remains unknown (Richardson, 2003). Few additional DBPs have been regulated over the years, with focus placed on DBPs generated during disinfection with chlorine, such as THMs and haloacetic acids (HAAs). Table 1.1 presents the maximum contaminant levels (MCLs) for DBPs in the drinking water (Australia) and recycled water (Queensland), and these are compared to those regulated in U.S. drinking waters.

1.2.2.2 Toxicity

Since the first regulation of DBPs by the US EPA, many studies investigated the toxicity of drinking water DBPs focusing on mutagenicity, genotoxicity, and toxicogenomic analyses using bioassays, *Salmonella typhimurium*, Chinese hamster ovary cells, or human cells (Cemeli et al., 2006; Itoh et al., 2011; Kargalioglu et al., 2002; Neale et al., 2012; Plewa et al., 2004; Richardson et al., 2008). Elevated DBP concentrations have shown an increased risk of cancer of the liver, kidney, and large intestines of laboratory animals (McDonald and Komulainen, 2005; Rudel et al., 2007), but humans have chronic long-term low-dose exposure so that animal studies are mostly useful for comparative effects of different chemical structures. In addition, adverse reproductive or developmental effects were observed in those animals (Andrews et al., 2004). Hence, some DBPs are known animal carcinogens but also are potential human carcinogens. Epidemiological studies found a causal relationship between the consumption of chlorinated water and bladder and colon cancers in humans (Cantor et al., 2010; Michaud et al., 2007; Villanueva et al., 2006). Furthermore, the consumption of chlorinated drinking water was linked to a variety of adverse reproductive outcomes, including spontaneous abortion, low birth weight, and intrauterine growth retardation (Nieuwenhuijsen et al., 2000; Richardson, 2003; Singer, 1999). Toxicological assays have shown that bromine-

and iodine-substituted DBPs are more toxic than their corresponding chlorine-containing counterparts, with the toxicity tending to increase in the order chlorinated < brominated < iodinated for a given class of DBPs (Plewa et al., 2004). Nitrogenous DBPs were found to be more genotoxic and cytotoxic than chlorinated DBPs (Muellner et al., 2007; Richardson et al., 2008), with haloacetonitriles (HANs), halonitromethanes (HNMs) and haloacetamides (HAcAms) being ~1 to 2 orders of magnitude more toxic than the THMs and HAAs (Muellner et al., 2007; Plewa et al., 2008a).

Table 1.1. Australian Guidelines for DBPs in Drinking Water and their Regulation in Recycled Water Compared to the U.S. Regulated Levels in Drinking Water

DBPs	Species	Australian Drinking Water Guideline (µg/L)	U.S. EPA MCL [#] (µg/L)	Queensland Public Health Regulation 2009 (µg/L)
Inorganic DBPs	Bromate	20	10	20
	Chlorite	800	1000	300
Aldehydes	Formaldehyde	500	NA	500
	Trichloroacetaldehyde	20	NA	20
Haloacetic acids	Bromoacetic acid	-		0.35
	Dibromoacetic acid	-		0.014
	Chloroacetic acid	150	60 as	150
	Dichloroacetic acid	100	HAA5*	100
	Trichloroacetic acid	100		100
Cyanogen halides	Cyanogen chloride	80	NA	80
Trihalomethanes	Bromodichloromethane			6
	Dibromochloromethane	250 as	80 as THM4	100
	Bromoform	THM4		100
	Chloroform			200
Halonitromethanes	Bromochloroacetonitrile	-	NA	0.7
	Dichloroacetonitrile	-	NA	2
N-nitrosamines	N-Nitrosodimethylamine	0.1	NA	0.01
	N-Nitrosodiethylamine	-	NA	0.01
	N-Nitrosomorpholine	-	NA	0.001

Notes: [#] MCL is the running annual average concentration for distribution system sample points.

* HAA5 is the sum of the 5 individual species listed in the previous column and the MCL value given is the running annual average concentration for distribution system sample points.

NA = no applicable regulated MCL exists for this analyte.

The toxicity of DBPs has been studied for more than 4 decades, but there are still controversies and uncertainties about explicit health effects in humans. Toxicity studies using animals are conducted at extremely high concentrations, only targeting specific DBPs. This approach is difficult to relate to the low, long-term DBP exposure experienced by humans, for example, through the consumption of disinfected drinking water. In addition, the contribution of measured individual DBPs only accounts for a small proportion of the overall genotoxicity of chlorinated water (Itoh et al., 2011). Because a large variety of DBPs is formed during disinfection, a synergistic effect by their combination might cause additional adverse health effects. One has to bear in mind that the contribution of individual DBPs to the overall toxicity depends on their concentration and intrinsic toxicity. As shown in Figure 1.1, the bromide- or

iodine-containing DBPs exhibit a higher relative toxicity compared to chlorine-based DBPs. Therefore, even if they are at lower concentrations than, for example, the regulated DBPs, they may be of higher relevance.

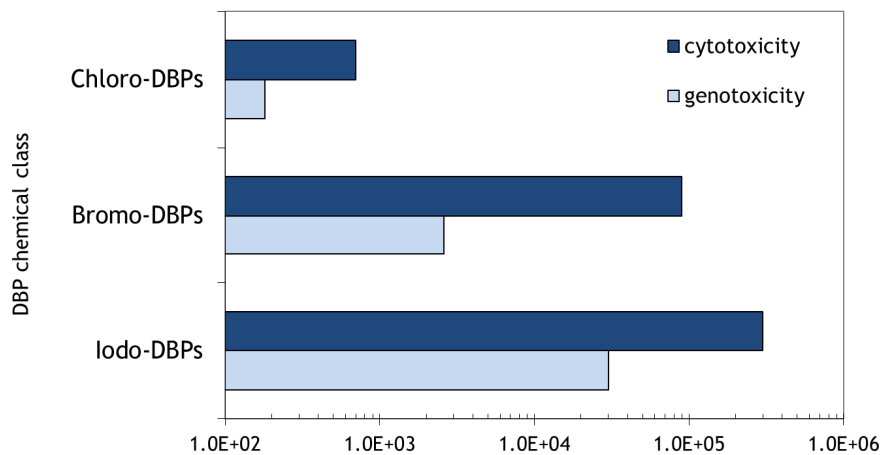


Figure 1.1. Unit CHO cell cytotoxicity and genotoxicity for different DBP groups.

Source: Adapted from Plewa et al. (2008b).

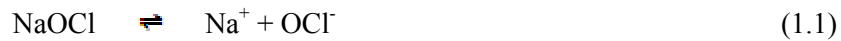
1.2.2.3 Occurrence

An occurrence study at drinking water treatment plants across the United States conducted by Krasner and colleagues (2006) found that various DBP classes beyond the regulated THMs and HAAs were formed after treatment with chlorine or alternative disinfectants (ozone, chlorine dioxide, and chloramines). DBPs including iodinated-THMs (I-THMs), chloral hydrate (CH), HANs, HACams, haloketones (HK), and HNMs were also measured, but at low $\mu\text{g/L}$ levels (75th percentile) of 2.0, 3.0, 4.0, 2.5, and 4.0, respectively. Although alternative disinfectants often lowered THM and HAA formation, they promoted the formation of I-THMs, HNMs and HACams (Krasner et al., 2006), which remain mostly unregulated but because of their toxicity are open for debated importance. The occurrence of DBPs at wastewater treatment plants (WWTPs) after the treatment of secondary effluent was investigated at 23 WWTPs in the United States. Besides THMs and HAAs, HANs, HKs, TCNM, and CH were also discovered after chlorination or chloramination of the secondary effluent at $\mu\text{g/L}$ levels (Krasner et al., 2009a).

1.2.3 Disinfectants

1.2.3.1 Free Chlorine

Chlorine is the most used disinfectant worldwide. The advantage of chlorine is that it can be produced easily and it is relatively inexpensive. Commonly, water disinfection with chlorine requires the application of the disinfectant at the beginning of the process (pretreatment) and at the end, in order to maintain a residual in the distribution system (post-treatment). As a chemical oxidant, chlorine can transform inorganics and organics present in the water matrix (Deborde and Von Gunten, 2008). During the chlorination of water with sodium hypochlorite (NaOCl), hypochlorite ions are released as shown in eq. 1.1:



The OCl^- ions released into the water are able to associate with protons to form HOCl (see eq. 1.2), which as a weak acid tends to undergo only partial dissociation in dilute solutions with a $\text{p}K_a$ of 7.5. Under typical water treatment conditions (pH 6–8) the primary occurring chlorine species are HOCl and ClO_2^- , with HOCl being the major reactive form. Free chlorine can usually be neglected under typical water treatment conditions, as free chlorine hydrolysis is almost complete at $\text{pH} > 4$.



1.2.3.2 Chloramines

Chloramine chemistry is more complex than the chemistry of free chlorine because several different species as well as free chlorine can be present simultaneously due to the unstable nature of the chloramines. Chloramine is usually formed by mixing ammonia with aqueous chlorine. During this reaction, three chloramine species can be formed: monochloramine (NH_2Cl), dichloramine (NHCl_2), and trichloramine (NCl_3). The equations for these reactions (1.3–1.5) are given in Table 1.2. along with equations 1.6 and 1.7 that show the products of reaction between chloramine species. The proportional formation of the different chloramine species is governed by temperature, contact time, but especially by the Cl:N ratio and pH. NH_2Cl formation is favored at pH 6.5 to 9 and a Cl:N mass ratio of 5:1, whereas NHCl_2 is favored at a higher Cl:N range and a lower pH range of 4 to 6 (Kirmeyer, 2004).

Table 1.2. Chloramine Reactions

Eq. No.	
(1.3)	$\text{HOCl} + \text{NH}_3 \rightleftharpoons \text{NH}_2\text{Cl} + \text{H}_2\text{O}$
(1.4)	$\text{HOCl} + \text{NH}_2\text{Cl} \rightleftharpoons \text{NHCl}_2 + \text{H}_2\text{O}$
(1.5)	$\text{HOCl} + \text{NHCl}_2 \rightleftharpoons \text{NCl}_3 + \text{H}_2\text{O}$
(1.6)	$\text{NH}_2\text{Cl} + \text{NH}_2\text{Cl} \rightleftharpoons \text{NHCl}_2 + \text{NH}_3$
(1.7)	$\text{NH}_2\text{Cl} + \text{NHCl}_2 \rightleftharpoons \text{N}_2 + 3\text{H}^+ + 3\text{Cl}^-$

Free chlorine generated by the reversible hydrolysis reaction of monochloramine is always present in solution (Jafvert and Valentine, 1992). Theoretical concentrations of free chlorine in solution have been calculated to increase with decreasing pH (Cimetiere et al., 2010) and observed to be about three times higher at pH 7 than at pH 8.5 for a chloramine concentration of 10 mg/L as Cl_2 (Morris and Isaac, 1983). Despite the hydrolysis to free chlorine, chloramines can decompose via general acid catalysis. In addition, acidic pH favors direct chlorine transfer to form NH_3Cl^+ , which is a very active chlorinating agent (Snyder and Margerum, 1982).

1.2.4 DBP Formation

DBPs form from the reaction between organic and inorganic precursors with a disinfectant. Besides chlorine, chloramines, chlorine dioxide, ozone, or even UV can oxidize a complex natural organic matter (NOM) molecule into simpler moieties, which are then able to react with additional chlorine or chloramines acting as a substitution agent (Krasner, 2009). Every disinfectant forms its own suite of DBPs (Richardson, 1998). During chloramination, for example, the formation of nitrogen-containing and iodine-containing DBPs is promoted. The inorganic precursors Br^- and I^- are mainly responsible for the speciation of the DBPs formed. The pH, temperature, reaction time, and disinfectant concentration also have an influence on DBP formation (Singer, 1994; Stevens et al., 1989).

1.2.4.1 Natural Organic Matter and Effluent Organic Matter Precursors

The composition and amount of NOM present in source waters can influence formation and speciation of DBPs. NOM can be quantified by carbon content in the water by means of total or dissolved organic carbon (TOC or DOC). The proportion of organic nitrogen in aquatic NOM (1–5%) is significantly lower than that of organic carbon (~50%) (Kristiana, 2007). The aromatic carbon content of NOM is higher in humic substances than in non-humic substances and has been linked to DBP formation (Singer, 1999). Westerhoff et al. (2004) proposed that the distribution of organic functional groups and carbon bonding in NOM influences reactivity with halogens and, therefore, with disinfectants.

Amino acids and other nitrogenous compounds have been suggested to act as potential precursors for CH via intermediate aldehyde formation (Trehy et al., 1986). On the other hand, trichloronitromethane (TCNM) formation may occur from many potential aliphatic, aromatic, nitrated, or aminated precursors (Merlet et al., 1985) and be elevated by the presence of nitrite during chlorination (Hu et al., 2010). The formation of HANs during chlorination has been associated with organic nitrogen-containing materials such as algal organic matter, N-compounds that serve as humic acid surrogates, as well as amino acids (Oliver, 1983; Trehy et al., 1986; Trehy and Bieber, 1981). Chlorination of amino acids can result in the formation of nitriles, leading to subsequent dichloroacetonitrile (DCAN) formation when accompanied by chlorine substitution (Trehy et al., 1986). During chloramination, HANs may be formed through reaction of NOM with HOCl that can be generated from chloramine hydrolysis or the nitrogen from monochloramine can be incorporated into HANs during their formation (Yang et al., 2007). Moreover, aldehydes and nitriles were shown to be intermediates formed during the reactions of monochloramine with organic N-compounds. 1,1-dichloropropanone (1,1-DCP) yields were found to be higher during chloramination compared to chlorination; meanwhile, 1,1,1-trichloropropanone (1,1,1-TCP) could only be detected in chlorinated water (Yang et al., 2007). These observations were explained by Reckhow and Singer (1985), where chlorination of fulvic acids led to 1,1-DCP as an intermediate by-product that could be further oxidized by chlorine to form 1,1,1-TCP. Hydrolysis and an additional chlorine attack on 1,1,1-TCP can result in chloroform formation (Krasner et al., 1989). On the other hand 1,1-DCP was observed to be very stable in the presence of monochloramine because this oxidant is not capable of causing further chlorine substitution and hydrolysis (Yang et al., 2007). A correlation between TOC and THM formation during chloramination was found, where a higher TOC concentration was related to a higher THM production (Zhang et al., 2010). The hydrophobic fraction of the NOM that includes aromatic and phenolic-type structures showed a higher THM formation potential compared to the hydrophilic fraction containing protein-, carbohydrate- and amino-type groups (Krasner et al., 1996).

In addition to NOM, secondary effluent contains effluent organic matter (EfOM) as DBP precursors, which is a mixture of synthetic organic compounds and soluble microbial products derived during biological wastewater treatment processes (Shon et al., 2006). Secondary effluents possess a higher TOC and DOC content compared to typical drinking water sources and can, therefore, provide more DBP precursors. During an occurrence study for 28 U.S. drinking water treatment plants, an average DOC of 2.44 mgC/L was measured (Lee et al., 2006), whereas levels ranging between 6 and up to 12 mgC/L (50th percentile) were reported for secondary effluents (Krasner et al., 2009b). Past work has shown that chlorination of secondary effluent generates DBPs with higher bromine incorporation and, therefore, more toxicity (Richardson et al., 2007) than chlorinated surface waters (Sirivedhin and Gray, 2005). Organic matter in EfOM is thought to be processed in a WWTP in less than a day, but residual EfOM may possess a higher organic nitrogen content (Mitch et al., 2009) with resulting higher levels of N-containing DBPs (Shon et al., 2006). Indeed, municipal secondary effluents were found to be rich in organic nitrogen containing ~ 3 mgN/L (Dotson et al., 2008; Westerhoff and Mash, 2002) and were shown to be a source of precursors for a wide range of DBPs (Krasner et al., 2008). As indicated, secondary effluent differs from traditional source water matrices used for drinking water. Therefore, it cannot be assumed with certainty that DBP formation will be affected in the same way by operational changes as in drinking water production.

1.2.4.2 Inorganic Species: Bromide and Iodide Precursors

In addition to organic precursors, inorganic species—in particular, bromide and iodide—can be involved in DBP formation and speciation. Bromide and iodide are naturally present in surface and groundwater from seawater intrusion and dissolution of geologic sources. Anthropogenic activities, such as chemical production, sewage and industrial effluents as well as seawater ingress into sewer systems, can elevate bromide and iodide levels (Magazinovic et al., 2004; Richardson et al., 2007). Iodide concentrations normally occur in $\mu\text{g/L}$ levels (Fuge and Johnson, 1986), whereas bromide levels can vary from nondetected up to 2 mg/L in surface and groundwater (Magazinovic et al., 2004). A mean of 0.03 mg/L and 0.057 mg/L of bromide was measured in U.S. source waters for the Information Collection Rule (U.S.EPA, 2006) and in a survey of U.S. drinking waters (Amy et al., 1994), respectively. An average of 6 $\mu\text{g/L}$ of iodide was found in drinking water treatment plants and median levels of 0.19 mg/L and 49 $\mu\text{g/L}$ for bromide and iodide, respectively, were measured in a survey of WWTP effluents (Krasner et al., 2009a).

Bromide and iodide can be oxidized by chlorine to hypobromous acid (HOBr , $\text{p}K_a = 8.8$) and hypoiodous acid (HOI , $\text{p}K_a = 10.6$), which, in turn, can react with NOM to generate brominated and iodinated DBPs (Bichsel and Von Gunten, 2000; Plewa et al., 2004; Rook, 1974). More HOBr is formed with increased bromide concentrations present in the water, which also can lead to a shift from chlorinated to brominated DBPs (Krasner et al., 2006; Richardson et al., 2003). Aqueous bromine has been found to react faster with NOM than aqueous chlorine (HOCl , $\text{p}K_a = 7.5$) (Symons et al., 1993). When both chlorine and bromine are present, bromine tends to act more as a substituting agent, whereas chlorine reacts preferentially as an oxidant (Westerhoff et al., 2004). Bromide reacts five orders of magnitude faster with free chlorine than with chloramine whereas, in contrast, iodine reacts quickly with both disinfectants (Table 1.3). The desired sink for iodide present in water is iodate (IO_3^-), which is formed because of further oxidation of HOI in the presence of excess free chlorine (reaction rate 52 $1/\text{M}\cdot\text{s}$ [Bichsel and Von Gunten, 1999]). On the other hand, HOI is relatively stable in the presence of monochloramine with a reaction rate of $<2.0 \times 10^{-3}$ $1/\text{M}\cdot\text{s}$ (Bichsel

and Von Gunten, 1999). For this reason HOI will preferably react with NOM and form undesired iodoorganic compounds during chloramination.

Table 1.3. Rate Constants for Iodide and Bromide Oxidation by Chlorine and Chloramine

	HOCl	NH ₂ Cl
Br ⁻ ↔ HOBr	1.5 x 10 ³ 1/M•s (Kumar and Margerum, 1987)	0.014 1/M•s (Trofe, 1980)
I ⁻ ↔ HOI	4.3 x 10 ⁸ 1/M•s (Nagy et al., 1988)	2.4 x 10 ¹⁰ x [H ⁺] 1/M ² •s (Kumar et al., 1986)

1.2.4.3 Bromine Incorporation

Brominated DBPs have been shown to be more toxic than their chlorinated counterparts (Richardson et al., 2007). This is of concern during HQRW production as previous work has shown that chlorination of secondary effluent can result in a shift from chlorine-containing to more bromine-containing DBPs as compared to surface waters (Sirivedhin and Gray, 2005). Bromine incorporation into DBPs can be influenced by Br⁻:Cl₂ and Br⁻:DOC ratios, as well as DOM characteristics (Cowman and Singer, 1996; Hua et al., 2006). Higher bromide concentration has been shown to lead to a shift to brominated THMs and HANs (Kumar and Margerum, 1987; Krasner et al., 1989), first, because the reaction rate between HOCl and bromide occurs faster than the reaction between HOCl and NOM (Westerhoff et al., 2004). Second, the available HOCl may have been consumed by bromide-generating HOBr, which may react with NOM. Besides the bromide concentration present, operational parameters including disinfectant dose, pH, temperature, and reaction time were also found to contribute to bromine incorporation into THMs and dihalogenated acetonitriles (DHANs) during chlorination of drinking water (Hua and Reckhow, 2012). During chlorination, bromide is oxidized to HOBr and hypobromite (OBr⁻), which are pH-dependent reactive brominating agents (Luong et al., 1982). During chloramination, bromide can react with monochloramine to produce active bromamine species (Bousher et al., 1990; Gazda et al., 1995; Trofe, 1980). Their formation varies in real waters because these reactions are sensitive to bromide concentration, chloramine speciation, and pH. However, the impact of specific conditions on bromine incorporation into THMs and DHANs during chloramination has not been extensively studied in the literature to date. One study by Hua and Reckhow (2012) focused on a drinking water matrix, chlorination, and mostly on a long contact time of 48 hours.

Bromine incorporation into NOM is faster than that of chlorine (Westerhoff et al., 2004). Therefore, different reactions may occur in the first hours of disinfection compared to longer contact times. Moreover, disinfectants, such as chlorine or chloramines differ in their reactive species depending on the pHs, which may influence bromine incorporation. The formation of bromine-containing DBPs during chloramination depends on the formation of bromamines, which varies in real waters depending on the chloramine speciation or bromide levels present. Therefore, different bromine incorporation behavior can be expected with the different disinfectants at varying operational parameters.

1.2.4.4 Effect of Operational Parameters on DBP Formation

The majority of previous DBP research has focused on the effect of operational parameters on DBP formation during the production of drinking water with 48 hours to 10 days of disinfectant contact time (Hua et al., 2006; Lee et al., 2007; Liang and Singer, 2003; Yang et al., 2007; Yang et al., 2010). It is well known that during chlorination of drinking water, THM formation increases with pH (Liang and Singer, 2003) and temperature (Stevens et al., 1976) as well as with chlorine dose and reaction times (Reckhow and Singer, 1985). The same latter trend has been observed for CH (Dabrowska and Nawrocki, 2009). HANs and HKs exhibit a reverse trend, showing a decrease in formation with increasing pH and chlorine dose that is due to hydrolysis and reactions with residual chlorine (Singer, 1994).

During chloramination, THM formation increases at lower pH values as a result of decomposition of chloramines to chlorine (Diehl et al., 2000, Zhang et al., 2010). Yang and co-authors (2007) investigated the parameters affecting chloroform (TCM), DCAN, 1,1-DCP and TCNM formation during chloramination of Suwannee River NOM. They found that longer reaction times and higher chloramine doses led to continued and increased chloroform formation over time for DCAN, 1,1-DCP, and TCM. In addition, pH values between 5 and 6 resulted in the highest DBP concentrations. Finally, an increase in temperature enhanced the formation of TCM but did not affect DCAN and 1,1-DCP. These findings are summarized in Table 1.4

Table 1.4. Summary of Impact of Operational Parameters on DBP Formation, Investigated During Chlorination or Chloramination

	Chlorination					Chloramination			
	THM	HAN	HK	TCNM	CH	THM	DCAN	1,1-DCP	TCNM
↗ Reaction time	↗	↗	↗	↗	↗	↗	↗	↗	↗
↗ pH	↗	↘	↘	↗	↗	↘	↗	↗	max. pH 7
↗ Temperature	↗	↘	↘	↗	↗	↗	→	→	N/A
↗ Disinfectant dose	↗	↘	↘	↗	↗	↗	↗	↗	N/A

Source: Hua and Reckhow, 2008; Kristiana, 2007; Yang et al., 2007.

Note: N/A = not available.

1.3 Membrane Technology in Water Reuse Applications

1.3.1 Membrane Chemistry

The first RO and NF membranes, made of symmetric cellulose acetate, are still in use for some applications. A big step forward in terms of membrane performance for both membrane types was the introduction of thin-film composite (TFC) membranes. Those are arranged with a dense ultrathin (~200 nm) selective layer placed on a porous support layer. The TFC membranes generally consist of three layers (Figure 1.2): The side of the membrane facing the feed water is the active surface layer, which is responsible for water permeation and solute rejection and is made up of polyamide (PA). The PA layer is placed on a spongy support layer

(polyether sulfone) by interfacial polymerization. The third layer is the fabric backing consisting of polyester.

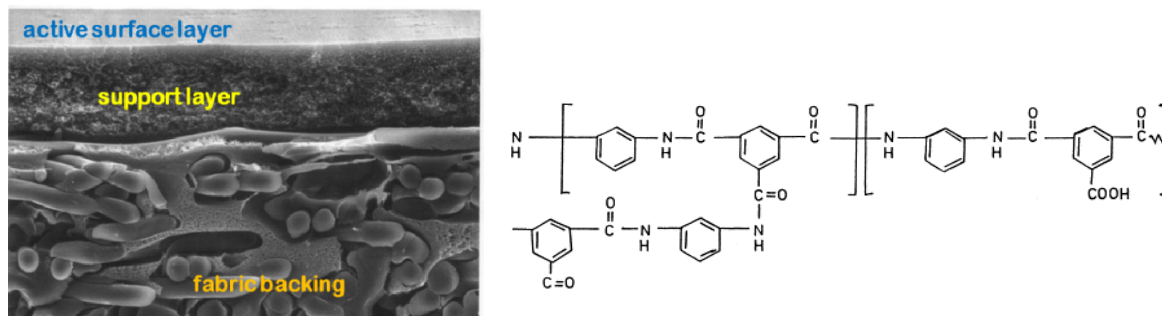


Figure 1.2. Cross section of a TFC membrane by scanning electron microscope and a typical chemical structure of the cross-linked polyamide polymer of the active surface layer.

Source: Wilf, 2007.

The selective PA layer can be optimized for the desired combination of solvent flux and solute rejection, whereas the porous support layer can be optimized for maximum strength and compression resistance combined with minimum resistance to permeate flow (Petersen, 1993). In order to increase the flux, the support layer is hydrophobic, making it favorable for the water dipole orientation. Because of these properties, the composite membranes usually exhibit higher rejection at lower operating pressures than the cellulose acetate blends. The most common RO membranes used in water treatment and seawater desalination are the TFC membranes based on aromatic polyamide (Kim and Kim, 2006; Petersen, 1993). The PA layer possesses acidic functional groups (Figure 1.2), which at the pH of water treatment (pH 6–8) leads to a negative surface charge as measured by the zeta potential. The added acidic functional groups consist of charged sulphone or carboxyl groups in order to increase the fouling resistance and the water flux through the membrane (Ozaki and Li, 2002); that is, a charged hydrophilic layer is attached to the hydrophobic support layer. The active surface layers of polyamide RO membranes, in general, have fully aromatic structures, whereas the active layers of NF membranes are manufactured with either fully or semi-aromatic structures (Petersen, 1993; Tang et al., 2009). NF membranes were developed to perform with a higher water permeability, which results in reduced rejection characteristics for smaller, less charged ions (e.g., NaCl) compared to RO membranes (Bergman, 2007). Therefore, NF membranes are believed to be “looser” and their larger pore size likely contributes to the higher water permeability. However, pores in the active surface layer of RO and NF membranes should be thought of as material-free void spaces in the dense polymer layer, representing tortuous paths for the solute and solvent to pass (Meares, 1976). Hence, there is no specific pore size, rather a pore size distribution of a range of various pore sizes.

The selective removal of multivalent ions by NF may be a combination of the sieving mechanism and charge exclusion in relation to the hydrated radius of the ions. Depending on the membrane itself, a combination of the mechanisms likely determines the order of ion rejection. Size exclusion plays an important role besides charge exclusion because the hydrated radius of the ions differs with the valence of the ion. Multivalent ions are strongly hydrated (Krestov, 1991) leading to a larger hydrated size and higher rejection. In terms of the thickness of the active layer, typical RO membranes are in the range ~150 to 200 nm in contrast to typical NF membranes, which can be as thin as 20 nm (Freger et al., 2002).

1.3.2 Practical Application of High-Pressure Membranes

A typical RO and NF membrane is produced in a spiral wound geometry. Two membrane sheets are glued on three sides, where the space between the glued sheets marks the permeate channel, ending in the perforated permeate tube. The water flows across the membrane sheets from the feed, to finally leave the module more concentrated at the concentrate side. The applied pressure is the driving force for the water to permeate from the feed to the permeate side of the membrane. The pressure along a spiral wound module decreases from the inlet to the outlet because of friction losses, and the crossflow velocity decreases because of the water loss to the permeate side.

Concentration polarization (CP) is a phenomenon resulting from the buildup of a boundary layer of more highly concentrated solute on the membrane surface than in the bulk liquid (Amjad, 1993). The water permeation at the membrane surface leads to a more concentrated solute layer, which, in turn, diffuses back into the bulk liquid. CP can cause several negative effects, including (a) an increase in the osmotic pressure at the membrane surface, which results in a lower water flux; (b) an increase in concentration gradient leading to increased solute passage; and (c) increased fouling or scaling because the surface concentration exceeds the maximum level of solubility. Greater mixing at the membrane surface reduces CP, which can be achieved by increasing the crossflow velocity or optimization of turbulence promoters or spacer placement (Williams, 2003).

During the RO or NF filtration process at full-scale treatment plants, several spiral wound modules are connected in series and held in one pressure vessel (Figure 1.3) in order to generate higher permeate water recoveries. Typical pressure vessels hold between 6 to 8 membrane modules and reach a recovery of ~50%. This configuration is chosen because with fewer modules the pressure vessel would be inefficient and with more modules the crossflow velocity would decrease to a level where CP occurs to a great extent, resulting in scaling.

Several pressure vessels in parallel, even if it is just one pair, make up one stage of the RO treatment train (Figure 1.3). The RO system shown in Figure 1.3 is a 2:1 stage array, with two pressure vessels in Stage 1 and one pressure vessel in Stage 2. The feed is split evenly between the pressure vessels in Stage 1, and the concentrate from Stage 1 is combined to be the feed for Stage 2. Because the flow and pressure across Stage 1 drops approximately by half, only one pressure vessel is required in Stage 2. An overall recovery of around 75% is typically achieved by a two-stage array. If higher recoveries are desired, more stages are necessary. The pressure vessel and multistage configuration leads to a higher recovery; however, it comes with the cost of pressure, permeate flux, and crossflow velocity loss and an ionic strength increase toward the tailing end. This, in turn, leads to higher osmotic pressure and less water permeation.

Changes in pressure, permeate flux, crossflow velocity and ionic strength have an impact on salt rejection and likely influence the rejection of DBPs. However, because of the effect of their inherent different properties on salts, the impact of these operational parameters cannot be expected to be the same.

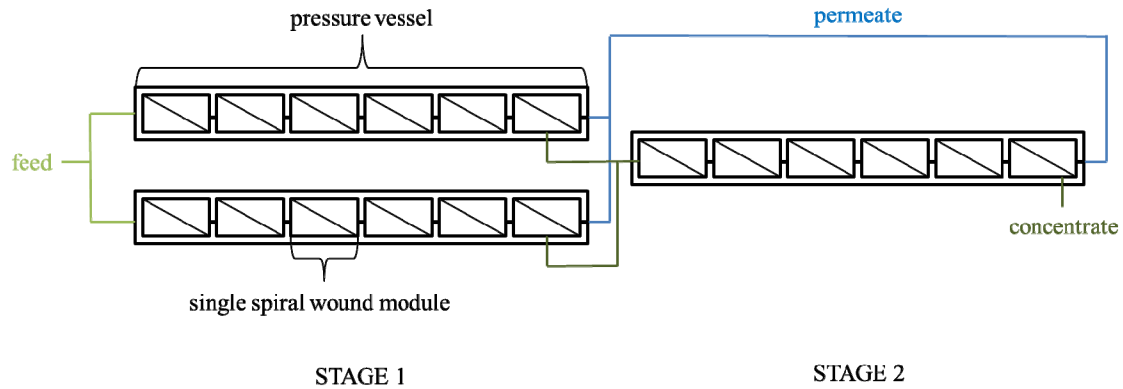


Figure 1.3. Two by one (2:1), two-stage RO train with two pressure vessels in Stage 1 and one pressure vessel in Stage 2.

Note: Each pressure vessel contains six spiral wound modules in series in this schematic.

1.4 Solute Rejection in High-Pressure Membranes

1.4.1 Rejection Mechanisms

Solute rejection mechanisms that have been identified in the literature are size exclusion, electrostatic repulsion, and adsorption and are visualized in Figure 1.4 (Berg et al., 1997; Kiso, 2001; Kiso et al., 1992; Van der Bruggen et al., 1998; Van der Bruggen et al., 1999).

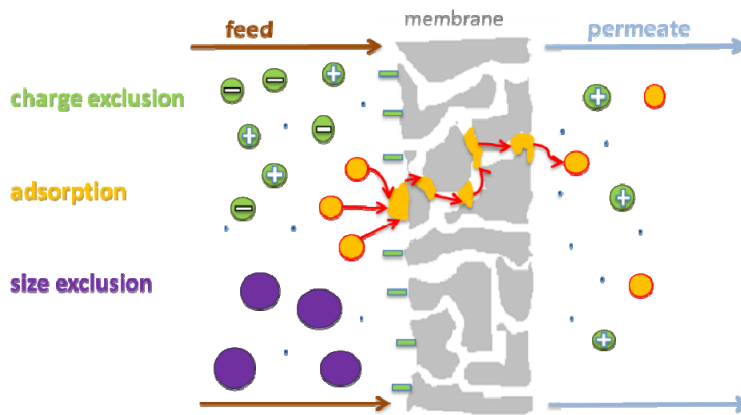


Figure 1.4. Visualization of the three solute removal mechanisms by high-pressure membranes.

Source: Adapted from Verliefde, 2008.

The rejection mechanisms are not only governed by the solute properties and membrane properties but also by the operational conditions, module and system design, and feed water quality. Membrane fouling has also been found to influence solute rejection that is due to altering the membrane surface and its inherent properties (Zularisam et al., 2006). The following section will explain these three removal mechanisms in further detail.

1.4.1.1 Size Exclusion

Size exclusion is the mechanism most easy to comprehend as it is a simple sieving process. RO and NF membranes are not regarded as possessing actual pores but rather material-free

void spaces in the dense polymer, which are formed naturally (Meares, 1976). It has been suggested that the pores for both membranes can be circular and noncircular in shape, open or closed, and possibly form a continuous and interconnecting network (Kamide and Iijima, 1994; Košutic et al., 2000). The porous membrane active layer structure can also be changed during postpolymerization membrane treatments by annealing, swelling, and pressurizing.

Size exclusion occurs when the solutes are larger than the effective pore size of the PA layer of the membrane. The dense molecular structure of the PA layer represents a physical barrier that can be characterized by the molecular weight cut-off (MWCO) of a membrane that is defined by the molecular weight of a solute retained by more than 90% (Van der Bruggen et al., 1999). In the literature, size exclusion is believed to be the dominant rejection mechanism for “large” molecules with a molecular weight >200 g/mol. NF is believed to remove organics with a molecular weight larger than 200 g/mol, whereas RO achieves good removals for solutes with a mass of 100 to 150 g/mol (Pinnekamp and Friedrich, 2003). Membranes with a low MWCO are commonly referred to as “tight” membranes compared to those with a higher MWCO, referred to as “loose” membranes.

1.4.1.2 Electrostatic Repulsion

Solute rejection based on charge exclusion was mainly developed for low pressure RO and NF membranes. These membrane types are constructed with an active surface layer carrying sulphonic or carboxylic groups (Ozaki and Li, 2002) that, depending on the pH of the aqueous solution, will leave the membrane negatively or positively charged. In the lower pH range, the membranes are positively charged, possessing an isoelectric point between pH 3 and pH 5 (Childress and Elimelech, 1996; Xu and Lebrun, 1999). Because the pH typically occurring in desalination and reuse applications is in the range of 6 to 8, the surface charge of the membrane is negative, which will repel solutes with the same charge because of electrostatic repulsion.

A high concentration of cations tends to neutralize the negative surface charge, forming a layer and consequently decreasing anion rejection. This cation attraction and accumulation on the surface layer also causes an uneven distribution of the cations in the bulk solution. Furthermore, the negative charges in the membrane become less than in the bulk, thus creating an electrical potential. This so-called Donnan potential influences the incoming ions by attracting cations and repelling anions. Therefore, an increasing Donnan potential would increase overall ion rejection by the membrane (Ong et al., 2002; Peeters et al., 1998).

Calculation of surface charge kinetic densities indicates that surface charge density is more dependent on anion concentration than on the solution concentration itself (Peeters et al., 1998). Surface charge densities proved to influence the rejection mechanism with charged solutes (Elimelech et al., 1994). The membrane with a higher surface charge demonstrated Donnan exclusion, whereas the one with a lower surface charge density exhibited a combination of Donnan and steric exclusion mechanisms. A rejection mechanism based on charge exclusion is very important for salt and charged solute removal. Charge exclusion by itself might not directly impact the rejection of uncharged solutes. But the amine, hydroxyl, and carboxylic functional groups can affect the membrane properties and indirectly influence solute rejection. It has been reported that with a variation in pH, changes in the membrane structure can occur. This structural change is attributed to stronger electrostatic interactions between the dissociated functional groups, leading to a pore shrinkage at high pH (López-Muñoz et al., 2009). Also, an increase in pore size with increasing pH was proposed in the literature (Donose et al., 2013). Hence, changes in pH not only influence the rejection of

charged solutes, but because of changes in the membrane structure, pH may influence the removal of uncharged organics.

1.4.1.3 Adsorption

Experiments with different hydrophobic compounds (Kimura et al., 2003; Kiso et al., 2000; Nghiem and Coleman, 2008; Nghiem and Schäfer, 2002; Williams et al., 1999) have shown a low rejection of these relatively nonpolar compounds. Their permeation through the membrane matrix is hindered by adsorption (partition) on and in the active surface layer of the membrane (Ben-David et al., 2006). It is believed that this adsorption occurs because of van der Waals (VDW) forces, hydrogen bonding, or hydrophobic interaction with the membrane polymer. Findings of different researchers (Kimura et al., 2003; Nghiem and Schäfer, 2002; Shan et al., 2009) agree with a multistep profile of rejection that consists of a combination of adsorption, diffusion through the membrane, and release into the permeate. The initial phase is dominated by adsorption causing an increase in rejection and related membrane structure change. This is followed by a decrease in rejection as diffusion of the solutes occurs increasing their release into the permeate. Finally, a pseudo-steady state rejection is observed where an equilibrium is reached between the uptake of contaminants at the feed side and its release following diffusion on the permeate side. The result is no further change in rejection. Consequently, the adsorption of hydrophobic compounds can lead to an overestimation of retention (Kimura et al., 2003; Kiso et al., 1992; Košutic et al., 2000) and the measurements have to be performed in a steady-equilibrium to accurately obtain the rejection efficiency of a membrane.

1.4.1.4 Membrane–Solvent–Solute Interactions

During RO membrane filtration, interactions take place among the membrane, the solute, and the water molecules. The transport of solutes and water through RO membranes is described as a combination of diffusive and convective transport. The main transport pathway for water is thought to be convection through the pores. In contrast, for organic solutes that are larger than the pore size, solution and diffusion through the membrane matrix might be the dominant pathway (Steinle-Darling et al., 2010). Uncharged solutes can approach the membrane surface where they likely follow the process in the solution–diffusion model (Wijmans and Baker, 1995). The solution–diffusion pathway may involve three major consecutive steps: (a) diffusion from the water phase into the pore of the membrane; (b) sorption onto the membrane followed by diffusion across the membrane (c) desorption from the permeate side of the membrane.

As shown by Clifford (1975), water in capillaries or small cavities can exist in a specific state, differing from that of bulk water. Research by Pusch (1990) shows that water either interacts strongly with the membrane matrix by H-bond interaction or exists in small clusters. This leads to the water partially losing its hydration capability for ions and nonelectrolytes in the membrane. In his findings, Luck (1987) denotes that in efficient RO membranes, the water exhibits a different structure and also forms weaker H-bonds in between the water matrix because of interaction with the membrane polymer. It is thought that the ability of water to form hydrogen bonds with the hydrophilic groups of the membrane polymer leads to the water flux through the membrane. Hence, solutes that form stronger hydrogen bonds with the polymer than the water molecules can partially displace water molecules and reduce the flux (Nghiem and Schäfer, 2002; Williams et al., 1999).

To increase the resistance against fouling, the membrane surface layer is designed to be more hydrophilic by adding acidic functional groups or blending hydrophobic and hydrophilic

materials together. However, hydrophilic and hydrophobic domains coexist in any polymeric membrane, leading to hydrophobic interactions as one adsorption mechanism. Attractive forces between hydrophobic surfaces have been observed in experiments of different researchers in more than 30 years of research on hydrophobic interaction (Huang and Chandler, 2002; Isrealachvili and Pashley, 1982; Meyer et al., 2006). In their review, Hammer and co-authors (2010) stated that an unexpectedly strong attractive force below distances of 200 Å could be measured between all the hydrophobic surfaces studied to date. The force was also observed above 200 Å up to several thousand Å, which has been mainly attributed to electrostatic attraction and/or bridging cavities (Ohnishi et al., 2000; Meyer et al., 2006). Hammer and co-authors (2010) show with their experiments that in the range of 10 to 200 Å the expected VDW attraction for typical hydrocarbon surfaces with Hamaker constants of $3 - 10 \times 10^{-21}$ J is not negligible. In the short range less than 10 Å, published results show that the attractive forces are greater than any possible VDW force (Kokkoli and Zukoski, 1998). These strong forces may be explained with water structuring effects associated with surface-induced changes in the orientation and/or density of water molecules and H-bonds at the water-hydrophobic interface (Ruckenstein and Churaev, 1991). As shown and still of debate, various effects/forces/interactions contribute to the measured force occurring between hydrophobic surfaces. Therefore, the term “hydrophobic interaction” shall be used in this report, accounting for the combination of the different fundamental interactions. Hydrophobic interactions between the active surface layer and hydrophobic solutes are an intrinsic property of the membrane filtration. Hydrophobic interaction occurs at hydrophobic sites within the surface layer polymer because the affinity between hydrophobic polymers of the membranes and the hydrophobic solutes is high (Braeken et al., 2005).

Polar compounds were also found to interact with the membrane surface layer, hence also being adsorbed by the membrane (Nghiem et al., 2002). Because of their functional groups the polar hydrophobic compounds possess the capacity to form hydrogen bonds. Kiso (2001) stated that polar groups within the compound had varying effects on the adsorption. By employing compounds with different functional groups, the effect of polar groups on adsorption decreases as follows: $-C(O)O- > -CO- > -OH- > -O-$. The H-bonding relies on sharing an electron pair between the functional groups of the membrane polymer and the solute. Matsuura and Sourirajan (1971) discovered during a study with porous cellulose acetate membranes looking at the rejection of alcohols and phenols that rejection decreased with increasing acidity and H-bonding ability. They concluded that increasingly polar compounds are able to sorb on and diffuse through the CA membrane because of H-bonding. Although H-bonding has been found to be solute- and membrane-dependent, uncharged compounds and positively charged compounds have been found to adsorb to polyamide TFC membranes via hydrogen bonding, besides small K_{ow} and H-bonding ability (Bellona et al., 2004; Van der Bruggen et al., 2001; Williams et al., 1999).

In conclusion, solutes with a high affinity for the membrane material can adsorb onto and partition into the membrane matrix more easily, facilitating diffusion through the membrane matrix (Kimura et al., 2003; Nghiem et al., 2004). The partitioning can take place via hydrophobic interaction or the formation of H-bonds. Hence, hydrophobic solutes possessing H-bonding sites might be less rejected by high-pressure membranes.

1.4.1.5 Rejection of DBPs by RO/NF Membranes

Research on DBP removal by RO and NF membranes is limited to a small number of studies looking at THMs, HAAs, HANs, and N-nitrosamines (Agus and Sedlak, 2010; Chalatip et al., 2009; Fujioka et al., 2012a; Linge et al., 2013; Steinle-Darling, 2008; Uyak et al., 2008; Waniek et al., 2002). Rejection of NDMA by RO membranes has been reported between 10 and 40% (Farré et al., 2011; Steinle-Darling et al., 2007), HANs higher than 50% (Agus and Sedlak, 2010; Linge et al., 2013) and removal efficiencies of HAAs between 90 and 100% (Chalatip et al., 2009; Xu et al., 2005), which is generally higher than the 60% rejection reported for THMs (Uyak et al., 2008; Waniek et al., 2002). Operational factors and solute properties have only been thoroughly studied for N-nitrosamines (Fujioka et al., 2012b; Steinle-Darling et al., 2007). It has been observed that an increase in pH and ionic strength leads to a minor impact only on the smaller nitrosamines, whereas increasing temperature leads to a significant drop in rejection for all nitrosamines (Fujioka et al., 2012b). In these studies, it is concluded that N-nitrosamine removal is mainly governed by size exclusion.

1.4.1.6 Proposed Mathematical Models Describing Organic Solute Rejection

Several different mathematical and mechanistic models for the description of solute transport through RO/NF membranes have been proposed in the literature. They can be classified in three major groups: (a) irreversible thermodynamic approaches, (b) solution-diffusion (SD) models, and (c) hydrodynamic models.

(a) *Irreversible thermodynamic model:* The first attempts to describe mass transport through a membrane were suggested by means of irreversible thermodynamics. The equations proposed by Kedem and Katchalsky (1963) and Spiegler and Kedem (1966) regarded the membrane as a black box where basic physical properties such as pore structure, charge density and transport mechanisms are not defined. Yet, it combines diffusive and convective transport as a function of hindrance coefficients. However, this approach allows the membrane to be characterized in terms of solute permeability and the degree of its ability to pass solvent in preference to solute. RO membranes are generally not regarded as possessing actual pores but rather void spaces in the membrane polymer. Hence, the black box model is suitable for mass transport prediction by RO membranes.

(b) *Solution-diffusion model:* The SD model assumes a nonporous dense membrane and is based on the diffusion of the solvent and solute through the membrane. Based on the solubility (partition coefficient) of the solute in and its diffusion rate through the membrane matrix, the SD model predicts solute rejection. SD is a widely accepted and applied model that, however, does not take into account solute–solvent membrane interactions nor convection effects such as pore flow (Williams, 2003). Therefore, the SD model does not adequately describe water or solute flux through the membrane. The solution-diffusion-imperfection model includes the pore flow in addition to diffusion, and the extended solution diffusion model includes the possible pressure dependence of the solute chemical potential. Neither model includes convection or viscous flow, both of which can lead to deviations in removal predictions.

(c) *Hydrodynamic model:* This assumes a uniform cylindrical pore structure and that the water transport occurs by viscous flow. It also allows for consideration of membrane matrix and membrane–solute interactions. The solute transport takes place by diffusion and convection in the membrane pores. A new approach proposed by Van der Bruggen and Vandecasteele (2002) was based on the Spiegler-Kedem equations, but the fundamental component is the

separation of the diffusive and convective transport contributions to the solute flux. Verliefe et al. (2009a) incorporated solute–membrane affinity in the convection–diffusion-based model. Because those models define a specific pore size, they are more accepted for NF membranes that are assumed to possess a certain larger pore size than RO. However, the commonly used hydrodynamic model has only one fitting parameter (pore radius) and that makes it difficult to fit rejection versus flux curves for multiple solutes.

Modeling approaches proposed for spiral wound modules combine the Spiegler-Kedem equations for solute and solvent transport, include concentration polarization, and apply a material balance (Mane et al., 2009; Senthilmurugan et al., 2005; Taniguchi and Kimura, 2000). When predicting solute rejection in single spiral wound modules sequentially, pressure vessels containing several spiral wound modules in series can be simulated. This allows up-scaling of rejection prediction from pilot- to full-scale. Organic solutes, which already show a low rejection at bench-scale or pilot-scale experiments, may show an even lower rejection at full-scale because of the higher recovery. Therefore, it is important to be able to predict their rejection at high recoveries in full-scale applications.

1.5 Summary

DBP formation has been extensively studied in drinking water but as shown in this literature review, secondary effluents have not, so far, received much attention. Because of their more complex and higher organic and inorganic precursor content, they cannot be assumed to act the same as a drinking water matrix when disinfected by chlorine or chloramines. Also, secondary effluents have been found to be richer in bromide which, in turn, can influence the formation of more cytotoxic bromide-containing DBPs. In addition, a wide range of chlorinated, iodinated, and nitrogenous DBPs have been found after disinfection of secondary effluent (Krasner et al., 2009a).

Once DBPs are formed, high-pressure membranes are often the last physical barrier in advanced water treatment. However, researchers have only investigated the rejection of THMs, HAAs, and N-nitrosamines in depth to date besides large datasets studying the rejection of larger molecules, such as pharmaceuticals. For example, the rejection of I-THMs, HNMs, and haloacetamides (HAcAms) has never been reported for high-pressure membranes; these are important DBPs because of their higher toxicity compared to the four chlorine- and bromine-containing THMs.

Three different removal mechanisms have been identified for RO/NF membranes; namely, size exclusion, electrostatic repulsion, and adsorption. Besides size exclusion, the mechanism of adsorption is of interest because solutes with a high affinity for the membrane material can adsorb onto and partition into the membrane matrix more easily facilitating diffusion and, therefore, decreasing solute rejection (Kimura et al., 2003; Nghiem et al., 2004). Partitioning can take place via hydrophobic interaction or the formation of H-bonds. DBPs, such as the THMs, I-THMs, and HNMs, have intermediate hydrophobicity whereas the HANs and HAcAms are polar and possess sites that can form H-bonds influencing their final rejection by the membranes.

1.6 Objectives

This project has three primary objectives, each now described with justification.

- ***Evaluate DBP occurrence in full-scale AWTPs and their formation and speciation during the disinfection of secondary effluent.***

Wastewater reclamation using secondary effluent has been recognized as one of the most effective ways to reduce the demand for limited natural freshwater sources. DBP formation processes could be different in drinking water treatment because of the contribution of EfOM, which contains a mixture of NOM, synthetic organic compounds, and soluble microbial products derived during biological wastewater treatment processes. Past work has shown that chlorination of secondary effluent can result in a shift from chlorine-containing DBPs to those with more bromine incorporation and, therefore, more toxicity (Richardson et al., 2007) compared to surface waters (Sirivedhin and Gray, 2005). Also, as secondary effluent employed in water reuse application differs from traditional source water matrices used for drinking water, it cannot be assumed with certainty that DBP formation will be affected in the same way by operational changes as in drinking water production. After disinfection of secondary effluent, HQRW production involves further treatment steps, which can influence the fate of the DBPs. Hence, the whole treatment train is of interest to fully comprehend DBP occurrence in the final treated water. Moreover, the importance of operational parameters in DBP formation, especially during the first 24 hours of reaction time, a common time frame during HQRW production, is not well understood. Also, because the temperature can vary with seasonal changes, it may have an impact on the formation or degradation of DBPs. In addition, the speciation of disinfectants, such as chlorine or chloramine, is sensitive to changes in pH. For the previously mentioned reasons, it is important to study DBP formation in a range of operational parameters, including different disinfection strategies (chlorination, pre- and inline-formed chloramines), contact times (0.5–24 hours), pH values (5.5–8.5), and temperatures (23–35° C). Thus, a lab-scale research approach applied experimental design techniques and evaluated response surface modeling techniques. In the interpretation of the results, besides DBP formation itself, particular attention was paid to the incorporation of bromine, analyzing the speciation of THMs and HANs.

- ***Determine the efficiency of DBP removal by RO and NF membranes at the bench- and pilot-scale.***

Only a small number of studies have studied DBP rejection behavior by RO and NF, and these were limited to the THMs, HAAs, HANs, and N-nitrosamines (Agus and Sedlak, 2010; Chalati et al., 2009; Fujioka et al., 2012a; Linge et al., 2013; Steinle-Darling, 2008; Uyak et al., 2008; Waniek et al., 2002). The rejection of individual DBPs of I-THMs, HNMs, HAAs, HKs, and CH have not been yet investigated. A wide range of these DBPs were found during an occurrence study in treated secondary effluents (Krasner et al., 2009a).

Operational parameters such as ionic strength, permeate flux, and crossflow velocity change significantly across a high-pressure treatment train and even in individual pressure vessels, which, in turn, potentially can influence DBP rejection. In addition, the feed solution's pH and temperature can also vary during membrane treatment at full-scale. The influence of parameters such as pH, pressure, ionic strength, and membrane type have been shown mainly for N-nitrosamines that are uncharged, hydrophilic organic compounds. For example, an increase in pH and ionic strength led to a minor impact only, whereas increasing temperature led to a significant drop in rejection for all nitrosamines (Fujioka et al., 2012b). Their

molecular size was determined as their main influential factor (Steinle-Darling et al., 2007). The 29 DBPs included in this study possess various intrinsic properties representative of their group with a wide range of molecular properties potentially influencing their rejection.

Attempts to explain the impact of molecular properties on solute rejection have been previously made for micropollutants and pharmaceuticals, which tend to be larger molecules than the DBPs in this study. A multiple linear regression (MLR)-based data interpretation is used in order to understand the influence of various DBP properties on their rejection by RO/NF membranes.

Besides DBP properties, the effect of pH (4.5–8.5), ionic strength (7–70 mM), temperature (23–36° C), crossflow velocity (0.04–0.16 m/s), and permeate flux (3–70 L/m²h) on the removal was investigated at bench- and pilot-scale.

- ***Gain further insight in DBP-membrane interactions and predict DBP removal rates at bench-, pilot- and full-scale RO processes.***

Sorption has been found to play an important role in micropollutant rejection (Schäfer et al., 2011). It can significantly alter or even reverse the dependency on size exclusion as a removal mechanism and lead to lower rejections. The sorption of DBPs on RO/NF membranes is investigated in this study after filtration experiments by desorption of the membrane active surface layer. Several models for organic solute rejection have been suggested in literature, which are important tools to understand and predict solute rejection. For modeling DBP rejection over a wide range of fluxes at bench-scale, the thermodynamic model approach (Spiegler-Kedem) was used. Besides sorption, high process recoveries have been found to have a negative influence on organic solute rejection (Fujioka et al., 2013b). Rejections measured at bench- and pilot-scale can, therefore, overestimate the solute rejection at full-scale. It is crucial to predict the removal of DBPs at high recoveries, especially those which are already poorly removed at bench-scale. This was achieved in this study by adapting and validating a mechanistic predictive model through data generated during pilot testing using three 4-inch modules in series under different operating conditions (permeate flux).

Chapter 2

Materials and Methods

2.1 Chemicals and Reagents

Trichloromethane (TCM), bromodichloromethane (BDCM), dibromochloromethane (DBCM), tribromomethane (TBM), triiodomethane (TIM), and chloral hydrate (CH) were purchased from Sigma-Aldrich (Castle Hill, Australia) and prepared at 5000 µg/mL in methanol (99.8%, Sigma-Aldrich). DCAN, trichloroacetonitrile (TCAN), bromochloroacetonitrile (BCAN), dibromoacetonitrile (DBAN), 1,1-DCP, 1,1,1-TCP, and TCNM were purchased as EPA 551B Halogenated Volatiles Mix at 2000 µg/mL each in acetone (Sigma-Aldrich). Dichloroacetamide (DCAcAm) and trichloroacetamide (TCAcAm) standards were also obtained from Sigma-Aldrich. Tribromonitromethane (TBNM), remaining HAcAms standards including bromochloroacetamide (BCAcAm), bromodichloroacetamide (BDCAcAm), dibromoacetamide (DBAcAm), chloriodoacetamide (CIAcAm), dibromochloroacetamide (DBCACAm), bromiodoacetamide (BIAcAm), diiodoacetamide (DIAcAm), tribromoacetamide (TBACAm) and iodinated-THMs (I-THMs), including dichloriodomethane (DCIM), bromochloriodomethane (BCIM), dibromiodomethane (DBIM), chlorodiiodomethane (CDIM), and bromodiiodomethane (BDIM) were purchased at the highest level of purity from Orchid Cellmark (New Westminster, BC, Canada). Cyanogen chloride (CNCl) in acetonitrile at various concentrations was obtained from SPEX CertiPrep. The concentration of the stocks were estimated by a combination of total organic carbon (TOC) and total nitrogen (TN) analysis and comparison of peak areas from previous runs of standards of known concentration. Cyanogen bromide (CNBr) (97%) solids were obtained from Sigma-Aldrich. Monochloroacetic acid (MCAA), monobromoacetic acid (MBAA), dichloroacetic acid (DCAA), bromochloroacetic acid (BCAA), trichloroacetic acid (TCAA), dibromoacetic acid (DBAA), bromodichloroacetic acid (BDCAA), dibromochloroacetic acid (DBCACAA), and tribromoacetic acid (TBAA) were purchased as EPA 552.2 Acids Calibration Mix (Supelco, 200–2000 µg/mL). NDMA (5000 µg/mL in methanol) and the EPA 521 Nitrosamine-mix containing NDMA, N-nitrosodibutylamine (NDBA), N-nitrosodi-n-propylamine (NDPM), N-nitrosomethylethylamine (NMEA), N-nitrosodiethylamine (NDEA), 1-nitrosopyrrolidine (NPYR), N-nitrosopiperidine (NPip) (2000 µg/mL in methanol), and N-nitrosomorpholine (Nmor) were obtained from Supelco. Deuterated *d6*-NDMA (Accustandard, 1000 µg/mL in dichloromethane) and *d14*-NDPA (Ultra Scientific, >98.9%,) were used as surrogate and internal standard, respectively. The molecular structure of the DBPs analyzed is shown in Table 2.1.

All chemicals used for chemical analysis were of analytical grade and commercially purchased. 1,2-dibromopropane (97%, Sigma-Aldrich) was used as internal standard for DBP analysis. 2,3-dibromopropionic acid (Sigma Aldrich, 98%) was used as an acid surrogate in the haloacetic acid analysis. Analytical grade 99.9% methyl tertiary-butyl ether (MtBE) was purchased from Sigma-Aldrich as Chromasolv® quality and used as extraction solvent. Sodium sulfate anhydrous (10–60 mesh) was purchased from Mallinckrodt Chemicals (Phillipsburg, USA). For solid phase extraction (SPE) used during nitrosamine analysis, U.S. EPA commercial charcoal optimized for NDMA analysis (Restek) was used.

Table 2.1. Chemical Structure of DBPs Analyzed

DBP	Structure	DBP	Structure	DBP	Structure	DBP	Structure
TCM		TCAN		DCAcAm		NDMA	
BDCM		DCAN		BCAcAm		NDEA	
DBCM		BCAN		DBAcAm		NPip	
TBM		DBAN		CIAcAm		Nmor	
DCIM		1,1-D DCP		BIAcAm		MCAA	
BCIM		1,1,1- TCP		DIAcAm		DCAA	
DBIM		TCNM		BDCAcAm		TCAA	
CDIM		TBNM		DBCACAm		MBAA	
BDIM		CNCl		TCAcAm		DBAA	
TIM		CNBr		TBAcAm		BCAA	
CH						TBAA	

Note: DBPs are listed by groups (only the four N-Nitrosamines that measured above the detection limit after completion of the experiments are included).

HPLC grade dichloromethane, methanol, and water were used for conditioning and cleaning the SPE cartridges. Finally, 99% decane (Sigma-Aldrich) was used as internal standard in the final concentration step.

Sodium azide (Sigma-Aldrich 99.99+%) was used as biocide for haloacetic acid samples. Diazald (99%, Aldrich), carbitol (also known as di(ethylene glycol)ethylether, 99+%, Aldrich), 45% potassium hydroxide (Fisher), methanol (HPLC grade, Fisher), and MtBE (Chromasolv 99.9%, Sigma-Aldrich) were used in diazomethane generation. During derivatization of the acids, anhydrous magnesium chloride (99+%, Aldrich) and silicic acid n-hydrate powder (J.T. Baker) were also used.

For the preparation of monochloramine solution, ammonium chloride (TraceSELECT®, ≥99.9% purity), and sodium hypochlorite solution (reagent grade, available chlorine 6–10%, Sigma Aldrich) were used. For pH adjustment, hydrochloric acid (Sigma-Aldrich, ≥32%), sodium hydroxide (SigmaUltra, ≥98%, pellets), and sulfuric acid (Sigma-Aldrich, ≥99%) solutions were prepared using analytical grade reagents and Milli-Q water. L-ascorbic acid Certified ACS grade (Sigma-Aldrich, ≥99%) was used for quenching chlorine and chloramine residuals. Commercial DPD test kits (Hach) were used for the analysis of free and total chlorine (DPD Total and Free Chlorine Reagent, powder sachets).

For the preparation of the background electrolyte solution for the membrane filtration experiments, NaCl was purchased from Univar® analytical reagents. In addition, magnesium sulfate (Mg_2SO_4 , Ajax Finechem Pty Ltd, ≥99.5%) was used for salt rejection tests. Potassium dihydrogenphosphate (KH_2PO_4 , Fluka, puriss. p.a., ≥99.5%) and sodium phosphate dibasic dihydrate ($Na_2HPO_4 \cdot 2H_2O$, Sigma-Aldrich, ≥99.5%) were used to prepare pH buffer solutions. Glycerol ($C_3H_8O_3$, Ajax Finechem Pty Ltd, ≥99.5%) was used for the determination of the membrane pore size.

For amperometric titration, electrolyte crystals (Watertest System Pty Ltd), buffer solutions pH 4 and 7 (Watertest System Pty Ltd), phenylarsene oxide (Watertest System Pty Ltd), iodine (I_2 , Scharlau, ≥99%), and potassium iodide (KI, Ajax Finechem Pty Ltd, ≥99.5%) was used.

2.2 Analytical Techniques

2.2.1 Halogenated Volatiles

2.2.1.1 Liquid–Liquid Extraction

For the analysis of volatile halogenated DBPs with gas chromatography electron capture detection (GC-ECD), the sample was liquid–liquid extracted as described by Weinberg et al. (2002): 30 mL aliquots were extracted in duplicate; the sample pH was adjusted to 3.5 using 0.2 M sulfuric acid; pH was tested using pH stripes (Hydrion® Brilliant Dip Stiks, pH range 0.0–6.0). Subsequently, the sample was extracted by adding 3 mL MtBE (containing 200 µg/L of 1,2-dibromopropane as an internal standard) and 10 g of pre-baked (at 500° C) sodium sulfate. Samples were vortexed for 1 minute. After settling for 5 minutes, 1.5 mL of the MtBE layer was transferred to two GC vials for injection.

2.2.1.2 GC Analysis

Analysis was performed on an Agilent 7890A GC with ^{63}Ni electron capture detector at 300° C; 2 µL sample volumes were injected by parallel double-pulsed splitless injection at

140° C; chromatographic separations on the GC-ECD were performed using an Agilent DB-5 column for quantification (30 m x 0.25 mm i.d., 1.0 µm film thickness); and an Agilent DB-1 column for confirmation (30 m x 0.25 mm i.d., 1.0 µm film thickness). The oven temperature program was used as follows: 35° C for 25 minutes, ramped to 100° C at 2° C/min and held for 2 minutes, then ramped to 200° C at 5° C/min, and the final ramp reaches 280° C at 50° C/min leading to a total run time of 81.1 minutes. This long run allowed for analysis of the halogenated volatiles and the HAcAms simultaneously.

2.2.1.3 Quality Control

Precision was measured using relative percent difference (RPD) of the duplicate analyses of each sample. RPD should be less than 10%. The coefficient of variation of all the internal standard responses for the complete set of samples must be less than 15%. Individual samples responsible for elevating this value above the threshold were flagged. Calibration curves were prepared before extraction of every sampling campaign or every second day during long experiments. The accepted recovery ranged between 80 and 120%. Secondary effluent and Milli-Q water blanks were included in every extraction. A calibration check standard was prepared in the mid-range of the standard calibration curve and was injected every 10 samples. If the detector response for this sample varied more than 10% from the previous injection, all samples analyzed between the two injections were flagged for investigation. The quantitation limit was 0.1 µg/L for all volatile halogenated DBPs and 0.5 µg/L for HAcAms.

2.2.2 Haloacetic Acids

2.2.2.1 Liquid-Liquid Extraction and Derivatization

The method used for the analysis of HAAs with GC-ECD is adapted from U.S. EPA Method 552.2 (Munch, et.al., 1995). Acid surrogate was added to 20 mL aliquots (each sample in duplicates) of each aqueous sample. The samples were acidified using 1.5 mL of concentrated sulfuric acid. Subsequently, the sample was extracted by adding 4 mL of MtBE (containing 100 µg/L of internal standard, 1,2-dibromopropane) and 10 g of (baked at 400° C) sodium sulfate. Samples were vortexed for 1 minute and 2 mL of the organic layer was transferred to volumetric flasks after settling. The sample was then derivatized by adding magnesium sulfate and diazomethane and then cooled in a refrigerator for 15 minutes. After allowing the sample to warm to room temperature over 15 minutes, the diazomethane was then quenched using silicic acid n-hydrate powder. The derivatized extracts were then transferred to two GC vials for injection.

2.2.2.2 GC Analysis

Analysis was performed on an HP 5890 series II GC with ⁶³Ni electron capture detector at 300° C; 1 µL sample volume was injected by splitless injection at 180° C; chromatographic separations on the GC-ECD were performed using a Zebron ZB-1 column for quantification (30 m x 0.3 m i.d., 1.0 um film thickness). The oven temperature program was as follows: 37° C for 21 minutes, ramped to 136° C at 5° C/min and held for 3 minutes, then ramped to 250° C at 20° C/min and held for 3 minutes.

2.2.2.3 Quality Control

Precision was measured using RPD of the duplicate analyses of each sample. RPD should be less than 15%. The coefficient of variation of all the internal standard responses for the complete set of samples must be less than 15%. The coefficient of variation of all the acid surrogate responses for the complete set of samples must be less than 15%. Individual samples responsible for elevating these values above the threshold were flagged and rerun when possible. Sensitivity check standards were run every 10 samples. Extraction/calibration check samples were prepared with each experiment, with accepted recovery range between 80 and 120%. Matrix spikes were performed with every experiment, with accepted recovery range between 80 and 120%. Milli-Q water and feed solution blanks were included every third day of the experiment. The quantification limit for all HAAs was 0.1 µg/L.

2.2.3 Cyanogen Halide Analysis

2.2.3.1 Liquid-Liquid Extraction

The method used for the analysis of CNXs with GC-ECD is adapted from the Cancho et. al. (2000) and Scimienti et. al. (1995). Because of the high vapor pressure of CNXs, 30 mL duplicate samples were extracted over ice. The samples were adjusted to a pH of less than 3 using 1 M sulfuric acid and then extracted by adding 3 mL of MtBE (containing 100 µg/L of internal standard, 1,2-dibromopropane) and 10 g of sodium sulfate (baked at 400° C). Samples were vortexed for 1 minute. After 5 minutes of settling, the MtBE layer was transferred to two gas chromatography vials for injection.

2.2.3.2 GC Analysis

Analysis was performed on an HP 6890 gas chromatograph with ⁶³Ni electron capture detector at 300° C; 1 µL sample volume was injected by splitless injection at 150° C with a carrier gas flow rate of 21.2 mL/min, then purged to the split vent at 1 minute. Chromatographic separations on the GC-ECD were performed using a Zebron ZB-1701 column for quantification (30 m x 0.25 m i.d., 0.25 µm film thickness). The oven temperature program was used as follows: initial temperature of 30° C, ramped to 35° C at 5° C/min and held for 7.5 minutes, then ramped to 220° C at 50° C/min and held for 12 minutes leading to a total run time of 24.2 minutes.

2.2.3.3 Quality Control

Precision was measured using RPD of the duplicate analyses of each sample. RPD should be less than 20%. The coefficient of variation of all the internal standard responses for the complete set of samples must be less than 15%. Individual samples responsible for elevating these values above the threshold were flagged and rerun when possible. Sensitivity check standards were run every 10 samples. Extraction/calibration check samples were prepared with each experiment. Milli-Q water and feed solution blanks were included every third day of the experiment. The quantification limit for the technique was 5 µg/L CNCl and 20 µg/L CNBr.

2.2.4 N-Nitrosamines

2.2.4.1 Solid Phase Extraction

The method used for N-nitrosamines analysis is based on US EPA Method 251 (Munch and Bassett, 2004). Charcoal cartridges (Restek) were conditioned with 8 mL of dichloromethane, followed by 15 mL of methanol and 25 mL of HPLC water. The cartridges were allowed to dry completely during dichloromethane and methanol cleaning but not during the last cleaning with HPLC water. The flow rate for sample loading was adjusted to <10 mL/min. After sample loading, the cartridges were cleaned with 16 mL HPLC water and dried under vacuum for a minimum of 1 hour.

For elution, 30 mL of dichloromethane was passed through the charcoal cartridge connected to a 6 mL tube packed with previously dried sodium sulfate; 50 µL decane/15 mL sample was added as internal standard during the nitrogen blow down as final concentration step; 1 mL of the concentrated extract was collected for analysis.

2.2.4.2 GC-MS Detection

Samples were analyzed at Queensland Health, Forensic and Scientific Services (QHFSS) by capillary GC-MS (Finnigan Trace G.C. Ultra and Finnigan Trace DSQ) with detection in positive chemical ionization mode using 99.99% anhydrous ammonia as the chemical ionization gas. Ammonia inlet pressure was 100 kPa and the reagent gas flow for chemical ionization was 3.5 mL/min; 2 µL samples were injected in splitless mode into the GC at 250° C. The column used was ZB-5MS (30 m x 0.25 mm i.d., 1.0 µm film thickness). The initial oven temperature was 40° C held for 1 minute and then ramped at 40° C/min to 265° C where it was held for 5.4 minutes. Helium gas at 1 mL/min was used as carrier gas.

2.2.4.3 Quality Control

To evaluate the percentage of recovery of the extraction 50 µL of a 0.5 mg/L deuterated NDMA stock solution in methanol solvent (25 ng/L) were added as surrogate to each 1 L sample. Every batch was accompanied by a standard spiked solution at 50 ng/L and a blank to determine the performance of the extraction and the possible NDMA contamination in the water used for cleaning. Deuterated *d6*-NDMA was used as surrogate standard. The accepted recovery was given as 70% by the US EPA Method 251. The detection limit for the technique was 5 ng/L.

2.2.5 Free and Total Chlorine Analysis

For the determination of the concentration in the NaOCl stock solution and during the preparation of monochloramine, free and total chlorine concentrations were measured in duplicate using the N,N-diethyl-p-phenylenediamine (DPD) colorimetric method following Standard Method 4500-CIG (APHA, 1999).

For free and total chlorine residuals measurements in secondary effluent an amperometric chlorine titrator (Wallace & Tiernan, Siemens) employing back titration was used, which is the recommended determination method in wastewater samples (White, 2011). The concentration of chloramines was calculated by subtracting free chlorine from total chlorine.

2.2.6 Secondary Effluent Characterization

2.2.6.1 pH, Conductivity, UV_{254}

pH and conductivity were measured with a Mettler Toledo SevenEasy. UV_{254} absorbance was measured using a Varian-Cary 50 bio spectrophotometer (Varian, Australia) after 0.45 μm filtration (0.45 μm Nylon filters, 47 mm diameter, PM separation, Australia) of the secondary effluent.

2.2.6.2 Chlorine/Chloramine Demand

Demand tests were carried out by applying a range of chlorine or monochloramine doses to 100 mL aliquots of secondary effluent sample. After these demand test samples were held headspace-free for 24 hours at 23° C, the chlorine or monochloramine residuals were measured and plotted against disinfectant dose. In experimental samples, the appropriate dose to achieve a target residual of 1 mg/L as Cl_2 after 24 hours was selected.

2.2.6.3 Bromide and Iodide Analysis by Ion Chromatography

Samples for bromide and iodide analysis were analyzed at QHFSS by a Metrohm 861 advanced compact ion chromatograph (IC). The eluent was suppressed chemically using 100 mM sulfuric acid, reducing the baseline to approximately 10 $\mu\text{S}/\text{cm}$. This was further reduced to approximately 1 $\mu\text{S}/\text{cm}$ by using a carbon dioxide suppressor. A sodalime eluent absorber was used to stop carbon dioxide from the atmosphere changing the eluent composition.

For bromide, 100 μL of 5000 mg/L ethylene diamine was added to 10 mL of sample. Ethylene diamine preserves the integrity of the sample by binding hypobromous acid/hypobromite, which is an intermediate formed as a by-product of the reaction of either ozone or hypochlorous acid/hypochlorite with bromide ion. If hypobromous acid/hypobromite is not removed from the matrix, further reactions may form bromate ion. The sample loop used was a 50 μL loop. The analytical and guard columns were a Thermo AS23 and Thermo AG23, respectively. The eluent was a mixture of 2.4 g sodium carbonate and 0.34 g sodium bicarbonate made up to 5 L with Milli-Q water. The sample run time was 33 min and the eluent flow rate was 1 mL/min.

For iodide analysis, the sample loop was 100 μL and the eluent flow rate was 1.5 mL/min. The column and guard column were Thermo AS22 and Thermo AG22, respectively. The eluent was a mixture of 2.25 g sodium carbonate and 0.42 g sodium bicarbonate made up to 5 L with Milli-Q water. The sample run time was 34 minutes.

The quantitation limit for bromide and iodide was 0.02 mg/L.

2.2.6.4 Nonpurgeable Organic Carbon Analysis

Nonpurgeable organic carbon (NPOC) was measured at the Advanced Water Management Centre (AWMC) using a JENA multi N/C 3100 instrument. For the NPOC analysis, the samples were acidified adding 17 μL of 2 M hydrochloric acid in 20 mL sample bottles; 99.99% pure oxygen with a flow rate of 200 mL/min was fed into the analyzer for the combustion; CeO_2 was used as an oxidation catalyst and 200 μL was added into the samples. After, the samples were injected into the combustion tube and heated at 850° C. This was done

for 20 seconds under constant stirring and a purge flow rate of about 100 mL/min. The standard solutions were 0.5 to 100 mg/L potassium hydrogen phthalate for calibration purposes. Dissolved organic nitrogen (DON) was calculated as the difference between total kjeldahl nitrogen (TKN) and NH₄-N nitrogen. TKN was measured using a Lachat QuickChem method 10-107-06-2-D. Ammonium nitrogen was measured on a Lachat flow injection analyzer as per the Lachat QuickChem method 31-06-1-A. Nitrate and nitrite were also measured 203 on a Lachat flow injection analyzer as per the Lachat QuickChem method.

For each sample, acceptable precision was a relative standard deviation of less than 3% from the analysis of three sample replicates. The detection limit for the NPOC was 1 mg/L and 0.2 mg/L for TKN, 0.02 mg/L for P-PO₄, 0.04 mg/L for NH₄-N and NO₃-N, and 0.02 mg/L for NO₂-N.

2.2.6.5 Zeta-Potential Measurement

Membrane zeta potential was measured by a SurPASS electrokinetic analyzer (Anton Paar GmbH, Graz, Austria) with an adjustable gap cell and using 1.0 mM NaCl as electrolyte solution. The cell channel height was adjusted to 100 ± 10 µm. The solution pH was automatically titrated from 7 to 2 using hydrochloric acid. All measurements were conducted at room temperature monitored by the instrument at approximately 23° C. The zeta potential of each membrane was calculated from the streaming potential using the Fairbrother-Mastin approach.

2.3 Sampling

2.3.1 WWTP Secondary Effluent

To study the DBP formation kinetics, large volume secondary effluent grab samples were obtained from the Bundamba and Gibson Island WWTPs, South East Queensland. When sampling the WWTPs, Bundamba could receive the secondary effluent as a mix of effluent from up to four plants including Bundamba, Oxley Creek, Goodna, and Wacol. All five WWTPs include biological nutrient removal and achieve typical total nitrogen levels of 5 mg/L or lower. Phosphorus removal varies among the plants, with total phosphorous averaging around 3 mg/L. Details on all WWTPs treatment processes are given in Tables 2.2 to 2.6.

2.3.1.1 Bundamba Wastewater Centre

The Bundamba Wastewater Centre is a 23 ML/d-capacity biological nutrient removal (BNR) plant, currently servicing approximately 75,000 people and industries around Ipswich. The outline of the process is given in Table 2.2 (Gardner et al., 2008).

2.3.1.2 Oxley Creek Wastewater Treatment Plant

The Oxley Creek WWTP is a full nitrogen and phosphorus removal plant that was newly upgraded in 2006 to a 65 ML/d BNR plant servicing 260,000 people and industries in Brisbane's southern suburbs. The source breakdown is 80% domestic and 20% industrial. The outline of the process is given in Table 2.3 (Gardner et al., 2008).

Table 2.2. Characteristics of the Bundamba Wastewater Centre

Process Stage	Description
Primary treatment	Screening and aerated grit channel
Secondary treatment (incl. nutrient removal)	Secondary treatment is by carousel-type extended aeration oxidation ditch, with mechanical surface aerators. The 5-Stage Bardenpho bioreactor is followed by secondary sedimentation tanks.
Sludge age	9–10 days
Tertiary treatment	Currently, disinfection is by gas chlorination
Effluent quality (nutrients)	Total nitrogen <3.6 mg/L Total phosphorous <1.1 mg/L

Table 2.3. Characteristics of the Oxley Creek Wastewater Centre

Process Stage	Description
Primary treatment	Screening and grit removal
Secondary treatment (incl. nutrient removal)	Secondary treatment is by an oxidation ditch configuration for nitrogen removal and some biological phosphorus removal. Additional phosphorus removal is achieved with alum precipitation. The bioreactor is followed by secondary sedimentation tanks.
Sludge age	18–22 days
Tertiary treatment	Disinfection by ultraviolet light: Min. dose of 35 mJ/cm ² ; target dose of 50 mJ/cm ²
Effluent quality (nutrients)	Total nitrogen <5 mg/L Total phosphorous <3 mg/L

2.3.1.3 Goodna Wastewater Treatment Plant

The Goodna WWTP is a mainly domestic catchment with full nitrogen but no major phosphorus removal. The 22 ML/d plant serves 40,000 people and industries in the western suburbs of Brisbane and Ipswich. The outline of the process is given in Table 2.4 (Gardner et al., 2008).

Table 2.4. Characteristics of the Goodna Wastewater Centre

Process Stage	Description
Primary treatment	Screening and grit removal
Secondary treatment (incl. nutrient removal)	Biological nutrient removal by the Modified Ludzack-Ettinger process, followed by secondary sedimentation tanks
Sludge age	9–10 days
Tertiary treatment	Disinfection by chlorine gas
Effluent quality (nutrients)	Total nitrogen <5 mg/L Total phosphorous <6.7 mg/L

2.3.1.4 Wacol Wastewater Treatment Plant

The Wacol WWTP is a 5.6 ML/d BNR plant, servicing 33,600 people. The outline of the process is given in Table 2.5 (Gardner et al., 2008).

Table 2.5. Characteristics of the Wacol Wastewater Centre

Process Stage	Description
Primary treatment	Screening and grit removal
Secondary treatment (incl. nutrient removal)	Activated sludge by secondary sedimentation tanks and using a 5-Stage Bardenpho bioreactor
Sludge age	25–28 days
Tertiary treatment	UV disinfection
Effluent quality (nutrients)	Total nitrogen <2.2 mg/L Total phosphorous <3.3 mg/L

2.3.1.5 Gibson Island Wastewater Centre

The Gibson Island WWTP is a full nitrogen and phosphorus removal plant of 46 ML/d, servicing 200,000 people and industries in east Brisbane. The outline of the process is given in Table 2.6 (Gardner et al., 2008).

Table 2.6. Characteristics of the Gibson Island Wastewater Centre

Process Stage	Description
Primary treatment	Screening and aerated grit channel
Secondary treatment (incl. nutrient removal)	A small anaerobic mixing zone is followed by a carousel-type oxidation ditch with anoxic and aerobic zones. Some enhanced biological phosphorus removal occurs in the anaerobic zone, but there is no additional chemical precipitation of phosphorus. The oxidation ditch is followed by secondary sedimentation tanks.
Sludge age	13–15 days
Tertiary treatment	Not applicable
Effluent quality (nutrients)	Total nitrogen <2.5 mg/L Total phosphorous <3.8 mg/L

2.3.2 AWTP Sampling Campaigns

For studies of DBP formation and rejection at full-scale, two AWTPs (Bundamba and Gibson Island) located in South East Queensland (Australia) were sampled four and three times, respectively. Bundamba was sampled once in January (event B ‘a’) and October 2010 (event B ‘b’) and twice in November 2010 (events B ‘c’ and ‘d’); whereas Gibson Island was sampled twice in February 2011 (events GI ‘a’ and ‘b’) and once in March 2011 (event GI ‘c’). Analytical duplicate grab samples were collected in clear, acid-pretreated screw cap sample vials with PTFE-lined silicone septa. Because of the volatility of the DBPs, samples were collected headspace-free, kept on ice for transport, and stored at 4 °C for extraction the following day. To quench the residual disinfectant, ascorbic acid was added to the vials at twice the required stoichiometric concentration. Travel blanks accompanied the samples during the sampling event. The water characteristics of the sampled secondary effluent between the various sampling campaigns are summarized in Table 2.7.

Figure 2.1 shows the sampling locations throughout the AWTP treatment train. The sample locations chosen at the AWTPs follow the whole treatment train and include the incoming secondary effluent source water before disinfectant addition, UF filtrate before sodium bisulfite (antiscalant) and sulphuric acid (pH adjustment) addition, RO feed, RO permeate, RO concentrate after the advanced oxidation process (AOP), and the final treated water.

Before RO filtration, pre-formed monochloramine (2 mg/L as Cl₂) is added to the secondary effluent. The contact time of pre-formed monochloramine with the water is different at Bundamba and Gibson Island. A relatively long contact time of 28 hours was used at Bundamba (events B ‘c’ and ‘d’) in contrast to half an hour of contact time at Gibson Island. The 28 hours at Bundamba is the result of an intermediate buffer tank for the disinfected secondary effluent before the water undergoes membrane filtration. During events B ‘a’ and ‘b’ the disinfection strategy at Bundamba AWTP was forming chloramines inline, where

ammonia is added prior to chlorine without an intermediate buffer tank, which resulted in an effective contact time of 2 hours.

Table 2.7. Characteristics of Secondary Effluent in Sampling Campaigns at Bundamba (B) and Gibson Island (GI) AWTP, and Freshly Sampled Secondary Effluent at Bundamba and Gibson Island WWTP for Kinetic Studies

Parameter	Units	B	B	B	B	B	GI	GI	GI	GI	LOD
		Kinetics	(a)	(b)	(c)	(d)	Kinetics	(a)	(b)	(c)	
DOC	(mg/L)	9.91	9.05	9.03	10.7	9.34	8.79	7.75	6.43	6.94	1.00
SUVA	(L/mg/m)	2.15	n.a.	n.a.	n.a.	2.57	n.a.	n.a.	n.a.	n.a.	-
pH		7.2	7.6	6.5	7.1	7.2	6.8	6.3	6.4	6.3	-
Conductivity	(μ S/cm)	901	906	1168	1044	1054	n.a.	1215	1257	1233	-
NH ₄ -N	(mg/L)	0.10	0.16	0.06	<0.03	0.08	<0.03	0.28	0.10	0.15	0.03
NO _x -N	(mg/L)	3.28	2.17	1.00	0.55	1.54	0.60	1.02	0.71	0.45	0.03
NO ₂ -N	(mg/L)	0.08	0.13	0.09	<0.03	0.15	<0.03	0.15	0.09	0.08	0.03
DON	(mg/L)	1.40	1.17	1.10	1.29	1.39	0.95	0.86	0.82	0.88	0.03
Bromide	(mg/L)	0.26	n.a.	n.a.	n.a.	0.30	n.a.	n.a.	n.a.	n.a.	0.02

Notes: n.a. = not analyzed; LOD = limit of detection

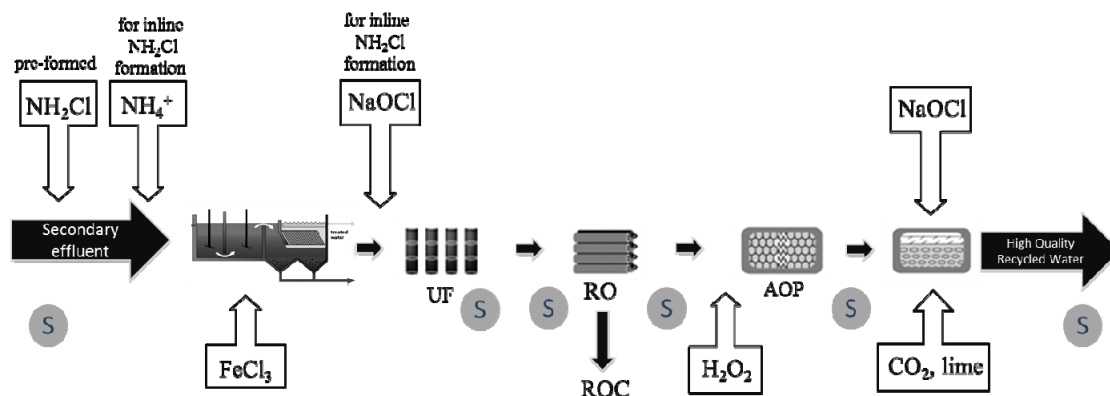


Figure 2.1. Scheme of the AWTPs studied.

Notes: MF = microfiltration, SBS = sodium bisulfite, RO = reverse osmosis, AOP = advanced oxidation process. ROC = reverse osmosis concentrate. S corresponds to sampling points.

Secondary effluent before disinfectant addition was sampled to determine the background levels of DBPs. The effect of RO on DBP rejection was measured using data from samples collected immediately after addition of chloramine in the RO feed and the combined RO permeate in a total of seven different sampling campaigns.

Besides the difference in chloramine contact time, Bundamba and Gibson Island use RO membranes from two different suppliers—TFC-HR (Koch) and ESPA2 (Hydranautics), respectively. Both plants have a three stage, 85% recovery design, and approximate filtration fluxes of 18 L/m²h. Gibson Island secondary effluent showed a slightly higher salinity (Table 2.7) mainly because of industrial discharge.

2.4 DBP Formation Kinetic Studies in Sampled Secondary Effluent

2.4.1 Disinfectant Preparation

Monochloramine stock solutions were prepared freshly before each experiment because monochloramine auto decomposes at high concentrations. Prior to its preparation, the free chlorine concentration in the hypochlorite stock solution was determined. Using this value, the volume of hypochlorite stock solution to be added dropwise to an ammonium chloride solution was calculated to achieve an ammonia-to-free chlorine molar ratio of 1.2:1.

Inline-formed chloramination was achieved by first adding ammonium chloride to the sample and after mixing for 1 minute, sodium hypochlorite was added to the stirred mixing reactor such that the molar ratio of added ammonia to added free chlorine was 1.2:1.

2.4.2 Secondary Effluent Stability Tests

Because secondary effluents are biologically active, their stability was tested during a storage time of 2 weeks. The following stabilization strategies were tested during 14 days of storage:

1. Refrigeration at 4° C

2. Filtration on day of sample collection through Whatman filter no. 1 (11 µm pore size and 47 mm diameter) and storage at 4° C over 14 days
3. Autoclaving at 121° C for 60 minutes on day of sample collection with a TOMY ES-315 autoclave and storage at 4° C for 14 days
4. Acidification at pH 3 with H₂SO₄ on day of sample collection and storage at 4° C over 14 days

For the evaluation of source water stability, DBP formation was measured during 72 hours contact time with disinfectant using the fresh unaltered secondary effluent and compared with DBP formation from the same effluents after 14 days of storage time without any treatment as well as with stabilization strategies 1–4. Results (Table 2.8 for chlorination and Table 2.9 for chloramination) indicate that the secondary effluent was unstable over a time frame of 14 days. In particular, autoclaving the secondary effluent significantly (RPD >25%) affected the formation of DBPs, except for the HKs. Both tables show that DBP formation was least impacted by the 14 days of storage of the unaltered secondary effluent.

Table 2.8. Stability of DBPs Formed During Chlorination of Secondary Effluent and after Subsequent Storage

DBPs	(A) unaltered			(B) filtered			(C) autoclaved			(D) acidified		
	RPD 0.5h	RPD 24h	RPD 48h	RPD 0.5h	RPD 24h	RPD 48h	RPD 0.5h	RPD 24h	RPD 48h	RPD 0.5h	RPD 24h	RPD 0.5h
TCM	-4	-35	-24	-7	-26	-11	20	2	18	4	-5	19
BDCM	-27	-50	-12	-36	-47	-6	34	27	59	-28	-26	14
DBCM	-6	-29	-17	-15	-27	-12	85	76	77	-22	-15	-12
TBM	-18	-24	28	-26	-30	23	-35	-29	22	-47	-38	9
TCAN	-38	-40	45	-29	-17	60	35	62	98	-31	-7	68
DCAN	10	-20	-7	3	-20	-5	70	34	28	-17	-19	-8
BCAN	17	-11	-20	-4	-22	-28	86	34	9	-24	-19	-31
DBAN	16	-9	-23	-9	-23	-37	43	3	-33	-35	-34	-51
CH	-9	-78	-53	4	-42	-22	70	77	88	-50	-40	-26
TCNM	1	-30	-30	-7	-33	-29	-32	-37	-48	-111	-119	-117
1,1-DCP	7	-5	9	-9	-3	5	-14	-31	-23	-32	-12	-7
1,1,1-TCP	-27	-63	-57	-27	-52	-43	-1	3	4	-43	-47	-46

Notes: (A) stored 14 days at 4°C; (B) filtered through 11µm and stored 14 days at 4°C; (C) autoclaved and stored 14 days at 4°C; and (D) acidified to pH 3 and stored 14 days at 4°C. Values in table are RPDs of DBP concentrations after holding compared to initial values. Those that varied by more than 25% are shaded.

Table 2.9. Stability of DBPs Formed during Chloramination of Secondary Effluent and after Subsequent Storage

DBPs	(A) unaltered			(B) filtered			(C) autoclaved			(D) acidified		
	RPD 0.5h	RPD 24h	RPD 48h	RPD 0.5h	RPD 24h	RPD 48h	RPD 0.5h	RPD 24h	RPD 48h	RPD 0.5h	RPD 24h	RPD 0.5h
TCM	<LOD	7	18	<LOD	47	37	<LOD	52	20	98	2	21
BDCM	<LOD	16	22	<LOD	-12	-21	<LOD	-40	-46	<LOD	-22	-34
DBCM	<LOD	-13	19	<LOD	-47	-37	<LOD	-61	-42	<LOD	-58	-58
TBM	<LOD	<LOD	<LOD	<LOD	<LOD	<LOD	<LOD	<LOD	<LOD	<LOD	<LOD	<LOD
TCAN	<LOD	-8	-55	<LOD	-6	-55	<LOD	-6	-53	<LOD	-14	-58
DCAN	18	-2	-5	<LOD	-1	-12	-67	-25	-20	-62	-46	-44
BCAN	<LOD	-12	-8	<LOD	-22	-19	<LOD	-24	-15	<LOD	-59	-53
DBAN	<LOD	<LOD	-64	<LOD	<LOD	-73	<LOD	<LOD	-72	<LOD	<LOD	-90
CH	<LOD	-47	-39	<LOD	-27	-31	<LOD	-33	-29	<LOD	-52	-63
TCNM	<LOD	9	2	<LOD	-13	-24	<LOD	16	25	<LOD	-108	-95
1,1-DCP	-5	-13	-3	-20	-9	-3	-64	-34	-21	-97	-21	-14
1,1,1-TCP	<LOD	-8	-15	<LOD	20	-1	<LOD	7	-22	<LOD	-20	-40

Notes: (A) stored 14 days at 4°C; (B) filtered through 11µm filters and stored 14 days at 4°C; (C) autoclaved and stored 14 days at 4°C; and (D) acidified to pH 3 and stored 14 days at 4°C. Values in table are RPDs of DBP concentrations after holding compared to initial values. Those that varied by more than 25% are shaded.

2.4.3 Gibson Island Secondary Effluent—72-Hour Kinetic Studies

Table 2.7 (column GI kinetics) characterizes the secondary effluent that was used for 72-hour kinetic experiments. Samples were taken after 0.5, 2, 4, 8, 24, 48, and 72 hours of contact time. Chlorine and monochloramine were added at a concentration of 10 mg/L as Cl₂, which resulted in a residual total chlorine concentration of 2 mg/L as Cl₂ after 72 hours of chloramination. All experiments were conducted in amber glass reactors at 23° C, protected from light, buffered (10 mM phosphate buffer pH 6.9) and headspace free to avoid volatilization. The initial solution was divided into eight 250 mL bottles after adding the disinfectant, so that each sampling point corresponded to an individual headspace-free bottle ensuring that no DBPs were lost by volatilization.

2.4.4 Bundamba Secondary Effluent—24-Hour Kinetic Studies

Secondary effluent sampled from Bundamba WWTP was dosed at 25 mg/L as Cl₂ with either sodium hypochlorite, pre-formed or inline-formed monochloramine based on the results of prior demand tests with free chlorine for a target residual of 1 mg/L as Cl₂ after 24 hours of contact time. Although chloramine demand is generally lower than the chlorine demand for the

same water, as was the case with this effluent, chloramines react slower than chlorine and, thus, require longer contact times to achieve the same degree of microorganism inactivation. In this study, DBP formation was compared on an equivalent dose basis to enable a comparison between the disinfectants as well as to produce a measurable formation for some of the DBPs that were otherwise measured close to or below their quantitation limit. Table 2.7 (Column B—Kinetics) characterizes the secondary effluent that was used for all experiments. The pH of the secondary effluent was adjusted to 5.5, 7, or 8.5 prior to disinfectant addition with sodium hydroxide or sulphuric acid and was monitored as stable throughout the duration of the experiment. The disinfectant was added to a 1500 mL amber glass reactor containing the sampled secondary effluent and adjustments to the water were made according to the experimental parameters to be examined. After mixing, the water was gently poured to fill five 250 mL amber glass bottles headspace-free to avoid loss of DBPs by volatilization. Each bottle provided the sample for each of the reaction times (0.5, 2, 4, 8, and 24 hours), which were extracted in duplicate within 24 hours of the completion of the reaction. It was assumed that such a high disinfectant concentration would prevent any biological activity in the samples. In fact, the CT value (750 mg/Lmin) for the applied chloramines was three times higher than what is necessary to inactivate bacteria (Leong et al., 2008). The variable parameters examined were temperature (23° C, 30° C, 35° C), pH (5.5, 7, 8.5) and three different disinfection strategies (free chlorine, pre-formed, and inline-formed monochloramine). After pH adjustment, the secondary effluent immediately was dosed with chlorine from a dilution of a concentrated sodium hypochlorite stock solution or pre- or inline-formed monochloramine.

2.5 Tools for Modeling and Experimental Design

2.5.1 Experimental Design

A full two-level three-factor factorial design (3^2) was employed to investigate the effect of temperature and pH on DBP formation using the three disinfection strategies at different reaction times but at constant disinfectant dose. The D-Optimal Design was chosen for the response surface modeling (RSM) as it maximizes the determinant of the information matrix $X'X$ of the design (Eriksson, 2008). The collected experimental data were analyzed by means of MLR so that each response (i.e., the individual DBP concentrations) could be treated individually. A compilation of MLR coefficients provides an overview of how all the factors affect the response. Besides the linear models, response surfaces were obtained by plotting the parameters pH and time against the response (concentration of individual DBPs) in three dimensions.

2.5.2 Statistical Analysis

For the RSM, the average of duplicate samples were used as actual response value. On the basis of the experimental data, second-order polynomial regressed equations were computed. Optimum parameters were defined by the software Modde® version 4.0. MLR and predictor selection procedures in MLR were done with Datalab®. Purely on the basis of mathematical criteria, predictors were selected with all possible combinations, starting with the predictor that has the highest simple correlation with the response. If the outcome of the model was significantly improved, this predictor was retained and the procedure was repeated. The predictor that accounts for the most new variance was added to the model and, if it made a significant contribution to the predictive power of the model, it was retained and another predictor was considered (Field, 2005). Analysis of variance (ANOVA) tests were also performed to test the significance of the evaluated factors. Outliers identified by normal probability plots were excluded from the MLR (Brereton, 2003). Coefficients that were

statistically significant at the 0.05 level and those with absolute values higher than the corresponding standard deviation were included in the model. Three replicates at the center points permitted calculation of the pure error, allowing the models to be tested if they suffered from significant lack of fit.

The DBP rejection by the Spiegler-Kedem approach was predicted using a nonlinear solver in MATLAB® version R2012. The full-scale simulation was performed in Excel® using an iterative approach.

2.6 Filtration Equipment and Protocols

2.6.1 Background Solution for Filtration Experiments

The background electrolyte solution for the filtration experiments at bench-scale consisted of 1 mM KH₂PO₄ and 7 mM NaCl and KH₂PO₄. The pH was adjusted to 6.8 using hydrochloric acid or sodium hydroxide. All solutions were prepared using analytical grade reagents and Milli-Q water. To maintain the pH at 6.8 over a minimum of 2 weeks, 1 mM KH₂PO₄ was used. To obtain a conductivity of around 900 µS/cm, 7 mM NaCl was used, which is a typical value for a secondary effluent measured during several secondary effluent samplings (Table 2.7).

2.6.2 RO/NF Membrane Characterization

One RO (ESPA2, Hydranautics, Oceanside, CA, USA) and one NF (NF90, Dow Filmtec, Minneapolis, MN, USA) membrane were used at the University of Queensland (UQ), whereas at the University of North Carolina (UNC) two RO (ESPA 2, Hydranautics, Oceanside, CA, USA, and SW 30, Dow Filmtec, Minneapolis, MN, USA) and one NF (NF90, Dow Filmtec, Minneapolis, MN, USA) membranes were used. These membranes were selected on the basis of their distinctly different effective pore sizes. The ESPA2 is a low-pressure RO membrane commonly used in water reuse applications (Fujioka et al., 2012a), whereas the SW30 is a “tighter” membrane than ESPA 2 and is used for desalination applications. The NF90 is a tight NF membrane used in softening and brackish water treatment applications (Van der Bruggen et al., 2008). The membrane coupons used for the filtration experiments were extracted from unused 4-inch modules in both cases. Both membranes are made of a polyamide thin film composite active surface layer with a microporous polysulfone support layer. Inherent characteristics of both membranes can be found in Table 2.10.

Using Milli-Q water at 18 L/m²h the pure water permeability was determined after membrane compaction over night at 11 bar with 0.35 MPa (ESPA2) and 0.14 MPa (NF90) at 23.5° C feed water temperature. The water permeability was determined as described by the following equations:

$$K_w = \frac{J_w}{S} \cdot \frac{1}{NDP \cdot TCF} \quad (2.1)$$

$$NDP = P_f - 0.5TMP - \pi_f \quad (2.2)$$

$$TCF = \left(\frac{1}{\exp\left(K \left(\frac{1}{273.15} + T\right) - \left(\frac{1}{298.15}\right)\right)} \right) \quad (2.3)$$

where J_w = transmembrane flux (L/m²h), S = membrane surface (m²), NDP = net driving pressure, TCF = temperature correction coefficient, P_f = feed pressure (bar), TMP = transmembrane pressure (bar), π_f = feed osmotic pressure (bar), K = membrane characteristic constant, T = temperature (°C).

Table 2.10. Characteristics of the RO and NF Membranes Used in this Study

Membrane	Pure water permeability ^a (L/m ² h•bar)	NaCl rejection ^b (%)	MgSO ₄ rejection ^c (%)	Zeta potential at pH 8 (mV)	Contact angle ^f (°)
ESPA2	5.6 (±0.3)	98.7 (±0.2)	-	-12.8 ^d	53
SW30	1.95	99.4 ^h ; 88.2% ^g	-	-15 mV ⁱ	62° ⁱ
NF90	11.9 (±0.5)	-	97.8 (±0.2)	-7.6 ^e	69

Notes: ^a Errors represent the standard deviation of 5 coupons for ESPA2 and NF90.

^b 1500 mg/L NaCl, 0.75 MPa

^c 2000 mg/L MgSO₄, 0.48 MPa

^d Compacted virgin membranes were measured in this study using a background electrolyte containing 1 mM NaCl using a SurPASS electrokinetic analyzer (Anton Paar GmbH, Graz, Austria)

^e Fujioka et al. (2012b)

^f Fujioka et al. (2013a);

^g observed salt rejection

^h from product specification sheet

ⁱ Tu et. al, 2011

The salt rejection was determined after the pure water permeability using a 1500 mg/L NaCl solution in MilliQ water at 7.5 bar for the ESPA2 and a 2000 mg/L MgSO₄ solution at 4.8 bar for the NF90 membrane. The salt rejection was calculated as follows

$$R_{salt\%} = \left(1 - \frac{C_{sp}}{C_{sf}} \right) \quad (2.4)$$

where $R_{salt\%}$ = salt rejection, C_{sp} = permeate salt concentration (μS/cm), and C_{sf} = feed salt concentration (μS/cm).

2.6.3 RO/NF Crossflow Filtration

2.6.3.1 Crossflow Flat-Sheet Setup

Experiments in this study were carried out on a flat sheet crossflow system (Figure 2.2). To minimize adsorption losses of the DBPs, all system components in contact with the water were built of stainless steel, glass, or Teflon. The feed reservoir of a volume of 20 L was made of clear glass, whereas the plumbed tubing and membrane cell consisted of stainless steel with an effective membrane area of 139 cm². A floating lid made of Teflon and placed in the reservoir on top of the liquid was used to reduce volatilization losses. The crossflow velocity was controlled at 0.12 m/s. Permeate flow was measured with a cylinder and a stopwatch and concentrate flow was controlled by a rotameter (Vögtlin Instruments AG, Switzerland).

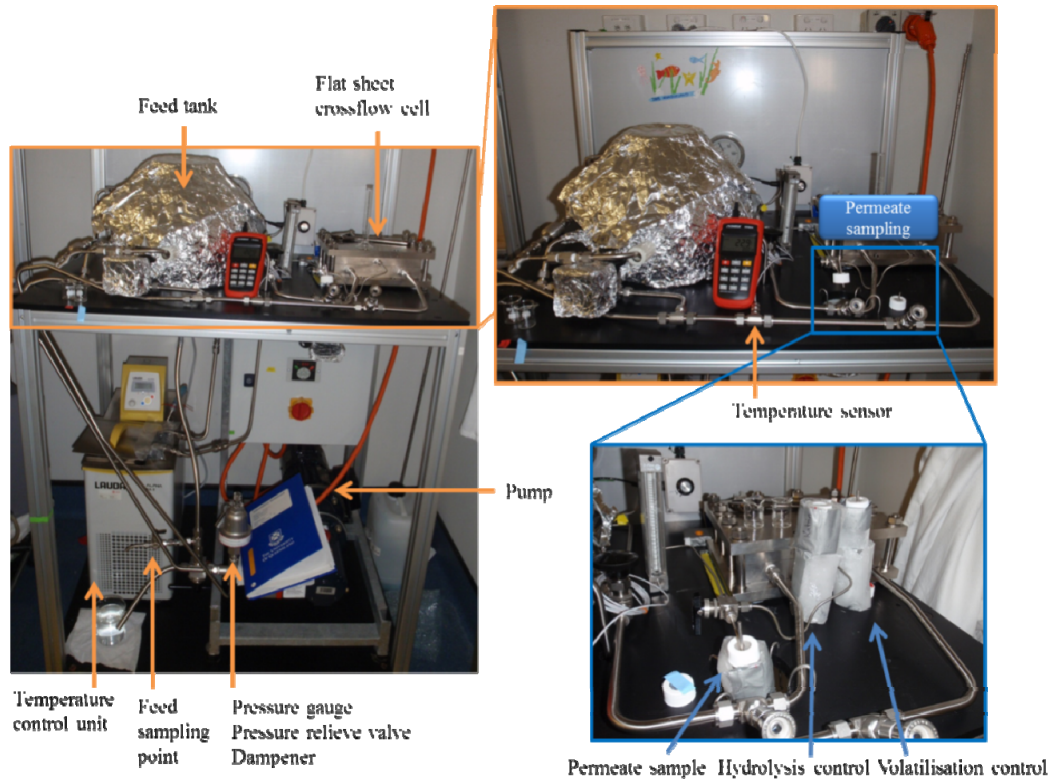


Figure 2.2. Photographs and flow diagram of the crossflow system.

Feed pressure was monitored with an analogue pressure gauge (Ashcroft, Stratford, CT, USA) and controlled with a back pressure needle valve (Swagelok, Melbourne, Australia) in the concentrate line. Temperature control and mixing was achieved by recirculating the feed solution through a stainless steel coil immersed in a temperature controlled bath (Lauda Alpha, Lauda-Königshofen, Germany). To avoid photo degradation losses of the I-THMs, the feed reservoir was protected from light. UNC's system was similar to this, with no differences in materials or flow configuration. The only variances consisted of a larger feed reservoir with a volume of 42 L, a floating Teflon lid was not used, and the water temperature was monitored inline but controlled by the adjustment of the room's temperature.

2.6.3.2 Filtration Protocol

Prior to each experiment the selected membrane coupon was rinsed thoroughly with Milli-Q water. To ensure a stable permeate flux, the membrane coupon was compacted overnight at 11 bar using Milli-Q water. When measuring the pure water permeability, the transmembrane pressure was reduced to 3.5 bar and 1.5 bar after compaction for the ESPA2 and NF90, respectively, to reach a flux of about 18 L/m²h. Salt rejection was determined using a 1,500 mg/L NaCl solution at 7.5 bar for the ESPA2 and a 2,000 mg/L Mg₂SO₄ at 4.8 bar for the NF90. Membrane coupons were used in the DBP study after achieving a minimum salt rejection of 98.5% for the ESPA2 and 97% for the NF90. After rinsing the system thoroughly, the Milli-Q water was replaced with 14 L of background electrolyte solution consisting of 7 mM NaCl and 1 mM KH₂PO₄. The latter was chosen to be able to maintain a pH at 6.8 over a minimum duration of 2 weeks; whereas the former was used to obtain a conductivity of around 900 µS/cm, which is typical for a secondary effluent (Ayache et al., 2012). Unless otherwise stated, the temperature was kept constant at 23.5±0.5° C, pH was 6.8, crossflow velocity was 0.12 m/s, and the flux was adjusted to 18 L/m²h (named hereinafter as the baseline operational conditions). At UNC, the transmembrane pressure was reduced to 3.7 bar after compaction for all membranes tested.

Stock solutions of all DBPs calculated for a volume of 14 L were first dissolved in approximately 50 mL of background electrolyte solution that was then added into the concentrate line leading to the feed reservoir for final mixing. THMs, CH, HAcAms, HANs, and HNMs were spiked at an initial concentration of 50 µg/L and the I-THMs at 20 µg/L (referred hereinafter as the baseline concentration). To ensure steady state prior to measurement of rejection as a function of the variable parameters, the membrane was first conditioned by continuously recirculating both permeate and concentrate for 6 days. Experiments investigating the effect of operational factors were then conducted in a randomized order to avoid systematic bias.

At UNC, the membrane coupons were used in the DBP study after achieving a minimum salt rejection of 98% for the ESPA 2 and 95.3% for the NF90. Unfortunately, with a limited amount of the SW 30 membrane, none of the coupons tested were able to achieve the expected salt rejection as indicated by the specification sheets, only reaching 88% rejection of 1500 mg/L NaCl. Despite this, the rejection of DBPs by the SW30 was still evaluated, but results must be interpreted with great caution. The pure water permeability of SW30 was still significantly lower than both ESPA 2 and NF 90, indicating the apparent pore size distribution was potentially lower for SW30. The baseline operational conditions consisted of a temperature 21.0° C (±0.5° C), pH 7 (±0.5), crossflow velocity of 0.12 m/s (±0.1 m/s), and flux of 18 L/m²h (±1 L/m²h).

At UNC THMs, HANs, Cl₃NM, I₃CH, HKs, and CNCl were spiked at 50 µg/L; CNBr was spiked at 175 µg/L, and HAAs were spiked at 5–50 µg/L initially.

2.6.3.3 Desorption Protocol

To test for the DBP sorption on the RO/NF membranes, immediately after the filtration experiment a piece of the exposed membrane was cut and placed in a 40 mL vial containing 3 mL of MtBE plus internal standard. For 7 days at 4° C and protected from light, the vial was then stored upside down, so that only the active surface layer was in contact with the MtBE. For each experiment, a minimum of nine pieces were cut from the exposed coupon. During the storage of 7 days the “desorption” samples were accompanied by duplicate control samples kept in the same 40 mL vials. The control samples consisted of 3 mL MtBE spiked with all DBPs at 10 µg/L. No losses were observed.

2.6.4 RO Pilot-Scale Filtration at The University of Wollongong

2.6.4.1 4-Inch Pilot-Scale Setup

The pilot system comprises three 4-inch glass-fibre pressure vessels, a 300 L polypropylene feed reservoir, stainless steel pipes in the feed stream and PVC pipes in the permeate stream (Figure 2.3). Each pressure vessel holds one 4-inch RO membrane element.

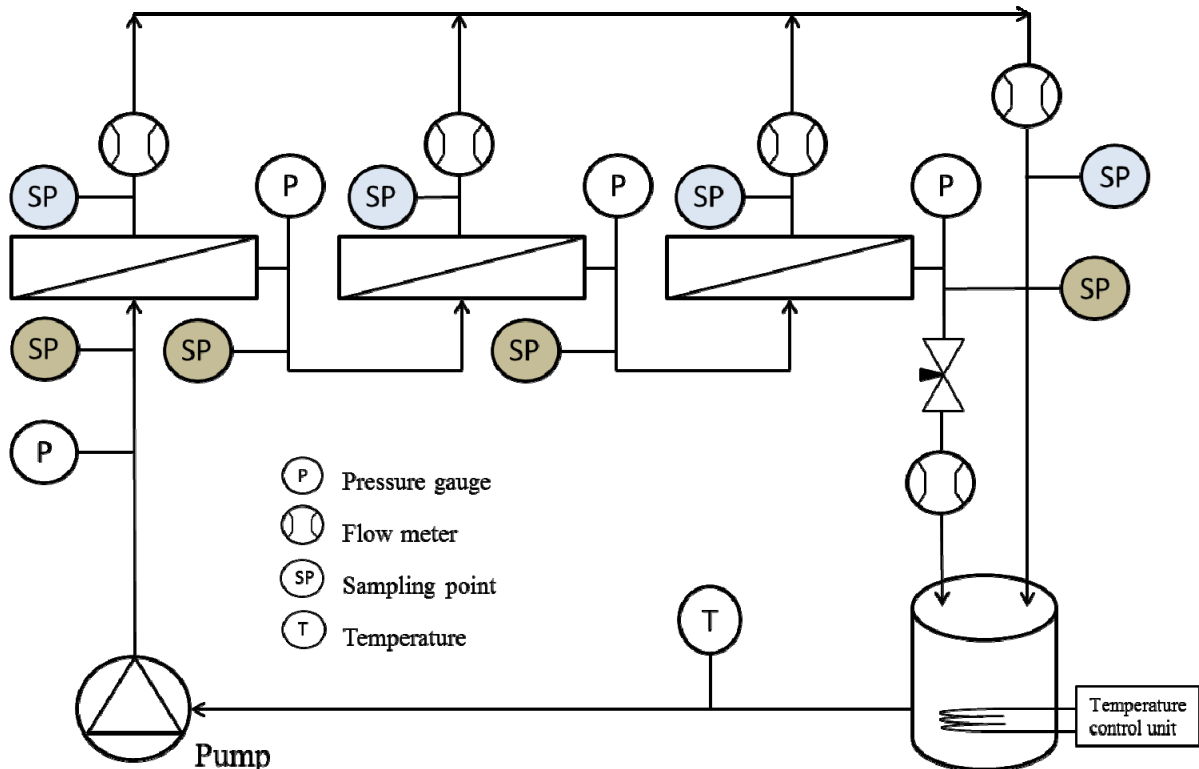


Figure 2.3. Flow diagram of the pilot-scale plant.

The feed solution was transported from the feed reservoir to the first pressure vessel by a high-pressure pump (CRN 3-25, Grundfos, Bjerringbro, Denmark), and the concentrate of the first pressure vessel was transferred to the second pressure vessel followed by the third pressure vessel. Permeate and concentrate were returned back into the feed reservoir. The permeate flow rate and cross flow rate were both monitored by flow meters and regulated by a globe

valve and the speed controller of the pump. Feed solution temperature was conditioned in the feed reservoir using stainless steel heat exchanging pipes connected to a chiller/heater unit (Aqua Cooler S360PD-CT, Chester Hill, NSW, Australia).

2.6.4.2 Filtration Protocol

Prior to the first filtration experiment, the membrane system was operated at approximately 10 bar for 12 hours using 100 L of Milli-Q water. Following the start-up stage, the Milli-Q water in the feed was conditioned with 7 mM NaCl and 1 mM KH₂PO₄ and adjusted to pH 6.8. Afterward, the stock solution consisting of THMs, EPA 551.B mix, CH, DCaAm, and TCaAm was introduced into the feed to obtain a concentration of approximately 10 µg/L after 3 days of recirculation. The permeate flux was then adjusted to 9 L/m²h and stepwise increased up to 27 L/m²h. In separate experiments, the feed pH was changed to 5.5 and 8.5. In general, the feed temperature during the experiments was kept at 23±0.1° C, except for two experiments at 10° C and 35° C. During the experiments, feed pressure was measured at the entrance to each RO element and at the exit of the third element. The system was operated for 3 days before the first samples were taken for analysis, to ensure the rejection of compounds had been stabilized. From each sampling point, a 60 mL sample was collected for immediate liquid–liquid extraction. The overall water recovery from the three elements in series was 30%.

Chapter 3

DBP Formation During the Treatment of Secondary Effluent

3.1 DBP Occurrence and Fate across Two AWTPS

Two AWTPs, Bundamba and Gibson Island located in South East Queensland (Australia), were sampled two and three times, respectively. Bundamba was sampled twice in November 2010 (events “a” and “b”), whereas Gibson Island was sampled twice in February 2011 (events “a” and “b”) and once in March 2011 (event “c”). The source water for both AWTPs is secondary effluent from WWTPs that use biological nutrient removal processes and achieve typical TN levels of 5 mg/L or lower but leave a high organic content for the formation of DBPs. Before RO filtration, pre-formed monochloramine (2 mg/L as Cl₂) is added to the secondary effluent. The contact time of pre-formed monochloramine with the water is different at Bundamba AWTP and Gibson Island AWTP. A relatively long contact time of 28 hours was used at Bundamba in contrast to half an hour of contact time at Gibson Island. Secondary effluent before disinfectant addition was collected to determine the background levels of DBPs. Besides the difference in chloramine contact time, Bundamba and Gibson Island receive different secondary effluents as source water. The source water characteristics for both plants during the different sampling campaigns and bench-scale studies are summarized in Table 3.1. Figure 3.1a shows the DBPs measured during two sampling campaigns at Bundamba (a,b) and three sampling campaigns at Gibson Island (a,b,c) AWTPs in the RO feed after disinfection with pre-formed monochloramine at a concentration of 2 mg/L as Cl₂. Figure 3.1b shows the DBP formation after disinfecting the source waters of both AWTPs for 24 hours with pre-formed monochloramine at pH 6.8 under controlled conditions at bench-scale.

The secondary effluents used for bench-scale experiments sampled at Bundamba (B-c) and sampled at Gibson Island (GI-d) are characterized in Table 3.1. The disinfectant dose employed was 10 mg/L as Cl₂ based on a disinfectant demand test targeting a residual of 1 mg/L as Cl₂ after 24 hours of contact time. The comparison among the various sampling campaigns allowed an evaluation of the effect of monochloramine contact time on the formation of DBPs at full-scale. However, in order to account for the different source waters at each plant, a more controlled evaluation was obtained from tests on these waters at bench-scale. Apart from TBM, other DBPs such as TCM, BDCM, DBCM, TCAN, DCAN, BCAN, DBAN, CH, TCNM, and both HKs could be detected during the sampling campaigns in at least one of the AWTPs. The concentrations of DBPs observed were generally low, with maximum values observed for TCM and 1,1-DCP. Even after 28 hours contact time at Bundamba, the concentrations were less than 3 µg/L. The sum of the concentrations of the four regulated trihalomethanes—TCM, BDCM, DBCM, and TBM (THM4) ranged from 0.7 to 5.7 µg/L. This is in accordance with previous results from Krasner and co-authors (2009a) who measured THM4 concentrations of 0.6 and 4.1 µg/L (median and 90th percentile, respectively) in chloraminated secondary effluents. Also, a good correlation could be seen for the sum of the four HANs formed at Bundamba and Gibson Island (0.6–2.4 µg/L) and HAN levels detected by Krasner and co-authors (2009a) who measured 0.3 and 2.8 µg/L (median and 90th percentile, respectively). TCNM was only detected at Gibson Island with an average

value of $0.21 \pm 0.03 \mu\text{g/L}$. HKs were found consistently at both plants, with 1,1-DCP ranging from 0.8 to 2.7 $\mu\text{g/L}$ and 1,1,1-TCP ranging from 0.2 to 0.7 $\mu\text{g/L}$.

Table 3.1. Water Characterization for Bundamba (B) AWTP and Gibson Island (GI) AWTP

	B-a	B-b	B-c	GI-a	GI-b	GI-c	GI-d
DOC (mg/L)	10.67	9.34	6.96	7.75	6.43	6.94	8.97
SUVA (L/mg/m)	n.a	2.57	3.33	n.a	n.a	n.a	n.a
pH	7.09	7.18	7.65	6.32	6.39	6.3	n.a
Conductivity ($\mu\text{S/cm}$)	1044	1054	823	1215	1257	1233	n.a
Phosphate-P (mg/L)	0.78	0.14	0.73	3.58	0.71	2.23	1.00
NH ₄ -N (mg/L)	0.00	0.08	0.10	0.28	0.1	0.15	0.01
NO _x -N (mg/L)	0.55	1.54	2.23	1.02	0.71	0.45	0.06
NO ₂ -N (mg/L)	0.01	0.15	0.09	0.15	0.09	0.08	0.01
DON (mg/L)	1.29	1.39	0.73	0.86	0.82	0.88	0.95
Bromide (mg/L)	n.a	0.30	0.23	n.a	n.a	n.a	n.a

Notes: N.A. = not analyzed; B-a B-b, G-a to G-c = sampling campaigns;
B-c and GI-d = secondary effluent sampled for bench-scale studies

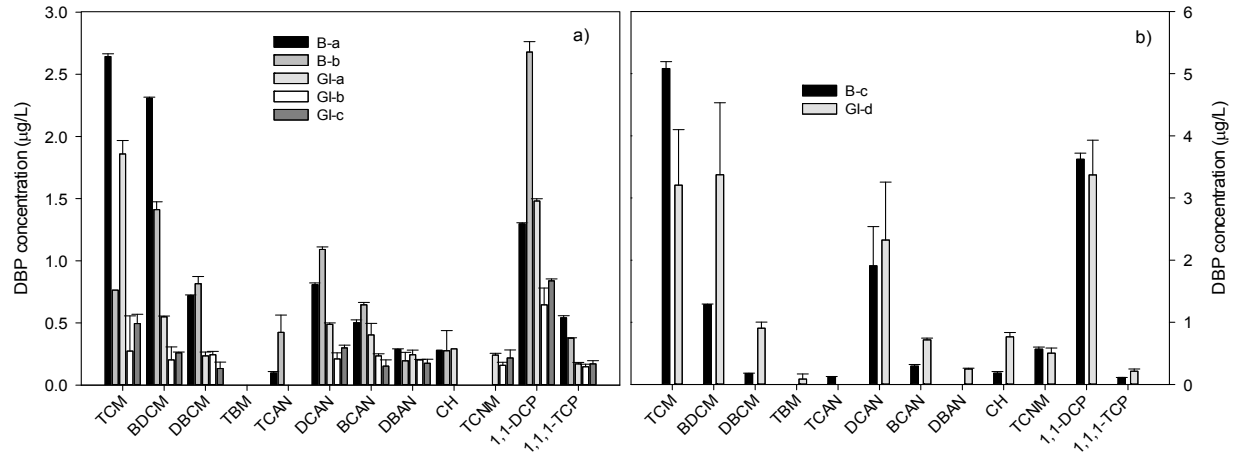


Figure 3.1. (a) DBP formation at full-scale from reaction of secondary effluent with monochloramine at Bundamba (B) and Gibson Island (GI) AWTP; (b) DBP formation after bench-scale disinfection of secondary effluent sampled at Bundamba and Gibson Island with pre-formed monochloramine (10 mg/L as Cl₂) for 24 hours at pH 7.

Note: Error bars indicate the absolute difference between the duplicate experiments.

At Gibson Island, 55% less THM4 was generated (with the shorter contact time of 30 minutes) in comparison to Bundamba (with a contact time of 28 hours). This can be attributed to a time dependent formation, as shown during bench-scale studies, where THM4 formation increased gradually without notably slowing down up to 48 hours (see Figure 3.2). Similar TCM formation behavior during 72 hours of chloramination was observed by Yang and co-authors (2007). Even after this long contact time, the maximum individual species' concentration formed was 5.9 µg/L (data not shown), which is significantly lower than the 100 to 200 µg/L Public Health Regulation Standards for TCM, TBM, and DBCM for recycled water supplied to augment a supply of drinking water in Queensland (Public Health Regulation, 2005). BDCM, however, is regulated at a much lower 6 µg/L limit (Public Health Regulation, 2005). During the sampling campaigns, the concentrations of BDCM at Bundamba and Gibson Island were 1.9 ± 0.5 µg/L and 0.3 ± 0.1 µg/L, respectively, indicating that the contact time and disinfection strategy were appropriate for maintaining the formation of BDCM below the maximum Public Health Regulation Standard.

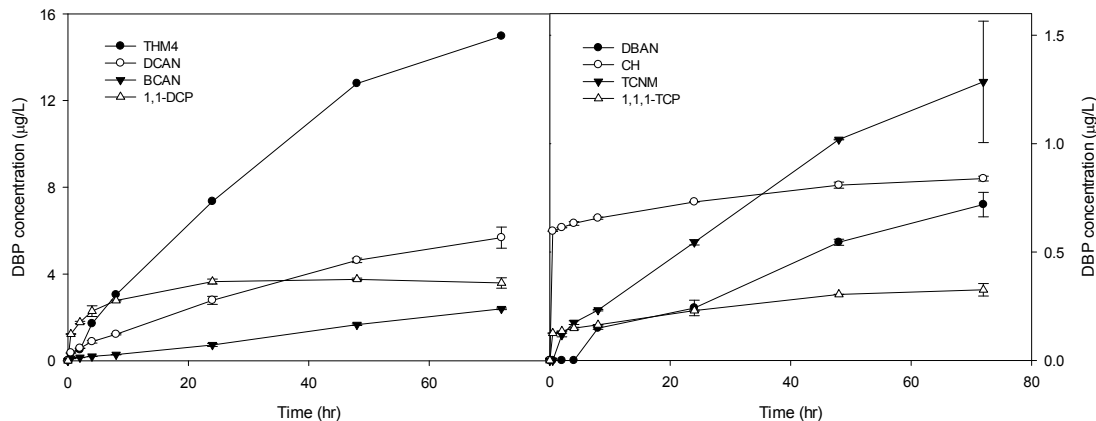


Figure 3.2. Average DBP formation during pre-formed chloramination with source water of Gibson Island at pH 7 and 10 mg/L as Cl₂.

Note: Error bars show the absolute difference of duplicate samples.

A steady increase of chloroform formation over 3 days of contact time was also observed by Hua and Reckhow (2008) who disinfected drinking water treatment intakes with monochloramine. It is noteworthy that even after a long contact time between source water and disinfectant, TBM could not be measured during the sampling campaigns at either AWTP despite background bromide levels of 0.3 mg/L. Because the reaction of chloramine with bromide to form active halogenating agents is slow ($k = 0.014 \text{ l/M}\cdot\text{s}$ [Trofe, 1980]), TBM formation was likely to be below the limit of detection even after the long contact times at the AWTPs. During the bench-scale experiments, TBM concentrations could only be detected in the chloraminated Gibson Island source water after 24 hours contact with a 10 mg/L monochloramine (as Cl₂) dose. In contrast to the gradual increase of the THMs, 1,1-DCP and 1,1,1-TCP showed a rapid initial formation followed by a slower rate of increase—34% of 1,1-DCP and 39% of 1,1,1-TCP formed within 0.5 hours (Figure 3.2), which was also observed at full-scale with 1,1-DCP concentrations found to be higher at Gibson Island (Figure 3.1a). TCNM was consistently found during the sampling campaigns at Gibson Island but was not detected at Bundamba. Regarding the contact time and the kinetics of TCNM, it could be expected to be formed after 28 hours at Bundamba, as a steady increase in TCNM formation during 72 hours was observed during kinetic experiments. Research by Merlet et al. (1985) suggests that the formation of TCNM may occur from many potential precursors whether aliphatic, aromatic, nitrated, or aminated, indicating that the formation seen during the sampling campaigns in this study may have been precursor related. Song and co-authors (2010) could only detect TCNM in one out of five municipal WWTPs practicing chlorination. Consistent TCNM formation after 24 hours with an average of $0.9 \pm 0.1 \text{ }\mu\text{g/L}$ in both source waters for Bundamba and Gibson Island (Figure 3.1b) during the bench-scale studies confirms the presence of TCNM precursors in the secondary effluents. After long contact times of 28 hours at Bundamba, losses of TCNM from volatilization (Henry's Law constant of $3.7 \times 10^{-3} \text{ atm}\cdot\text{m}^3/\text{mol}$) may outweigh the potential TCNM formation at the plant.

Of particular concern is the formation of HANs during the production of HQRW because the Queensland regulation for recycled water used to augment a drinking water supply set a maximum value of 2 µg/L and 0.7 µg/L for DCAN and BCAN, respectively (Public Health Regulation, 2005). The average values measured at Bundamba and Gibson Island were $0.6 \pm 0.3 \text{ }\mu\text{g/L}$ and $0.4 \pm 0.2 \text{ }\mu\text{g/L}$, respectively with individual values up to 1.1 µg/L and

0.6 µg/L. Concentrations of DCAN, BCAN, and DBAN during bench-scale formation experiments also showed a steady increase (Figure 3.2). The influence of the contact time on the formation can also be seen at full-scale. When comparing the average HAN concentrations of the two sampling events at Bundamba (a, b) with the average of those at Gibson Island (a–c), 42% and 30% less DCAN and BCAN were formed at Gibson Island with its much shorter chloramine contact time. Contact time is particularly important for Gibson Island regarding the formation of bromine-containing HANs and THMs because the source water contained a higher bromine presence from industrial discharge. This is important because bromine-containing DBPs are suspected to be more toxic than their chlorine-containing analogues (Richardson et al., 2007). Although bromide concentrations for the sampled waters are not available, concentrations of 0.5 mg/L on average with up to 0.8 mg/L were measured monthly over a timeframe of 1 year (2010) at Gibson Island compared to an average of 0.2 mg/L (maximum 0.4 mg/L) found in the secondary effluent of Bundamba. The greater presence of bromide in Gibson Island secondary effluent likely led to the higher bromine incorporation in DHANs and THMs compared to experiments conducted with secondary effluent sampled at Bundamba (Figure 3.1b). During disinfection of secondary effluent from Gibson Island, DBAN and TBM could only be measured after a contact time of 24 hours. Therefore, it is recommended to closely control the parameter of contact time to avoid the more toxic bromine-containing DBPs and the formation of HANs above the Public Health Regulation Standard.

3.2 DBP Occurrence and Fate across the Treatment Train

The sample locations chosen at the AWTPs follow the whole treatment train, and include the incoming secondary effluent source water, microfiltration (MF), RO feed after coagulation, RO permeate, RO concentrate after the advanced oxidation process (AOP), and the final treated water as depicted in Figure 3.3.

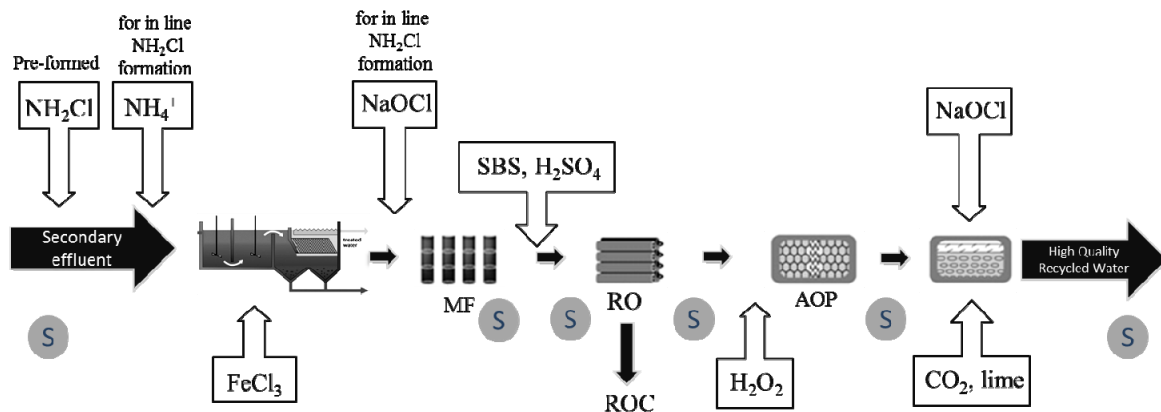
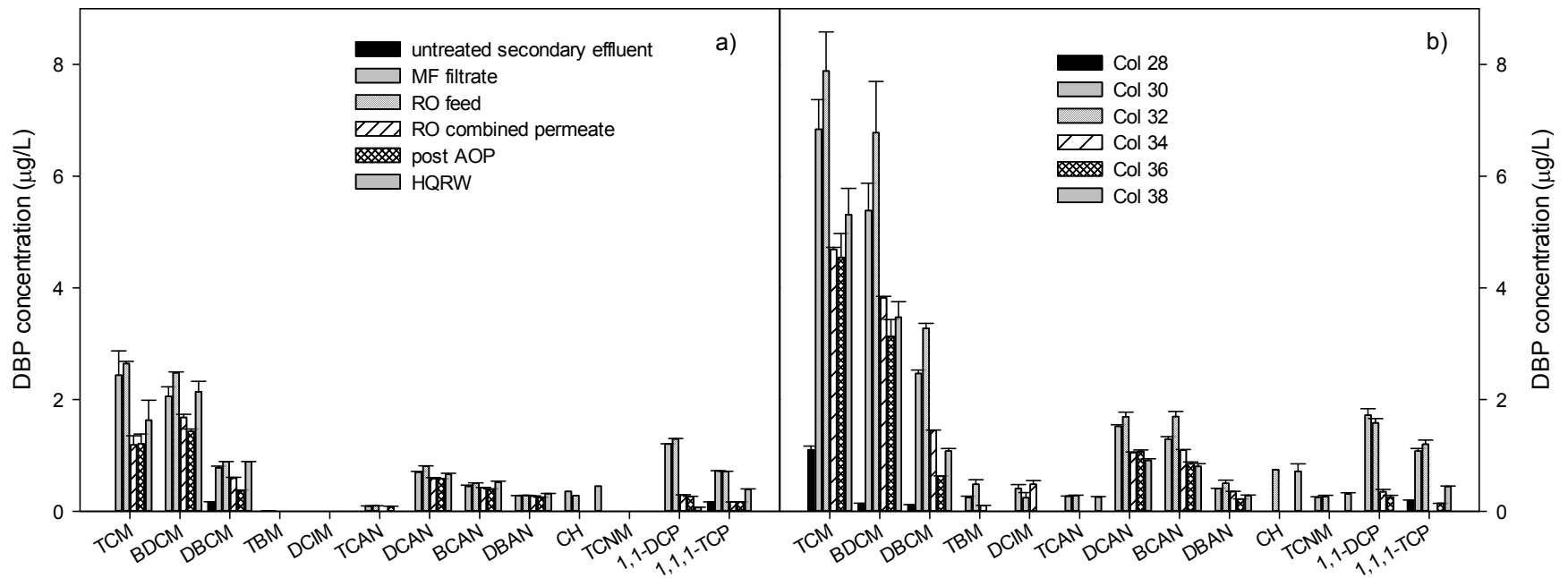


Figure 3.3. Scheme of the AWTPs studied.

Notes: MF = microfiltration, RO = reverse osmosis, AOP = advanced oxidation process. SBS = sodium bisulfite, ROC = reverse osmosis concentrate. S corresponds to sampling points.

Influent secondary effluent at the AWTPs was not disinfected at the WWTPs. Therefore, no DBPs, except TCM (around 1 µg/L), DBCM, and 1,1,1-TCP (close to their limits of detection) were measured in the incoming secondary effluents during the five sampling campaigns. This observation confirms that all the DBPs measured at the AWTP are, in fact, generated as a result of the chloramination of the secondary effluent. Figure 3.4 shows the fate of the DBPs across the treatment train at Bundamba during two separate sampling campaigns. The difference between those two sampling events was the change in disinfection strategy from forming the chloramines inline to the addition of pre-formed monochloramine. Monochloramine was produced inline by adding ammonia in the secondary effluent before coagulation and sodium hypochlorite in the MF feed water (Figure 3.3). The chloramine contact time varied within both disinfection strategies from 2 hours during inline chloramination to 28 hours during the application of pre-formed monochloramine because of an intermediate tank providing more time for disinfection during pre-formed chloramination. Even with a 4-hour shorter contact time, the formation of all DBPs was higher during inline chloramination. At Bundamba AWTP the more toxic bromine-, iodine-, and nitrogen-based DBPs, including TBM, DCIM, and TCNM not seen with pre-formed monochloramine (three sampling campaigns) were, however, found after inline chloramination (two sampling campaigns) with a disinfectant concentration of 2 mg/L as Cl₂ for both strategies. It is assumed that NOM and EfOM present in the secondary effluent compete for the free chlorine with the added ammonia. The reaction of the chlorine with the NOM and EfOM can result in DBP formation likely leading to the higher DBP formation observed at the AWTP. Also the reaction of free chlorine with bromide is five orders of magnitude faster than with monochloramine (Bousher et al., 1990; Trofe, 1980). Thus, TBM could be formed because of the faster reacting HOBr. These hypotheses are further investigated in Section 3.3.2.



After MF filtration, the DBPs continue to form as seen by the higher concentrations in the RO feed compared to the MF filtrate (Figure 3.4). Subsequently, the RO membranes removed the DBPs to different extents. Taking the average rejections over the five different sampling campaigns, at Bundamba AWTP the rejection of the bulky trichlorinated DBPs ranged from 95% for TCNM, 90% for TCAN to >97% for 1,1,1-TCP and CH, which in several cases were completely removed. On the other hand, THM removal varied between 30 and 55%. In the literature, the poor removal of THMs by RO membranes was related to their adsorption and consequent diffusion through the membrane matrix (Xu et al., 2006). Low removals between 10 and 30% were also observed for the dihalogenated HANs. HANs are polar substances that likely sorb to the membrane by hydrogen bonding, subsequently diffusing through the membrane.

The advanced oxidation process (AOP) showed a positive influence on the oxidation of certain DBPs. In fact, Chen and co-authors (2010) showed that DBPs are photosensitive to various degrees. They found that the nitrogenous compared to the carbonaceous DBPs and the bromine- or iodine-substituted species compared to the chlorinated analogues are more susceptible to photolysis. At Bundamba, DCIM was almost completely oxidized by the AOP, whereas the RO membrane was unable to reject it. The auxiliary effect for DBP removal during the AOP was also observed for DBCM and DBAN, which showed a low rejection by the RO membranes. It is interesting that the concentration of some of the DBPs increased after the final disinfection with chlorine suggesting that the AOP can enhance the formation potential of specific DBPs. CH, for example, which was completely removed by the RO membranes was formed again after the final chlorination step (Figure 3.4). A possible explanation may be that the AOP breaks carbon and hydrogen bonds and, therefore, facilitates the chlorine attack as shown, for example, by Gerrity et al. (2009) for an increase in THM formation potential. Hydroxyl radicals generated during the AOP are known to react with NOM to form aldehydes, which in the presence of chlorine can react further to produce CH. DBP formation after final disinfection could mean that after RO membrane filtration there are DBP precursors present in solution that do not react with chloramines but react with chlorine. All the DBPs measured in the final treated water were below the guideline values for augmentation of drinking water supplies although the concentrations of DCAN and BCAN were close to the guideline values of 2.0 and 0.7 µg/L, respectively.

3.3 Effect of Operational Parameters on DBP Formation in Secondary Effluent

As shown in Section 3.2, contact time and the chloramination strategy (inline or pre-formed) may be important parameters to consider for DBP minimization during HQRW production. However, for a deeper understanding of DBP formation and control it is important to identify the factors controlling the formation process because these may be variable at full-scale application. For instance, source water temperature can change because of seasonal variation and increase up to 30° C in summer (Almedeij and Aljarallah, 2011). Source water pH prior to membrane filtration is generally adjusted within the range of pH 6 to 8 (Ning and Troyer, 2007). During HQRW production, in addition to chlorine, chloramines can be applied by two different strategies to the treatment train either added pre-formed or formed inline by adding ammonia and chlorine separately in the treatment train. To understand the effect of operational parameters on the formation of TCM, BDCM, DBCM, TBM, TCAN, DCAN, BCAN, DBAN, 1,1-DCP, 1,1,1-TCP, TCNM, and CH during each of the disinfection strategies, isotherm batch studies were performed on the source water at various contact times up to 24 hours at three pH values (5.5, 7, and 8.5) and three temperatures (23, 30, and 35° C).

The set of kinetic data for all the studied DBPs at 23° C is presented in Appendix A, Figures A.1 to A.12.

3.3.1 pH and Time Dependent Formation

The concentration of all measured DBPs was higher during chlorination than during chloramination (both pre-formed and inline-formed chloramine) at all pH values. It should, however, be pointed out that nitrosamines, an important class of DBPs formed by chloramines in the presence of appropriate precursors (Shah and Mitch, 2012), were not measured in this study. Overall lower DBP formation occurred with those containing bromine, which is suspected to be more toxic than chlorine-containing analogues (Richardson et al., 2007). It is noteworthy to remark that despite background bromide levels of 0.3 mg/L, DBAN and TBM could only be measured after long contact times (8 and 24 hours, respectively) when using pre-formed monochloramine at pH 7 and then only at concentrations of 0.2 and 0.1 µg/L compared to 1.8 and 0.7 µg/L after 24 hours contact with free chlorine. Maximum concentrations of DBPs measured at pH 7 and 23° C after 24 hours of contact time during chlorination were 227, 38.8, 62.4, 1.3, and 16.8 µg/L for THM4, HAN4, CH, TCNM, and HK, respectively. During inline-formed chloramination these values decreased to 26.7, 10.4, 2.4, 1.8, and 6.0 µg/L. Values measured during pre-formed chloramination were 17.9, 6.1, 1.2, 1.4, and 4.6 µg/L for THM4, HAN4, CH, TCNM, and HK, respectively.

Figure 3.5 compares the DBP formation within the different disinfection strategies after 24 hours contact time at 23° C at the three pH values. As has been widely observed, THM formation increased with pH and yields were higher with chlorination than with chloramination. The largest differences were found for BDCM and DBCM formation whose concentrations were up to 400-fold times higher at pH 8.5 (Figure 3.5 c) but only two-fold higher at pH 5.5 (Figure 3.5 a) during chlorination in comparison to pre-formed chloramination. As suggested earlier, at high pH values, THMs can be produced as degradation by-products from the hydrolysis of other DBPs such as 1,1,1-TCP and TCAN (Nikolaou et al., 2001). During chloramination, higher levels of THMs were formed at lower pH as a result of hydrolysis of monochloramine to free chlorine (Diehl et al., 2000; Zhang et al., 2010). In addition, acidic pH favors direct chlorine transfer to form NH_3Cl^+ , a very active chlorinating agent (Snyder and Margerum, 1982). In this current work, pre-formed monochloramine generated 40% more free chlorine at pH 5.5 than at pH 7 after 24 hours of reaction time at 23° C. CH followed the trend of THM formation as it was generated at concentrations 20, 50, and up to 250 times higher during chlorination compared to pre-formed chloramination at pH 5.5, 7, and 8.5, respectively (Figure 3.5).

Less difference in the formation of the four studied HANs was observed. However, they were also generated at higher concentrations during chlorination compared to any of the chloramination strategies. In particular, chlorine generated between 3 and 12 times more HANs than chloramines with the exception of BCAN at pH 8.5, which was measured between 20 and 50 times higher during chlorination. Essentially, at pH 8.5 during chloramination, no formation of DBPs containing only bromine (no chlorine) was observed, and there was only a slow formation of mixed bromine- and chlorine-containing DBPs with concentrations close to their quantitation limit.

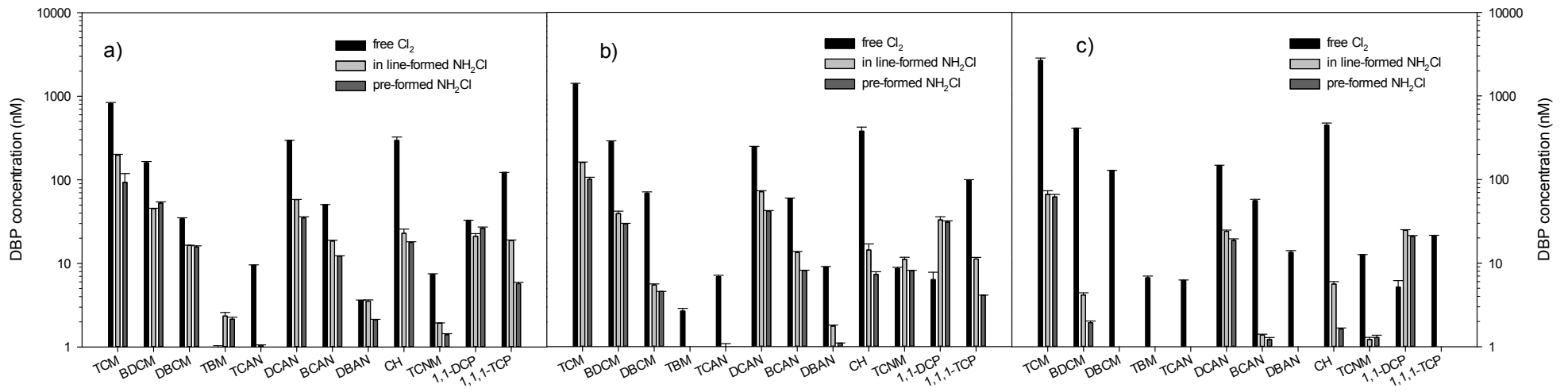


Figure 3.5. DBP formation after 24 hours (a) pH 5.5, (b) pH 7, and (c) pH 8.5 for each disinfection strategy (25 mg/L Cl₂) at 23°C.

Figure 3.6a and b show the THM, HAN, HK, TCNM, and CH formation kinetics during 24 hours of chlorination at pH 7 with an initial fast rate followed by a second slower phase. Yielding maximum concentrations already after 30 minutes was 1,1-DCP compared to 49% of 1,1,1-TCP, more than 50% of bromine-containing DHANs (DHAN-Br), and less than 40% of DCAN and TCAN. Bromine-containing DHANs may form faster than HAN-Cl as HOBr reacts more rapidly with NOM than HOCl (Symons et al., 1993). Only 25% of the 24-hour TCM concentration was formed after 30 minutes. Among all the scenarios evaluated, free chlorine produced higher levels of DBPs than the same dose of chloramines except for 1,1-DCP at pH 5.5 and 23° C. The 1,1-DCP formed during chloramination is more stable as explained in the model developed by Reckhow and Singer (1985) who suggested that during chlorination 1,1-DCP is oxidized by free chlorine to form 1,1,1-TCP, which then hydrolyzes to chloroform.

Figure 3.7 shows the formation kinetics of TCNM and CH at 23° C and the different pH values for each of the disinfection strategies. During chloramination, highest TCNM yields were measured after 24 hours at pH 7; whereas no significant difference in formation could be seen between pH 5.5 and 8.5. Conversely, more TCNM was formed with increasing pH during chlorination. Formation pathways proposed in the literature involve a nitroalkane intermediate that can be formed by both disinfectants (Shah and Mitch, 2012). However, the halogenation of the nitroalkane is rate limited by its deprotonation, which is promoted with increasing pH (Merlet et al., 1985; Orvik, 1980) leading to the increased formation with pH. On the other hand, after 24 hours of inline chloramination at pH 7, formation exceeded the levels obtained during chlorination. Joo and Mitch (2007) observed a similar behavior after 3 days contact time at pH 7 with chloramine when using the model compounds monomethylamine and *n*-propylamine as primary amine precursors. Hydrolysis of monochloramine releases free chlorine whose rate is higher at acidic conditions (Jafvert and Valentine, 1992). Also monochloramine has been found to contribute a nitrogen source to some extent during TCNM formation (Yang et al., 2012). The impact of pH on TCNM formation during chloramination is a complex combination of chloramine utilization and speciation, monochloramine hydrolysis, and TCNM degradation.

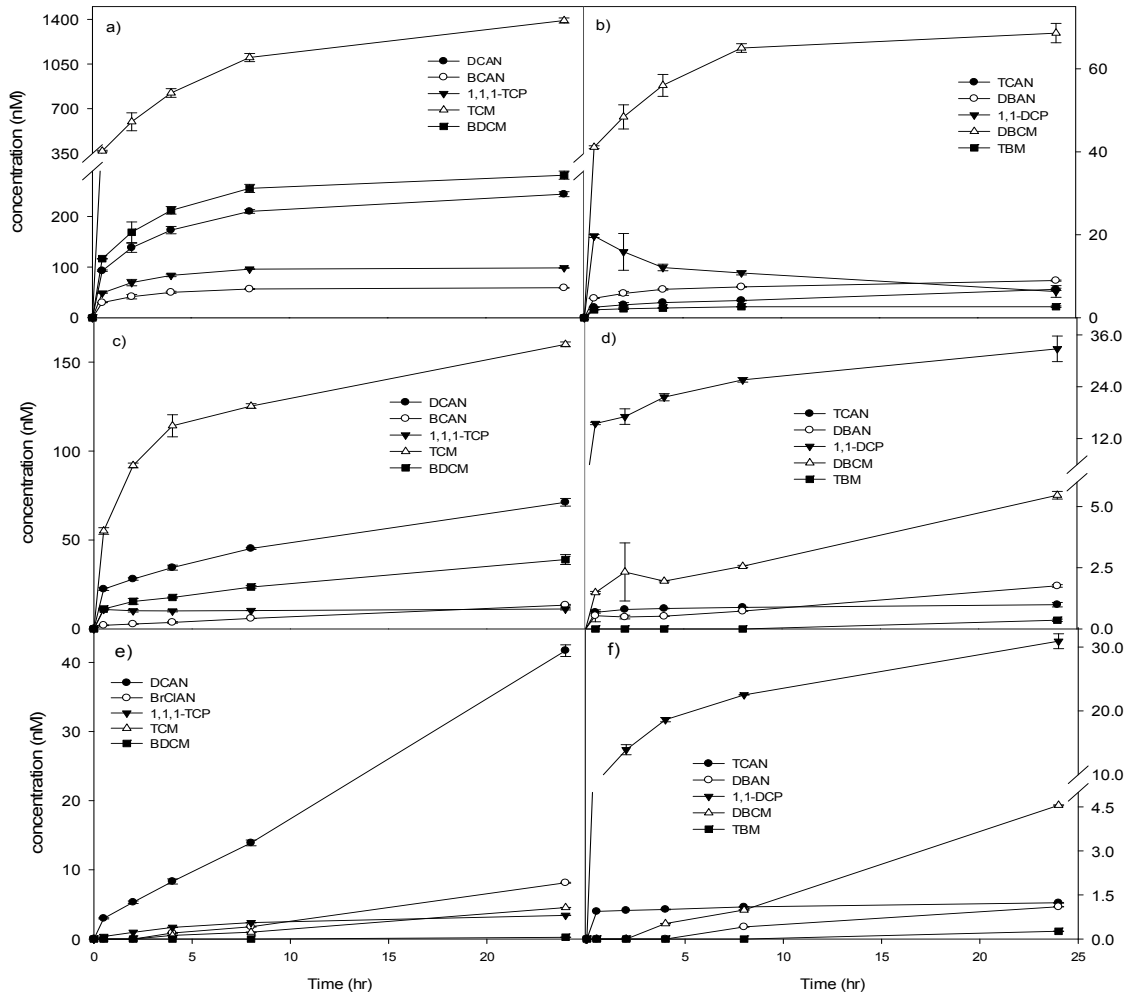


Figure 3.6. DBP formation kinetics during 24 hours for each disinfection strategy (pH 7, 25 mg/L as Cl₂) at 23° C.

Notes: (a)–(b) chlorination, (c)–(d) inline-formed chloramination, and (e)–(f) pre-formed monochloramine.

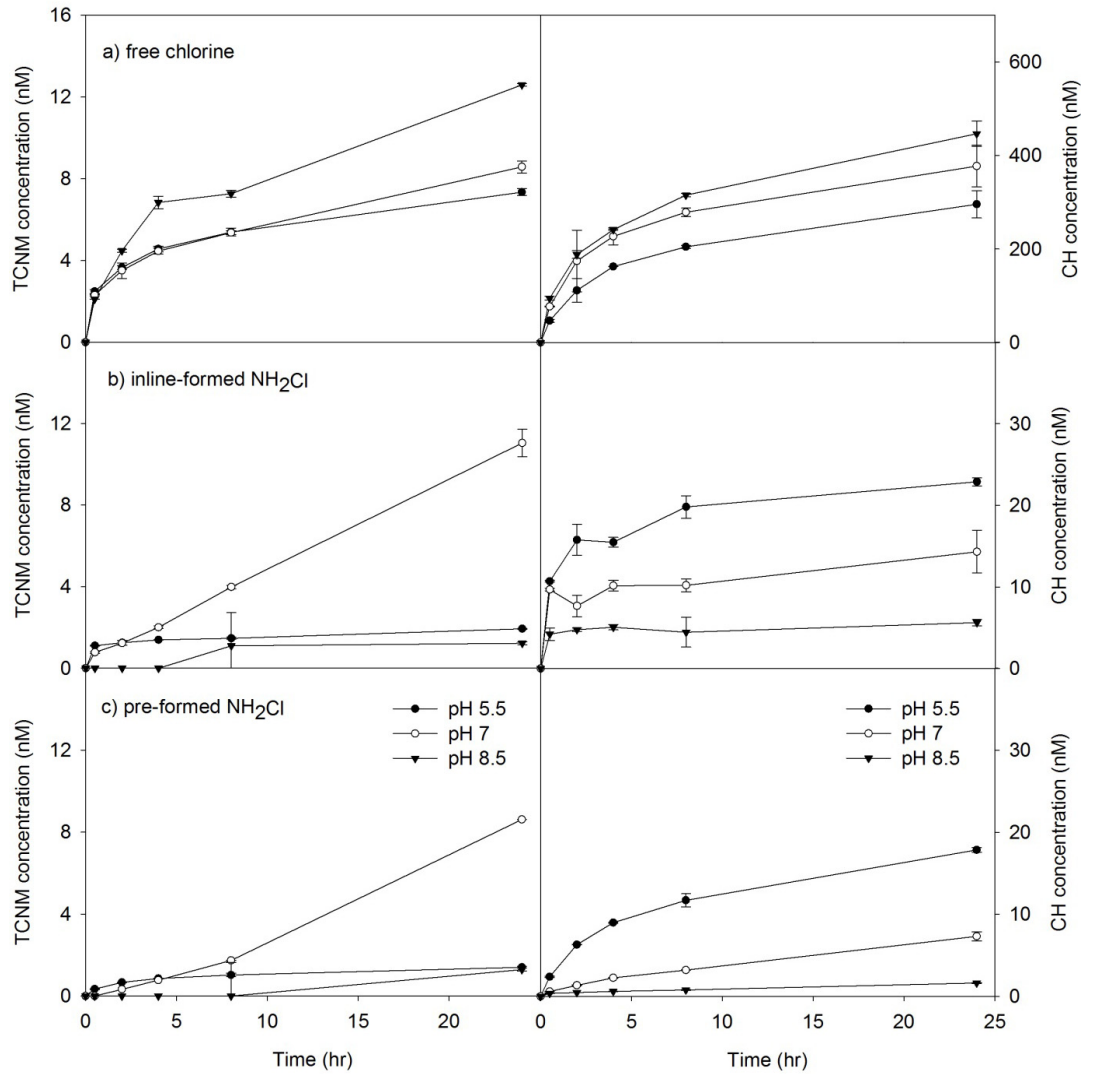


Figure 3.7. TCNM and CH formation kinetics in secondary effluent during each of the disinfection strategies, 24 hours of reaction time at 23° C and pH 5.5, 7, and 8.5 and 25 mg/L as Cl_2 .

3.3.2 Formation of DBPs during Pre-Formed Versus Inline-Formed Chloramination

All DBPs showed an initial faster rate of formation and overall higher yield from secondary effluent reaction with inline-formed than with pre-formed monochloramine (Figure 3.6 c–f). The higher yields are in agreement with the higher total chlorine consumption during inline compared to pre-formed chloramination at pH 7 (Figure 3.8). Similar profiles were obtained at the other two pH values with the highest consumption at pH 8.5 during chlorination and at pH 5.5 during chloramination. The DBPs formed at highest concentrations in both scenarios were TCM, BDCM, and CH with yields after 30 minutes contact time an order of magnitude higher than the other DBPs. Their formation is favored at high pH during chlorination; whereas the situation for chloramination is the reverse. Concentrations of all DBPs formed after 24 hours of inline chloramination exceeded those from pre-formed chloramination in the pH range studied except 1,1-DCP at pH 5.5.

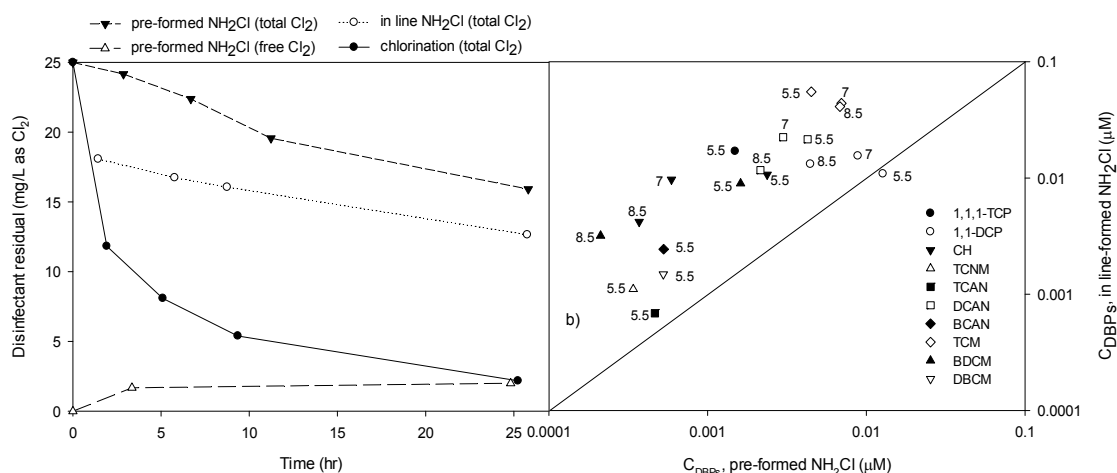


Figure 3.8. Comparison of (a) time dependent disinfectant residuals at pH 7 during chlorination, inline and pre-formed chloramination, (b) DBPs formed after 30 minutes of reaction time during inline and pre-formed chloramination.

Notes: Corresponding pH 5.5, 7, or 8.5 plotted beside symbol. The line represents the 1:1 ratio of inline to pre-formed chloramine DBP formation.

During inline chloramination, ammonia and free chlorine are added separately to the secondary effluent and chloramines form *in situ*. Secondary effluent is a heterogeneous mixture of NOM and EfOM competing for the free chlorine (forming DBPs) and the added ammonia (forming chloramines) during inline chloramination. The strongest effect between the chloramination strategies was seen for trichlorinated DBPs, including CH (Figure 3.7), 1,1,1-TCP, TCM, and TCNM (Figure 3.6 c–f). Faster reaction of chlorine with NOM than ammonia may account for the higher levels during inline chloramination. TCNM, BCAN, and DBAN could not be detected during 0.5, 2, and 4 hours of reaction time, respectively. Following initial detection during both strategies, DHANs and TCNM showed a continuous formation over time; whereas CH formation leveled off and HK formation slowed down after 30 minutes. During inline-formed chloramination, HKs, CH, and DHANs reached their maximum concentration at high pH faster than with pre-formed monochloramination (Appendix A, Figures A.1 to A.12) depending on temperature before undergoing base-catalyzed hydrolysis.

The effect of inline- versus pre-formed monochloramine on the formation of nitrosamines was not studied in this project, but it seems prudent to cite some of the main results from another study that part of this team has conducted. In general, it was found that the use of pre-formed monochloramine drastically reduced the formation of nitrosamines in secondary effluent (Farré et al., 2011). For example, such an effluent treated with 10mg/L pre-formed monochloramine formed <5ng/L and 16ng/L NDMA after 8-hour and 24-hour exposure time, respectively. Upon treatment with the same concentration of inline-formed monochloramine, 18ng/L and 310ng/L were formed in the same effluent after 8 hours and 24 hours.

3.3.3 Impact of Temperature

Elevated temperature leads to a slower formation rate and even degradation for DCAN, HK, and CH during inline chloramination compared to their formation during pre-formed chloramination (Figure 3.9).

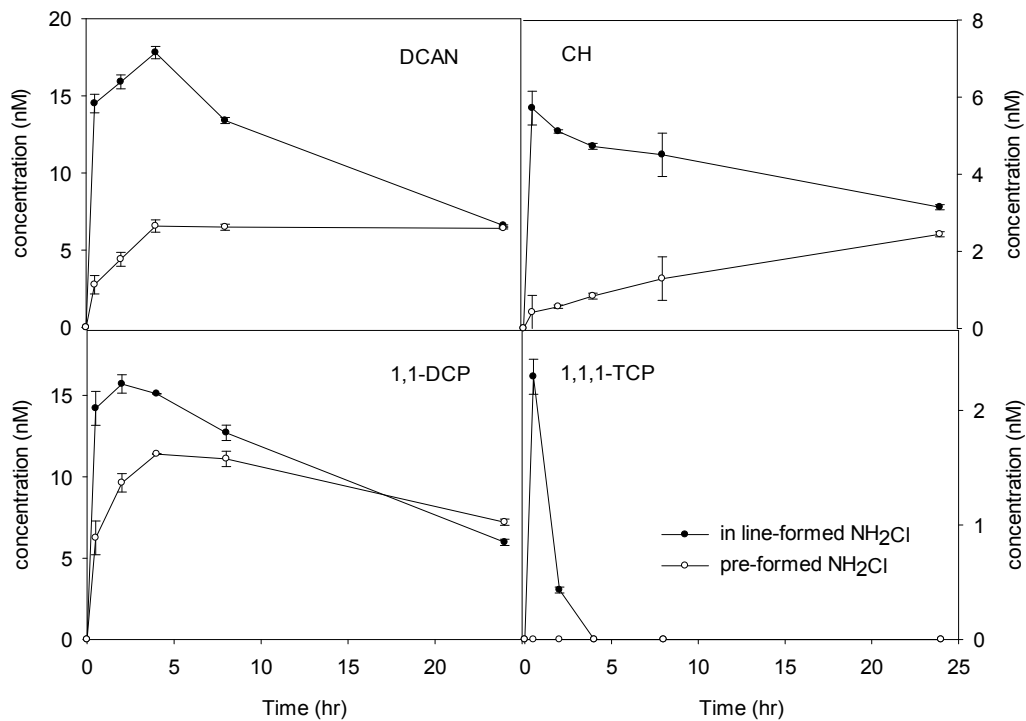


Figure 3.9. DCAN, CH, 1,1-DCP, and 1,1,1-TCP formation kinetics during inline-formed and pre-formed chloramination (25 mg/L Cl₂) at 35° C and pH 8.5.

Thus, long reaction times at alkaline pH and elevated temperature may lead to equal concentrations with both disinfection strategies. As a result of their decomposition, the degradation of the DBPs during inline chloramination might lead to an increased formation of their degradation products. For example, 36% more TCM, which is the hydrolysis and decomposition product of 1,1,1-TCP and CH, was formed with a temperature increase from 23 to 35° C during inline chloramination compared to pre-formed chloramination. It has been observed that 1,1,1-TCP reaches its maximum after 7 hours of reaction time at pH 7.5, 22° C and a chloramine dose of 5 mg/L as Cl₂ (Yang et al., 2007). In this current study, the 1,1,1-TCP formation rate with pre-formed monochloramine, much like that for DHANs,

exceeded the rate of degradation after 24 hours reaction time at pH 7 and 5.5. Applying their similar behavior in terms of continuous formation during 24 hours, however, may be based on different formation pathways. The initial formation of DHANs involves organic nitrogen precursors, whereas a slower simultaneous but continuous formation occurs from chloramine incorporation into organic precursors (Huang et al., 2012). On the other hand, continued 1,1,1-TCP formation occurs when free chlorine produced from acid catalyzed and temperature facilitated autodecomposition of monochloramine, reacts with 1,1-DCP (Jafvert and Valentine, 1992; Vikesland et al., 2001).

3.3.4 Response Surface Analysis for Chlorination and Chloramination

Response Surface Modeling (RSM) was chosen to develop multivariate linear regression models for establishing a mathematical connection between several process parameters (pH, temperature, reaction time) and the DBPs formed in laboratory batch experiments employing free chlorine and chloramine. The main objective was to determine which one of these process parameters influences DBP formation strongest and if they interact with each other. An entirely hypothetical example for interaction would be, for example, if temperature would have no impact on DBP formation except at low pH. In this case, temperature and pH would interact and have a different impact on DBP formation than changes in any of the two process variables alone.

Such multivariate models were developed for the formation of TCM, BDCM, DBCM, TBM, TCAN, DCAN, BCAN, DBAN, 1,1-DCP, 1,1,1-TCP, TCNM, and CH depending on pH, temperature, and reaction time. Disinfectant dose and disinfection strategy were kept constant, as significant differences on DBP formation were observed depending on the employed disinfection strategy. Table 3.2 summarizes the experimental factors used and their corresponding levels employed in the experimental design.

Very briefly, the RSM methodology develops an optimized experimental design to obtain the required experimental data to establish a mathematical function typically based on simple polynomials that provide an approximation of the relation between process variables (or factors) and a target variable with reasonable accuracy. It will depend on the desired statistical power as to which experimental design is chosen. After the experiments have been conducted, typically in a randomized order to prevent systematic errors affecting the result, simple multivariate regression analysis is performed. However, in most cases, the process variables will be normalized (i.e., mean subtraction divided by standard deviation) before the least square regression analysis is conducted to derive the polynomial equation. This way the absolute values of the modeled coefficients in the polynomial expression can be compared and are directly reflective of the magnitude of the influence that the respective process variable has upon the target (i.e., DBP formation).

To describe the complex relations of the different factors influencing DBP formation, a polynomial with higher degree, such as a quadratic or second order model, was applied. The degrees of freedom for each compound and model are listed in Table 3.3. The coefficients represent the effect of each independent parameter and their interaction on DBP formation. Information about model adequacy in terms of explained variation (R^2) and predicted variation (Q^2) of the model were evaluated and are presented in Table 3.3.

Table 3.2. Experimental Factors for Each Disinfection Strategy and Corresponding Levels Investigated

Free Chlorine			Inline-formed NH ₂ Cl			Pre-formed NH ₂ Cl		
Run	pH	Temp	Run	pH	Temp	Run	pH	Temp
1	5.5	23	10	5.5	23	19	5.5	23
2	7	23	11	7	23	20	7	23
3	8.5	23	12	8.5	23	21	8.5	23
4	5.5	30	13	5.5	30	22	5.5	30
5	7	30	14	7	30	23	7	30
6	8.5	30	15	8.5	30	24	8.5	30
7	5.5	35	16	5.5	35	25	5.5	35
8	7	35	17	7	35	26	7	35
9	8.5	35	18	8.5	35	27	8.5	35
			31	7	23	28	7	30
						29	7	30
						30	7	30

Notes: Temp = temperature in °C. For every run, samples were taken at 0.5, 2, 4, 8, and 24 hours of reaction time.

When Q^2 values exceed 0.5, the predictive ability of the model was considered acceptable and excellent when values exceeded 0.8 (Lundstedt et al., 1998). All models, except those for TCNM, TCAN, and 1,1-DCP, showed an excellent predictive ability with $Q^2 = 0.84$ to 0.99. For TCNM, TCAN, and 1,1-DCP, predictive ability was acceptable as Q^2 values ranged from 0.51 to 0.96, 0.64 to 0.88 and 0.74 to 0.92, respectively.

Table 3.3. Obtained Explained (R^2) and Predicted (Q^2) Variation of the Models for Chlorination, Pre- and Inline-Formed Chloramination, and their Respective Degrees of Freedom (DF)

Disinfection Strategy		TCAN	DCAN	BCAN	DBAN	CH	TCNM	1,1-DCP	1,1,1-TCP	TCM	BDCM	DBCM	TBM
Pre-formed NH_2Cl	Q^2	0.77	0.98	0.97	0.97	0.94	0.62	0.85	0.92	0.93	0.93	0.95	0.84
	R^2	0.85	0.99	0.99	0.98	0.96	0.72	0.92	0.95	0.96	0.96	0.97	0.93
	DF	32	35	39	39	38	41	40	39	38	36	35	39
Inline-formed NH_2Cl	Q^2	0.64	0.86	0.99	0.95	0.94	0.51	0.74	0.98	0.93	0.87	0.84	0.84
	R^2	0.74	0.96	0.99	0.98	0.96	0.69	0.86	0.99	0.98	0.93	0.92	0.92
	DF	38	36	36	36	37	34	35	34	36	37	36	37
Free chlorine	Q^2	0.88	0.91	0.80	0.96	0.88	0.96	0.92	0.88	0.92	0.94	0.93	0.89
	R^2	0.93	0.95	0.89	0.98	0.93	0.97	0.95	0.92	0.96	0.96	0.96	0.92
	DF	33	32	27	30	35	35	32	33	37	37	37	38

3.3.4.1 Free Chlorine

Figure 3.10 compares the normalized linear regression coefficients during chlorination. All three parameters (pH, time, and temperature) affect DBP formation to a different extent. Interaction involved all three parameters leading to pH*temp and pH*time coefficients (quadratic and interaction coefficients can be found in Appendix A, Figures A.13 and A.14). DBP formation is significantly affected at the 0.05 level by pH—for THMs, CH, TCNM, and DBAN it is positively affected, whereas for HKs, TCAN, DCAN, and BCAN it is negative. Increasing pH decreases the stability of non-THM DBPs in terms of base catalyzed hydrolysis facilitating their degradation to THMs. Both HKs are intermediate DBPs that can be further degraded at high pH from the reaction with chlorine and further hydrolysis to chloroform (Yang et al., 2007). The different trends between DBAN and the other HANs can be explained by differences in base-catalyzed hydrolysis (Singer, 1994) whose rates are higher with larger numbers of halogen substituents but lower with increased bromine incorporation (Glezer et al., 1999). Thus, highest concentrations were found for TCAN and DCAN at pH 5.5, for BCAN at pH 7, and at pH 8.5 for DBAN.

Temperatures up to 35° C (Figure 3.10) positively influences DBP formation with time except for the HKs whose degradation is accelerated at higher temperature. For DHANs with a higher number of bromine atoms, their higher formation occurs with increasing temperature because hydrolysis of Br-HANs is slower than for Cl-HANs. DBP formation is a net result of simultaneous formation and degradation leading to significant interactions among pH, temperature, and time. In this study, HANs were observed to be generally more hydrolysable and prone to reactions with residual chlorine than were THMs. Thus, for DCAN and BCAN squared terms and interaction between pH*temp and pH*time are influencing negatively and to a greater extent than THM-Br (Appendix A, Figure A.14). The curvilinear term time² is significant for all DBPs studied (Appendix A, Figure A.13) because their rate of formation decreases after an initial fast formation, indicating fast reactions with chlorine.

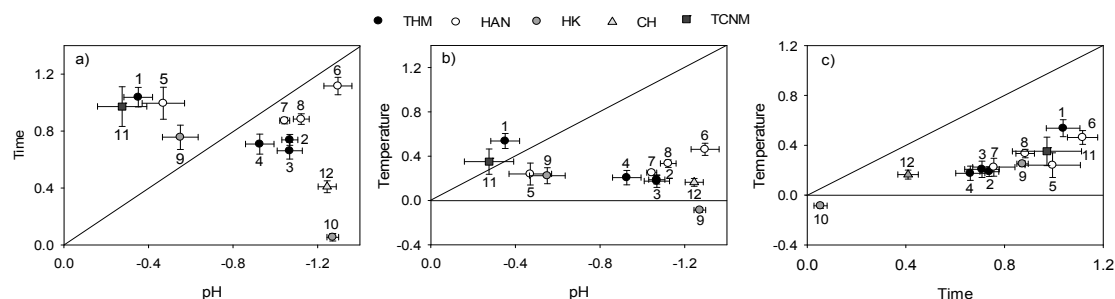


Figure 3.10. Comparison of normalized linear regression coefficients pH, time, and temperature during chlorination.

Notes: Error bars correspond to the standard error that is due to the model. (1) TCM, (2) BDCM, (3) DBCM, (4) TBM, (5) TCAN, (6) DCAN, (7) BCAN, (8) DBAN, (9) 1,1-DCP, (10) 1,1,1-TCP, (11) TCNM, (12) CH.

3.3.4.2 Pre-Formed Chloramines

Figure 3.11 shows the normalized linear regression coefficients of DBPs during pre-formed chloramination in relation to each other. Generally, those DBPs that form slowly (strong time dependence) are less dependent on pH. Although this relation is weak, DCAN shows a clearly distinct behavior (Figure 3.11a). In the absence of free chlorine, DCAN is stable at acidic conditions

(pH < 5.4), but degrades under neutral and basic conditions (Reckhow et al., 2001). Glezer and co-authors (1999) also investigated the stability of HANs and found that they undergo base-catalyzed hydrolysis, whereas the stability increases upon substitution of chlorine with bromine atoms. Furthermore, because of a change in the protonation level, reduced reactivity of precursors with monochloramine at high pH may contribute to the lowest DBP formation occurring at pH 8.5.

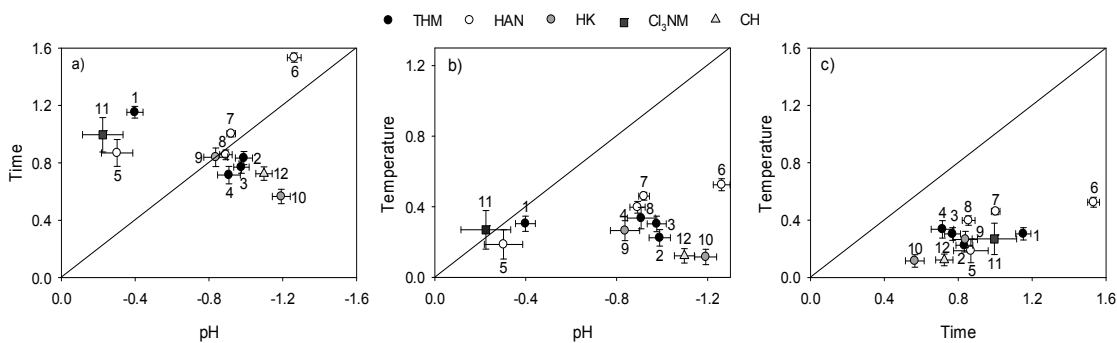


Figure 3.11. Comparison of normalized linear regression coefficients pH, time, and temperature during pre-formed chloramination.

Notes: Error bars correspond to the standard error that is due to the model. (1) TCM, (2) BDCM, (3) DBCM, (4) TBM, (5) TCAN, (6) DCAN, (7) BCAN, (8) DBAN, (9) 1,1-DCP, (10) 1,1,1-TCP, (11) TCNM, (12) CH.

In addition, at 25° C and pH < 6 monochloramine/dichloramine coexist (Jolley and Carpenter, 1982). Dichloramine has been proven to produce less DCAN and 1,1-DCP than monochloramine (Yang et al., 2007), which is reflected in a lower formation of those DBPs at pH 5.5 compared to pH 7. Also, free chlorine generated by the reversible hydrolysis reaction of monochloramine is always present in solution (Jafvert and Valentine, 1992) and has been found to play a significant role in the formation of chloroform during chloramination of model compounds (Cimetiere et al., 2010). Theoretical concentrations of free chlorine in solution have been calculated to increase with decreasing pH (Cimetiere et al., 2010) and observed to be about three times higher at pH 7 than at pH 8.5 for a chloramine concentration of 10 mg/L as Cl₂ (Morris and Isaac, 1983). Experimental results show 1.4 mg/L more free chlorine at pH 5.5 than at pH 7 after 24 hours of reaction time at 23° C when using pre-formed monochloramine. This is in agreement with higher observed formation for THMs, 1,1,1-TCP, and CH at pH 5.5 compared to pH 7.

Contact time governs formation of TCM, TCNM, and HANs other than DBAN, whereas pH is more important for the formation of the HKs, CH, DBAN, and remaining THMs. Time dominates over pH for the formation of TCNM because of its linear formation during 24 hours of reaction time (see Figure 3.7). Squared and higher order terms of the predictor factors shape the curvilinear response surface. Time squared is a significant coefficient in the models for TCAN, 1,1-DCP, 1,1,1-TCP, TCM, and CH as their formation is initially rapid but then slows down leading to the necessity of this curvilinear term for the models. Interaction among pH, temperature, and reaction time during DBP formation is particularly important for the DHANs and bromine-containing THMs. The DBPs most influenced by the interaction terms pH*temp, pH*time, temp*time and pH*temp*time were in the order DCAN, BCAN, DBAN, and THM-Br (Appendix A, Figures A.15 and A.16). A continuous formation at pH 5.5 and pH 7 with no further increase at pH 8.5 is reflected in strong pH*time interaction factors for bromine-containing DBPs and DCAN. Other chlorine-containing DBPs more susceptible to changes in pH and degradation involved squared factors. In comparison to time and pH, temperature is the parameter least influencing DBP formation (Figure 3.11), but in general an increase of DBP formation as a result of temperature increase could be seen. The DHANs in the

order DCAN>BCAN>DBAN were most affected by temperature changes, whereas CH and 1,1,1-TCP were the least affected with their coefficients being around 76% smaller compared to DCAN. Decreasing chlorine but increasing bromine content in CH, HK, DHANs, and THM-Br can lead to a lower dependency on pH, but in general the formation of THM-Br and DHAN-Br is less effected by time and pH with increasing bromine incorporation in the molecule (Appendix A, Figure A.16).

3.3.4.3 In-line-Formed Chloramines

Reaction conditions appear to affect the formation of DBPs during in-line-formed and pre-formed chloramination very similarly. One apparent difference is that 1,1,1-TCP is less affected by time and negatively affected by temperature (Figure 3.12). After an initial fast formation that is due to available free chlorine being added separately, 1,1,1-TCP reached its maximum yield after less than 2 hours with no further formation (pH 5.5) or degradation (pH >7 and >30° C). The slower formation rate and even degradation for DCAN, HK, and CH (pH 8.5 and >30° C) compared to their formation during pre-formed chloramination after an initial fast formation produces curvature in the models. Therefore, time² is significant for HK, CH, and DHANs during in-line chloramination. Continuous formation during pre-formed chloramination may be explained by free chlorine released because of monochloramine hydrolysis at pH lower than pH 7. Longer reaction times such as 24 hours at higher than neutral pH and at temperatures exceeding 30° C can diminish the benefit of lower HK, CH, and DHANs concentrations with pre-formed chloramine. In contrast, differences between the two chloramination strategies were small for THM-Br at neutral pH and below.

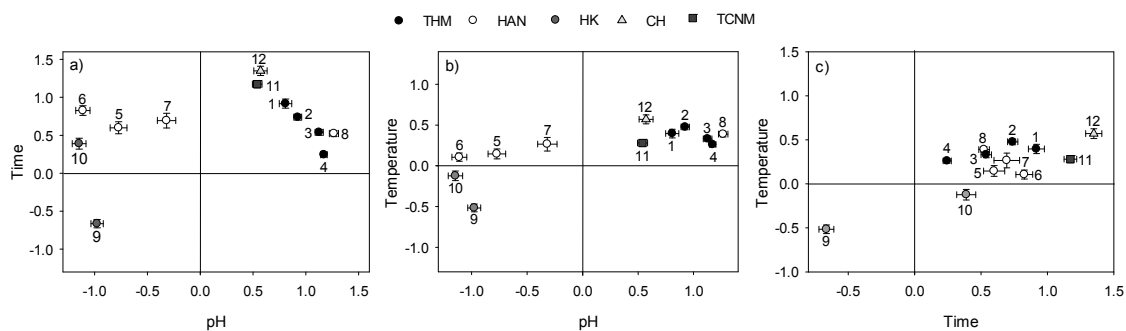


Figure 3.12. Comparison of normalized linear regression coefficients pH, time, and temperature during in-line-formed chloramination.

Notes: Error bars correspond to the standard error that is due to the model.

(1) TCM, (2) BDCM, (3) DBCM, (4) TBM, (5) TCAN, (6) DCAN, (7) BCAN, (8) DBAN, (9) 1,1-DCP, (10) 1,1,1-TCP, (11) TCNM, (12) CH.

3.4 Investigation of Bromine Substitution during Chlorination and Chloramination of Secondary Effluent

As reported in Section 3.2, brominated THMs and DHANs were consistently found in secondary effluents treated with chloramine and chlorine. Bromine incorporation can be quantified by the bromine incorporation factor (BIF), which can be calculated among a class of halogenated DBPs (Gould et al., 1983). It is calculated by dividing the molar amount of bromine incorporated in the DBP species by the total molar halogen concentration of the DBP species (Eq 3.1), allowing for a simplified interclass comparison (Obolensky and Singer, 2005). Equation 3.2 is given as an example for the THMs. The BIF can range from 0 to 1, so that for THMs a value of 0 would mean TCM was the only THM species present and a value of 1 would represent only TBM formation. The 0 to 1 value can also be expressed as percentage of bromine incorporation (i.e., 0 to 100%).

$$BIF = \frac{\Sigma(\text{molar concentration} \times \#Br)}{\Sigma(\text{molar concentration}) \times (\# \text{halogens})} \quad (3.1)$$

$$BIF (THM) = \frac{BDCM + 2 \times DBCM + 3 \times TBM}{3 \times (TCM + BDCM + DBCM + TBM)} \quad (3.2)$$

Table 3.4 provides a summary of important reactions involving bromide during water treatment and their respective rate constants. During chlorination, bromide is oxidized to HOBr and hypobromite (OBr^-) as shown in Eq. 3.3, the speciation of which is pH-dependent (HOCl pKa = 7.5, HOBr pKa = 8.7).

Table 3.4. Bromide–Chlorine–Chloramine Reactions Relevant dring Water Treatment Conditions

Eq	Reaction	Rate Constant (1/M•s)	Reference
(3.3)	$\text{HOCl} + \text{Br}^- \rightarrow \text{HOBr} + \text{Cl}^-$	1.5×10^3	(Kumar and Margerum, 1987)
(3.4)	$\text{NH}_2\text{Cl} + \text{Br}^- \rightleftharpoons \text{NH}_2\text{Br} + \text{Cl}^-$	0.014	(Trofe, 1980)
	$2\text{NH}_2\text{Cl} + \text{H}^+ + \text{Br}^- \rightleftharpoons \text{NHBrCl} + \text{Cl}^- + \text{NH}_4^+$	2.8×10^6	(Valentine, 1986)
(3.8)	$\text{NH}_2\text{Cl} + \text{HOBr} \rightleftharpoons \text{NHBrCl} + \text{H}_2\text{O}$	2.9×10^5	(Gazda et al., 1995)
(3.5)	$\text{NH}_2\text{Cl} + \text{H}^+ \rightleftharpoons \text{NH}_3\text{Cl}^+$	2.8×10^1	(Bousher et al., 1990)
(3.6)	$\text{NH}_3\text{Cl}^+ + \text{Br}^- \rightarrow \text{NH}_2\text{Br} + \text{Cl}^-$	6×10^4	(Bousher et al., 1990)
(3.7)	$\text{HOBr} + \text{NH}_3 \rightleftharpoons \text{NH}_2\text{Br} + \text{H}_2\text{O}$	7.5×10^7	(Wajon and Morris, 1980)

Besides HOBr and OBr⁻, other reactive bromine species such as Br₂, Br₂O, BrOCl, or BrCl can be present (Beckwith and Margerum, 1997). However, at the pH range relevant for water treatment, their concentrations are minor (five orders of magnitude lower) compared to HOBr and OBr⁻. During chloramination, bromide can react with monochloramine (NH₂Cl) to produce the active bromine species bromochloramine (NHBrCl; Bousher et al., 1990; Gazda et al., 1995; Trofe, 1980). Past work has identified two rate-limiting reactions for the oxidation of bromide in the presence of NH₂Cl (Bousher et al., 1990; Vikesland et al., 2001). First, bromide can react with the monochlorammonium ion (NH₃Cl⁺) to form monobromamine (NH₂Br) (Eq. 3.5–3.6). Hydrolysis of NH₂Cl can also produce free chlorine, which then reacts with bromide to generate HOBr (Eq. 3.3). HOBr is an important halogenating agent that can react with ammonia to form NH₂Br (Eq. 3.7) and with monochloramine to form NHBrCl (Eq. 3.8). The oxidation of bromide by NH₃Cl⁺ generally dominates over the reaction between bromide and the free chlorine produced by NH₂Cl hydrolysis during typical drinking water treatment conditions (Vikesland et al., 2001). Immediately after their formation, HOBr and NH₂Br undergo further rapid reactions to produce chlorobromamines. The major species produced is NHBrCl, which is a very reactive brominating agent (Valentine et al., 1986; Vikesland et al., 2001).

Operational parameters, including disinfectant dose, pH, temperature, and reaction time were found to contribute to bromine incorporation into THMs and DHANs during chlorination of drinking water (Hua and Reckhow, 2012). During chlorination, bromide is oxidized to HOBr and OBr⁻, which are pH-dependent reactive brominating agents (Luong et al., 1982). During chloramination, bromide can react with monochloramine to produce active bromamine species (Bousher et al., 1990; Gazda et al., 1995; Trofe, 1980). The formation of reactive bromine species from monochloramine varies in real waters because these reactions are sensitive to bromine concentration, chloramine speciation, and pH. In addition, bromamines and NHBrCl do not react as readily with NOM as HOBr (Symons et al., 1993). However, the impact of specific conditions on bromine incorporation into THMs and DHANs during chloramination has not been extensively studied in the literature to date other than on the Br⁻:Cl₂ and Br⁻:DOC ratios and DOM characteristics (Cowman and Singer, 1996; Hua et al., 2006; Hua and Reckhow, 2007; Liang and Singer, 2003; Symons et al., 1993). A recent study by Hua and Reckhow (2012) investigated the influence of operational parameters on bromine incorporation but focused on a drinking water matrix, chlorination for THMs and DHANs, and mostly on a long contact time of 48 hours. The investigation of short contact times (<24 hours) is of interest in the context of HQRW production as disinfectant contact times normally range from ½ hour up to 1 day. Because bromine incorporation into NOM is faster than that of chlorine (Westerhoff et al., 2004), the first hours of disinfection are important to understand. Therefore, one objective of this study was to assess and quantify the impact of operational parameters during the treatment of secondary effluent. Response surface modeling (RSM) was used to further evaluate the impact of the individual parameters on bromine incorporation within the different strategies and the complex relationships between parameters.

3.4.1 Impact of Disinfection Strategy and Reaction Time

Figure 3.13 shows the individual THM and DHAN formation kinetics during disinfection with chlorine, pre-formed chloramines and inline-formed chloramines at pH 7 and 23° C. As expected, chlorine formed the highest concentration of all DBPs followed by inline-formed chloramines and pre-formed monochloramine. During chlorination and inline-formed chloramination, an initial fast rate of formation was followed by a second slower phase, where TCM, BDCM, DCAN, and BCAN were the major species formed. Similar behavior was seen for TCM during pre-formed chloramination. After 30 minutes of inline chloramination, 30% of the 24-hour concentrations of TCM, BDCM, DBCM, and DHANs were formed. During chlorination, more than 50% of DHAN-Br and 40 to 70% of THM-Br were formed after 30 minutes, relative to their concentrations at 24 hours. When pre-formed monochloramine was used at pH 7, DBAN and TBM could only be measured after 8 and 24 hours of contact time, respectively, despite a background bromide level of 0.3 mg/L. Their slow formation can be explained by the slow reaction of chloramine with bromide to form active halogenating agents ($k = 0.014 \text{ l/M}\cdot\text{s}$ [Trofe, 1980]).

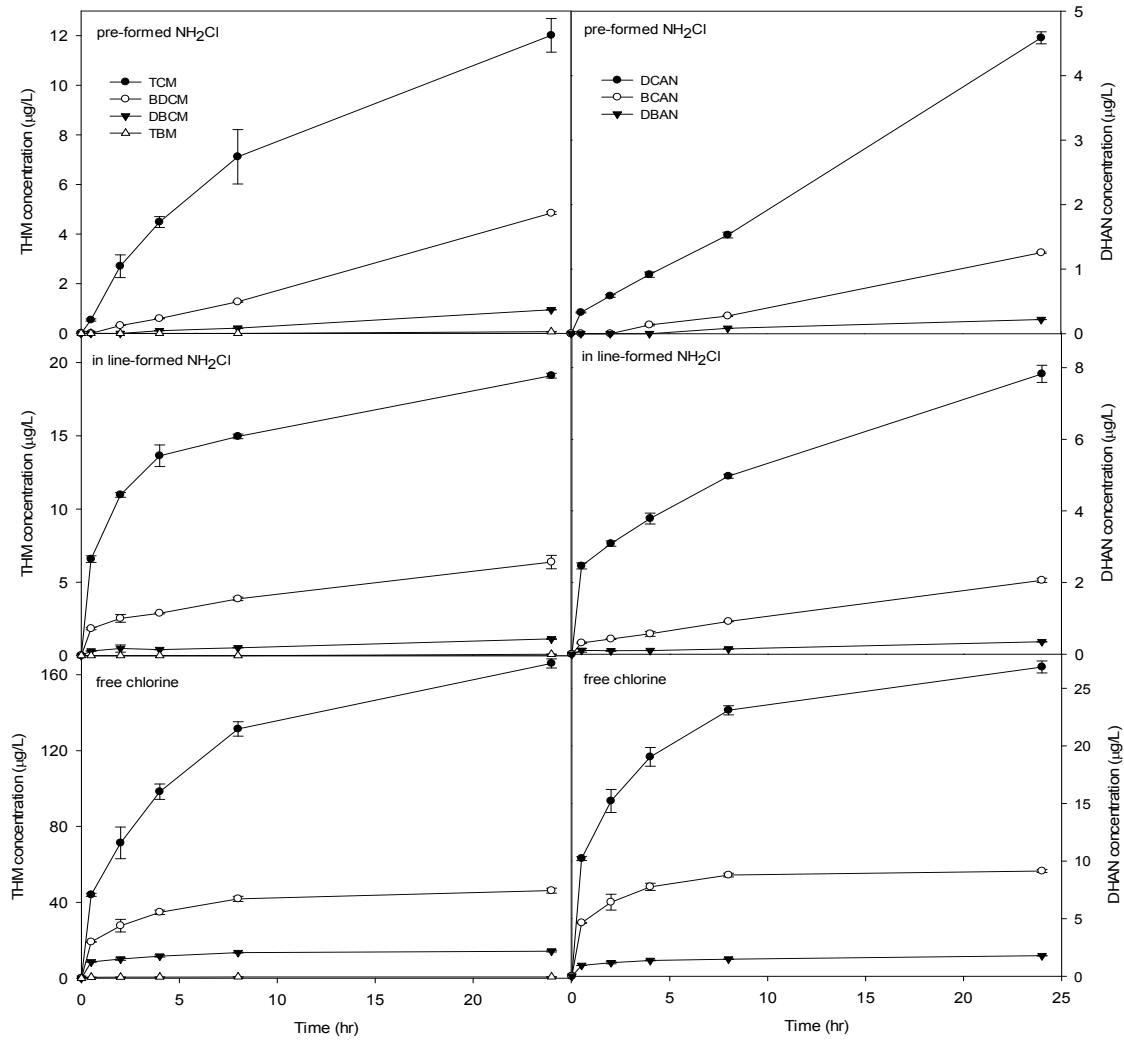


Figure 3.13. THM and DHAN formation during chlorination, pre- and inline-formed chloramination at pH 7 and 23° C.

Notes: DOC 9.9 mg C/L, disinfectant dose 25 mg/L as Cl_2 . Error bars indicate the absolute difference between duplicate samples.

The BIFs for THMs and DHANs of the three different disinfection strategies are shown in relation to contact time in Figure 3.14 (a–c).

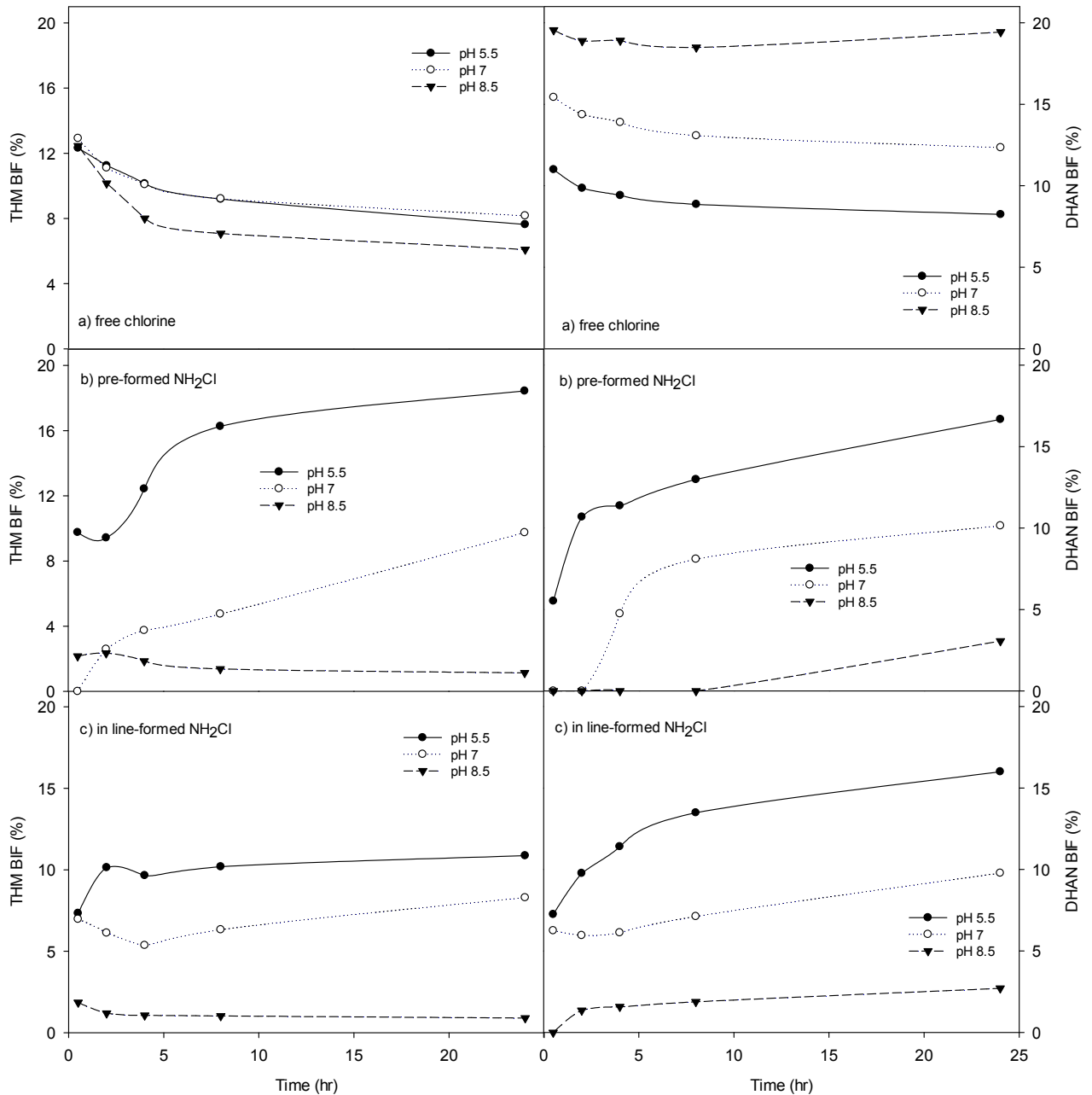


Figure 3.14. THM and DHAN BIF during (a) chlorination, (b) pre-formed chloramination, and (c) inline-formed chloramination in relation to contact time.

Notes: DOC 9.9 mg C/L, disinfectant dose 25 mg/L as Cl_2 .

Among all disinfection strategies, the highest BIF values in THMs and DHANs were observed at the first contact time sampled after 30 minutes of chlorination. The reaction of bromide is five orders of magnitude faster with free chlorine ($k = 1.5 \times 10^3 \text{ l/M}\cdot\text{s}$ [Kumar and Margerum, 1987]) than with NH_2Cl ($k = 0.014 \text{ l/M}\cdot\text{s}$ [Trofe, 1980]), which could account for the difference in formation between chlorination and chloramination in the first hours of disinfection. After the fast bromine incorporation during chlorination, the BIFs of both the THMs and DHANs gradually decreased over the 24 hours of contact time. Chlorine was present in excess relative to bromide and, therefore,

chlorine stays available for reaction with NOM, whereas bromide may quickly be consumed after disinfectant addition. This is indicated by the continuous formation of TCM, although the difference in yields of THM-Br and DHAN-Br was marginal after longer contact times (>8 hours) (Figure 3.13).

In contrast to chlorination, bromine incorporation gradually increased after 4 hours during pre- and inline-formed chloramination. Bromine incorporation into THMs and DHANs during pre-formed chloramination was only observed after 4 hours, whereas during inline chloramination more than 6% bromine incorporation was observed after half an hour. After a decrease in the first 4 hours of inline chloramination, the BIF converged with the gradually increasing bromine incorporation under pre-formed chloramination. During inline chloramination, ammonia and free chlorine were added separately to the secondary effluent and chloramines are formed in situ. The free chlorine did not readily react with the ammonia or NOM during inline chloramination resulting in HOBr formation, which reacts faster with NOM compared to bromamines (Symons et al., 1993). In addition, the ammonia in the solution can react with bromine instead of chlorine to form bromamines, which have a fast reaction (7.5×10^7 1/M•s [Wajon and Morris, 1980]) and likely contributed to the BIF already occurring after 30 minutes of inline chloramination. The formation of NH_2Cl when adding ammonia and chlorine separately is fast ($k = 4.2 \times 10^6$ 1/M•s [Jafvert and Valentine, 1992]), whereas in contrast the reaction of chloramines with bromide to form active brominating agents is slow ($k = 0.014$ 1/M•s [Trofe, 1980]). This may be the reason yields of THM-Br and DHAN-Br occurred only after 4 hours of contact time during the addition of pre-formed monochloramine.

Although chlorination always resulted in the highest DBP yields, the BIFs for THMs and DHANs differed by less than 1.5% between chlorinated and chloraminated samples after 24 hours (pH 7, 23° C). The greatest differences in bromine incorporation between the disinfection strategies occurred at short contact times. The increase during chloramination and gradual decrease during chlorination resulted in similar THM and DHAN BIFs between the two disinfection strategies after 24 hours (Figure 3.14).

3.4.2 Impact of pH

Another impact on the extent of bromine incorporation into THMs and DHANs was caused by pH (Figure 3.14). During chlorination, no significant difference was observed for bromine incorporation into THMs between pH 5 and 7, which is consistent with the study of Hua and Reckhow (2012) who suggested that the relative competition of bromine and chlorine for DBP formation was not influenced by the pH in that range. On the other hand, bromine incorporation decreased as pH was increased from 7 to 8.5 and also gradually decreased by 5 to 6% over 24 hours of contact time for both DBP classes (Figure 3.14). Other DBPs that are formed during chlorination, such as 1,1,1-TCP and CH, can degrade to TCM through a base-catalyzed reaction. Therefore, the decrease in BIF over time and with increasing pH during chlorination could be caused by the increased production of TCM as a degradation product. In contrast to the behavior of the THMs, DHAN bromine incorporation increased by 11% as pH was increased from 5.5 to 8.5. As stated earlier, DHAN hydrolysis is base-catalyzed, but the stability of the DHANs increases with an increasing number of bromine atoms in the molecule (Glezer et al., 1999). Therefore, the higher bromine incorporation with increasing pH may be caused by the lower hydrolysis of BCAN ($k_{\text{HYD}} = 1.20 \times 10^{-3}$ [Bieber and Trehy, 1983]) and DBAN ($k_{\text{HYD}} = 8.15 \times 10^{-4}$ [Bieber and Trehy, 1983]) compared to DCAN ($k_{\text{HYD}} = 1.87 \times 10^{-3}$ [Reckhow et al., 2001]). The impact of the pH also has to be interpreted in terms of the degree of protonation of the reacting species, that is, HOCl/OCl⁻ and HOBr/OBr⁻. HOBr has a higher pKa (8.7) than HOCl (pKa = 7.5). Hence, at pH 8.5, the majority of bromine is still present as HOBr and chlorine is mostly present as OCl⁻. Because the protonated form is the more active halogenating agent, more DHAN-Br relative to DHAN-Cl is formed at high pH values.

With a 24-hour contact time, the percentage of BIF increased from 4 to 11 between pH 5.5 to 7 for both DBP groups and chloramination strategies (Figure 3.14). However, DHAN bromine incorporation was slow, with the first bromine incorporation at pH 7 arising after only 4 hours of contact time. The higher bromine incorporation into THMs at lower pH during pre-formed chloramination (BIF = 18 and 1% for pH 5.5 and 8.5, respectively) could also be promoted by less degradation of other chlorinated DBPs into TCM at lower pH. This hypothesis is also supported by the decreasing THM BIF over time at pH 8.5 (Figure 3.14), which was similar to the trend observed during chlorination.

3.4.3 Impact of Temperature

Figure 3.15 shows the impact of temperature during chlorination and both chloramination strategies at all pH values (pH 5.5, 7, and 8.5). In accordance with the study by Hua and Reckhow (2012), increasing temperature from 23 to 35° C at pH 7 did not affect THM BIF during chlorination and no significant variation in DHAN BIF was reported. The results observed in our study were in agreement. During pre-formed chloramination, temperature had no effect on the THM BIF, but DHAN BIF increased by almost 4%, which corresponds to a 27% increase between 23 and 35° C at pH 7 (Figure 3.15). The enhanced bromine incorporation within the DHANs during chloramination and chlorination potentially is due to stronger hydrolysis of the solely chlorine substituted DHANs. In contrast to pre-formed chloramination, the THM BIF decreased with temperature by 3% during inline-formed chloramination.

3.4.4 Evaluation of Impact of Operational Parameters on BIF with RSM

The same experimental design as described in Section 3.3.4 was used to develop multiple linear regression models for predicting the bromine incorporation into THMs and DHANs depending on pH, temperature, and reaction time. Disinfectant dose and disinfection strategy were kept constant, as significant differences on DBP formation were observed depending on the employed disinfection strategy. To describe the complex relations of the different factors influencing bromine incorporation, a higher-degree polynomial was applied (i.e., quadratic or second order model). The degrees of freedom for each compound and model and information about the model adequacy in terms of explained variation (R^2) and predicted variation (Q^2) of the model are presented in Table 3.5.

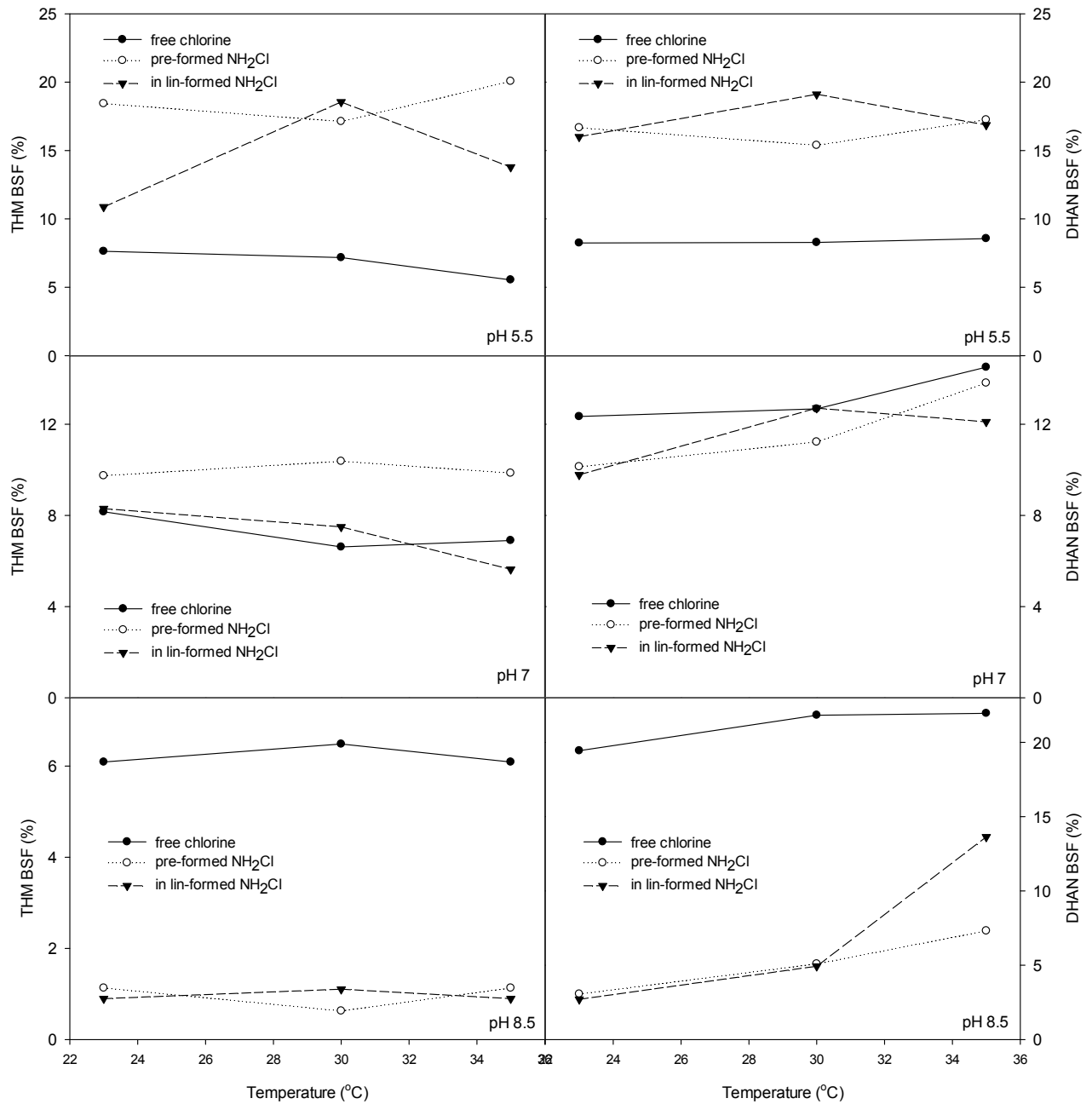


Figure 3.15. Effect of pH and temperature on THM and DHAN BIF during chlorination, pre- and inline-formed chloramination.

Notes: 24-hour contact time, DOC 9.9 mg C/L, disinfectant dose 25 mg/L as Cl₂.

Table 3.5. Explained (R^2) and Predicted (Q^2) Variation of the Models for Chlorination, Pre- and Inline-Formed Chloramination, and their Respective Degrees of Freedom (DF)

Model	THM			DHAN		
	DF	R^2	Q^2	DF	R^2	Q^2
Chlorination	39	0.908	0.878	37	0.956	0.940
Pre-formed NH_2Cl	45	0.914	0.871	46	0.912	0.817
Inline-formed NH_2Cl	34	0.937	0.907	38	0.956	0.938

Figure 3.16 shows the standardized regression coefficients of DBPs produced during chlorination, pre-, and inline-formed chloramination. All predictors were standardized during the regression procedure. Standardized predictors are not dependent on the units of the variables; therefore, they are directly comparable. ANOVA analysis indicated that pH, temperature, and time were significant at the 0.05 level in contributing to the observed variations for all three disinfection strategies. The models for both DBP groups also included interaction and/or squared terms to adequately describe the bromine incorporation.

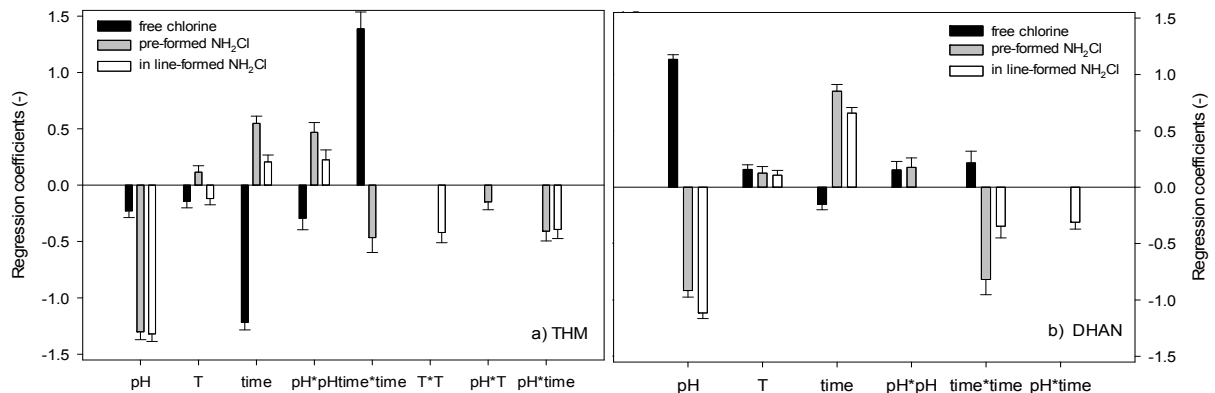


Figure 3.16. Comparison of standardized linear, quadratic, and interaction regression coefficients for (a) THM BIF and (b) DHAN BIF during chlorination, pre- and inline-formed chloramination.

Notes: Error bars correspond to the standard error due to the model. T = temperature.

During chlorination, the increase of all three parameters (pH, temperature, and time) led to a decrease in bromine incorporation with time being the major factor describing the THM BIF. Bromine is a more efficient substitution agent than chlorine (Westerhoff et al., 2004). Because bromine substitution is more rapid than chlorine, most of the brominated DBPs are formed after a short contact time. As the contact time progresses and because of its excess, more chlorine than bromine is available for reaction, generating more chlorinated THMs and, thus, the BIF decreases. Chlorination did not involve an interaction term, but squared terms $pH*pH$ and $time*time$ appeared to be significant. Squared terms result in a curvilinear shaped model. $time*time$ is an important term because the BIF decreased rapidly in the first hours, followed by a period of slower decrease. pH had no impact between pH 5.5 and 7, but at pH 8.5 the BIF decreased leading to a significant $pH*pH$

contribution. Nonetheless, time is the major factor influencing the bromine incorporation of the THMs during chlorination because the regression coefficients of pH and time are five and eight times lower than time, respectively.

In contrast to chlorination, pH was the most important parameter during chloramination, followed closely by time. pH is a central parameter as THM-Br formation may involve bromamines as oxidizing agents. The oxidation of bromide by monochloramine is acid-catalyzed and results in active haloamine species such as NHBrCl (Trofe, 1980). However, the key reaction involved may be the decay of monochloramine to products, including NH_3Cl^+ , NHCl_2 , and HOCl at low pH. Those can then react with HOBr and NH_2Br to produce chlorobromamines the major species of which is NHBrCl , a very reactive brominating agent (Valentine et al., 1986; Vikesland et al., 2001). Interaction involved all three parameters leading to $\text{pH} \cdot \text{T}$ and $\text{pH} \cdot \text{time}$ coefficients for BIF prediction during pre-formed chloramination. pH and time are dependent on each other as the difference in BIF values at the different pH values changes with contact time. For example, between pH 5.5 and 8.5 the difference in BIF at 30 minutes of contact time was 8%, which increased to 17% after 24 hours. There was a continuous increase in bromine incorporation at low pH, whereas the BIF stayed low at high pH (Figure 3.16).

Similar to the THMs, all three parameters, as well as the square terms $\text{pH} \cdot \text{pH}$ and $\text{time} \cdot \text{time}$, were significant in DHAN BIF during chlorination. The decrease in DHAN bromine incorporation also slowed down after a fast decrease in the first hours of disinfectant contact. Temperature, time, and the squared terms only played a small role in the model, whereas pH was the major influencing parameter during chlorination. DHANs undergo base-catalyzed hydrolysis, but their stability increases with increased bromine incorporation (Glezer et al., 1999). Therefore, DCAN reacts more than DHAN-Br to pH changes, resulting in a strong impact on the BIF with lowest values at low pH (Figure 3.14a).

During chloramination, contact time was almost as important as pH. During inline chloramination, pH tended to be slightly more influential, likely because of the pH dependency of the active chlorine species (HOCl/OCl^-), which could be present because of the chlorine that did not react with ammonia to form chloramines. This would explain the fast bromine incorporation during inline chloramination. $\text{Time} \cdot \text{time}$ is significant because bromine incorporation over time is described by an initial fast period followed by a period of slower incorporation with pre-formed monochloramine.

Chapter 4

DBP Removal by RO and NF Membranes— Influence of Operational Parameters, Solute, and Solution Properties

4.1 Preliminary Experiments

4.1.1 Volatilization, Hydrolysis, and Adsorption of DBPs

During the bench-scale crossflow system experiments, the suite of DBPs studied can be lost because of volatilization, hydrolysis, and/or adsorption. Combined losses by volatilization, adsorption, and hydrolysis were evaluated by spiking the DBP mix at baseline conditions into the background electrolyte solution during 5 days in the experimental setup without a membrane present. A sample was taken from the system after homogenization and kept at the same conditions for the same time frame without a head space to estimate DBP hydrolysis alone. The DBPs in this hydrolysis control showed an increase in concentration of TCM, DCACAm, BCACAm, and DBACAm, whereas the remaining DBPs in the mixture were broken down by hydrolysis (Figure 4.1a). This observation is supported by previous studies identifying TCM as a hydrolysis by-product of 1,1,1-TCP and TCAN (Glezer et al., 1999; Nikolaou et al., 2001), whereas DCACAm, BCACAm, and DBACAm could be formed as degradation products of their corresponding HANs (Glezer et al., 1999). In fact, DCACAm was not spiked during the test, which proved that its occurrence was caused by the degradation of the other DBPs. The behavior of DCACAm represented in Figure 4.1 a,b was determined by comparing the formation after 5 hours and the final sampling point at 5 days. To investigate the observed increase for these specific DBPs, additional batch tests for the different DBP families were independently prepared as follows: (1) THM4, (2) I-THMs + CH, (3) HKs + HANs + TCNM, and (4) HACams, which were all kept headspace-free under the same experimental conditions. BIACAm and DIACAm data are missing in the batch hydrolysis experiment because of analytical problems. As observed previously, TCM was generated as a result of 1,1,1-TCP degradation. DCACAm, BCACAm, and DBACAm were suspected to be formed as degradation products of their corresponding HANs. The batch hydrolysis test solely containing HACams showed that not only can HANs augment DCACAm, BCACAm, and DBACAm formation, but also the transformation of BDCACAm, DBCACAm, and TBACAm. The hydrolysis of the HACAm during the batch tests appeared to be slower than within the feed solution mix. On the basis of these batch tests, the highest hydrolysis rates were confirmed for TCAN (88%) and TCNM (83%), similar to previously published literature (see Table 4.1). Also in agreement with the literature, a negligible hydrolysis of DCIM, THM-Br, and <15% hydrolysis of DHANs and CH was measured. Sixty-five percent of 1,1,1-TCP and 16% of 1,1-DCP were hydrolyzed after 5 days. In addition, 1,1-DCP hydrolysis was 80% less than expected from the published hydrolysis constant (Table 4.1). The subtraction of the percentage of hydrolysis as determined in the DBP mix solution from the total DBP losses allowed the estimation of the combined losses by volatilization and adsorption, although the latter two mechanisms could not be distinguished from one another (Figure 4.1a). The losses that were due to these two mechanisms were significant (i.e. >15%) for all DBPs except the HANs and 1,1,1-TCP, and was accounted for during the interpretation of the data. The most volatile DBP with a Henry's Law constant of $3.7 \times 10^{-3} \text{ atm}\cdot\text{m}^3/\text{mol}$ was TCM. For this DBP, losses exceeded the formation occurring from the degradation of the other DBPs present. Yet, remaining concentrations were

sufficient for analysis. Although the experimental setup was solely built of stainless steel, glass, and Teflon with a floating lid in the feed tank, losses of DBPs from these three mechanisms could not be prevented. Except for TCAN, CH, and TCNM that were re-spiked in the system after 3 days, concentrations of DBPs measured after 5 days of recirculation were high enough to allow for the investigation of their rejection by RO and NF membranes.

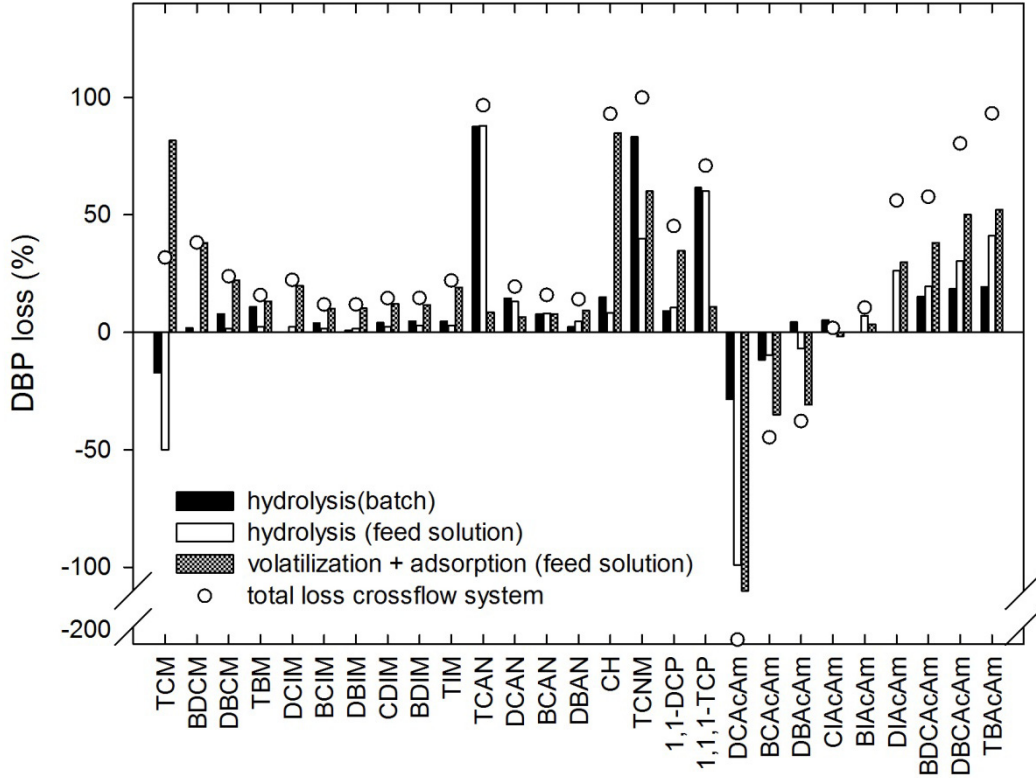


Figure 4.1. Percentage of DBP loss from hydrolysis within feed solution mix (white bars), percentage of DBP loss from hydrolysis during batch tests for THM4, I-THM+CH, HKs+HANs+TCNM, and HAcaMs (black bars), and losses from volatilization and adsorption (grey bars).

Notes: White dots correspond to the total loss during recirculation within the experimental setup without membrane for the duration of 5 days (all solutions spiked at 50 µg/L except the I-THMs at 25 µg/L in milliQ water adjusted at pH 6.8, 7 mM NaCl, and 1 mM KH₂PO₄).

Table 4.1. DBP Properties

Disinfection By-product	Abbrev.	MW	MV ^a	Mwidth ^a	DM ^b	H-Acc	Log K _{ow} ^c	K _{hyd}	K _H
(1) Trichloromethane	TCM	119	70	2.38	1.72	0	1.97	c 6.45 x 10 ⁻⁵	3.67 x 10 ⁻³
(2) Dichlorobromomethane	BDCM	164	75	2.44	1.82	0	2.10	c 1.18 x 10 ⁻³	2.12 x 10 ⁻³
(3) Bromodichloromethane	DBCM	208	79	2.54	1.66	0	2.16	c 3.14 x 10 ⁻⁴	7.83 x 10 ⁻⁴
(4) Tribromomethane	TBM	253	83	2.52	1.19	0	2.40	c 3.65 x 10 ⁻⁵	5.35 x 10 ⁻⁴
(5) Dichloroiodomethane	DCIM	211	81	2.47	2.10	0	2.03	ⁱ 2.88 x 10 ⁻⁷	6.82 x 10 ⁻⁴
(6) Bromochloroiodomethane	BCIM	255	85	2.57	1.80	0	2.11	-	2.23 x 10 ⁻⁴
(7) Dibromoiodomethane	DBIM	300	90	2.57	1.19	0	2.20	-	7.30 x 10 ⁻⁵
(8) Chlorodiiodomethane	CDIM	302	92	2.47	1.84	0	2.53	-	1.45 x 10 ⁻⁴
(9) Bromodiiodomethane	BDIM	347	96	2.56	1.09	0	2.62	-	4.73 x 10 ⁻⁵
(10) Triiodomethane	TIM	394	102	2.59	0.88	0	3.03	-	3.06 x 10 ⁻⁵
(11) Trichloroacetonitrile	TCAN	144	87	2.92	1.33	1	2.09	^d 6.26 x 10 ⁻²	1.34 x 10 ⁻⁶
(12) Dichloroacetonitrile	DCAN	110	73	2.43	2.44	1	0.29	^e 1.87 x 10 ⁻³	3.79 x 10 ⁻⁶
(13) Bromochloroacetonitrile	BCAN	154	77	2.44	2.69	1	0.38	^f 1.20 x 10 ⁻³	1.26 x 10 ⁻⁶
(14) Dibromoacetonitrile	DBAN	199	82	2.52	2.73	1	0.47	^f 8.15 x 10 ⁻⁴	4.06 x 10 ⁻⁷
(15) Chloral hydrate	CH	165	105	3.12	2.33	2	0.99	^c 1.00 x 10 ⁻³	5.71 x 10 ⁻⁹
(16) Trichloronitromethane	TCNM	164	93	3.09	2.21	3	2.09	^c 4.60 x 10 ⁻²	2.05 x 10 ⁻³
(17) Tribromonitromethane	TBNM	298	106	3.18	3.13	3	1.59	-	6.45 x 10 ⁻⁸
(18) 1,1-Dichloropropanone	1,1-DCP	127	92	2.84	1.14	1	0.20	^g 2.20 x 10 ⁻²	6.15 x 10 ⁻⁶
(19) 1,1,1-Trichloropropanone	1,1,1-TCP	161	107	3.01	2.82	1	1.12	^h 6.40 x 10 ⁻¹	2.17 x 10 ⁻⁶
(20) Dichloroacetamide	DCAcAm	128	87	2.71	2.17	2	0.19	-	1.39 x 10 ⁻⁹
(21) Bromochloroacetamide	BCAcAm	172	91	2.96	2.36	2	0.00	-	4.54 x 10 ⁻¹⁰
(22) Dibromoacetamide	DBAcAm	217	95	2.83	2.61	2	0.09	-	1.49 x 10 ⁻¹⁰
(23) Chloroiodoacetamide	CIAcAm	219	97	2.79	2.35	2	0.41	-	2.94 x 10 ⁻¹⁰
(24) Bromoiodoacetamide	BIAcAm	264	102	2.91	2.70	2	0.50	-	9.62 x 10 ⁻¹¹
(25) Diiodoacetamide	DIAcAm	311	108	2.89	2.86	2	0.92	-	6.23 x 10 ⁻¹¹
(26) Bromodichloroacetamide	BDCAcAm	207	105	3.04	2.67	2	-	-	-
(27) Dibromochloroacetamide	DBCACAm	251	109	3.10	3.12	2	-	-	-
(28) Trichloroacetamide	TCAcAm	162	101	3.06	3.71	2	1.04	-	4.89 x 10 ⁻¹⁰
(29) Tribromoacetamide	TBAcAm	296	114	3.28	3.48	2	1.10	-	1.71 x 10 ⁻¹¹

Table 4.1 DBP Properties (continued)

Disinfection By-product	Abbrev.	MW	MV ^a	H-Acc	Log Kow ^c	pK _a
(30) Dichloroacetic acid	Cl ₂ AA	129	84.05	5	0.52	2.3
(31) Dibromoacetic acid	Br ₂ AA	218	92.74	5	0.70	1.6
(32) Trichloroacetic acid	Cl ₃ AA	163	98.17	5	1.44	1.72
(33) Chloroacetic acid	ClAA	95	69.97	5	0.34	3.06
(34) Bromoacetic acid	BrAA	139	74.32	5	0.43	2.64
(35) Bromodichloroacetic acid	BrCl ₂ AA	208	102.51	5	1.53	1.45
(36) Tribromoacetic acid	Br ₃ AA	297	111.2	5	1.71	0.71
(37) Bromochloroacetic acid	BrClAA	173	88.39	5	0.61	1.97
(38) Dibromochloroacetic acid	Br ₂ ClAA	252	106.85	5	1.62	1.12
(39) Cyanogen chloride	CNCl	61	42.16	1	-0.38	-
(40) Cyanogen bromide	CNBr	106	45.22	1	-0.29	-

Notes: MW = Molecular Weight (g/mol), MV = Molecular Volume (Å³), Mwidth = Molecular Width (Å), DM = Dipole Moment (Debye), K_{hyd} = Hydrolysis Constant (1/H), K_H = Air-Water Partitioning Coefficient (Atm-m³/mol), H-Acc = H-Bond Acceptor

Notes and Sources: ^a ChemAxon; ^b Predicted, ChemBio3D Ultra 12.0; ^c EPIsuite; ^d pH 7.2, 20° C, Croue and Reckhow (1989); ^e pH 7.0, Reckhow et al. (2001); ^f pH 7.3, Bieber and Trehy (1983); ^g 21° C, Nikolaou et al. (2001); ^h pH 7.0, Reckhow and Singer (1985); ⁱ pH 7.0, 25° C, Mabey and Mill (1978)

4.1.2 Time Required to Achieve Steady State DBP Removal

The removal of uncharged organic compounds has been shown to be time dependent when solutes exhibit an affinity to the membrane (Kimura et al., 2003). Because of adsorption of the compounds and the subsequent diffusion through the membrane matrix, rejection would decrease over time until steady state is reached. Therefore, care has to be taken when studying hydrophobic DBPs such as THMs and I-THMs; because of their intermediate hydrophobicity ($\log K_{ow}$ up to 3), they are expected to interact with the membrane. To ensure that stable rejection is achieved, the membrane has to be conditioned before adjusting the various parameters. Indeed, results show that several days of recirculation were required to reach a quasi-steady-state rejection. The time required varied from 6 days for I-THMs (Figure 4.2a for RO and 4.2b for NF) to only 2 days for the rest of the DBPs to equilibrate (Figure 4.2c for RO and 4.2d for NF).

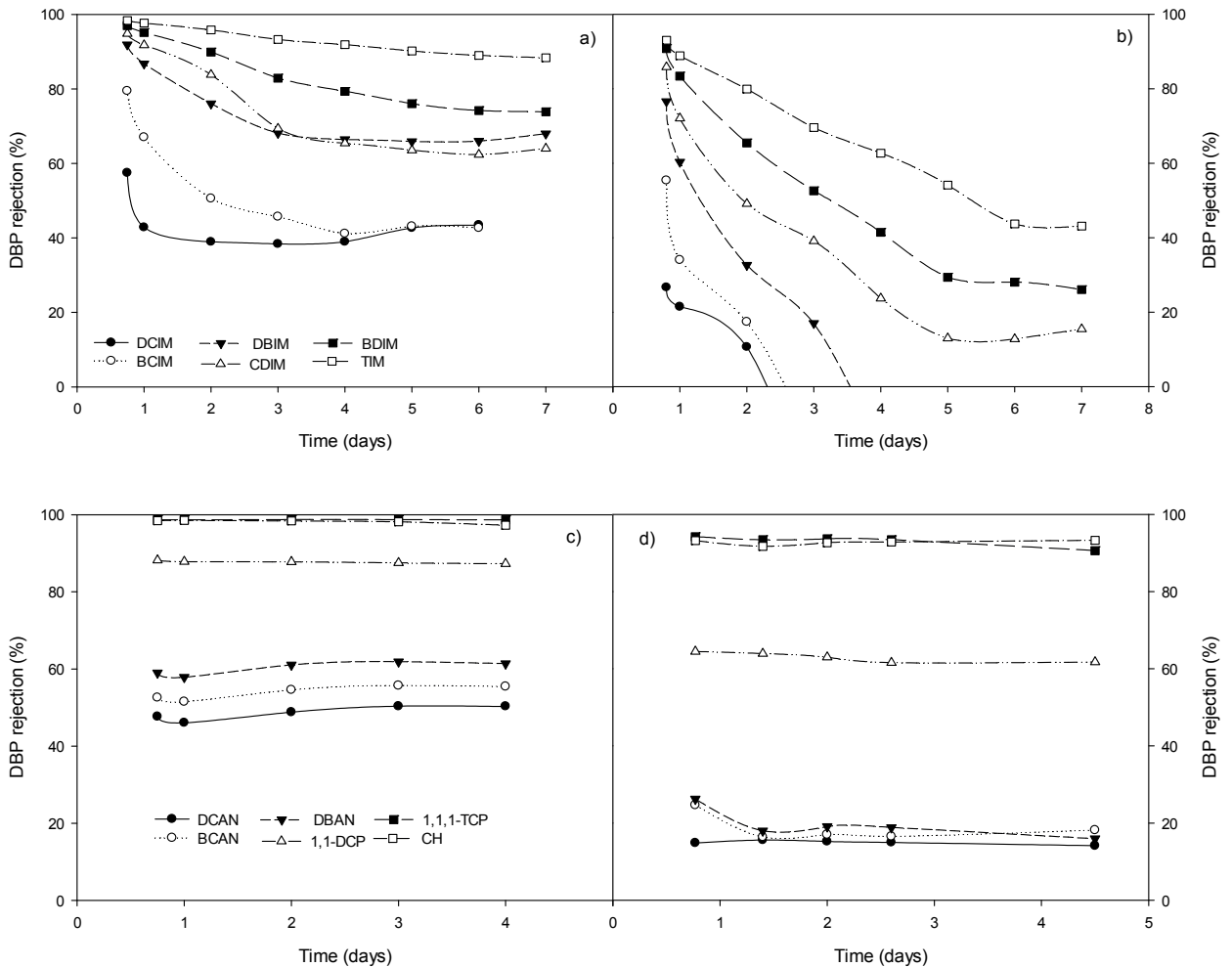


Figure 4.2. DBP rejection over time by RO (a and b) and NF (c and d).

Notes: Permeate flux 18 L/m²h, feed pH 6.8, crossflow velocity 0.12 m/s, 7 mM NaCl, 1 mM KH₂PO₄, feed temperature 23.5° C.

The time of 2 days to establish steady-state rejection for the THMs is in accordance with findings of Kim et al. (2007) who stated that a 48-hour pre-equilibration was necessary for

two of the THMs, including TCM and TBM. It is interesting that with the NF membrane, DCIM, BCIM, and DBIM were initially well rejected as high as 80% after the first day for DBIM, but then sharply decreased with a complete passage of these compounds after 2 to 3 days (Figure 4.2b). These results clearly show the time dependency of the rejection in the early stage of the trials and the need to account for this during the experiments. For this reason, it was decided that all rejection tests would be carried out after at least 6 days of equilibration.

4.1.3 Feed Concentration

To ensure that there is no competition for functional sites between different groups of DBPs within the membrane polyamide layer, which potentially could lead to biased results, a control experiment was performed with the NF membrane. The feed solution of the control experiment solely contained the intermediate hydrophobic THMs and the polar DHANs and HKs. The THMs could not be removed by the NF membrane. The DHANs showed a poor removal of 10 to 14%; whereas 1,1-DCP and 1,1,1-TCP could be removed by 70% and 97%, respectively. For comparison, a mix of 29 DBPs, including I-THMs, THMs, HAcAms, HNMs, CH, HANs, and HKs was applied. The I-THMs, were used because they are more hydrophobic than THMs, whereas HAcAms, HNMs, and CH were added because of their higher polarity. DHAN rejection from this solution was similar to that from the initial feed at 13 to 15% ($\pm 2-4\%$); whereas 1,1-DCP and 1,1,1-TCP rejection was $65 \pm 2\%$ and $94 \pm 2\%$, respectively. This implies that the competition of the various DBPs for the active sites in the membrane polymer is negligible.

4.1.4 Sample Collection

Samples were always collected and kept on ice until extraction; however, to ensure that there was no significant loss of DBPs because of volatilization during sample collection and transport, a controlled experiment was performed and repeated several times throughout the study. Three vials were filled with feed solution containing a known concentration of DBPs. The first vial was opened during feed sampling, the second vial was opened during permeate sampling, and the third vial remained unopened. There were never significant differences for any DBP between the three volatilization control samples, indicating the losses that were due to volatilization during sample collection were negligible.

4.2 DBP Rejection by RO and NF Membranes

4.2.1 Rejection by Different RO and NF Membranes

Figure 4.3a shows the DBP rejection tested at UQ by the ESPA 2 (RO) and NF 90 (NF) membranes after reaching steady state at baseline conditions. For these DBPs, results at UNC were similar to those at UQ (see Figures C.1 and C.2 in Appendix C). The rejection of these DBPs by SW 30 (RO) versus NF 90 (NF) can be seen in Figure 4.4 and rejection of SW 30

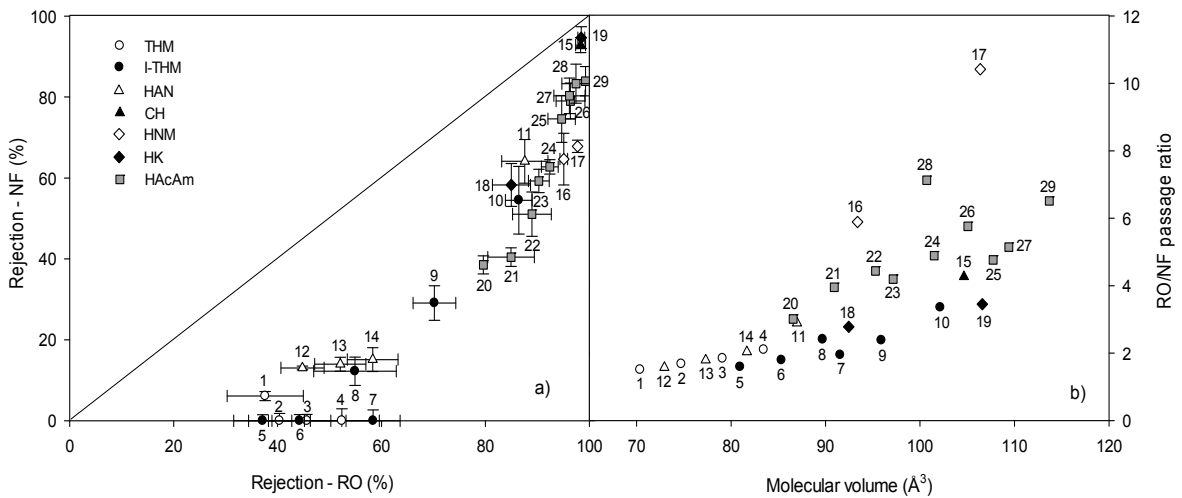


Figure 4.3. (a) DBP rejection by NF versus RO and (b) the ratio of DBP passage between RO and NF in relation to their molecular volume.

Notes: Error bars indicate the standard deviation between 8 different coupons for the RO and 4 different coupons for the NF membrane (permeate flux 18 L/m²h, feed pH 6.8, crossflow velocity 0.12 m/s, 7 mM NaCl, 1 mM KH₂PO₄, feed temperature 23.5° C).

See Table 4.1 for DBP identity associated with number values on the graph.

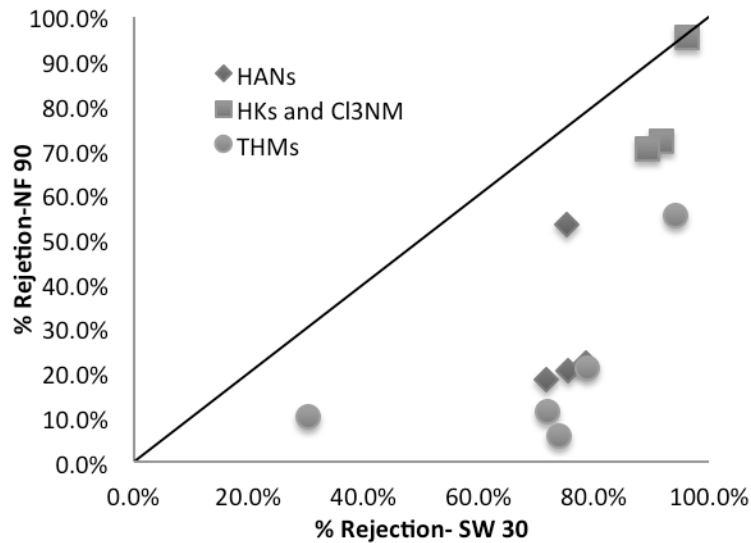


Figure 4.4. DBP rejection by NF 90 (NF) versus SW 30 (RO).

Notes: Four replicates per point. Feed pH 7, crossflow velocity 0.12 m/s, 7 mM NaCl, 1 mM KH₂PO₄, feed temperature 21 ° C, flux 18 L/m²hr.

(RO) versus ESPA 2 (RO) can be seen in Figure 4.5. The rejection of HAAs and CNXs by the three membranes is displayed in Figures 4.5 and 4.6, respectively. DBP rejection by the membranes varied widely from an apparent negative rejection of CNBr and CNCl that was due to concentration polarization to >90% rejection of HAAs. However, the rejection for

almost all neutral DBPs was considerably higher for RO membranes than for NF, with CNBr being the only exception.

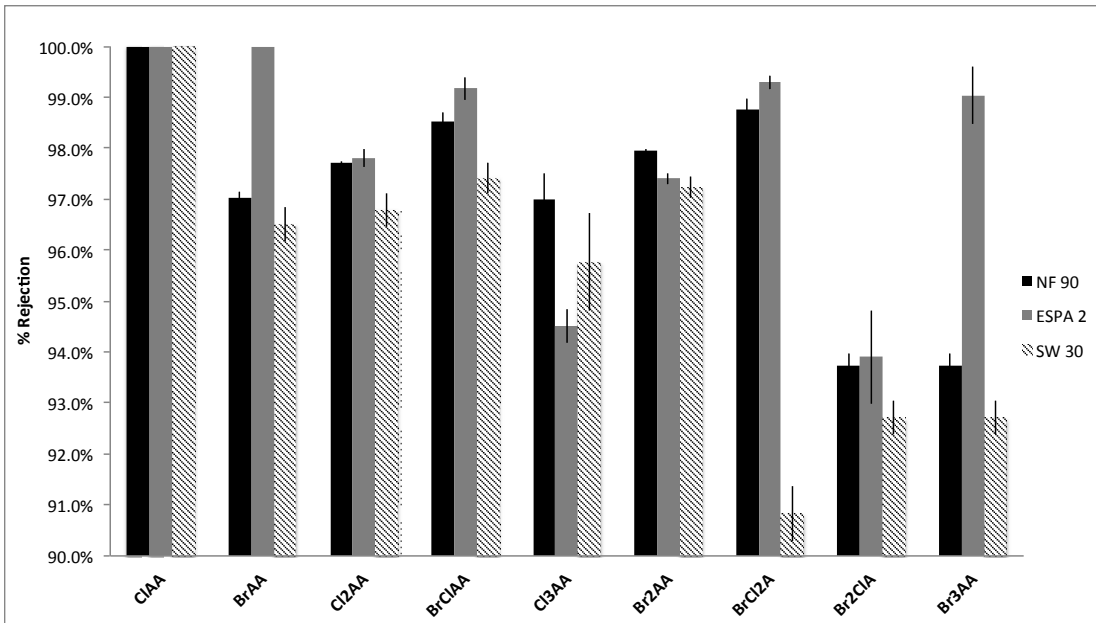


Figure 4.5. Comparative HAA rejection by three membranes.

Notes: Error bars indicate the standard error between four rejection values. Feed pH 7, crossflow velocity 0.12 m/s, 7 mM NaCl, 1 mM KH₂PO₄, feed temperature 21 °C, flux 18 L/m²hr.

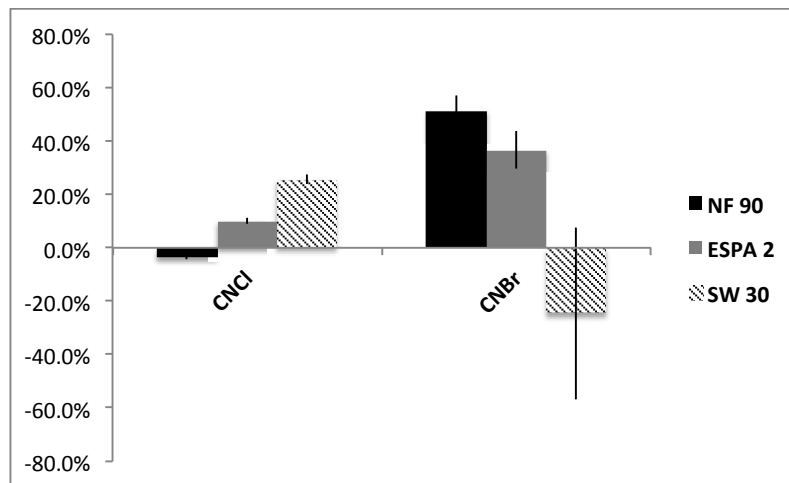


Figure 4.6. Comparison of CNX rejection by three membranes.

Notes: Error bars indicate the standard error between four rejection values (feed pH 7, crossflow velocity 0.12 m/s, 7 mm NaCl, 1 mM KH₂PO₄, feed temperature 21 °C, flux 18 L/m²hr).

Pores in the active surface layer of RO and NF membranes should be thought of as material-free void spaces in the dense polymer layer, presenting tortuous paths for solutes and solvent to pass through (Meares, 1976). NF membranes were developed with a larger pore size than RO membranes to perform with a higher water permeability, which also results in reduced

rejection characteristics for smaller, less neutral, and low-charged ions (e.g., NaCl) compared to RO membranes (Bergman, 2007). Therefore, NF membranes are believed to be “looser” and their larger pore size is likely to contribute to the higher water permeability. Desalination membranes, such as SW30, are generally “tighter” and more hydrophobic than low-fouling RO membranes like ESPA 2. Consequently, the overall lower DBP rejection of neutral DBPs by NF 90 as compared to both RO membranes along with ESPA 2 compared to SW30 appears to be related to size exclusion as well as to solute membrane affinity (as shown in Figures 4.3 to 4.6).

Solutes with a high affinity for the membrane material can adsorb onto and partition into the membrane matrix more easily, facilitating diffusion through the membrane matrix (Kimura et al., 2003; Nghiem et al., 2004). The partitioning can take place via hydrophobic interaction or by the formation of H-bonds. Hence, solutes that are hydrophobic and/or possess H-bonding sites might be less rejected by high-pressure membranes. HAcAms, for example, possess two H-bonding donor as well as acceptor sites that can form H-bonds with the membrane polymer and subsequently facilitate their diffusion to the permeate side. The membrane polymers are made of polyamide that is polarized because of the amine and oxygen in the structure. The HAcAm H-bonding capacity and polar nature may lead to the lower solute rejection through both NF and RO membranes compared to DBPs with similar molecular size such as CH, HKs, and HNMs. Although the CH, HKs, and HNMs also possess H-bonding moieties on their respective carbonyl and nitro groups, HAcAms have two H-acceptor sites, hold two H-donor sites, and have higher dipole moments. Hydrophobic interaction leading to reduced rejection may also explain why some HAAs were rejected less by SW 30 than ESPA 2, as SW 30 is thought to be more hydrophobic.

Cyanogen halides (CNXs) are very small with a molecular volume that is about half or less than half of all other DBPs, leading to high passage through the membranes. Differences in the rejection of CNBr by the RO membranes compared to the NF membrane are insignificant (ranges overlap). However, CNCl is not rejected by the NF membrane at all but was somewhat by the RO membranes (10–25%). CNCl has a lower rejection value than CNBr for the NF 90 and ESPA 2 membranes. This is likely because of the smaller molecular size of CNCl as compared to CNBr. However, CNBr appears to be rejected less by the SW 30 than CNCl, although the ranges of rejection are close to overlapping. This may be due partially to the more hydrophobic nature of SW 30 than both NF 90 and ESPA 2, but also could be due to the lower precision in the measurement of CNBr. These compounds also may be particularly vulnerable to concentration polarization, with negative rejections observed and additional evidence as described later. When a great deal of concentration polarization occurs, it could result in lower observed rejections. This also may explain partially the differences in rejection between CNCl and CNBr.

The smallest DBPs in the suite studied at UQ were the THMs and DHANs, which have similar molecular volumes. DHANs were rejected less than 20% by the NF membrane, whereas THMs, DCIM, BCIM, and DBIM were rejected by less than 10%. THMs and I-THMs are hydrophobic and so, as previously discussed, hydrophobic adsorption may be facilitating their passage through the membrane polymer, which contains polar and hydrophobic sites that interact with the DBPs. The greater pore size of the NF membrane offers a facilitated entry into the pore and the internal surface area allows DBP adsorption and subsequent easier diffusion to the permeate side. For comparison, the adsorption of hydrophobic hormones has also been found to increase with increasing pore size (Semião and Schäfer, 2013).

At UQ, the only THM that showed some minor rejection (<10%) with the NF membrane was TCM. This was thought to be a result of its formation in the feed because of degradation of CH and 1,1,1-TCP (Glezer et al., 1999; Nikolaou et al., 2001) and thus the use of a higher concentration in the calculation of rejection. At UNC, however, TCM, BDCM, and TBM were rejected at 10%, 11%, and 21%, respectively, on average by NF 90, and CH was neither spiked nor observed. This indicates that the rejection of TCM may be actually occurring, as opposed to the result of breakdown of other DBPs on the feed side only.

4.2.2 Reverse Osmosis

The rejection of the DBPs by ESPA 2 in relation to their intrinsic properties, including molecular weight, molecular volume, $\log K_{ow}$, and dipole moment is shown in Figure 4.7. Rejection values for HAAs and CNXs are not included in Figure 4.7; however, CNXs show similar patterns as previously described, having low molecular size and also having low rejection by RO membranes. The rejection of HAAs by ESPA 2 and SW 30 in relation to their intrinsic properties including molecular volume, $\log K_{ow}$, and pK_a is shown in Figure 4.8. Results for the relationship between rejection by SW 30 and physical-chemical properties are similar to that of ESPA 2.

As can be seen, increasing molecular size tends to increase DBP rejection. The smaller DBPs, however, do not show a strong correlation. For example, BCIM, DBIM, and BDIM have the same molecular width, but exhibit a wide range of rejection (44% to 70%). On the other hand, similar rejections are obtained among the THMs, I-THMs, and DHANs, but those vary in their molecular volume. The THMs and I-THMs are intermediate hydrophobic with $\log K_{ow}$ values ranging from 2 to 3. The hydrophobicity may lead to hydrophobic interaction with the membrane active surface layer. The adsorption facilitates the diffusion through the membrane matrix on the permeate side leading to lower rejections compared to their molecular size. The DHANs are not as hydrophobic but are polar, which, in turn, can lead to H-bonding within the membrane matrix similar to the hydrophobic interaction facilitating the diffusion and leading to lower rejection.

As HAAs are equally charged under baseline conditions and are likely rejected by electrostatic repulsion, it would be expected that they would all have similar rejection, as shown in Figure 4.8 and, in fact, there is only a 9 to 10% difference in the most to least rejected HAA. However, both molecular volume and $\log K_{ow}$ appear to be somewhat correlated with rejection for both RO membranes, with the relationship being slightly stronger with $\log K_{ow}$.

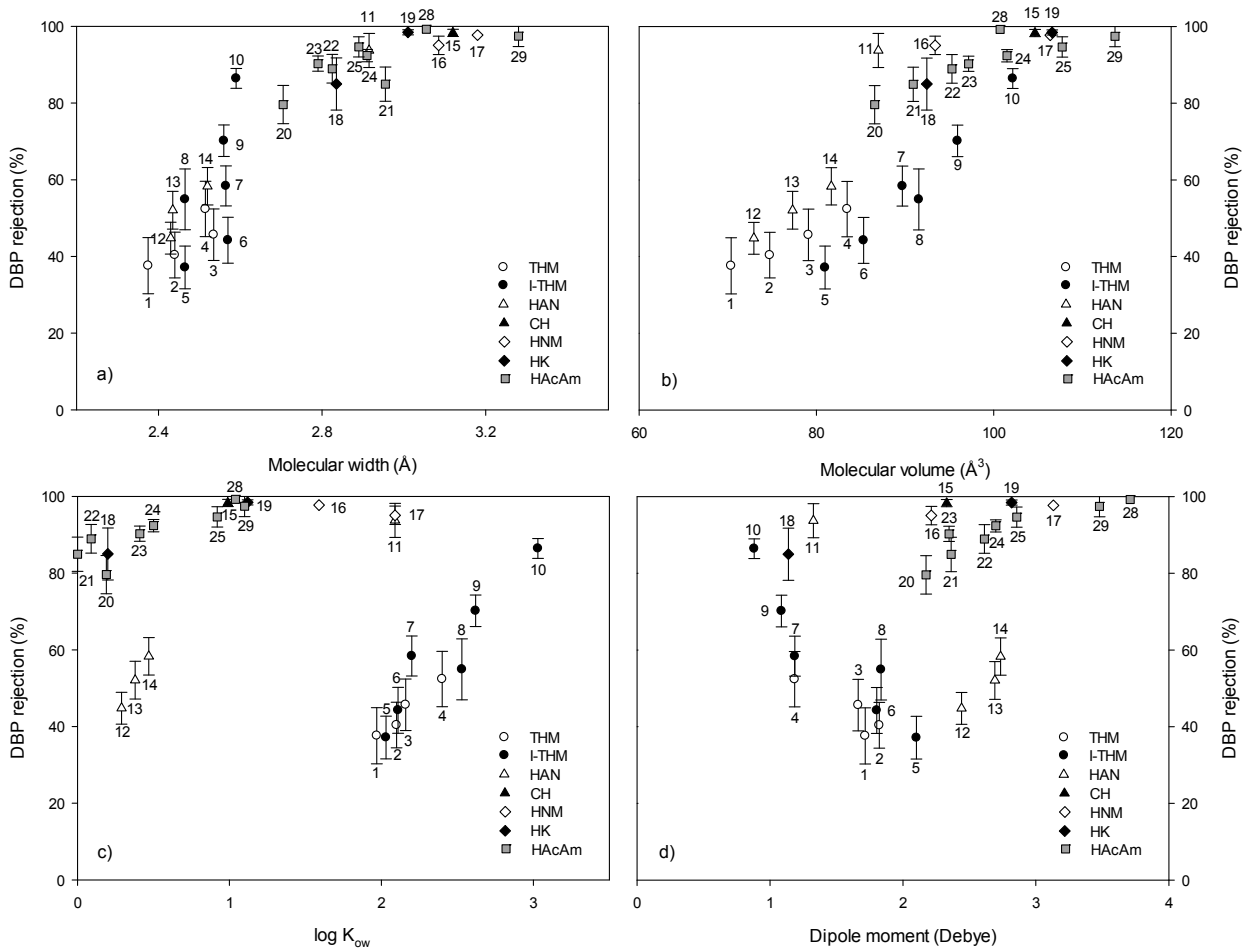


Figure 4.7. DBP rejection by RO as a function of DBP properties (a) molecular width, (b) molecular volume, (c) $\log K_{ow}$, and (d) dipole moment.

Notes: Error bars indicate the standard deviation among eight different coupons (permeate flux 18 L/m²h, feed pH 6.8, crossflow velocity 0.12 m/s, 7 mM NaCl, 1 mM KH₂PO₄, feed temperature 23.5° C). See Table 4.1 for DBP identity associated with number values on graph.

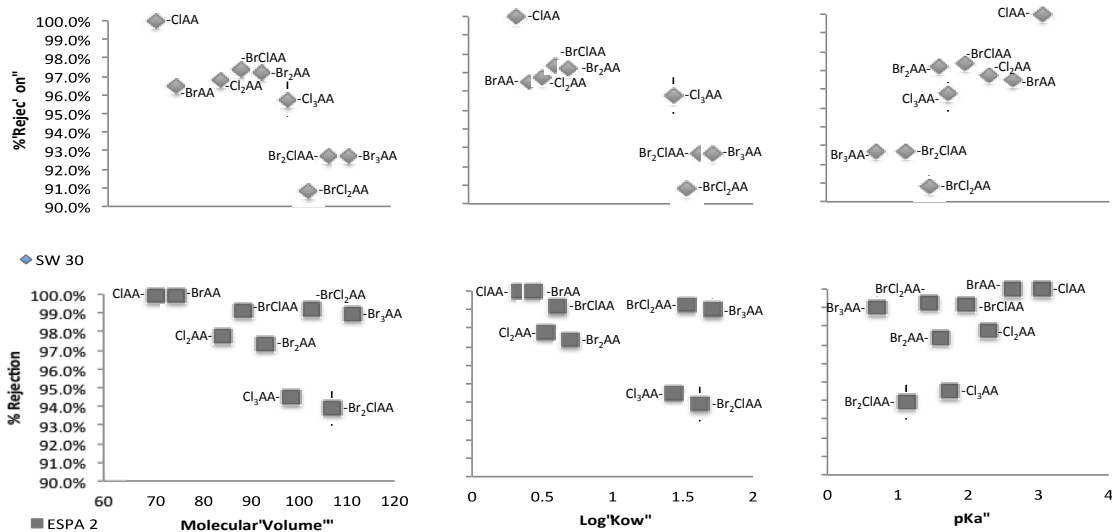


Figure 4.8. HAA rejection by SW 30 (top row) and ESPA 2(bottom) as a function of properties: (a) molecular volume, (b) Log Kow, and (c) pKa.

4.2.3 Nanofiltration

The rejection of the DBPs by NF in relation to their intrinsic properties, including molecular weight, molecular volume, log Kow, and dipole moment is shown in Figure 4.9. Increasing rejection correlates to increasing molecular size as represented by width and volume as shown with RO. Previous studies (Bellona and Drewes, 2005; López-Muñoz et al., 2009; Nghiem et al., 2004) have challenged this particular NF membrane with inert organic tracers and estimated the pore size by applying different models of between 0.34 and 0.38 nm. Because all DBPs included in the study (Table 4.1) possess a molecular width smaller than the estimated pore size, exclusion is possibly the major removal mechanism involved. However, uncharged organic solutes can show low rejection because of hydrophobic adsorption (Kimura et al., 2003). The hydrophobic interaction of the THMs and I-THMs may lead to low or even negative removal of those DBPs by the NF membrane. The HACams and HNMs were less rejected compared to HKs and CH with similar volumes. Looking at TCNM versus 1,1-DCP and comparing TBNM with 1,1,1-TCP, even with similar volumes (93 \AA^3 vs 92 \AA^3 and 106 \AA^3 vs 107 \AA^3) TCNM and TBNM show 13% and 27% less rejection, respectively. Those DBPs have several functional groups that can interact with the functional groups of the membrane polymer via dipole–dipole interaction or H-bonding (Schäfer et al., 2011). The hydroxyl group in CH and the nitromethane or nitrile groups in DHANs, HNMs, and HACams can act as H-bond acceptors. Not only do the HNMs possess two more H-bond acceptor sites, but they are also more hydrophobic. Membrane interaction that is due to adsorption and H-bonding may play an important role besides size exclusion as it facilitates the mitigation of the HNMs on the permeate side. Two H-bond donor and acceptor sites as well as the increasing dipole moment with increasing size may negatively influence the removal of HACams. DHANs are polar, but they are significantly smaller than the pore size of the membrane; hence, they will easily pass.

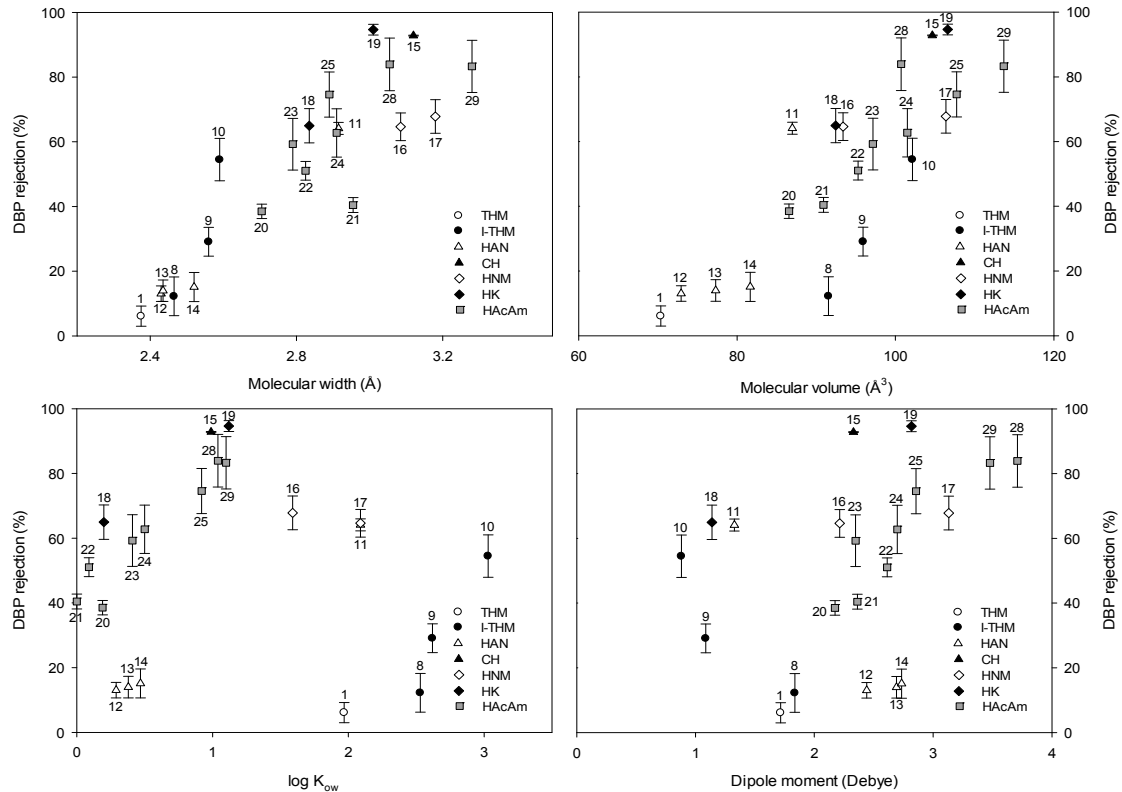


Figure 4.9. DBP rejection by NF as a function of DBP properties: (a) molecular width, (b) molecular volume, (c) log K_{ow}, and (d) dipole moment.

Notes: Error bars indicate the standard deviation among four different coupons (permeate flux 18 L/m²h, feed pH 6.8, crossflow velocity 0.12 m/s, 7 mM NaCl, 1 mM KH₂PO₄, feed temperature 23.5° C). See Table 4.1 for DBP identity associated with number values on graph.

Results for HAAs are similar to those seen with RO membranes, where HAAs are very well rejected because of electrostatic repulsion. CNBr is fairly well rejected by the NF membrane, whereas the smaller CNCl is not rejected at all.

4.2.4 Multiple Linear Regression

MLR, a statistical analysis tool, was applied to the experimental results to determine which physico-chemical properties contributed significantly to DBP rejection. Sorption potential was indicated by a solute's solubility in water and its log K_{ow}. Polar surface area, H-bond acceptor sites, H-bond donor sites, polarizability, and dipole moment were chosen to account for polarity and the capacity of the DBP to participate in H-bonding. DBP properties represent the predictors of their behavior, and their rejection is the single response variable. On the basis of purely mathematical criteria, predictors were selected with all possible combinations starting with that which has the highest simple correlation with the response. If the outcome of the prediction was significantly improved, this predictor was retained and the procedure was repeated. A good model will explain as much of the variance of the DBP rejection as possible using the smallest number of predictors. The predictor selection procedure used a sequence of partial F tests to evaluate the significance of a variable. F ratio was calculated by dividing the average improvement in prediction by the model by the average difference between the model and observed data. An increasing F ratio indicates if

the initial model significantly improved in predicting DBP rejection. R^2 correlation accounts for how much of the variability in the outcome was accounted for by the predictors. An improved correlation meant more of the variation in DBP rejection was explained by the new added predictors. For the final model, the predictors were selected in terms of explaining a large amount of the variation in DBP rejection, whereas the F ratio ($p < 0.01$) still significantly improved DBP rejection prediction. The variance inflation factor (VIF) was used as an indicator for multicollinearity. The parameters chosen for this model did not show multicollinearity as the VIF values for all MLRs was below 4 (Table 4.2 and 4.3).

Table 4.2. MLR Regression Statistics—RO Membranes

DF=27	Coefficient (RO)	Std. Error	t	P	F	VIF
Constant	73.269	1.097	66.768	<0.001	99.18	
Molecular weight (g/mol)	-6.174	1.661	-3.716	0.001		2.207
Molecular volume (\AA^3)	19.921	1.919	10.383	<0.001		2.944
Polar surface area (cm^3)	11.029	2.010	5.486	<0.001		3.232
Dipole moment (Debye)	-7.602	1.619	-4.695	<0.001		2.097

Notes: t = t-test, P = p-value (significance level), F = F-value, VIF = variance inflation factor

Table 4.3. MLR Regression Statistics—NF Membranes

DF=27	Coefficient (RO)	Std. Error	t	P	F	VIF
Constant	40.030	1.710	23.406	<0.001	169.7	
Molecular weight (g/mol)	-18.008	2.009	-8.965	<0.001		1.328
Molecular volume (\AA^3)	37.003	2.009	18.422	<0.001		1.328

Notes: t = t-test, P = p-value (significance level), F = F-value, VIF = variance inflation factor

Various recommendations for acceptable levels of VIF have been published in the literature, ranging between 4 and 10 (Hair et al., 1995; Pan and Jackson, 2008). All predictors were standardized prior to the regression procedure to remove dependence on units of measurements making them more directly comparable and to provide a better insight into the importance of the individual predictors in the model.

For the RO membrane, molecular weight (MW), molecular volume (MV), polar surface area (PSA), and dipole moment (DM) were the predictors found to be significant at the 95% confidence interval ($p < 0.05$ at $n=29$) with an adjusted R^2 value of 0.938 and F ratio of 99. No multicollinearities were observed between the predictors. The summary of the regression for each of the four predictors is shown in Table 4.2 and these values are used to calculate the predicted rejection (Equation 4.1):

$$Rejection_{RO}(\%) = 73.3 + 19.9MV + 11.0PSA - 7.6DM - 6.2MW \quad (4.1)$$

The predictor coefficients in the equation indicate the individual contribution of each predictor to the model. As the size exclusion mechanism directly links to molecular size, a solute with higher molecular volume would lead to its increased rejection. This trend is represented by the positive relationship of MV in Eq. 4.1, which affects DBP rejection to the greatest and appears to be a well-suited geometric parameter for rejection description. Although MW has previously been correlated with organic solute rejection (Steinle-Darling et al., 2007; Van der Bruggen et al., 1999), MV, in fact, may be a better representative for the size of the molecule because bromine and/or iodine atoms present in the structure of many DBPs are very heavy but not correspondingly more voluminous, leading to a high specific density of the molecule and explaining the negative coefficient for MW. This is also clearly evidenced by the macroscopic properties of the molecules TIM, TBM, and TCM, which have respective densities of 4.01, 2.89, and 1.48 g/cm³ but whose MVs are 102, 83, and 70 Å³. CDIM with a MW of 302 g/mol is the third largest of the suite of DBPs in terms of MW but the median of the MV dataset, and it shows a rather low rejection of 55%. The rest of the I-THMs show similar behavior. Properties describing polarity of the DBPs complement the molecular size and geometry in Equation 4.1 because the DBPs have several functional groups. The hydroxyl groups in CH and the nitrile, nitro, or amine group in HANs, HNMs, and HAcAms, respectively, provide polar surface areas and increased dipole moments. I-THMs and other THMs have lower dipole moments than the other DBPs but showed a trend of decreasing rejection with increasing DM, which lead to a negative correlation of dipole moments in the equation.

When performing MLR for DBP rejection by the NF membrane, only the predictors related to molecular size (i.e., MW and MV) appeared to be significant for a good description of rejection ($R^2 = 0.928$), as shown in Eq. 4.2.

$$Rejection_{NF}(\%) = 40.0 + 37.0MV - 18.0MW \quad (4.2)$$

The pore size of NF90 was estimated in different studies to be in the range 0.34 to 0.38 nm (Bellona and Drewes, 2005; López-Muñoz et al., 2009; Nghiem et al., 2004). Because all the DBPs are smaller than or in the range of the membrane pore size (Table 4.1), size exclusion is likely to be a dominant mechanism, and this is indicated in Eq. 4.2.

Figure 4.10 correlates predicted to experimentally measured rejection for all DBPs tested.

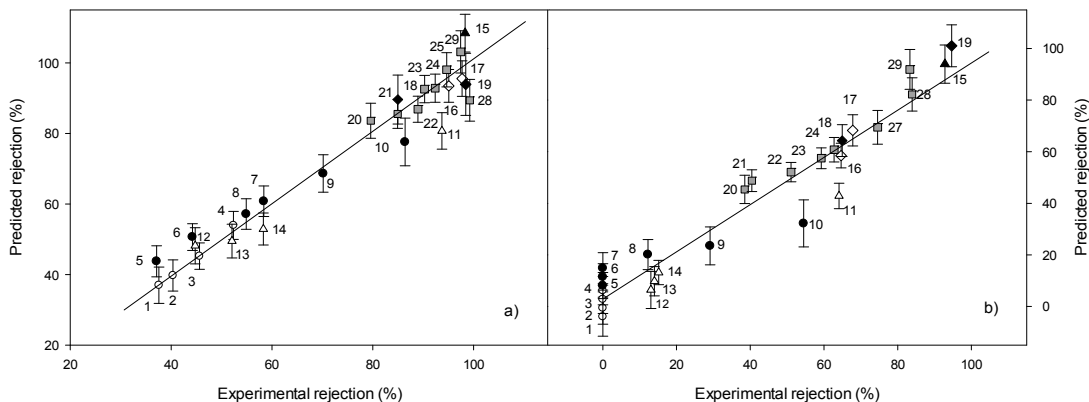


Figure 4.10. Multiple linear regression prediction by (a) RO and (b) NF.

Note: Error bars indicate the 95% confidence intervals.

4.3 Impact of Operational Parameters on the Rejection of DBPs

Although the rejection of 29 DBPs was measured as a function of operational parameters for both ESPA 2 and NF 90, the behavior of BCAN, DCACAm, 1,1,1-TCP, and TIM is selected for description in subsequent figures because these DBPs represent the different functionalities and properties of all those chemicals tested. BCAN represents the small polar HANs that showed low rejection. DCACAm is a midsize molecule with median rejection and represents the polar HACams that possess H-bonding/accepting capacity. 1,1,1-TCP was chosen as one of the largest molecules with highest rejection among the DBPs evaluated. TIM is the most hydrophobic DBP in the suite. HAAs and CNXs were also measured as a function of some of the operational parameters for ESPA2, and the results are discussed in the subsequent sections.

4.3.1 Transmembrane Flux

BCAN, DCACAm, 1,1,1-TCP, and TIM rejection are shown as a function of transmembrane flux for ESPA 2 and NF 90 in Figure 4.11. The impact of flux on the original suite of DBPs seen at UQ were similar to the results at UNC shown in Appendix C, Figure C.4.

The pressure increase with increased flux should not induce any significant changes in the membrane pore size as the membrane was compacted prior to the experiment at higher pressures than that corresponding to the highest flux tested here. Generally for the RO membrane, the rejection of DBPs, except TIM, CNXs, and HAAs, increased with increasing flux. However, the degree to which transmembrane flux impacted rejection varied depending on the group of DBPs, with the greatest impact occurring for the THMs and the HANs. For HANs, HACams, HKs, CH, and HNM, the greatest impact in rejection was seen at fluxes of between 3 and 18 L/m²h. Above this value, rejection remained relatively stable. On the other hand, THM rejection continuously increased over the full range of permeate fluxes studied up to 60 to 70%. Except for THMs, the HANs are the smallest DBPs in the suite studied. Therefore, at higher permeate fluxes, the diffusive flux for those DBPs becomes small compared to the water flux, which, in turn, leads to low concentrations in the permeate resulting in higher rejection. The convective flux of solutes through a membrane is caused by

pressure differences, whereas the diffusive flux is due to a concentration difference (Spiegler and Kedem, 1966). The larger DBPs (e.g., 1,1,1-TCP, CH, TCNM, BIAcAm, DIAcAm, BDCAcAm, DBCAcAm, TCAcAm, TBAcAm) were marginally affected (<8%) by the changes in permeate flux because the diffusive flux of those DBPs is always low. The increased solute-membrane affinities within the I-THMs with increasing hydrophobicity led to a decreased variation of rejection with increasing permeate flux. In particular, TIM did not show a change in rejection. To maintain similar rejection values over the flux range, the diffusive flux needs to increase with increasing permeate flux. As proposed by Déon et al. (2013), increasing pressure (inducing the higher flux) can increase the solute concentration on the membrane surface, which, in turn, leads to a higher concentration gradient and a decrease in rejection.

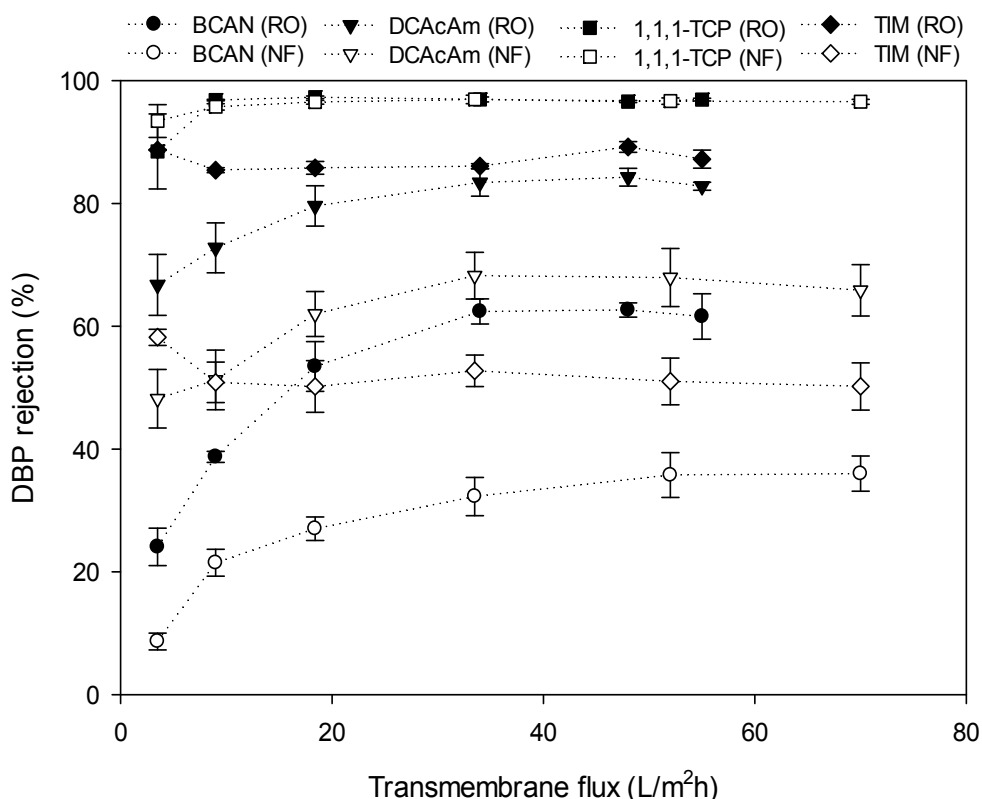


Figure 4.11. Rejection of BCAN, DCAcAm, 1,1,1-TCP, and TIM as a function of transmembrane flux.

Notes: Error bars indicate the propagation of uncertainty between duplicate samples (feed pH 6.8, crossflow velocity 0.12 m/s, 7 mM NaCl, 1 mM KH₂PO₄, feed temperature 23.5° C).

Similar to the RO membrane, the rejection of all DBPs by the NF membrane was most sensitive to changes at fluxes below 18 L/m²h. The THM4 and the three I-THMs—DCIM, BCIM, and DBIM—were not rejected at baseline conditions, but decreased concentrations in the permeate could be seen starting at 35 L/m²h with a maximum rejection of 25% at a permeate flux of 70 L/m²h. BDIM and TIM were not affected by changes in the permeate flux in contrast to the other DBPs including CDIM, which showed increasing rejection with increasing permeate flux. For TIM, the highest rejection of 58% in the flux range was actually observed at the lowest flux because of the compound’s adsorptive interactions with the membrane. DCAcAm with a log K_{ow} of 0.2 has minimal adsorptive interactions and, hence, a relatively wide range of rejection as a function of permeate flux is expected. This

occurs because of the diffusive solute flux being rather large compared to the solvent flux at low permeate fluxes; whereas at higher permeate fluxes, the solute flux becomes small compared to the solvent flux. As with the RO membrane, the larger well-rejected DBPs (i.e., 1,1,1-TCP, CH, BDCAcAm, DBCAcAm, TCACAm, and TBACAm) show only little variation in rejection over the flux range studied.

The rejection of CNXs by ESPA 2 as a function of transmembrane flux is shown in Figure 4.12. The rejection of the CNXs was not significantly affected by the changes in permeate flux, likely because of the previously mentioned mechanism of increased concentration polarization leading to a higher concentration at the membrane surface and decreased rejection. CNXs seem particularly sensitive to concentration polarization as indicated by negative rejections and the lack of change with flux.

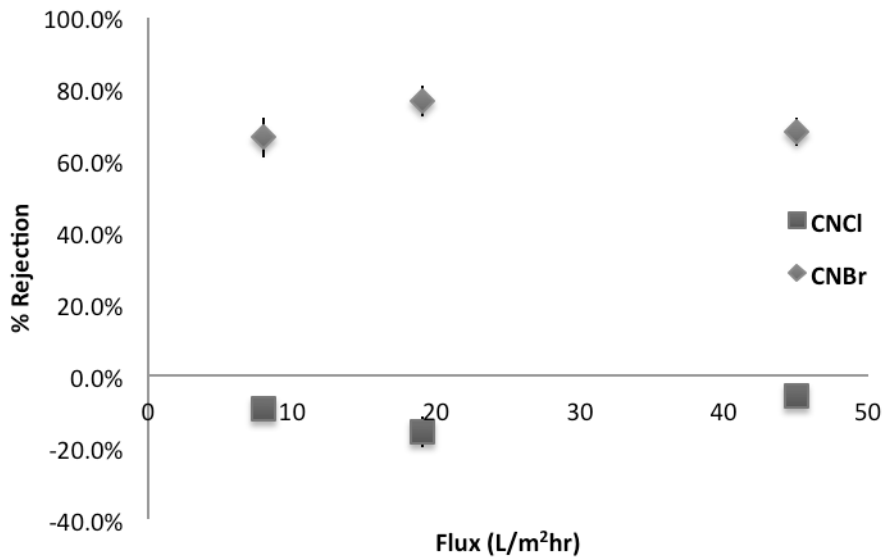


Figure 4.12. Rejection of CNXs by ESPA2 as a function of transmembrane flux.

Notes: Feed pH 7, crossflow velocity 0.12 m/s, 7 mM NaCl, 1 mM KH₂PO₄, feed temperature 21° C). Error bars indicate the standard error between four rejection values.

The rejection of HAAs by ESPA 2 as a function of transmembrane flux is shown in Figure 4.13. As with TIM, the rejection of HAAs did not change much with changes in flux. HAAs are likely rejected because of electrostatic repulsion, which does not change with flux and would result in unchanged rejection.

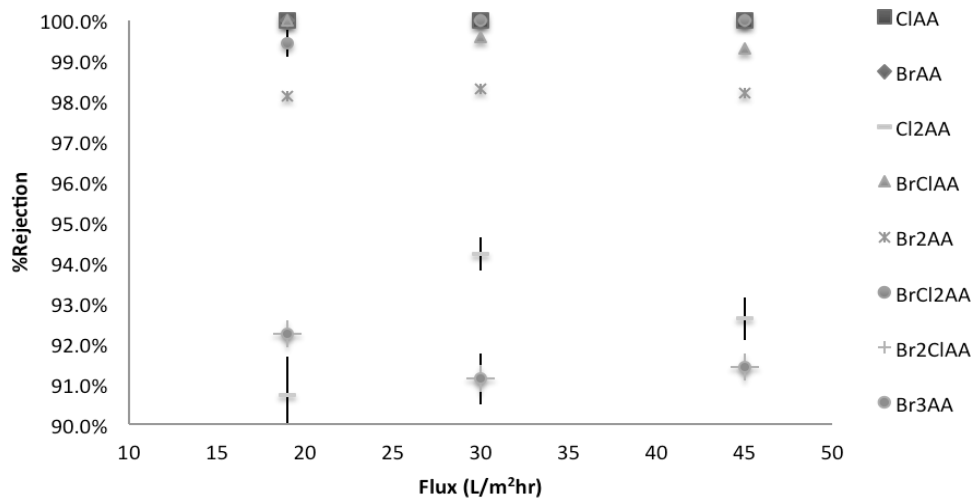


Figure 4.13. Rejection of HAAs by ESPA2 as a function of transmembrane flux.

Notes: Feed pH 7, crossflow velocity 0.12 m/s, 7 mM NaCl, 1 mM KH₂PO₄, feed temperature 21° C). Error bars indicate the standard error between four rejection values.

4.3.2 Crossflow Velocity

Figure 4.14 shows DBP rejection by the RO and NF membrane as a function of crossflow velocity.

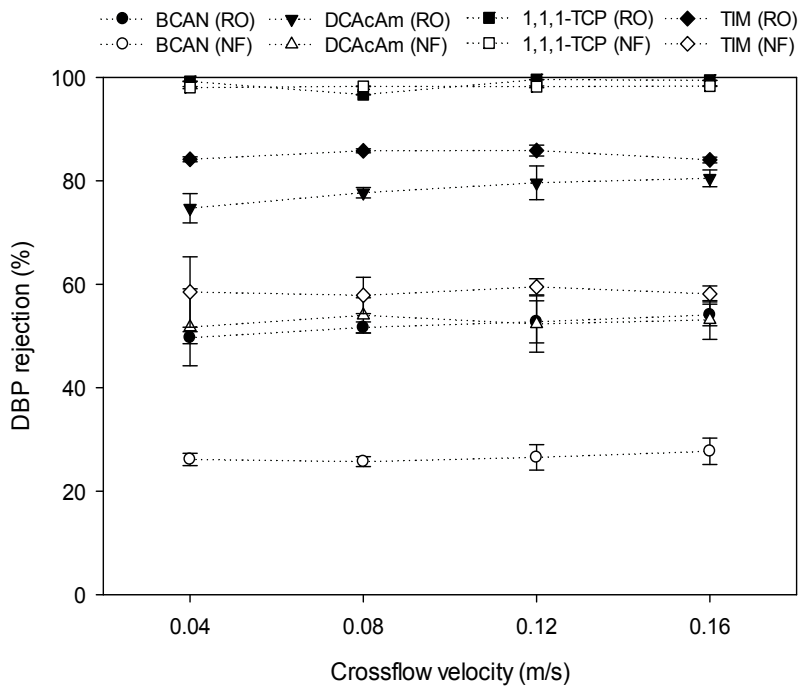


Figure 4.14. Rejection of BCAN, DCACAm, 1,1,1-TCP, and TIM as a function of crossflow velocity.

Notes: Error bars indicate the propagation of uncertainty between duplicate samples (permeate flux 18 L/m²h, feed pH 6.8, 7 mM NaCl, 1 mM KH₂PO₄, feed temperature 23.5° C).

An increase in crossflow velocity of the feed solution leads to a greater mixing at the membrane surface and decreased concentration polarization (Amjad, 1993) and should result in increased DBP rejection. Changes from 0.04 to 0.16 m/s across the RO membrane resulted in an 8 to 11% increase in rejection for DHANs and 5% for DCACAm, which is greater than the experimental error for these smaller molecules and explained by increased cross flow velocity reducing concentration polarization at the membrane-bulk solution interface (Nunes and Peinemann, 2010). The increase in crossflow velocity can decrease the thickness of the concentration polarization layer contrary to what is induced by a pressure increase. This change in concentration polarization layer thickness contributes to the rejection increase observed experimentally. When concentration polarization occurs, solute concentration on the membrane surface is higher than in the bulk solution. On the other hand, larger DBPs (HKs, HNMs, CH, and the remaining HAcAms) and those which tend to interact with the membrane polymer (THMs and I-THMs) were not affected by changes in crossflow velocity. The adsorption of THMs and I-THMs into the RO membrane material will cause their concentration to be higher on the membrane surface than in the polarization layer. Subsequently, they will not be affected by changes in the concentration polarization layer induced by increased turbulence with increasing crossflow velocity.

Changes in crossflow velocity did not influence the rejection of DBPs by the NF membrane.

4.4 Impact of Feed Solution

4.4.1 Temperature

Figure 4.15a shows the DBP rejection as a function of temperature (23 to 35° C) as observed at UQ where a temperature increase between 23° C and 35° C led to a decrease in the rejection of BCAN by the RO membrane from 47 to 26% and for TIM from 88% to 70%. In addition, membrane permeability increased with increasing temperature, and salt rejection decreased 0.5% for RO and 2.5% for NF across the temperature range. These observations are in accordance with previous studies that also observed an increased neutral solute passage and permeability with increased temperature at constant flux (Arsuaga et al., 2008; Ben Amar et al., 2007). The decreased rejections may be a result of the thermal expansion of the active membrane surface layer. Previous research reported polymer relaxation at elevated temperatures that subsequently reduced the filtration hindrance of neutral solutes (Nilsson et al., 2006; Sharma et al., 2003). The contribution of increasing pore size is supported by the increase of permeability when correcting for viscosity (Figure 4.16).

In Figure 4.15b, the impact of a temperature increase from 23° C to 35° C is scaled and related to the molecular volume. The results suggest that the impact becomes greater with smaller molecular volume because an expanding effective pore size can better facilitate the entry of small molecules into the membrane matrix. In addition to the increased pore size, an increase in diffusion rate into the membrane matrix caused by the decrease in viscosity of the water-DBP solution may contribute to lower DBP rejection. Moreover, high temperatures were found to increase partitioning (Tan et al., 2002), which could be the reason why the I-THMs are impacted more by a change in temperature compared to other DBPs of similar size (Figure 4.15b).

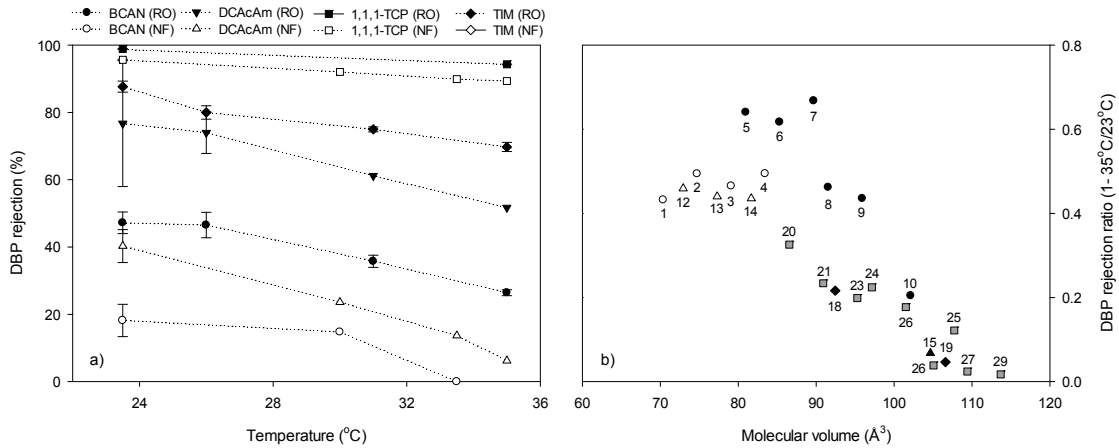


Figure 4.15 (a) Rejection of BCAN, DCACAm, 1,1,1-TCP, and TIM as a function of temperature; (b) DBP rejection as inverse ratio (1–35° C to 23° C) in relation to molecular volume by RO, with 0 meaning no impact caused by the temperature change.

Notes: (a) Error bars indicate the propagation of uncertainty between duplicate samples; (b) permeate flux 18 L/m²h, feed pH 6.8, crossflow velocity 0.12 m/s, 7 mM NaCl, 1 mM KH₂PO₄

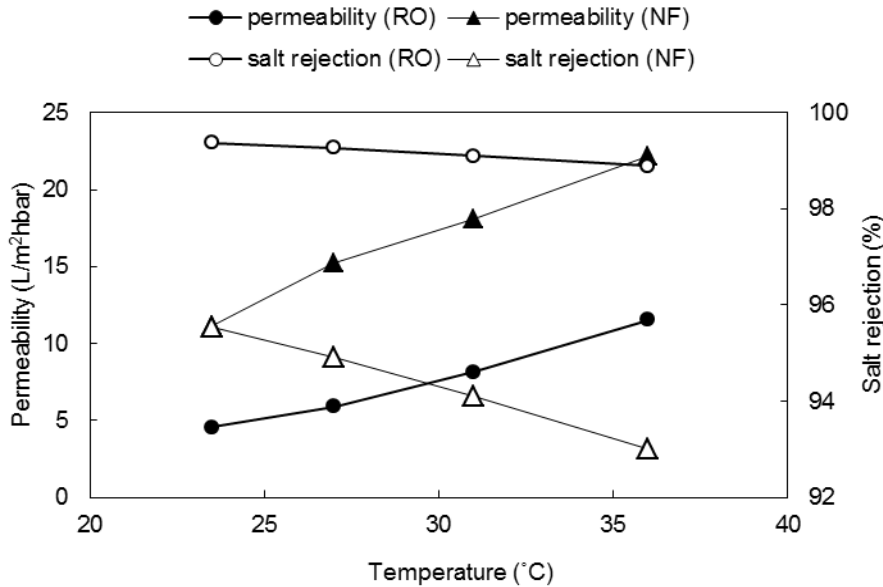


Figure 4.16. Effect of temperature on salt rejection and permeability of RO and NF membranes.

Note: Permeate flux 18 L/m²h, feed pH 6.8, crossflow velocity 0.12 m/s, 7 mM NaCl, 1 mM KH₂PO₄.

The impact of temperature on the rejection of the THMs, HANs, HKs, and Cl₃NM were also evaluated at UNC as shown in Appendix C, Figure C.5, and was found to be similar to the results at UQ. However, a lower temperature was also tested (10° C) to evaluate what may happen in cooler climates. For almost all DBPs, the rejection increased at the lower temperature, following the same pattern observed at UQ, likely because of decreased pore size.

The rejection of CNXs by ESPA 2 as a function of temperature is shown in Figure 4.17. CNXs had decreased rejection at 10° C, and CNCl specifically had significantly negative rejection at 10° C; this is likely due to increased concentration polarization from the decreased pore size and increased water viscosity, which leads to a high concentration at the membrane surface and an apparent negative rejection. The increase in temperature from 21 to 30° C did not have a significant impact on the rejection of either CNCl and CNBr. Because CNXs have small molecular volume and are likely rejected mostly by exclusion at 20° C, the slight increase in pore size between 21° C and 30° C does not significantly alter the rejection values.

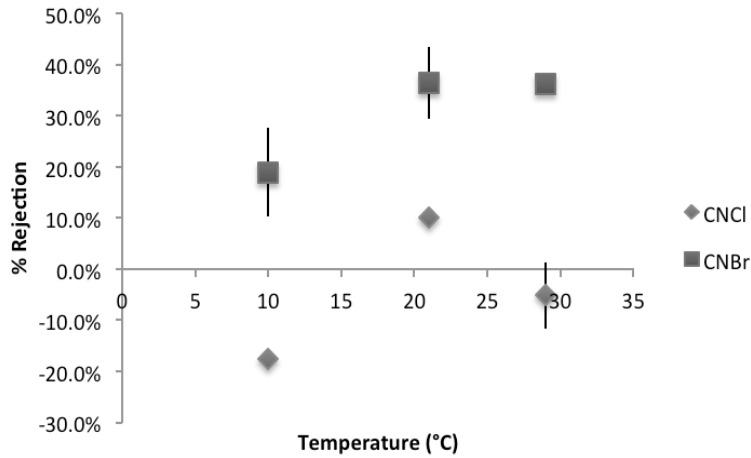


Figure 4.17. Rejection of CNXs by ESPA2 as a function of temperature.

Notes: Feed pH 7, crossflow velocity 0.12 m/s, 7 mM NaCl, 1 mM KH₂PO₄, flux 18 L/m²hr. Error bars indicate the standard error between four rejection values.

Figure 4.18 shows the effect temperature has on the rejection of HAAs. Temperature does not appear to affect their rejection, perhaps because the surface charge and, thus, electrostatic repulsion does not change in this temperature range.

4.4.2 pH

The active polyamide membrane surface layer contains amine, hydroxyl, and carboxylic functional groups that may affect the solute rejection mechanism upon changes in the solution pH. It has been reported that in the range of acidic to basic pH values, changes in the membrane structure can occur. This structural change is attributed to stronger electrostatic interactions between the dissociated functional groups, leading to a pore shrinkage at high pH (López-Muñoz et al., 2009). However, an increase in pore size with increasing pH was proposed in the literature (Donose et al., 2013). In this current study, the permeability of the NF membrane decreased slightly by 0.3 L/m²h bar across a pH range from 4.5 to 8.5, whereas it did not change at all with the RO membrane (Figure 4.18), a finding repeated at UNC.

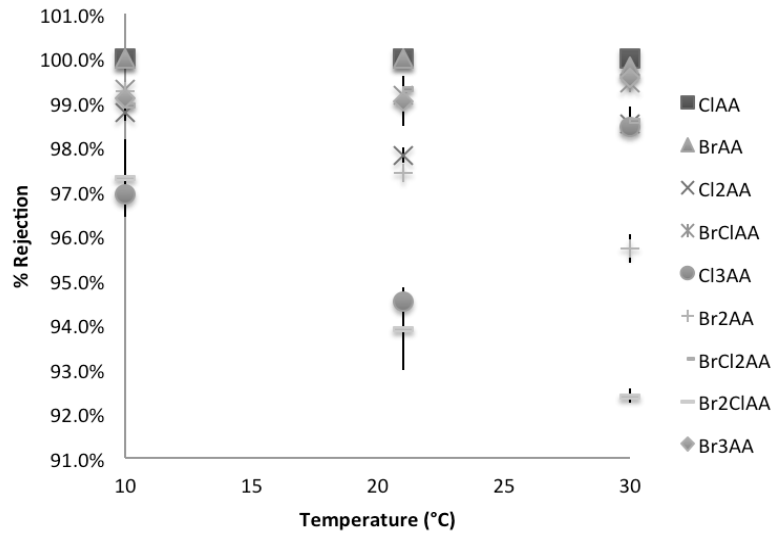


Figure 4.18. Rejection of HAAs by ESPA2 as a function of temperature.

Notes: Feed pH 7, crossflow velocity 0.12 m/s, 7 mM NaCl, 1 mM KH₂PO₄, flux 18 L/m²hr. Error bars indicate the standard error between four rejection values.

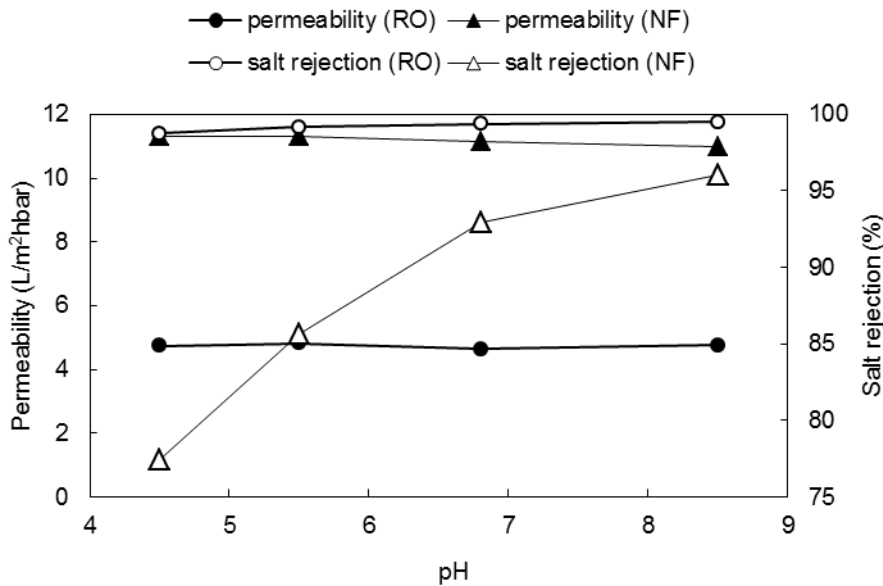


Figure 4.19. Effect of pH on salt rejection and permeability of RO and NF membranes.

Notes: Permeate flux 18 L/m²h, crossflow velocity 0.12 m/s, 7 mM NaCl, 1 mM KH₂PO₄, feed temperature 23.5° C.

Salt rejection by RO and NF can be explained through reduced solubility of ions in the membrane matrix compared to the solvent and through Donnan exclusion, two effects contributing simultaneously to this phenomenon. Donnan exclusion becomes more dominant in NF as salts become more soluble inside the membrane because of the greater pore size

(Peeters et al., 1998). Because RO size exclusion is the dominant mechanism of rejection for neutral DBPs, the effect of pH on rejection is small.

BCAN with a molecular volume of 77 \AA^3 is among the smallest DBPs tested, and, therefore, its rejection could be affected by minor changes in the void spaces in the RO membrane matrix. However, the observed changes were not significant enough to draw a firm conclusion (see Figure 4.20). On the other hand, increased rejection of HAcAms with increasing pH was seen with the NF membrane; 16% for DCACAm, 12% for BCACAm, 10% for DBACAm, and 10% for CIACAm. DBP transport through the membrane may be facilitated by H-bonding between the membrane polymer and the DBP. HAcAms, because of their intrinsic functional groups, possess two H-bond donor and acceptor sites. With increasing pH, however, the increased concentration of hydroxide ions can interfere with H-bonding between the membrane and the polar HAcAms, leading to an increased rejection.

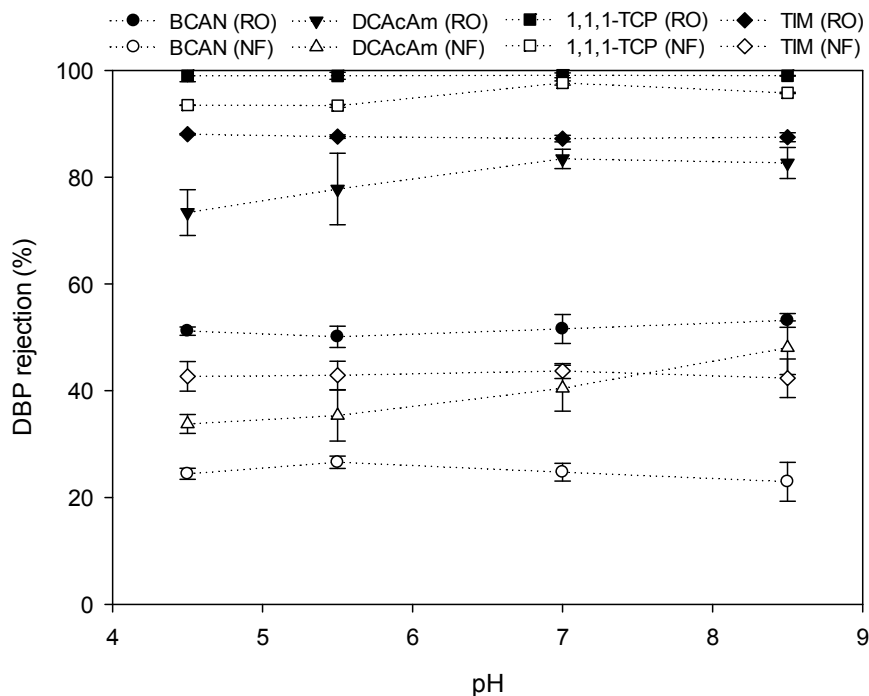


Figure 4.20. Rejection of BCAN, DCACAm, 1,1,1-TCP, and TIM as a function of pH.

Notes: Error bars indicate the propagation of uncertainty between duplicate samples (permeate flux $18 \text{ L/m}^2\text{h}$, crossflow velocity 0.12 m/s , 7 mM NaCl , $1 \text{ mM KH}_2\text{PO}_4$, feed temperature 23.5° C).

The THMs and I-THMs were not affected by changes in pH during either RO or NF filtration; THMs and I-THMs with $\log K_{ow} > 2$ are more hydrophobic than the other DBPs and, therefore, interact more with the membrane. Their removal may be essentially governed by adsorption, which is not affected by minor changes in either surface charge or pore size of the membranes. Similar to the findings in the UQ experiments, the overall rejection of THMs, HANs, HKs, and TCNM by ESPA 2 did not appear to be affected by change in pH (see Figure C.5 in Appendix C)

The CNXs were the smallest DBPs tested with molecular volumes in the 40 \AA^3 's range. Their rejection by ESPA 2 did appear to be affected by change in pH (see Figure 4.21), increasing with pH. This may support the idea that pore size decreases with increasing pH.

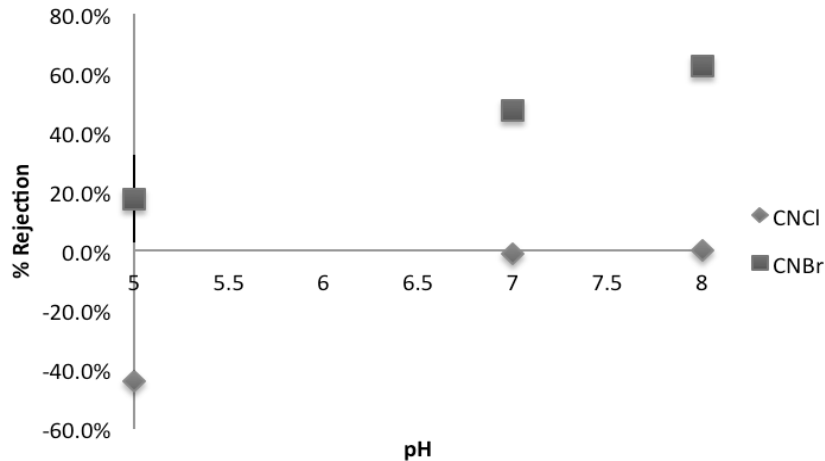


Figure 4.21. Rejection of CNXs by ESPA2 as a function of pH.

Notes: Crossflow velocity 0.12 m/s, 7 mM NaCl, 1 mM KH₂PO₄, flux 18 L/m²hr, feed temperature 21° C. Error bars indicate the standard error between four rejection values.

Figure 4.22 shows the rejection of HAAs, thought to be rejected by electrostatic repulsion by ESPA2 as a function of pH. As pH increases, the negative charge on the ESPA2 membrane surface increases, which could potentially increase rejection of charged species such as HAAs. Because the rejection of HAAs are already so high at pH 7, the increase in negative surface charge from pH 7 to pH 8 does not appear to affect the rejection. However, some of the HAAs do appear to have increased rejection from pH 5 to pH 7, but the increases are still minimal between 3 to 5% and may not be significant.

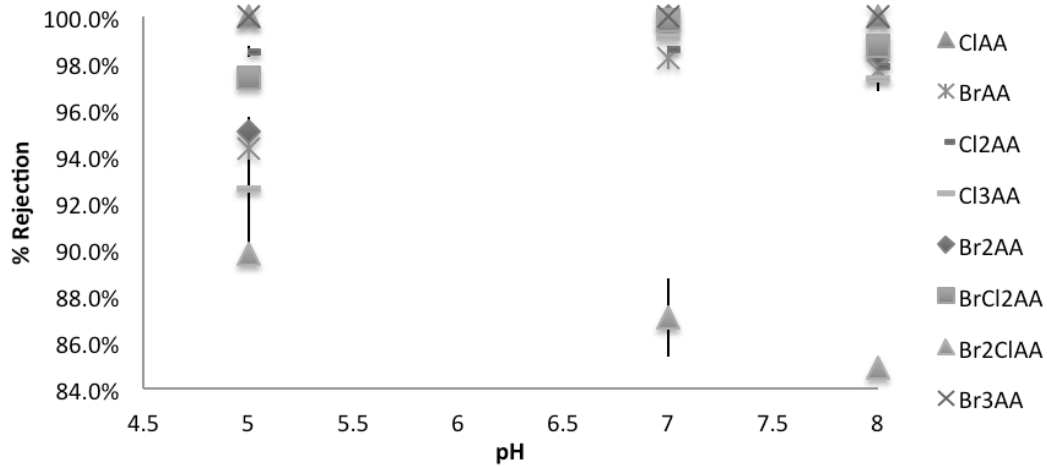


Figure 4.22. Rejection of HAAs by ESPA2 as a function of pH.

Notes: Crossflow velocity 0.12 m/s, 7 mM NaCl, 1 mM KH₂PO₄, flux 18 L/m²hr, feed temperature 21° C. Error bars indicate the standard error between four rejection values.

4.4.3 Ionic Strength

Solution ionic strength can affect the properties of both membrane and DBPs. An increased ion concentration may partially increase the screening of the membrane charge (i.e., to some degree counter-ions in solution may screen the polar functional groups) associated with polar DBPs reducing their hydrodynamic radius and leading to a smaller apparent solute size (Schäfer et al., 2003). In addition, it was previously reported that an increase in ionic strength may lead to an increase in mean pore size (Bargeman et al., 2005). However, the rejection of all DBPs during RO and NF filtration was not affected when the ionic strength in the feed was increased from 7 to 70 mM NaCl. The only exception was the group of HAcAms during NF filtration that showed an increased rejection with increasing ionic strength (Figure 4.23). For example, the rejection of DCaAcAm increased by 15% with an increase in ionic strength from 7 to 70 mM NaCl. With increasing ionic strength the negative charges on the membrane can be increasingly shielded by counter ions in the solution.

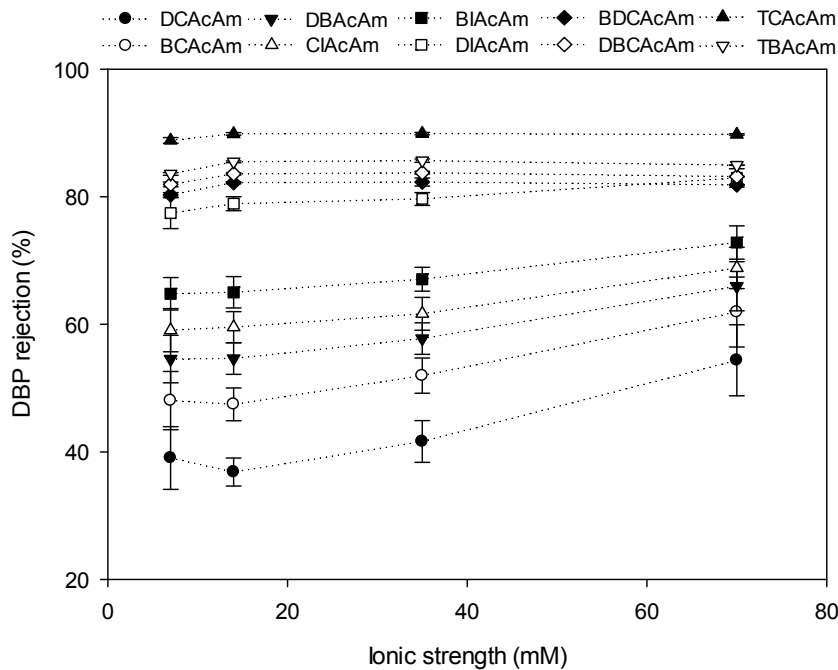


Figure 4.23. Rejection of HAcAms by NF as a function of ionic strength.

Notes: Error bars indicate the propagation of uncertainty between duplicate samples (permeate flux 18 L/m²h, feed pH 6.8, crossflow velocity 0.12 m/s, 1 mM KH₂PO₄, feed temperature 23.5° C).

It has been reported that with the increasing ionic strength of the solution that is due to the compression of the electrical double layer, the overall charge of RO and NF membranes decreases (Childress and Elimelech, 1996; Deshmukh and Childress, 2001). The theory of a lower surface charge caused by the higher ionic strength in solution is in accordance with the observed decreased salt rejection of 1.3% and 5.8% for RO and NF, respectively. The impact of ionic strength may have been too small relative to other parameters to induce significant changes in DBP rejection by RO.

HAcAms have the capacity to interact with the membrane polymer through H-bonding. Therefore, the increasing shielding of the membrane surface charge may lead to less

HAcAm-membrane interaction. Because of their polarity, HAcAms possess dipole moments ranging from 2.2 to 3.7 Debye. Van der Bruggen et al. (1999) suggested that the negative charges of the functional groups on the membrane surface can direct the opposite charge of the dipole of a compound toward the surface and, therefore, facilitate entry into the pore. The increased rejection with increasing ionic strength may be a result of decreased directing of the HAcAms toward the pore. The highest impact on rejection was seen for DCACAm with 15%. The effect is reduced for the larger HAcAms (e.g., DIACAm rejection only increased by 5%). DCACAm is the smallest and most cylindrical of the HAcAms. Increasing halogen content in the molecule and also the substitution of the smaller chlorine atom with the larger bromine or iodine atom causes the shape of the HAcAms to become longer and more cylindrical (e.g., DCACAm) and eventually to become a more bulky molecule (e.g. TBACAm).

4.4.4 Modeling DBP Rejection

Operational parameters, such as transmembrane flux, crossflow velocity, temperature, pH, and ionic strength were included in the MLR modeling resulting in a large comprehensive dataset with a sample size of 500 measurements. There are several advantages associated with a large dataset; first, a calibration and a subsequent validation of the developed MLR model can be performed confidently; and second, an extremely wide range of rejection values (i.e., 5–100%) is embraced. One half of the data was used to build the model, then the model was applied to the other half of the data. Rejection data of two THMs, three I-THMs, two HANs, CH, four HAcAms, and 1,1,1-TCP were used for model calibration (n=286), and the remaining were used for model validation (n=214).

Figure 4.24 illustrates the calibration and validation models obtained to describe the DBP rejection depending on molecular properties and operational parameters where the measured rejection is plotted against the predicted rejection. The resulting correlation of calculated and measured data was nearly identical for the calibration ($R_{cal}^2 = 0.922$) and the validation ($R_{val}^2 = 0.913$) dataset, which gives great confidence in the capability of the MLR to predict rejection of small organic contaminants for a broad diversity of operational parameters.

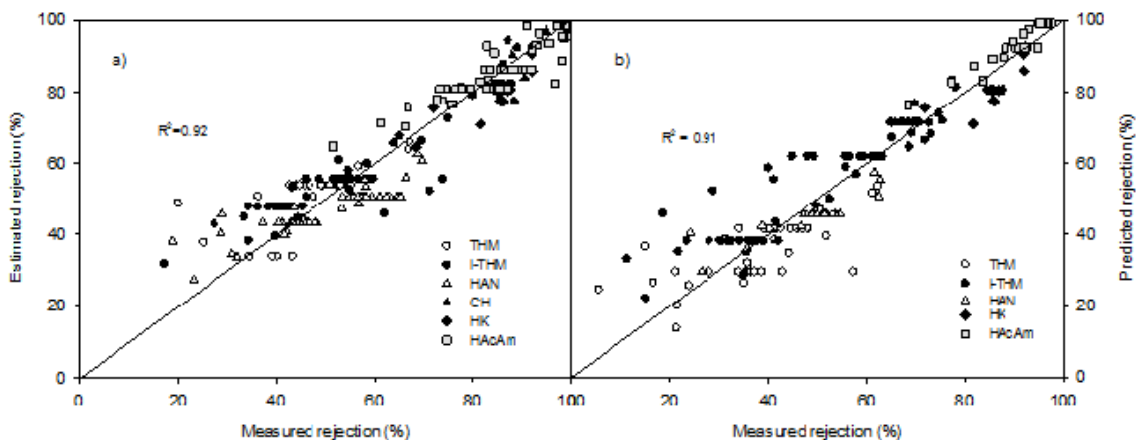


Figure 4.24. Multiple linear regression of DBP rejection by RO: (a) calibration model and (b) validation model.

Similar to the MLR, using only molecular properties (Section 4.2), PSA, MV, and DM were significant at the 95% confidence level. The operational parameters temperature and flux also

significant at the 95% confidence level complement the linear relationship describing solute rejection (eq. 4.3) with an adjusted quality of fit of $R^2=0.901$.

$$\text{Rejection (\%)} = -38.7 + 0.6\text{PSA} + 1.5\text{MV} - 5.9\text{DM} - 1.3\text{Temp} + 0.3\text{Flux} \quad (4.3)$$

To allow for inter-comparison of the regression coefficients, the data was normalized obtaining a similar adjusted quality of fit of $R^2=0.922$. As provided by the normalized model (eq. 4.4), the impact of the different parameters follows the order $\text{PSA} > \text{MV} > \text{DM} > \text{Temperature} > \text{Flux}$. Temperature was found to have a greater impact than transmembrane flux, highlighting the importance of temperature changes on the rejection of small organic solutes, especially with regard to its negative correlation.

$$\text{Rejection (\%)} = 69.5 + 16.5\text{PSA} + 15.2\text{MV} - 10.1\text{DM} - 3.8\text{Temp} + 3.6\text{Flux} \quad (4.4)$$

The coefficients used in eqs. 4.3 and 4.4 are summarized in Table 4.4.

Table 4.4. Calibration Model Statistics (Data Normalized)

DF=284	Coefficient (RO)	Std. Error	t	P	F	VIF
Constant	69.541	0.391	177.8	<0.001	6576	
Polar surface area (cm ³)	16.475	0.670	24.58	<0.001		2.731
Molecular volume (Å ³)	15.168	0.437	34.19	<0.001		1.280
Dipole moment (Debye)	-10.111	0.623	-16.22	<0.001		2.335
Temperature (°C)	-3.841	0.390	-9.826	<0.001		1.011
Flux (L/m ² h)	3.649	0.390	9.833			1.011

Notes: t = t-test, P = p-value (significance level), F = F-value, VIF = variance inflation factor

To gain further confidence in the predictive power of the model for other known contaminants that were not used for model development, the obtained relationship (eq. 4.3) was applied to N-Nitrosamine rejection data adapted from Fujioka and co-authors (2012b). NDMA, NMEA, and NPyr, which exhibit the lowest rejection out of the group of N-Nitrosamines studied were used for this exercise. Their low rejection and small size make them the most challenging N-Nitrosamines for the model. As seen in Figure 4.25, the developed model successfully simulated the N-Nitrosamine rejection across a wide range of rejection, temperatures (10–40° C), and transmembrane fluxes (5–60 L/m²h).

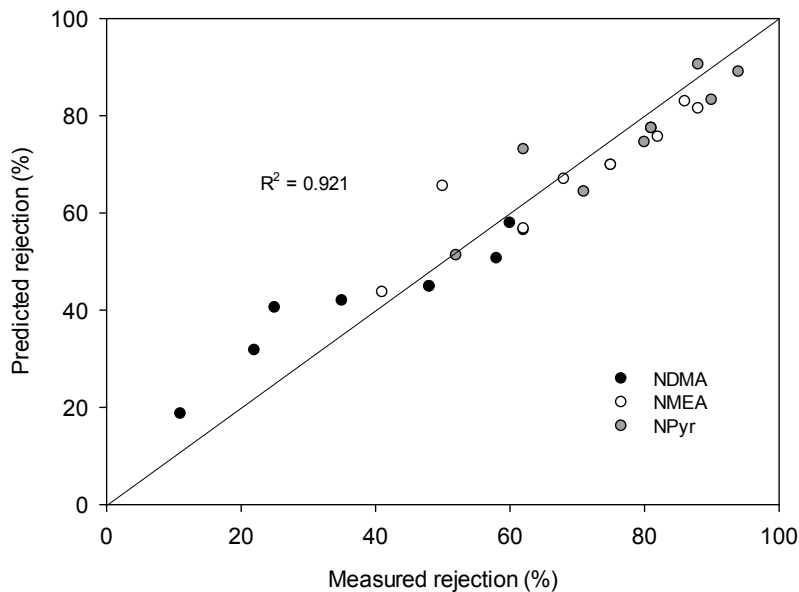


Figure 4.25. Comparison of the application of rejection data obtained with the developed MLR and measured N-Nitrosamine rejection data.

Source: Adapted from Fujioka et al, 2012b.

4.5 DBP Rejection at Pilot-Scale (RO)

4.5.1 Rejection of DBPs and N-Nitrosamines with Spiral Wound Elements

During the rejection tests at pilot-scale with THMs, HANs, CH, HK, DCaAm, and TCaAm, N-nitrosamines (NDMA, NDEA, Npip, and Nmor) were also included for study as a quality control measure. The experiments were performed with the pilot-scale experimental setup in the laboratory of A/Prof. Long Nghiem at the University of Wollongong. The properties of the N-nitrosamines analyzed are summarized in Table 4.5.

Table 4.5. Nitrosamine Properties

N-Nitrosamine	Abbrev.	MW ^a	MV ^a	Mwidth ^a	Log K _{ow} ^a	DM ^b	H-Acc
^c (30) N-nitrosodimethylamine	NDMA	74	72.7	2.4	-0.6	3.7	3
(31) N-nitrosodiethylamine	NDEA	102	106.7	2.7	0.5	3.7	3
(32) N-nitrosopiperidine	Npip	114	104.6	3.0	0.7	3.7	4
(33) N-nitrosomorpholine	Nmor	116	112.3	2.5	-1.4	2.7	3

Notes: ^a Source: ChemAxon, ^b Predicted: ChemBio3D Ultra 12.0, ^cnumber in parenthesis represents the identified DBP on Figure 4.26; MW = Molecular Weight (g/mol), MV = Molecular Volume (Å³), DM = Dipole Moment (Debye), H-Acc = H-Bond Acceptor.

The DBP rejection with the spiral wound RO membrane varied to a great extent from 39 to almost a 100%. A general trend to be observed was increasing rejection with molecular volume and width (Figure 4.24). The removal of the nitrosamines was found to be in a wide range with the lowest removal of NDMA at 39% and an almost complete removal of Nmor. In addition to their molecular size, the intrinsic properties of the N-nitrosamines might lead to additional interaction with the membrane polymer causing lower rejection. It is interesting that DBPs with similar molecular volumes to NDMA, NDEA, and Npip such as TCM, CH,

and 1,1,1-TCP, showed a 17, 6, and 5% higher removal, respectively. Although showing high rejections of greater than 90% with an analytical error of less than 6%, the experimental error was not determined because of a single pilot-trial.

The lower rejection of the N-nitrosamines might be influenced by two factors. First, they are not hydrophobic but possess between three and four H-bond acceptor sites compared to zero to two sites for the non-nitrosamine DBPs. Passage through the membrane via interaction with the abundant H-acceptor sites of the membrane polymer may be facilitated for the N-nitrosamines by their higher number of active sites in the molecule. Second, the N-nitrosamines possess a cylindrical shape as well as high dipole moments (2.7–3.7 Debye). Because of the cylindrical shape, they can thereby enter more easily into “effective pores” of the membrane as well as being directed to the pore by their dipole moments.

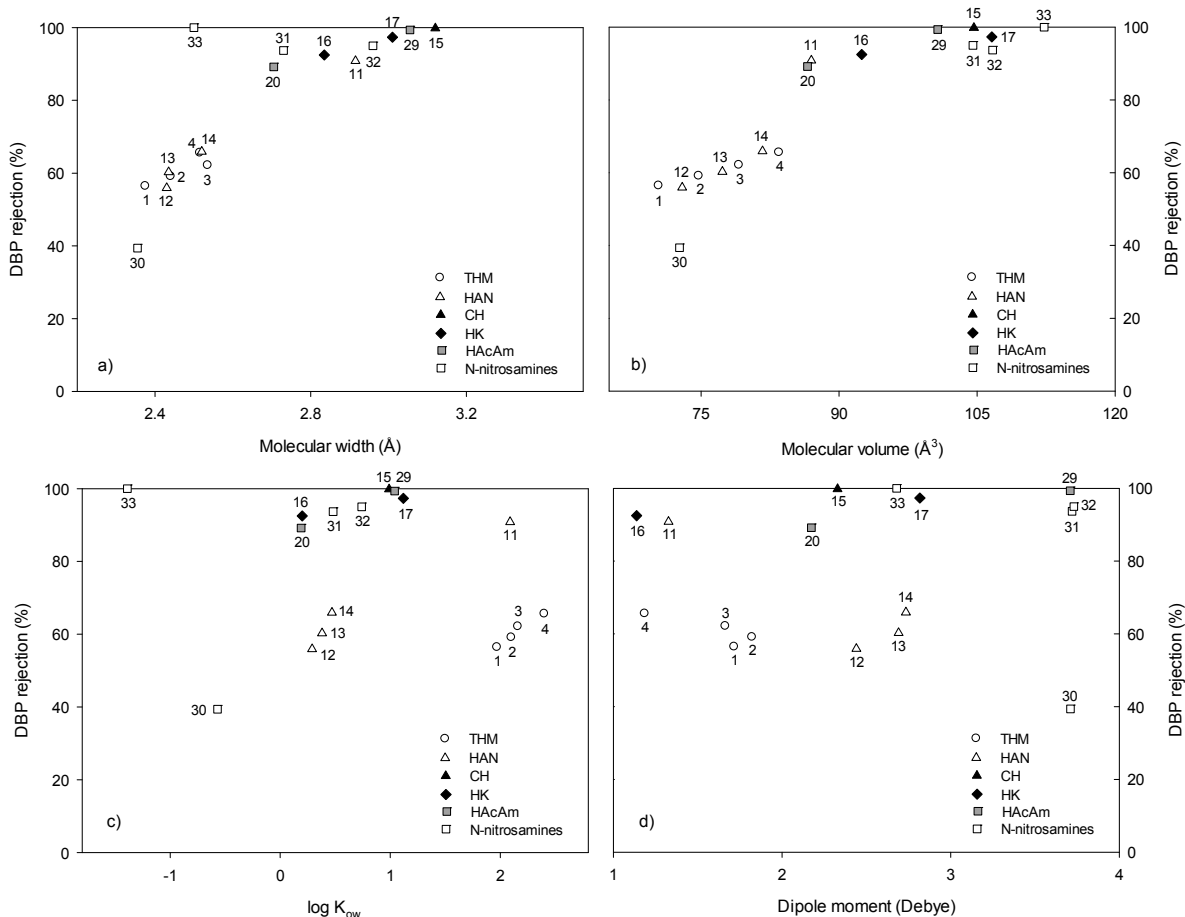


Figure 4.26. DBP rejection by RO at pilot-scale as a function of DBP properties (a) molecular width, (b) molecular volume, (c) log K_{ow} , and (d) dipole moment.

Notes: Error bars indicate the standard deviation among eight different coupons (permeate flux 18 L/m²h, feed pH 6.8, 7 mM NaCl, 1 mM KH₂PO₄, feed temperature 23.5° C).

High rejections of more than 99% were achieved for the of bulky trichlorinated DBPs, including 1,1,1-TCP, TCACAm, and CH with a volume >100 Å³ for which size exclusion may be the dominant mechanism. The rejection of the smaller DBPs such as the THMs and DHANs ranged between 56 and 66%. In addition to size exclusion, THMs have a smaller

volume and DHANs have H-bonding to influence rejection. THMs can interact via their intermediate hydrophobicity and the DHANs by their polarity. DCACAm and TCAN have the same molecular volume of 87 Å³, but DCACAm is 9% rejected less than TCAN. The higher dipole moment of DCACAm (2.2 compared to 1.3 Debye) may lead to assisted entry into the “pore” because of the direction of the positive charge.

To further elucidate the influencing DBP properties, MLR with 17 DBPs was performed. Similar to the bench-scale experiments, molecular geometry (MV, molecular width [Mwidth]) and the polarity of the DBPs (DM, PSA) were able to accurately describe the rejection with the spiral wound module (eq. 4.5) with an adjusted R² = 0.946 and an F value of 71.62. Further statistics for the MLR can be found in Table 4.6. MV positively affects the DBP rejection to the greatest degree, followed by the DM as an important predictor. A high dipole moment negatively influences the rejection, especially the N-nitrosamines. NDMA shows the lowest rejection but is not the smallest DBP with regard to the MV. However, it has one of the highest dipole moments (3.7 Debye).

$$Rejection_{pilot} (\%) = 77.9 + 15.0 MV - 7.1 DM + 4.9 Mwidth + 4.7 PSA \quad (4-5)$$

Table 4.6. MLR Statistics RO—Pilot-Scale

DF=16	Coefficient (RO)	Std. Error	t	P	F	VIF
Constant	77.796	1.13	68.818	<0.001	71.62	
Molecular volume (Å ³)	15.025	1.755	8.562	<0.001		2.268
Molecular width (Å)	4.896	1.776	2.756	0.017		2.323
Dipole moment (Debye)	-7.132	1.647	-4.331	<0.001		1.997
Polar surface area (cm ³)	4.683	1.866	2.51	0.027		2.564

Notes: t = t-test, P = p-value (significance level), F = F-value, VIF = variance inflation factor

Comparing the regression models for bench- and pilot-scale, both molecular size and polarity appeared to be significant for prediction of DBP rejection. Although MV and DM contribute to a similar extent, PSA had a stronger impact in bench-scale experiments. It is interesting that MW contributed negatively at the bench-scale, whereas Mwidth indicated higher rejections at the pilot-scale. This might be related to the absence of I-THMs during the pilot trials. The negative coefficient for MW may be explained by the heavy iodine atoms that are not correspondingly more voluminous and, therefore, give rise to a high specific density of the I-THM molecule.

4.5.2 DBP Rejection: Coupon Versus Single Spiral Wound Element

Figure 4.27 compares the DBP rejection measured with a single membrane coupon in the crossflow system (bench-scale) to the rejection measured with spiral wound modules (pilot-scale) at 30% recovery. With both experimental setups the same RO membrane (ESPA2) and operating conditions (permeate flux 18 L/m²h, feed pH 6.8, 7 mM NaCl, 1 mM KH₂PO₄, feed temperature 23.5° C) were used. As seen in Figure 4.27, the crossflow system underestimated the rejections of the THMs, DHANs, and DCACAm. The higher rejection at pilot-scale may be a combination of several influencing factors. One of these might be the difference in crossflow velocity, which at bench-scale was 0.12 m/s, whereas at pilot-scale it was higher at 0.16 m/s. As shown in Section 4.4.2, increasing crossflow velocity can increase the rejection of the HAcAm and DHANs because increased crossflow velocity reduces concentration

polarization at the membrane–bulk solution interface, which leads to an increased rejection (Nunes and Peinemann, 2010). Besides the crossflow velocity, the larger membrane surface area of the spiral wound modules may contribute to the underestimation of rejections at the bench-scale. When scaling up, the membrane-surface-area-to-feed-volume ratio is increased. The larger available surface area provides many more active sites for interaction with the DBPs. In the case of the THMs, which are the most hydrophobic in the DBP suite ($\log K_{ow}$ 2–2.4), the higher adsorption capacity of the membrane may lead to their higher removal. On the other hand, the higher removal of the DHANs and DCACams may be more related to their inherent polarity as well as H-bonding abilities and the increased capacity of the membrane for dipole–dipole interaction and H-bonding.

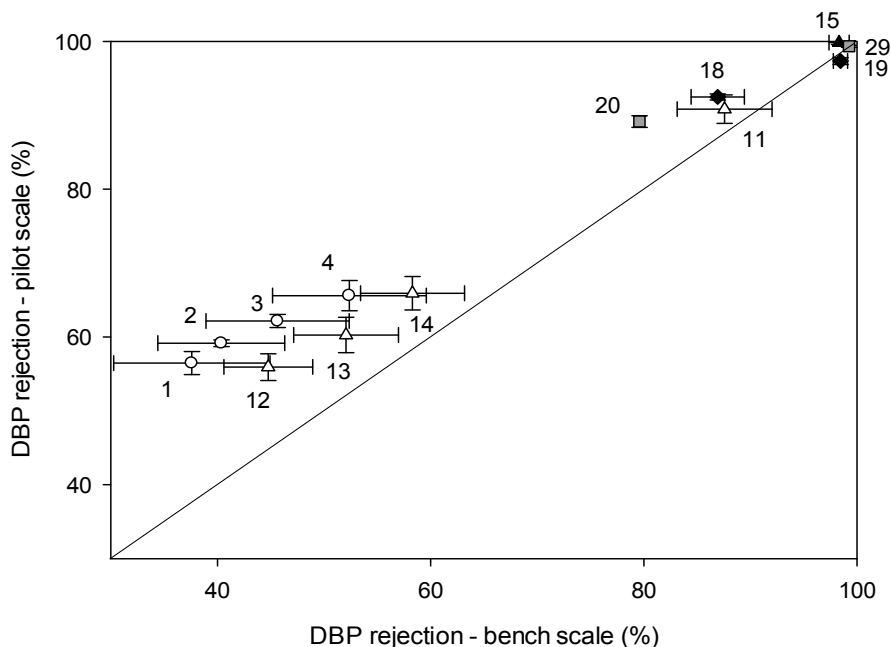


Figure 4.27. DBP rejection in the crossflow system at bench-scale in relation to a spiral wound module at pilot-scale.

Notes: Horizontal error bars indicate the standard deviation among eight different coupons with the crossflow system, and the vertical error bars indicate a duplicate sample with the pilot system (permeate flux 18 L/m²h, feed pH 6.8, 7 mM NaCl, 1 mM KH₂PO₄, feed temperature 23.5° C).

4.5.3 Temperature, pH, and Flux Effects between Pilot- and Bench-Scale

Figure 4.28 shows the influence of transmembrane flux, pH, and temperature on the rejection of BDCM, DBAN, 1,1-DCP, and DCACAm. Those DBPs were chosen as representative of their groups for their inherent properties—THMs (intermediate hydrophobic), HANs (polar), HK (little interaction), and HACams (H-bond donor/acceptor).

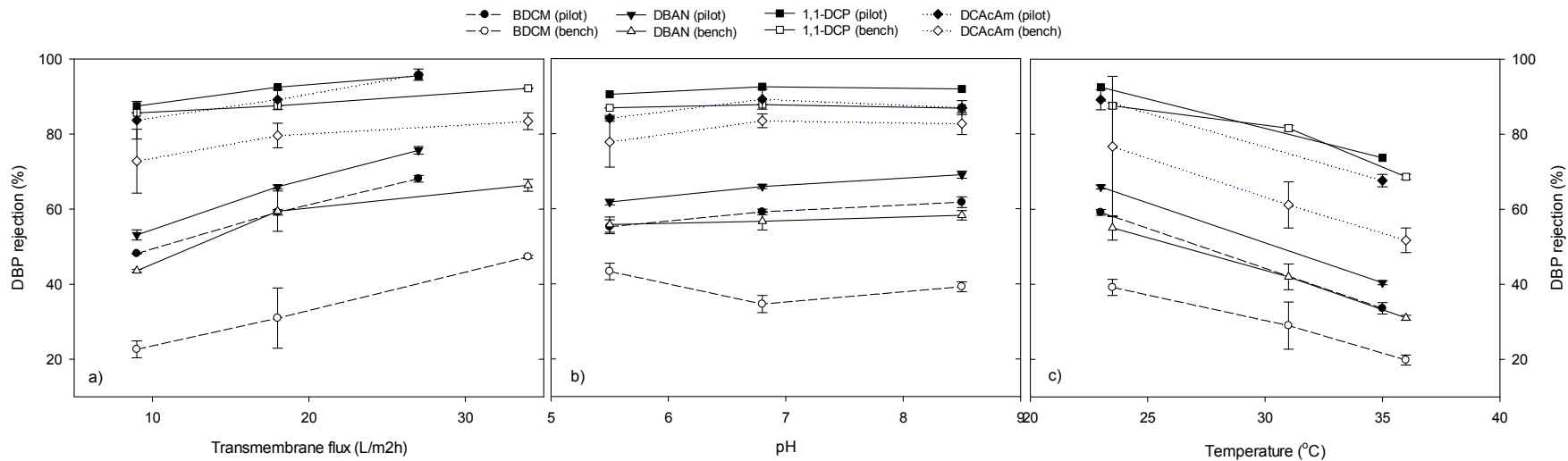


Figure 4.28. Impact on BDCM, DBAN, 1,1-DCP, and DCACAm rejection at pilot- and bench-scale by (a) transmembrane flux, (b) pH, and (c) temperature.

Notes: Error bars indicate the propagation of uncertainty between duplicate samples (depending permeate flux 18 L/m²h, feed pH 6.8, 7 mM NaCl, 1 mM KH₂PO₄, feed temperature 23.5° C).

Figure 4.28a shows that the impact of transmembrane flux was similar to the bench-scale experiments, where increasing flux led to increasing DBP rejection for all DBPs. The greatest impact of a flux increase between 9 and 18 L/m²h was seen at both scales for the DHANs with a difference of around 13% at pilot-scale and 16% at bench-scale followed by the 1,1-DCP, DCACAm, and THMs with 5 to 11% at both scales.

During the pilot tests, DHAN and DCACAm rejection was impacted to a greater extent compared to the crossflow system at fluxes greater than 18 L/m²h. To reach the same recovery with 27 L/m²h, the crossflow velocity increased by a third at pilot-scale, whereas the crossflow velocity stayed constant within the crossflow system because of its very low recoveries. Increasing crossflow velocity leads to increased turbulence, which weakens the effect of concentration polarization leading to increased rejection.

At bench-scale increasing pH did not lead to conclusive changes in DBP rejection, whereas at pilot-scale the rejection of the THMs and DHANs showed a slight increase of 5 to 9% with increasing pH (Figure 4.28b). It has been proposed that increasing pH can lead to pore shrinkage caused by stronger electrostatic interactions among the dissociated functional groups of the membrane polymer (López-Muñoz et al., 2009). Because THMs and DHANs were the smallest DBPs studied, their rejection could be affected by minor changes in the void spaces in the RO membrane matrix. The impact of pH may have become apparent with the spiral wound module because the polymer is able to move more freely in the spiral wound module compared to the coupon held firmly in the crossflow cell.

Figure 4.28c shows the difference in DBP rejection between 23° and 35° C. It can be seen that increasing temperature caused a significant decrease (20–26% at pilot-scale, 16–25% at bench-scale) in the rejection of DCACAm, 1,1-DCP, DHANs, and THMs. Increasing temperature leads to polymer expansion, which results in decreased rejection (Nilsson et al., 2006; Sharma et al., 2003). TCM, BDCM, DBCM, DCAN, and BCAN were affected 5% more by the temperature increase at pilot, whereas with the larger DBPs this observation was not as apparent.

Figure 4.29 tries to elucidate this further by relating DBP rejection ratio at 35° C to 23° C with the size of the DBPs, where 0 represents no difference in DBP rejection between 35° C and 23° C.

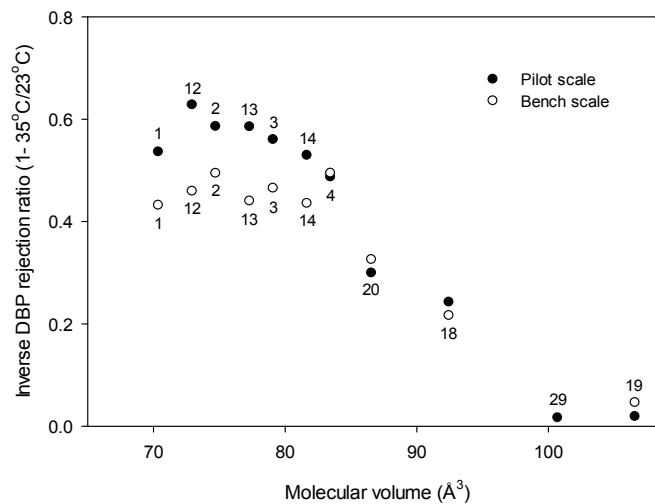


Figure 4.29. Inverse DBP rejection ratio 35° C versus 23° C as a function of molecular volume, with 0 meaning no difference in rejection between 35° C and 23° C.

As shown, the impact of temperature is easing off with increasing molecular size. However, one difference between the crossflow system and the pilot-scale can be seen—the impact of temperature increasingly affects all the DBPs decreasing in size, whereas the size made no difference for the smallest DBPs (THMs and DHANs). This observation may be related to a shift in pore size distribution with temperature.

4.5.4 Impact of Recovery

During the pilot-scale test, three 4-inch RO membrane elements were connected in series; that is, the feed solution was transported from the feed reservoir to the first module and the concentrate of the first module was transferred to the second module followed by the third module. The recovery increased by 10% per element, to reach a final recovery of 30% after the third module. At baseline conditions (18 L/m²h, pH 6.8, 23.5° C) the recovery did not affect the rejection of the HKs and TCaAcAm. Even though those DBPs did not express a change in rejection, their concentrations in the permeate did increase with increasing recovery because of the higher concentration in the feed. On the other hand, THM, DHAN, and DCaAcAm rejection decreased with increasing recovery, which may be caused by a greater concentration gradient across the membrane because of their lower rejection. In addition, increasing recovery comes with a drop in pressure and a decrease of the crossflow velocity, which may contribute to the lower rejection.

Recovery was not influenced by temperatures below 10° C. However, the highest impact in terms of decreasing DBP rejection with increasing recovery was observed when increasing the feed solution temperature (see Figure 4.30).

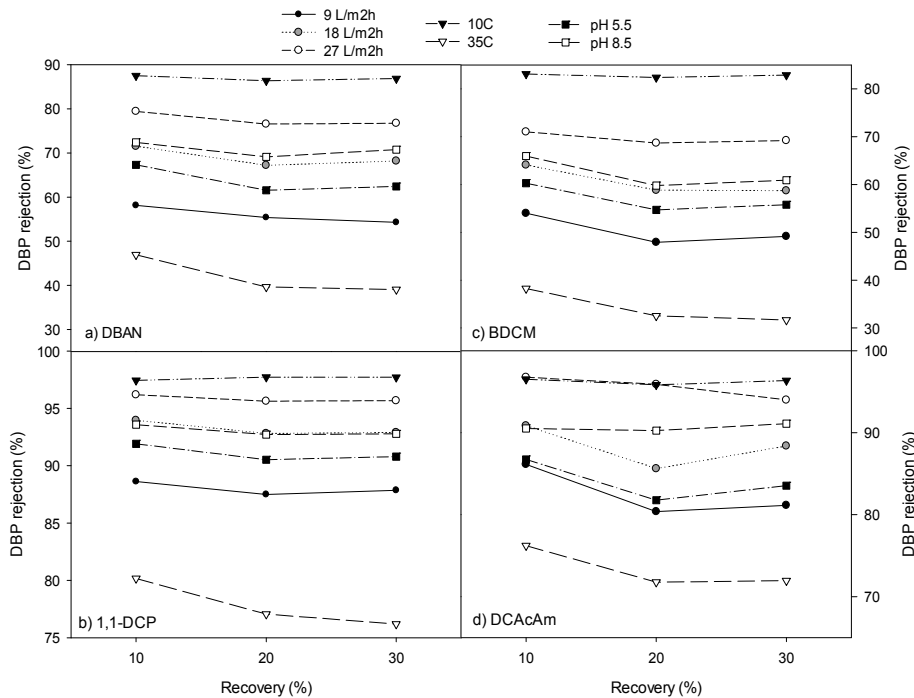


Figure 4.30. Impact of recovery on rejection of (a) DBAN, (b) 1,1-DCP, (c) BDCM, and (d) DCaAcAm at various transmembrane flux, pH, and temperature.

Note: Permeate flux 18 L/m²h, feed pH 6.8, 7 mM NaCl, 1 mM KH₂PO₄, feed temperature 23.5° C.

The transmembrane flux also had an influence; a stronger rejection decrease was observed at 9 L/m²h compared to 27 L/m²h (e.g., DBAN 5% at 9 L/m²h and only 2% at 27 L/m²h between 10 and 30% recovery). It has been reported that diffusion may play an important role in the transport of organic solutes

across NF membranes (Chellam and Taylor, 2001). Because at lower transmembrane fluxes the diffusive flux of the DBPs becomes greater compared to the water flux, the increased diffusion rate may also contribute to decreasing rejection with increasing recovery.

4.5.5 Model Application to Pilot-Scale Data

The model developed using bench-scale data showed excellent results. To test for better prediction using pilot-scale data, the rejection data obtained during pilot-testing was also used to calibrate and validate a model for DBP rejection prediction. Including the operational parameters (pH, temperature, and transmembrane flux) and splitting the data set into half, 126 data points were used for both model calibration and validation. The resulting correlation for the calculated and measured data showed a large difference between the calibration ($R_{cal}^2 = 0.881$) and the validation ($R_{val}^2 = 0.659$) datasets. This lowers the confidence in the capability of the MLR to predict rejection of small organic contaminants for a broad diversity of operational parameters. However, when applying the model to nitrosamine data that was not used for calibration/validation, a good prediction for NDMA was obtained (Figure 4.31a). On the other hand, the highly rejected NDEA and Npip (measured rejections >83% by eq. 4.6) were underestimated by up to 25% (Figure 4.31a).

$$Rejection(\%) = -48.9 + 56.3 Mwidth - 5.9 DM - 1.2 Temp + 0.6 Flux \quad (4.6)$$

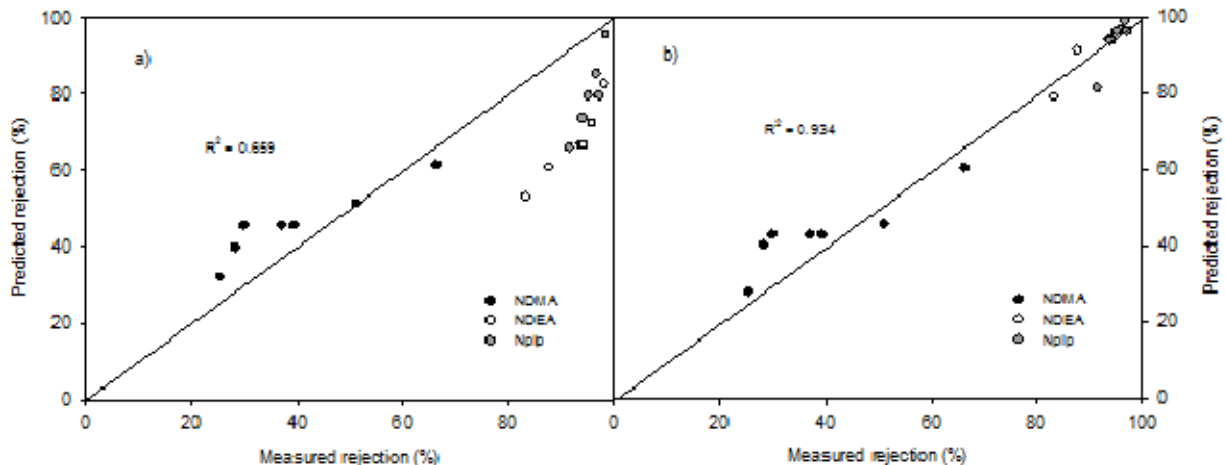


Figure 4.31 Comparison of the application of rejection data obtained with the developed MLR with (a) pilot-scale and (b) bench-scale data and measured N-Nitrosamine rejection data during pilot-scale trials.

Similar to the model obtained at the bench-scale, the main influencing parameters were the molecular size, polarity, temperature, and transmembrane flux. As for the greater dataset and better outcomes between model calibration and validation as compared to the pilot-scale model, the bench-scale model was tested against pilot-scale rejection data. As seen in Figure 4.31b, all three nitrosamines could be predicted well and show an excellent correlation of $R^2 = 0.934$. This indicates the applicability of the model beyond the bench-scale testing.

Chapter 5

Rejection of DBPS by RO and NF Membranes— Modeling Bench-, Pilot- and Full-Scale

5.1 Transport Model Description

5.1.1 Spiegler-Kedem (S-K) Model

The S-K model is based on the irreversible thermodynamics for steady state transport in pressure-driven membrane processes previously developed by Spiegler and Kedem (1966). It incorporates convection as well as diffusion and the transport of solvent (J_v) and solute (J_s) through an RO or NF membrane, which can be expressed as follows:

$$J_s = P_s \Delta x \left(\frac{dC}{dx} \right) + (1 - \sigma) C J_v \quad (5.1)$$

with

$$J_v = L_p (\Delta P - \sigma \Delta \pi) \quad (5.2)$$

where P_s = solute permeability coefficient, Δx = membrane thickness, C = concentration, σ = reflection coefficient, L_p = pure water permeability, ΔP = pressure difference between feed and permeate side, and $\Delta \pi$ = osmotic pressure difference between feed and permeate side. The solute permeability (P_s) is closely related to diffusivity and controls solute transport at low flux. The reflection coefficient (σ) represents the fraction of the solute reflected by the membrane in convective flow, ranging from 0 to 1 where $\sigma = 1$ can be interpreted as no solute passage. Thus, σ is a measure of the degree of semipermeability of the membrane reflecting its ability to pass solvent in preference to solute (Spiegler and Kedem, 1966). When integrating eq. 5.1 over the membrane thickness with boundary conditions set as $x = 0$, $C = C_p$, and $x = \Delta x$, $C = C_m$ (C_p = permeate concentration, C_m = membrane concentration) the rejection of a solute (R) becomes a function of solute permeability (P_s), reflection coefficient (σ), and solvent flux (J_v) as shown in eq. 5.3:

$$R = \frac{\sigma(1-F)}{1-\sigma F} \quad (5.3)$$

where F is

$$F = \exp\left(-\frac{1-\sigma}{P} J_v\right) \quad (5.4)$$

P and σ can be determined from the measured rejection (R) as a function of the permeate solvent flux (J_v). The diffusion contribution can be estimated experimentally by measuring the rejection at a wide range of permeate fluxes, as increasing solvent flux should increase the convective transport (Van der Bruggen et al., 2002; Wang and Chung, 2005). The nonlinear optimization was performed using a curve-fitting tool in

Matlab®. Parameters were estimated simultaneously using the quasi-Newton trust-region reflective method (Coleman and Li, 1996).

Parameter uncertainty was returned by the function based on a two-tailed t-test (95% confidence intervals) of the apparent linear approximation of parameter standard error, calculated from the covariance matrix. Correlation scales covariance to values of ± 1 where a high number is less favorable (± 1 indicates perfect linear relationship and 0 indicates no linear relationship). Interparameter correlation was seen for TCM and DCIM for the RO membrane with a correlation > 0.9 .

5.1.2 Steric Hindrance Pore (SHP) Model

The SHP model assumes that the membrane consists of a bundle of interconnected cylindrical capillaries with the pore radius (r_p) as the structural parameter. The calculated pore radius is, therefore, a hypothetical “pore radius” that assumes a membrane with uniform pores. In reality, the pores of the membrane do not possess the same size but rather a distribution of different pore sizes through which the solutes can permeate. Within the membrane pores, convection of uncharged solutes results from a combination of steric hindrance and interaction of the solutes with the pore walls. The SHP model derives the membrane pore size from eq. 5.5 (Nakao and Kimura, 1982):

$$\sigma = 1 - \left[1 + \frac{16}{9} \left(\frac{r_s}{r_p} \right)^6 \right] \left(1 - \frac{r_s}{r_p} \right)^6 \left[2 - \left(1 - \frac{r_s}{r_p} \right)^6 \right] \quad (5.5)$$

where σ = reflection coefficient (-), r_s = solute radius (Å), and r_p = pore radius (Å).

Therefore, the transport parameter (σ) obtained by the Spiegler-Kedem model can be used to estimate the membrane pore size derived from the SHP model (Nakao and Kimura, 1982).

5.1.3 Real Rejection Obtained by Concentration Polarization Model

During experimental work, the observed rejection (R_{obs}) of solutes is generally calculated by eq. 5.6, where C_p is the solute concentration in the permeate and C_f the solute concentration in the feed.

$$R_{obs} = 1 - \frac{C_p}{C_f} \quad (5.6)$$

To account for the concentration polarization effect, the real rejection (R_{real}) can be derived from the observed rejection that can be expressed as;

$$R_{real} = \frac{R_{obs} \left(\frac{J_v}{k} \right)}{1 + R_{obs} \left(\frac{J_v}{k} \right) - 1} \quad (5.7)$$

where the permeate flux (J_v) is based on the concentration polarization model (Mulder, 1991) and k is the mass transfer coefficient, which can be calculated by an empirical Sherwood relationship that takes into account the fluid properties (dynamic viscosity and velocity), solute properties (diffusivity), geometry of feed

channel (thickness), and flow conditions (Re , turbulence promoters). The related equations are described in detail in Section 5.4.1.3.

5.2 DBP Rejection Description by S-K Transport Models

5.2.1 NF Membrane—S-K–SHP Models

Because NF membranes have higher water permeabilities than RO membranes, they are believed to be “looser” and to possess a larger pore size. Nevertheless, pores in the active surface layer of both membranes should be imagined as material-free void spaces in the dense polymer layer, representing tortuous paths for the solute and solvent to pass (Mearns, 1976). However, because of the larger pore size, pore models are accepted to model solute passage through NF membranes. In order to further interpret the DBP transport through the NF membrane, the SHP model in combination with the S-K approach was used to estimate the theoretical pore radius of the NF membrane. It assumes that the membrane consists of a bundle of interconnected cylindrical capillaries with structural parameters (e.g., pore radius [r_p]).

The first step before obtaining the structural parameters is to correct the observed solute rejection with the concentration polarization model. Concentration polarization can influence the membrane selectivity as it enhances solute concentration at the membrane wall leading to a higher concentration gradient, which likely results in lower rejection. Therefore, the real rejection (R_{real} = corrected for concentration polarization) instead of the observed rejection (R_{obs}) is preferably used for the discussion of membrane permeation mechanisms (Tsuru et al., 2010). Figure 5.1a compares the observed rejection with the real rejection for DCAN, TIM, and Glycerol. At 18 L/m²h the observed and real rejections varied only between 0.4 and 2.2 percentage points for all DBPs. The difference becomes greater (1–9% for all DBPs) with increasing transmembrane flux (Figure 5.1a). Higher flux means higher pressure, which plays a major role on the solute accumulation at the membrane wall and concentration gradient.

After CP correction, σ and P were estimated with the S-K model. In turn, those parameters can be used to estimate the average pore radius r_p with eq. 5.5. The membrane pore size was estimated by permeation experiments using glycerol at various permeate fluxes. Glycerol was chosen for two reasons: first, it is a hydrophilic solute ($\log K_{\text{ow}} = -1.76$) and second, it has been reported that no spontaneous partitioning from solute-membrane affinity is to be expected (Verliefde et al., 2009a). Experimentally obtained rejection values for glycerol as a function of solvent flux and the fitted S-K model are plotted in Figure 5.1a. As the DBPs and glycerol are not perfectly spherical but more cylindrical in their shape, their geometry can be described by molecular width (defined as the extent of the conformer perpendicular to its maximal projection area) and molecular length (defined as the extent of the conformer perpendicular to its minimal projection area). Hence, the solute radius for glycerol was used as the molecular width (2.6 Å) and calculated with the same software (ChemAxon) used for the DBP property estimation. Molecular width was chosen over molecular length for r_p estimation because of a likely preferential orientation of the molecule toward the fixed charged groups on the PA layer. Hence, the polar moieties may direct the DBPs in an orientated rather than a random fashion (Nghiem et al., 2005). Solving eq. 5.5, the pore radius of the NF90 was estimated to be approximately 3.3 Å. Comparable pore radii have been previously reported for this membrane in various studies, ranging between 3.4 and 3.8 Å (Bellona and Drewes, 2005; López-Muñoz et al., 2009; Nghiem et al., 2004).

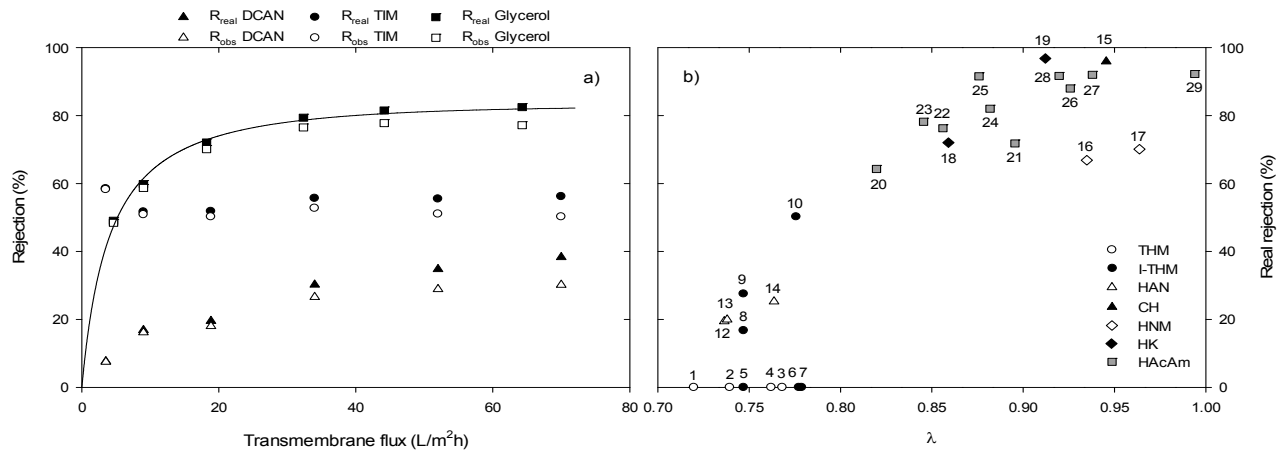


Figure 5.1. (a) Real and observed rejection of DCAN, TIM, and glycerol as a function of transmembrane flux; (b) DBP rejection versus λ .

Notes:

(a) Feed pH 6.8, crossflow velocity 0.12 m/s, 7 mM NaCl, 1 mM KH₂PO₄, feed temperature 23.5° C; solid line shows Spiegler-Kedem best fit for glycerol.

(b) $\lambda = r_s/r_p$ is the ratio of the solute radius to the calculated pore radius, permeate flux 18 L/m²h, feed pH 6.8, crossflow velocity 0.12 m/s, 7 mM NaCl, 1 mM KH₂PO₄, feed temperature 23.5° C.

Figure 5.1b plots DBP rejection against the ratio of the solute radius to the calculated pore radius ($\lambda = r_s/r_p$). Hence, λ can be interpreted as the DBP size in relation to the pore radius, where $\lambda = 1$ means the solute radius equals the pore radius. A trend of increasing rejection with increasing size can be seen indicating that size exclusion is a major mechanism for DBPs rejection during NF filtration. Nonetheless, for the smallest and larger DBPs close to the pore radius the trend is not that clear. Because all DBPs in this plot are uncharged, the mechanism of charge exclusion can be neglected. Therefore, the mechanism of adsorption either by hydrophobic interaction or H-bonding also needs to strongly influence the DBP rejection by NF. DBPs close to the membrane pore radius (e.g., TBNM and TBACAm) express similar rejection values as the smaller HKs or HAcAms. Because of their larger size, their access to the pore should be more hindered. Within the group of HAcAms, for example, increasing size correlates to increased dipole moment, which was proposed to facilitate pore entry and subsequent diffusion (Van der Bruggen et al., 1999). The THMs, I-THMs, and DHANs are the least rejected and also the smallest molecules; but DCIM, CDIM, and BDIM, for example, show a great variability in rejection although similar in size. Because of their intermediate hydrophobicity, the adsorption by hydrophobic interaction may lead to their lower rejection.

Figure 5.2a shows the results of the S-K fits for experimental rejection values of BCAN, CH, TCNM, 1,1,1-TCP, and TCACAm. Those DBPs were plotted as representative of their respective group and also to cover the wide range of rejections observed. CDIM, BDIM, and TIM rejection, however, could not be fitted because their rejection was found to decrease with increasing permeate flux, which is not permitted by the S-K model. On the other hand, the S-K approach provides a good estimation of the rejection of the remaining DBPs with little solute-membrane affinity (Figure 5.2a). The corresponding parameters of all fitted DBPs are listed in Table 5.1.

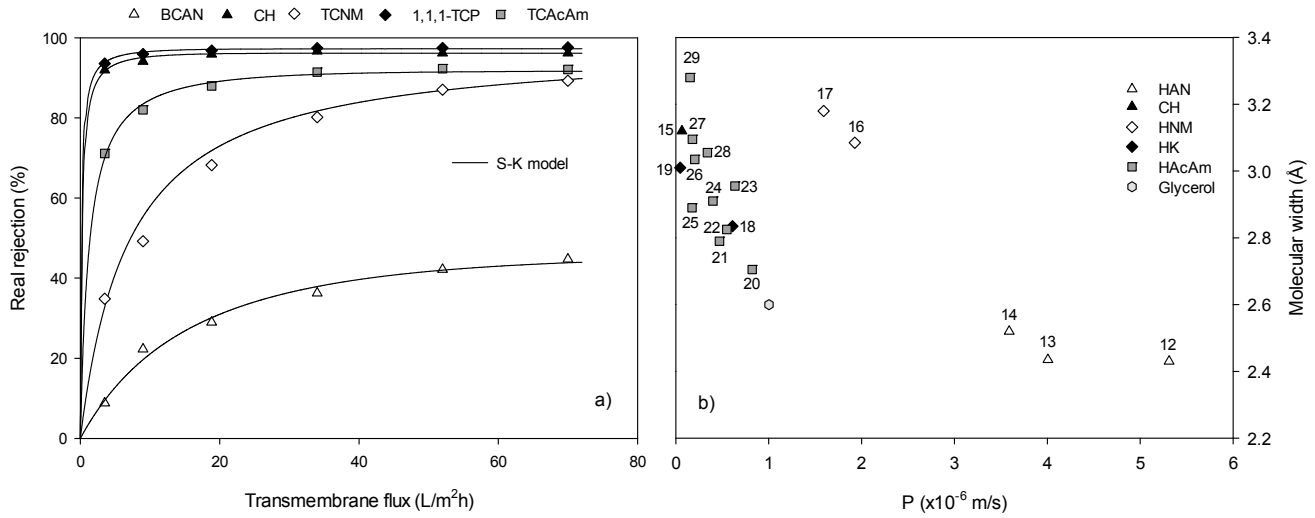


Figure 5.2. (a) Spiegler-Kedem best fits of DBP real rejection data for BCAN, CH, TCNM, 1,1,1-TCP, and TCACAm; (b) obtained permeability coefficient P in relation to solute molecular width.

Table 5.1. Fitted Transport Parameters for NF Membrane

Nr*	DBP	P (x10 ⁻⁶ m/s)	95% Confidence Bounds		σ (-)	95% Confidence Bounds		Correlation Coefficient
(12)	DCAN	5.31	2.30	8.32	0.40	0.31	0.49	0.89
(13)	BCAN	4.01	2.64	5.37	0.46	0.40	0.51	0.84
(14)	DBAN	3.59	1.66	5.52	0.47	0.39	0.56	0.81
(15)	CH	0.06	0.04	0.09	0.96	0.95	0.97	0.42
(16)	TCNM	1.93	1.32	2.53	0.97	0.86	1.00	0.87
(17)	TBNM	1.59	0.79	2.40	0.84	0.71	0.97	0.74
(18)	1,1-DCP	0.61	0.44	0.78	0.75	0.71	0.78	0.57
(19)	1,1,1-TCP	0.05	0.03	0.06	0.97	0.96	0.97	0.42
(20)	DCACAm	0.82	0.22	1.09	0.72	0.63	0.81	0.54
(21)	BCACAm	0.64	0.23	1.03	0.78	0.70	0.86	0.52
(22)	DBACAm	0.55	0.23	0.86	0.82	0.74	0.89	0.52
(23)	CIACAm	0.47	0.29	0.65	0.83	0.78	0.88	0.51
(24)	BIIACAm	0.40	0.23	0.57	0.86	0.82	0.91	0.50
(25)	DIACAm	0.17	0.08	0.27	0.93	0.89	0.97	0.46
(26)	BDCACAm	0.20	0.18	0.23	0.94	0.93	0.95	0.49
(27)	DBCACAm	0.18	0.14	0.21	0.94	0.93	0.95	0.48
(28)	TCACAm	0.34	0.29	0.39	0.92	0.90	0.93	0.53
(29)	TBACAm	0.15	0.11	0.20	0.94	0.92	0.96	0.46

Notes: Correlation scales covariance to values of ± 1 , where correlation coefficient values > 0.9 point out variables that can be considered highly correlated. *Denotes the species on figures throughout this report.

Except for CDIM, BDIM, and TIM, all the remaining DBPs exhibited an increased rejection with increasing permeate flux. The impact of the permeate flux varied within different DBP groups. CH, HKs, and HACAm reached their asymptote (i.e., maximum rejection) quickly at 18 L/m²h, whereas HNM and DHAN rejection was still increasing at 70 L/m²h. The S-K model estimates two solute- and membrane-dependent parameters to describe solute rejection. One is the reflection coefficient (σ) that indicates the

maximum rejection of the solute, as this parameter describes rejection at infinite flux (Soltanieh and Gill, 1981). The second parameter is the solute permeability (P) that is closely related to diffusivity and may be regarded as a measure of the solute transport by diffusion. The diffusive transport is a result of the concentration gradient, whereas the convective transport is related to the pressure difference across the membrane (Mulder, 1991). Figure 5.2b relates the permeability with the molecular width of the DBPs. A general trend seen is the solute permeability coefficient increasing with decreasing size of the DBPs. Lowest permeabilities, linearly decreasing with size (Figure 5.2b), can be observed for glycerol, CH, HKs, and HAcAms, which show high reflection coefficients (>0.7). In contrast, the DHANs and HNMs exhibit higher permeabilities compared to the DBPs with similar size and similar reflection coefficients. Hence, size exclusion may not be the major rejection mechanism for the HNMs as compared to glycerol, CH, HKs, and HAcAms. Rejection of the DHANs and HNMs did not reach the maximum in the wide flux range studied ($3\text{--}70\text{ L/m}^2\text{h}$), resulting in high reflection coefficients and permeabilities of 1.6 and $1.9 \times 10^{-6}\text{ m/s}$ for TBNM and TCNM, respectively.

5.2.2 RO Membrane—S-K Model

As stated in the previous section, the concentration polarization becomes more prominent at higher fluxes because the higher pressure increases the concentration on the membrane surface and, therefore, the concentration gradient. Correlation between the model parameters occur when the asymptote cannot be reached in the flux range studied, which is the case for THMs and DHANs. The correction for concentration polarization promotes this behavior, that is, the fitting curve becomes even steeper (Figure 5.3a). Correlation as a statistical term refers to the relation between two variables, in this case P and σ . Parameter correlation quantifies the degree of relation between the parameters where 0 means no relation and 1 a perfect linear correlation, which is undesirable during curve fitting. Correlation coefficients between 0.9 and 1.0 point out variables that can be considered highly correlated. When the correlation is >0.9 the confidence intervals (linear estimate) are not valid, the confidence region is unbounded or it shows a 0 vector overlap. Hence, the nonlinear correlated estimate (true) is to be used. The true estimate was returned by the function based on a two-tailed t-test (95% confidence intervals) on the apparent linear approximation of parameter standard error calculated from the covariance matrix. The observed rejections instead of the real rejections were used for the model fitting procedure for the RO data—first, because the correction for concentration polarization induced strong correlations between the parameters for the TCM, BDCM, and DCAN (>0.94) and second, the model parameters obtained with observed and real rejection showed similar trends (Figure 5.3b).

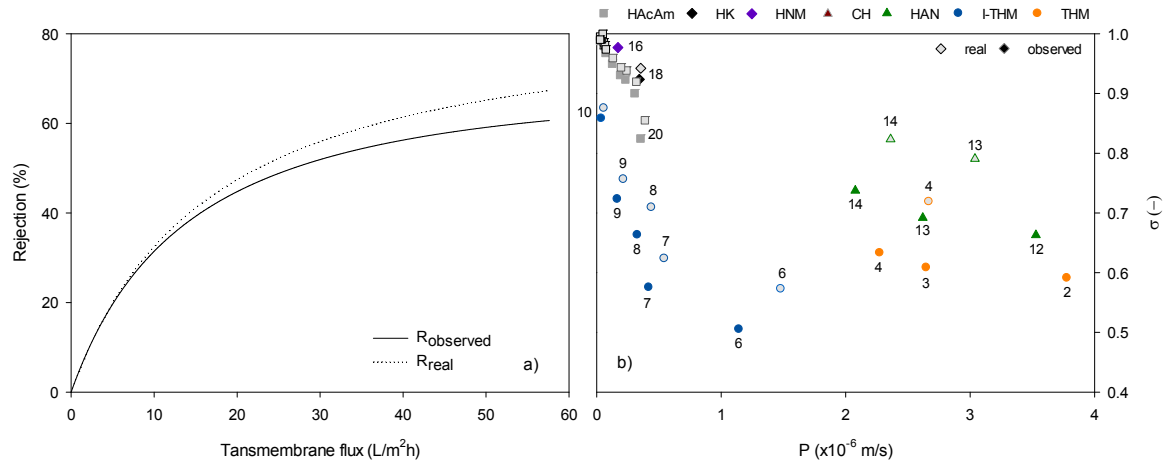


Figure 5.3. (a) Spiegler-Kedem best fit for DCAN observed and real rejection, (b) model parameters P and σ obtained for Spiegler-Kedem best fit with real rejection (grey-filled symbols) and observed rejection.

Figure 5.4 shows the results of the S-K model fits of experimental rejection data for representatives of the different groups of DBPs. The S-K model fitted the curve well through the experimental data points collected for TCM and DCIM (Figure 5.4a), but the model parameters (P, σ) showed a strong correlation (0.97). For this reason the obtained model parameters were excluded for further analysis. For TCM and DCIM, the model lost accuracy when the asymptote could not be reached in the flux range studied, which led to the 95% confidence region of BDCM and DBCM to be upper unbounded. Subsequently, the upper boundary of the reflection coefficient had to be set artificially to 1. In contrast, DBPs that were not significantly impacted by changes in the permeate flux, such as DBIM, CDIM, BDIM, and TIM, had their confidence region lower unbounded. The DHANs, HKs, CH, HNMs, and the HAcAms did not experience inter-parameter correlation and could be fitted well by the S-K model (Figure 5.4), providing a good estimation of their rejection. The relevant parameters for all fitted DBPs are listed in Table 5.2.

Table 5.2. Fitted Transport Parameters for RO Membrane

Nr [#]	DBP	P (x10 ⁻⁶ m/s)	95% Confidence Bounds*		σ (-)	95% Confidence Bounds*		Correlation Coefficient
(2)	BDCM	3.78	0.95	<i>u ub</i>	0.59	0.41	<i>l</i>	0.90
(3)	DBCM	2.65	0.34	<i>u ub</i>	0.61	0.42	<i>l</i>	0.85
(4)	TBM	2.27	0.80	<i>u ub</i>	0.63	0.50	<i>l</i>	0.81
(6)	BCIM	1.14	0.37	1.92	0.51	0.42	0.59	0.63
(7)	DBIM	0.33	<i>l ub</i>	0.62	0.66	<i>0</i>	0.73	0.46
(8)	CDIM	0.42	<i>l ub</i>	0.71	0.58	<i>0</i>	0.63	0.43
(9)	BDIM	0.17	<i>l ub</i>	0.29	0.72	<i>0</i>	0.76	0.42
(10)	TIM	0.04	<i>l ub</i>	0.16	0.86	<i>0</i>	0.88	0.41
(12)	DCAN	3.53	2.52	4.54	0.66	0.58	0.74	0.90
(13)	BCAN	2.62	1.65	3.59	0.69	0.60	0.79	0.85
(14)	DBAN	2.08	1.67	2.49	0.74	0.69	0.79	0.82
(15)	CH	0.04	0.03	0.05	0.99	0.98	1.00	0.50
(16)	TCNM	0.06	0.03	0.08	0.98	0.97	0.99	0.46
(17)	TBNM	0.17	0.12	0.22	0.98	0.95	1.00	0.59
(18)	1,1-DCP	0.34	0.30	0.39	0.92	0.91	0.94	0.59
(19)	1,1,1-TCP	0.06	0.03	0.10	0.98	0.96	1.00	0.49
(20)	DCAcAm	0.35	0.20	0.50	0.82	0.78	0.87	0.47
(21)	BCAcAm	0.30	0.24	0.37	0.90	0.87	0.93	0.54
(22)	DBAcAm	0.23	0.17	0.29	0.92	0.90	0.95	0.53
(23)	CIAcAm	0.19	0.14	0.23	0.93	0.91	0.95	0.51
(24)	BIAcAm	0.12	0.10	0.15	0.95	0.94	0.96	0.49
(25)	DIAcAm	0.07	0.04	0.10	0.97	0.95	0.98	0.48
(26)	BDCAcAm	0.04	0.03	0.05	0.99	0.98	0.99	0.51
(27)	DBCAcAm	0.03	0.03	0.04	0.99	0.99	1.00	0.55
(28)	TCAcAm	0.05	0.04	0.06	1	1.00	1.00	0.81
(29)	TBAcAm	0.03	0.02	0.03	0.99	0.98	0.99	0.47

Notes: Correlation scales covariance to values of ± 1 , where correlation coefficient values > 0.9 point out variables that can be considered highly correlated.

*Confidence bounds for the THMs and I-THMs except BCIM are the true estimate derived from the 95% confidence region; U Ub = Upper Unbounded, L Ub = Lower Unbounded (# denotes the species on figures throughout this report).

The SHP model was not used to estimate the pore radius of the RO membrane because the rejection of glycerol at various fluxes by the RO membrane resulted in $\sigma_{\text{glycerol}} = 0.99$. It has previously been recommended (Wang et al., 1997) not to apply the SHP model to a system of highly restricted passage. In comparison, because of their greater pore radius, pore models are more accepted and applicable for NF membranes ($\sigma_{\text{glycerol}} = 0.78$). For the hydrodynamic model, the ratio of solute to pore radius (λ) is a limiting factor because factors are only well defined when $0 < \lambda < 0.8$. Hence, the small pore radius of the RO membrane hardly allows for a value of $\lambda < 0.8$ and the application for this type of model with these membranes. In contrast, DBPs that were not significantly impacted by changes in the permeate flux, such as DBIM, CDIM, BDIM, and TIM, had a lower unbounded confidence region. The DHANs, HKs, CH, HNMs, and the HACams did not experience inter-parameter correlation and could be fitted well by the S-K model (Figure 5.4), providing a good estimation of their rejection. The corresponding parameters of all fitted DBPs are listed in Table 5.2.

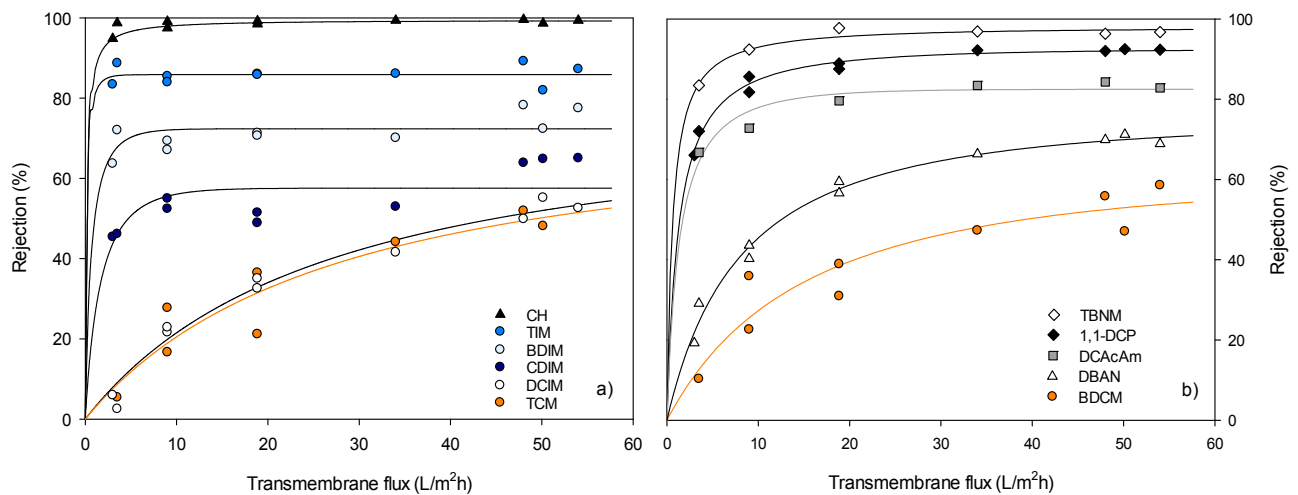


Figure 5.4. Spiegler-Kedem best fits (solid line) of experimental DBP rejection data by RO: (a) TCM, DCIM, CDIM, BDIM, TIM, and CH; (b) BDCM, DBAN, DCACAm, 1,1-DCP, and TBNM.

As already indicated by their different boundary conditions, DBPs do group as seen in Figure 5.5 where the fitted parameters P and σ are plotted against each other. The reflection coefficient, σ , indicates the asymptotic rejection value of the modeled compound and P may be regarded as a measure of the solute transport by diffusion. While σ is increasing, the permeability of the solutes is decreasing (Figure 5.5a), which correlates well with the increasing volume of HAMS, HKs, HNMs, and CH (Figure 5.5b).

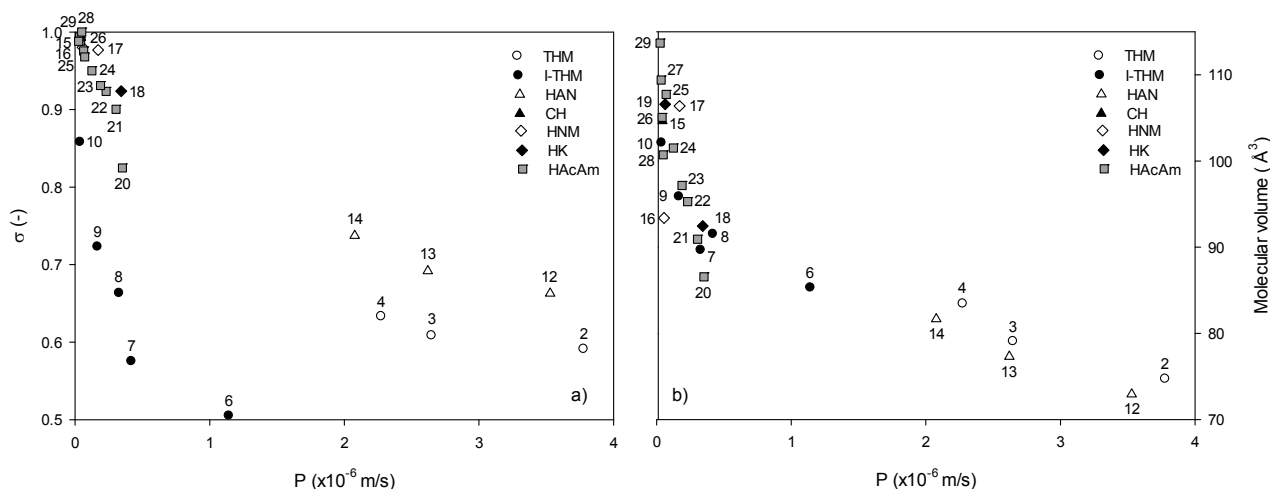


Figure 5.5. (a) Model parameters P and σ in relation to each other; (b) P in relation to molecular volume.

Notes: Error bars not shown to keep the data clearly represented, but the THMs, I-THMs and DHANs possess greatest uncertainty.

As with the NF membrane, HKs, CH, HNMs, and HAcAms that show high reflection coefficients (>0.8) also show lowest permeabilities that linearly decrease with size (Figure 5.5b). The HANs and THMs, on the other hand, show higher permeabilities in conjunction with lower reflection coefficients. The THMs exhibit a lower permeability and lower maximum rejection than DHANs, but they are slightly larger in comparison (Figure 5.5b). Hence, besides size exclusion, partitioning into the membrane by hydrophobic interaction may negatively influence their removal. In fact, Ben-David et al. (2006) concluded that thermodynamic factors, such as the partitioning, may play an important role in organic solute rejection. Partitioning may also be an important aspect for the I-THMs as they show lower σ -values as compared to HNMs, HAcAms, or HKs of similar size, and they are intermediately hydrophobic ($\log K_{ow} > 2.3$). It is interesting that they showed only little or no change in rejection with increasing permeate flux, which suggests that as water flux increases so too does solute flux.

As proposed by Déon (2013), increasing pressure (inducing the higher flux) can increase the solute concentration on the membrane surface, which, in turn, leads to a higher concentration gradient and a decrease in rejection. The model for the I-THMs then reaches the asymptote quickly (Figure 5.4 a,b) leading to low reflection coefficients with low permeabilities. The impact of increasing flux on I-THM rejection causes a decrease with increasing hydrophobicity in the order of CDIM < DBIM < BDIM < TIM, peaking in no impact for TIM. The more hydrophobic solutes were found to adsorb more on the PA layer (Kimura et al., 2003). Once adsorbed on the membrane, the solute can diffuse through the membrane matrix. Therefore, higher hydrophobicity facilitates solute passage, which, in turn, increases the solute flow with increasing flux from increased pressure and increased concentration on the membrane surface. The higher concentration on the membrane surface than in the concentration polarization layer also is experimentally supported by the observation that I-THM rejection did not express sensitivity to changes in crossflow velocity (Chapter 4).

Molecular size of the I-THMs increases in the same order as their hydrophobicity (CDIM < DBIM < BDIM < TIM) and rejection. Therefore, size exclusion also appears to play a role in I-THM rejection in addition to the adsorption mechanism. In comparison to less hydrophobic DBPs with similar size, the reflection coefficients (σ) of the I-THMs were lower. One example would be TIM ($\log K_{ow} = 3.03$, 102 \AA^3) similar in size to CH ($\log K_{ow} = 0.99$, 104 \AA^3) but exhibiting a reflection coefficient 0.13 lower than CH.

5.3 DBP–Membrane Interaction—Adsorption

As indicated by the different rejection behavior of the I-THMs observed during the modeling in Section 5.2, the adsorption of the DBPs to the membrane polymer may play an important role. For example, THMs and I-THM rejection may be negatively impacted by their hydrophobic interaction, that is, adsorption and subsequent sorption diffusion through the membrane matrix (Kimura et al., 2003; Kiso et al., 2001; Libotean et al., 2008; Nghiem and Schäfer, 2002). Adsorption of DBPs could not be directly measured during filtration experiments because losses in the feed and permeate could not be 100% related to adsorption because of additional losses by hydrolysis and volatilization. To test for adsorption of DBPs to the PA layer, the DBPs were desorbed of the active surface layer after the filtration experiments, exposing the membrane coupons to an organic solvent. Figure 5.6 shows the DBPs found on the active surface layer of the RO and NF membrane divided by their initial concentration (all DBPs 50 $\mu\text{g/L}$, except I-THMs 22 $\mu\text{g/L}$), resulting in the unit $\mu\text{mol L}/\mu\text{mol L}$. HAcAms are not shown in the graph because they were found below the limit of detection of 0.5 $\mu\text{g/L}$.

THMs, I-THMs, and HANs were consistently detected on both membrane polyamide surface layers. Because of their intrinsic properties, the amount of DBP mass adsorbed varied to a great extent. The THMs and I-THMs adsorbed the most, which might be related to their hydrophobicity ($\log K_{ow}$ 2 to 3). The less hydrophobic HANs, HNMs, HKs, and CH were also found on the membrane surface but at lower concentrations. The sorption mechanism for those DBPs may not solely be based on hydrophobicity but also on H-bonding and Van der Waals attraction because of their polar nature. Figure 5.6b shows the DBPs adsorbed on RO and NF in relation to the ratio of molecular width to $\log K_{ow}$. As seen, the adsorption increases with increasing hydrophobicity in relation to the molecular size. For example, I-THMs, TCAN, and HNMs have a similar K_{ow} to the THMs but are larger in size and, hence, have a higher width-to- K_{ow} ratio, resulting in lower adsorption. It is hypothesized that the adsorption is also influenced by molecular size because larger molecules are more hindered to access the membrane polymer where more adsorption sites are available. Such phenomena have actually been reported on different scales for granular activated carbon. Humic acids can only go into macropores and mesopores, and adsorption capacity is quickly exhausted; whereas micropollutants can also enter micropores and the capacity for adsorption is typically maintained much longer. The DHANs show considerable adsorption, more than the HNMs, HKs, and TCAN in spite of the fact that they are the least hydrophobic. Therefore, their membrane interaction may be governed by H-bonding and their small molecule size will enable adsorption. The HAcAms were found to be below their limit of detection as they might have not been well adsorbed because they are hydrophilic and larger in their molecular size.

Similar adsorption patterns of the different DBPs can be observed for the NF membrane. However, more mass was adsorbed on the NF, which might be related to the larger pore size providing more specific interaction sites. In addition to the greater mass adsorbed, the larger pore size facilitates the interaction of larger DBPs with the membrane. Therefore, the HNMs were found within the active surface layer of the NF membrane. HNMs are not only intermediately hydrophobic but also are able to form H-bonds.

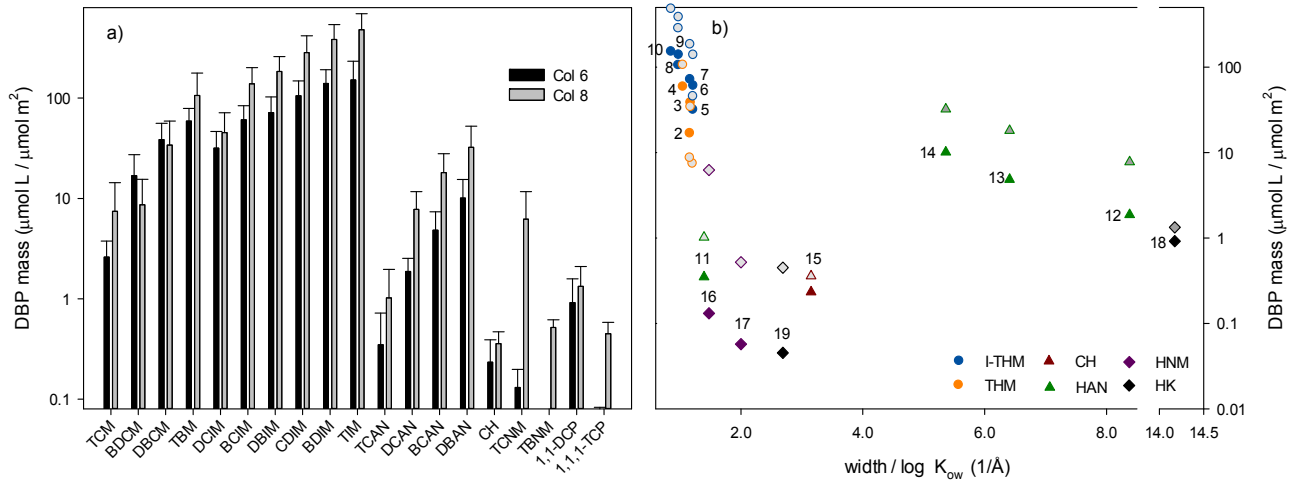


Figure 5.6. (a) Amount of DBP mass adsorbed on active surface layer after filtration experiments divided by the initial DBP concentration spiked at the beginning of the filtration experiments; (b) DBP mass adsorbed in relation to the ratio of DBP width to log K_{ow} .

Note: Error bars indicate the standard deviation between 5 membrane coupons for the RO and NF membrane resulting in total of 22 measurements for the RO and 34 measurements for the NF membrane.

5.4 Modeling DBP Rejection at Pilot- and Full-Scale

In addition to DBP rejection data collected during pilot-scale testing, DBP rejection was studied during a total of seven (4+3) sampling campaigns at two full-scale AWTPs. A major difference between pilot- and full-scale is the higher water recovery with 85% at full-scale compared to 30% of feed recovered as permeate at pilot-scale. The permeate recovery influences the solute and water flux as well as the membrane performance, because solute concentration increases toward the outlet of the pressure vessels and that leads to a greater concentration gradient resulting in lower rejection if referred to the initial feed concentration. The osmotic pressure increases because of increasing salt concentration in the feed causing a decrease in net driving pressure and transmembrane flux. Finally, the feed's crossflow velocity decreases toward the end of the pressure vessel.

At the time of sampling, Gibson Island AWTP used the ESPA2 membrane from Hydranautics, which was the same membrane chosen for the pilot testing; whereas Bundamba AWTP had installed the TFC-HR membranes from Koch. Figure 5.7 summarizes the rejection data at full-scale and pilot-scale. The combined permeate of the three-stage trains was used for calculation of the DBP rejection at both scales.

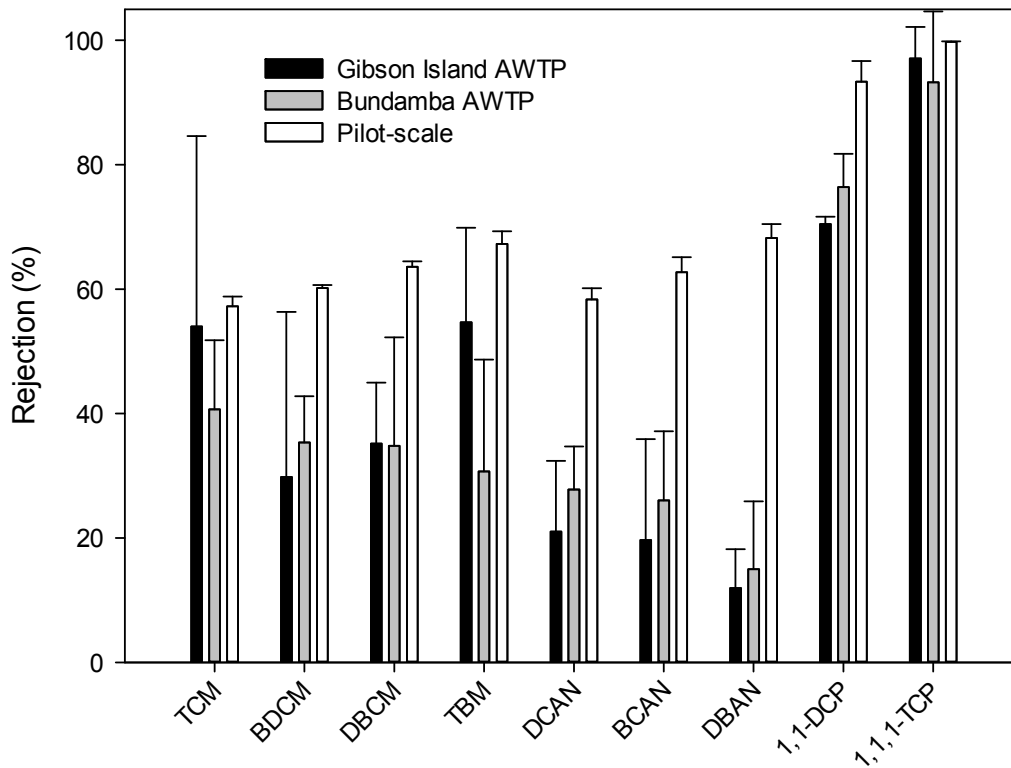


Figure 5.7. DBP rejection during full-scale RO filtration at Gibson Island AWTP (ESPA2), Bundamba AWTP (TFC-HR), and at pilot-scale (ESPA2).

Note: Error bars indicate the standard deviation among three sampling events for Gibson Island AWTP and four sampling events for Bundamba AWTP.

At the AWTPs, low removals of between 10 and 30% were observed for DHANs. The THMs showed a slightly higher removal that varied between 30 and 55%. On the other hand, a good removal was seen for the bulkier DBPs with approximately 70% for 1,1-DCP and 97% for 1,1,1-TCP. The comparison of pilot-scale experimental results with full-scale rejection indicates, depending on the group of DBPs, a similar-to-lower performance at full-scale. At pilot-scale, a higher rejection of between 30 and 55% of the DHANs and THMs, respectively, was observed. The difference between the different scales can be considered acceptable variation because of sampling on different days for 1,1,1-TCP. It is interesting that the difference between full- and pilot-scale was more pronounced for DHANs than for THMs (Figure 5.7). As observed in Chapter 4, varying crossflow velocity did not result in significant changes for THM rejection; whereas a decrease in crossflow velocity led to a lower DHAN rejection. Crossflow velocities decrease across the feed channel in a membrane module, but they decrease substantially across a pressure vessel with five to eight membrane modules in series. This change in crossflow velocity likely contributed to the stronger impact on DHAN rejection.

The considerable higher rejections at pilot-scale compared to the full-scale installations may be partly attributed to the feed water temperature. With $26 \pm 1^\circ \text{C}$ the feed water temperature was 3°C higher on site than during the pilot testing. However, the major contributing factor may be the permeate recovery, which at 85% is considerably higher at full-scale compared to the 30% at pilot-scale. The following mechanistic modeling approach aimed to predict rejection of THMs, DHANs, HKs, and two HAcAms at high recoveries as well as to simulate a multistage full-scale application.

5.4.1 Model for Spiral Wound Element

The modeling approach to predict DBP rejection with spiral wound modules combined the Spiegler-Kedem approach for transport, a material balance, and the Arrhenius relationship to include the impact of temperature. Similar approaches have been successfully reported in the literature (Mane et al., 2009; Senthilmurugan et al., 2005; Taniguchi and Kimura, 2000). The model was verified with data from pilot-scale studies at different permeate fluxes and resulting recovery. Equations for the modeling approach were derived for the spiral wound module, in which each leaf consists of two membrane sheets. The two sheets are separated by a permeate and feed channel on the opposite side of the membrane sheet (Figure 5.8). As depicted, the model divides the membrane area into m segments in l (length) direction and n segments in w (width) direction. The dimensions are calculated by eqs. 5.8 and 5.9;

$$\Delta x = \frac{l}{m} \tag{5.8}$$

$$\Delta y = \frac{W}{n} \tag{5.9}$$

The local grid area ($S_{i,j}$) through which the fluid flows and the feed flow rate at the entry grid point of the feed channel may be written as eq. 5.10;

$$S_{i,j} = 2 \cdot \frac{l \cdot W}{m \cdot n} \tag{5.10}$$

where i = index number along x-axis, j = index number along y-axis.

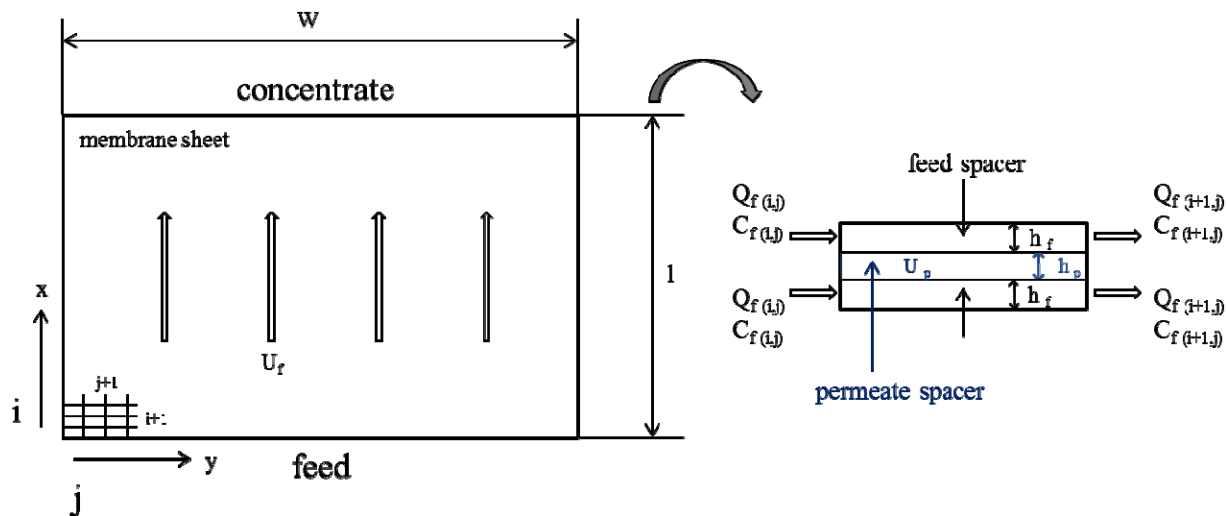


Figure 5.8. Single leaf of unwound spiral wound module divided into grid segments represented by index numbers i and j along x-axis and y-axis, respectively.

Notes: The flow in the feed channel is along the x-axis, in the permeate channel it is along the y-axis; Q_f = flow rate in feed channel (m^3/s) and C_f = feed solute concentration (kg/m^3).

5.4.1.1 Membrane Transport

The water transport through each segment was derived from the S-K model where the water flux (J_w) is defined by eq. 5.11:

$$J_w(i,j) = A \left((P_f(i,j) - P_p(i,j)) - \sigma (\pi_f(i,j) - \pi_p(i,j)) \right) \quad (5.11)$$

A = hydraulic permeability (m/Pa s), P_f = feed pressure (Pa), P_p = permeate pressure (Pa), π_f = osmotic pressure feed (Pa), π_p = osmotic pressure permeate (Pa). σ = reflection coefficient indicating the extent of water/solute coupling (dimensionless). σ -values for the various DBPs obtained in Section 5.3.1 were used in this model.

5.4.1.2 Pressure Drop

To obtain the hydraulic pressure drop for the feed and permeate channel, eqs. 5.12 and 5.13 are based on Darcy's law (Senthilmurugan et al., 2005):

$$P_f(i,j+1) + P_f(i,j-1) - 2P_f(i,j) = 2k_{fb}n_f U_f^{n_f-1} \mu \Delta x^2 \sum_1^i \left(\frac{J_w}{h_f} \right) \quad (5.12)$$

$$P_p(i,j+1) + P_p(i,j-1) - 2P_p(i,j) = 2k_{pb} \mu \Delta y^2 \sum_1^i \left(\frac{J_w}{h_p} \right) \quad (5.13)$$

where n_f = empirical fitting parameter, k_{fb} = friction parameter for feed channel, k_{pb} = friction parameter for permeate channel, h_f = feed channel height, h_p = permeate channel height.

5.4.1.3 Mass Transfer Coefficient

The mass transfer coefficient (k) can be obtained with an empirical Sherwood relationship that takes into account the fluid properties (dynamic viscosity and velocity), solute properties (diffusivity), geometry of feed channel (thickness), and flow conditions (Re, turbulence promoters). The presence of a feed spacer in spiral wound modules is necessitated to account for the turbulence promoters and provides increased mass transfer from a reduction of the boundary layer thickness. Winograd et al. (1973) proposed an empirical equation (eq. 5.14) for the mass transfer in narrow channels in the presence of turbulence promoters:

$$k = 0.758 \left(\frac{2K}{2-K} \right)^{0.8} \left(\frac{D}{h_f} \right) S_c^{-\left(\frac{1}{3}\right)} \left(\frac{Pe h_f}{\Delta l} \right)^{0.3} \quad (5.14)$$

K = efficiency of mixing net (dimensionless), D = diffusion coefficient, h_f = feed channel height, S_c = Schmidt number = (ν/D) (dimensionless), Pe = Peclet number = $2h_f U_f/D$ (dimensionless) and Δl = characteristic length of the mixing net (m). D and the dynamic viscosity (μ) estimation was given by Sekino (1994) as presented in eqs. 5.15 and 5.16:

$$D = 6.725 \cdot 10^{-6} \exp \left(0.1546 \cdot 10^{-3} C - \frac{2513}{T} \right) \quad (5.15)$$

$$\mu = 1.234 \cdot 10^{-6} \exp \left(0.00212C + \frac{1965}{T} \right) \quad (5.16)$$

5.4.1.4 Osmotic Pressure

The osmotic pressure can be obtained by eq. 5.17 given by Miyake (1939):

$$\pi = (0.6955 + 0.00257T) \cdot 10^8 \frac{C}{\rho} \quad (5.17)$$

where T (° C) is the temperature, ρ the solution density (kg/m³), and C (kg/m³) is the concentration of all constituents in the solution.

The density can be obtained by the correlation in eq. 5.18 given by Sekino (1994):

$$\rho = 498.4M + \sqrt{248400M^2 + 752.4MC} \quad \text{with } M = 1.0069 - 2.5727 \cdot 10^{-4} T \quad (5.18)$$

5.4.1.5 Mass Balance

Flow rates and solute concentrations (Q_p , C_f , C_p) were determined by a mass balance using an iterative approach in Excel to solve the set of equations. The mass balance approach was chosen because the modeled parameters change in the spiral wound module depending on their location on the membrane leaf because of a pressure drop and solute concentration. The pressure, solute concentration, and flow rate on the inlet of the spiral wound module for the feed channel was set as follows:

$$Q_{f(i,j)} = \frac{Q_{f0}}{n \cdot n_L} \quad (5.19)$$

$P_{f(i,j)} = P_{f0}$, $P_{p(i,j)} = \text{standard atmosphere}$ ($i = 1$ to m and $j = n$), $C_{f(i,j)} = C_{f0}$, $C_{p(i,j)} = C_{p0}$, ($i = 1$ and $j = 1$ to n and $n_L = \text{number of leaves}$).

Feed and permeate flow rates of the next grid segment are calculated from eqs. 5.20 and 5.21:

$$Q_{f(i+1,j)} - Q_{f(i,j)} = -J_{v(i,j)} S_{L,i} \quad (5.20)$$

$$Q_{p(i,j)} = 2 J_{v(i,j)} \Delta x \Delta y \quad (5.21)$$

The solute concentration in the feed is calculated from eq. 5.22:

$$C_{f(i+1,j)} = \frac{Q_{f(i,j)} C_{f(i,j)} - Q_{p(i,j)} C_{p(i,j)}}{Q_{f(i+1,j)}} \quad (5.22)$$

The solute permeate concentration, which also results in the overall solute permeate concentration (C_{pT} kg/m³), is calculated from eq. 5.23:

$$C_{p(i+1,j+1)} = \sum_{i=1}^m \sum_{j=1}^n \frac{C_{L,i} S_{L,i} n_L}{Q_{pT}} \quad (5.23)$$

with which the overall solute rejection can be calculated from eq. 5.24:

$$R = \left(1 - \frac{C_{pT}}{C_{f0}} \right) \quad (5.24)$$

The overall recovery can be obtained in eqs. 5.25 to 5.27 from the overall permeate flow rate (Q_{pT} m³/s):

$$Q_{pT} = \sum_{i=1}^m \sum_{j=1}^n (Q_{v,i,j}) n_L \quad (5.25)$$

$$\text{Recovery} = \frac{Q_{pT}}{Q_{f0}} \quad (5.26)$$

$$R_{\text{cumulative}} = \frac{\left(\frac{C_{f,i,j}}{C_{f0}}\right)}{(Q_{i,j})} \quad (5.27)$$

5.4.1.6 Calculation of Larger Membrane Systems

In order to reach high recoveries at full-scale treatment plants, RO filtration can be performed in several stages that consist of several pressure vessels each. In a pressure vessel, between five and up to eight membrane modules are typically placed in series. As observed during the pilot-scale tests in Chapter 4, increasing product water recovery can lead to a decreased DBP rejection. To predict the performance of a pressure vessel operating at higher recoveries than a single spiral wound module, the mass balance for one module was solved in series. The output data, including salt and DBP concentrations, feed and permeate pressure, and feed and permeate flow rate, of each of the grid segments of the first module was used as a starting point for the following spiral wound module. Summarizing, a pressure vessel consisting of n spiral wound elements was simulated by repeating the previous calculations on each spiral wound element consecutively.

5.4.2 Model Validation

The rejection of 12 DBPs, including THMs, DHANs, HKs, DCACAm, and TCACAm was determined experimentally at pilot-scale. The rejection data of the listed DBPs was used to determine the predictive ability of the described model. The model makes several assumptions including the validity of Darcy's law for the feed and permeate channel, that it is a 2-dimensional transport, that the system is at steady state, and the validity of the solution-diffusion model for water transport through the membrane. Hence, the membrane is assumed nonporous and there is no transport within pores of the membrane.

The hydraulic permeability (A) was obtained iteratively with adjusting the initial guess of A until the predicted value of Q_p converges to ≤ 0.001 of the measured Q_p .

input: $Q_f, P_f \rightarrow$ model \rightarrow output: $Q_{p\text{-predicted}}$

↓ adjust A until

$$1 - \frac{Q_{p\text{-predicted}}}{Q_{p\text{-measured}}} \leq 0.001$$

Input parameters P_f and Q_f and the output parameter Q_p of the model were obtained during pilot tests at baseline conditions (i.e., 18 L/m²h, 23° C, 7 mM NaCl, 1 mM KH₂PO₄ and pH 6.8). To estimate the feed side friction coefficient, the described algorithm was repeated to again reach a permissible error of ≤ 0.001 .

The value of A was estimated at 1.17×10^{-8} and k_{fb} at $2.06 \times 10^9 \text{ 1/m}^2$ using DCAN experimental data. DCAN was chosen as it is the smallest (73 \AA^3) nonhydrophobic ($\log K_{ow} = 0.29$) in the suite studied. As will be shown further in the text, the estimated parameters also were well suited for the additional DBPs. The value for the friction coefficient ($k_{fp} = 1.10 \times 10^{10} \text{ 1/m}^2$) for the permeate channel was taken from the literature (Avlonitis et al., 1991).

The predictive model can be used as an analytical tool when model predictions match observed experimental values within an acceptable range of error. Data obtained during pilot-scale testing was in good agreement with the theoretical model predictions of P_f and permeate flux as shown Figure 5.9a,b. The error between the predicted and the observed values for P_f for all three fluxes predictions was less than 0.7% and less than 3% for the following two membrane modules. Only at $27 \text{ L/m}^2\text{h}$ did the model overestimate the pressure after the third membrane module by 6.8%. The transmembrane flux also correlated well with experimental observations with a maximum error of 3.3% across all fluxes and the three membrane modules.

The net driving pressure is the main driving force for filtration, which, in turn, influences solute rejection during RO filtration. As observed (Figure 5.9a for feed pressure) and modeled, the pressure drops along the module on both sides of the membrane leaf from friction within the feed and permeate channel. The predicted pressure profile along the channel for the permeate side shows that the maximum pressure at the inlet of the membrane module drops to its lowest value at the outlet. With the water passing across the spiral wound module, the solute concentration on the feed and permeate side becomes more concentrated. Besides the solutes, the salt in solution also increases, which leads to an increased osmotic pressure and a decrease in water permeation.

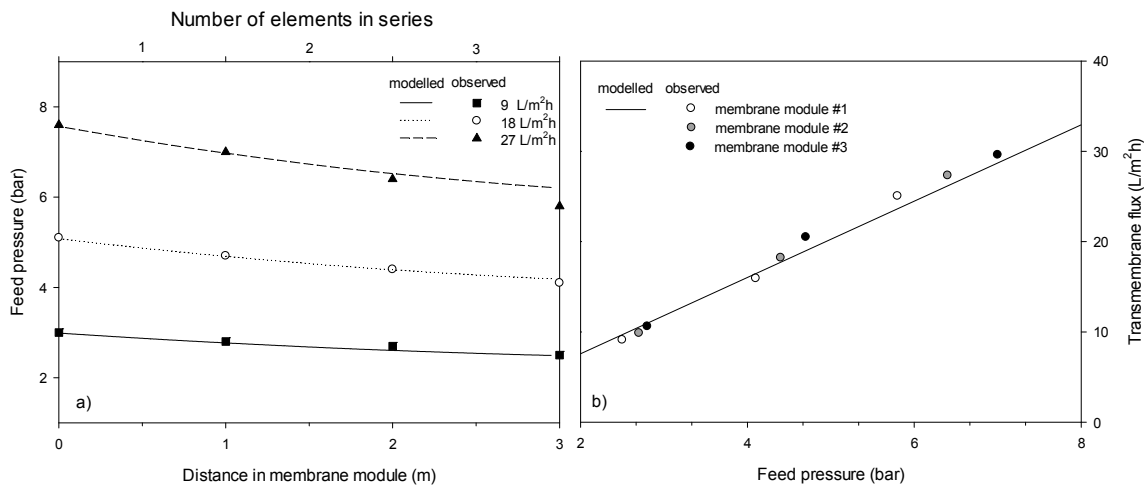


Figure 5.9. (a) Observed and modeled feed pressure along three spiral wound modules in series; (b) observed and modeled transmembrane flux as a function of the feed pressure at one spiral wound module.

The predicted and measured overall rejection values of BDCM, DCAN, 1,1-DCP, and DCACAm during the pilot testing of one spiral-wound module at three permeate fluxes is shown in Figure 5.10. Those are displayed as representative of their respective groups. As seen, the model fits are in very good agreement with the experimental data over the whole flux range studied. The well rejected HACams and HKs could be predicted with an error less than 0.5% at all three fluxes. Errors for the THMs and DHANs ranged between 0.2 and 2.4%.

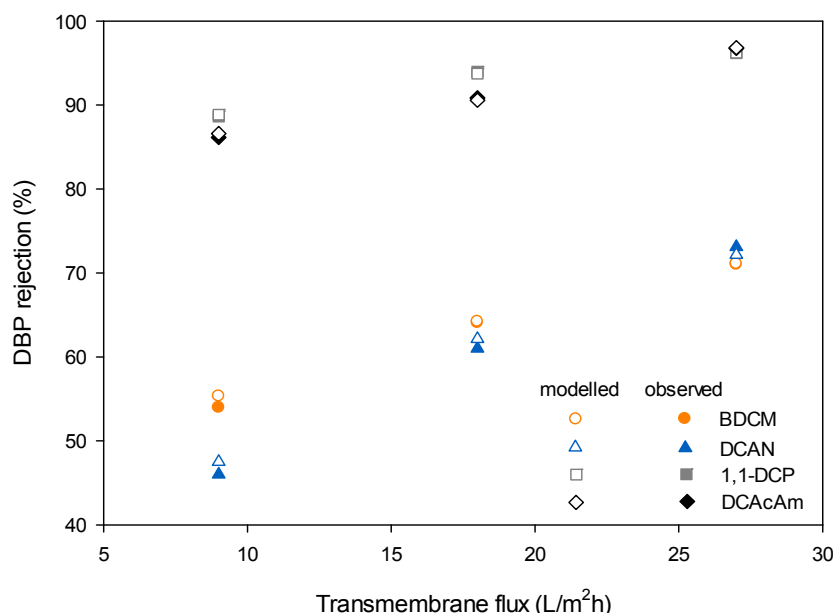


Figure 5.10. Modeled and observed rejection of BDCM, DCAN, 1,1-DCP, and DCACAm as a function of transmembrane flux.

In conclusion, theoretical model predictions of P_f and flow rates are within reasonable error of experimental data acquired at pilot-scale. Good DBP rejection predictions were obtained in the transmembrane flux range of 9 to 27 L/m²h.

5.4.3 Model Application

5.4.3.1 Single-Stage Single-Pass Simulation

In order to properly predict DBP rejection at full-scale, the model was used to simulate DBP rejection at high recoveries, as one pressure vessel usually contains six to eight membrane modules in series leading to a recovery of ~50%. Because three spiral wound membrane modules were installed in series at the pilot-scale system, experimental data could be collected for a recovery up to 30%. This allowed testing the model for accuracy of DBP rejection predictions for more than one module. As shown in Figure 5.9a, the feed pressure was accurately predicted for all three modules at all fluxes.

Figure 5.11 shows the effect of recovery on the DBP rejection at 18 L/m²h. As observed earlier, the recovery had a negative effect on the DBP rejection. BDCM, DCAN, 1,1-DCP, and DCACAm rejection decreased by 5.4, 4.2, 1.1, and 2.5%, respectively, when increasing the recovery from 10 to 30% during pilot-scale experiments.

A high recovery results in lower rejections and is caused by several different factors. Driven by the concentration gradient, solute permeation increases as the concentration of the solutes increases until the end of the pressure vessel. Besides the solutes, the salt in the solution also increases, which leads to an increased osmotic pressure and a decrease in water permeation. In addition, the pressure loss along the pressure vessel leads to a lower transmembrane flux, which, in turn, can lead to lower solute rejection because of a greater diffusive flux of the solutes compared to the water flux.

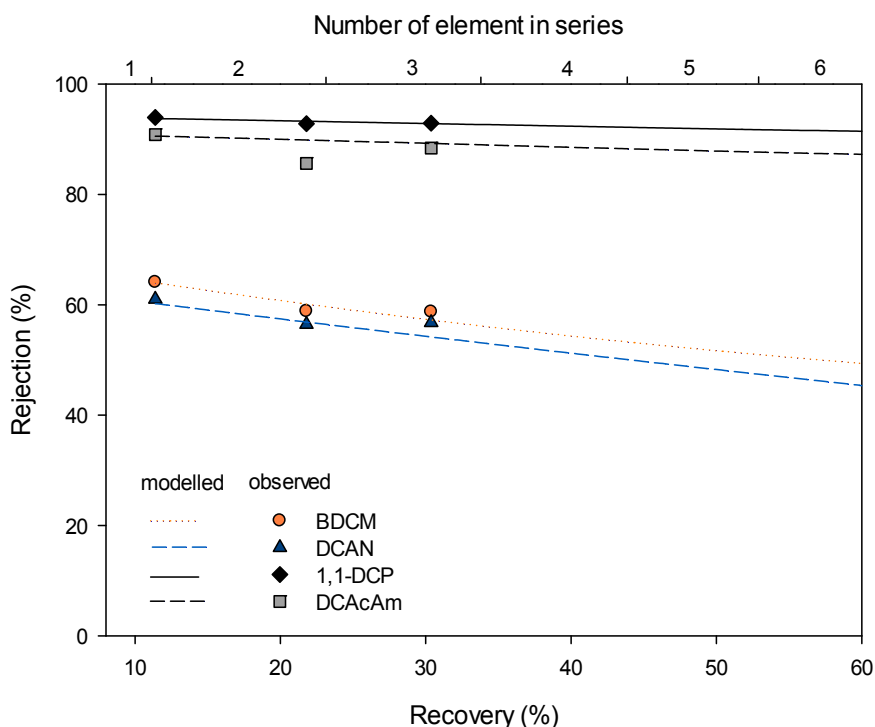


Figure 5.11. Impact of recovery on the rejection of BDCM, DCAN, 1,1-DCP, and DCACAm (18 L/m²h).

The rejection prediction of a pressure vessel holding six membrane elements in series is in good agreement with the observations at pilot-scale (Figure 5.11). The model results show that the impact of recovery is more pronounced for the smaller DBPs, including the DHANs and THMs. This is in agreement with the observations between pilot- and full-scale. The larger well-rejected HKs and HAcAm are less impacted because their diffusive flux and concentration gradient is already low as compared to the DHANs and THMs.

5.4.3.2 Three-Stage Single-Pass Simulation

In a three-stage process the concentrate from the first stage serves as the feed for the second stage, which serves as the feed for the third stage. Hence, the feed becomes more and more concentrated. Figure 5.12 shows the development of BDCM, DCAN, 1,1-DCP, and DCACAm rejection across three stages of pressure vessels holding six membrane modules in series.

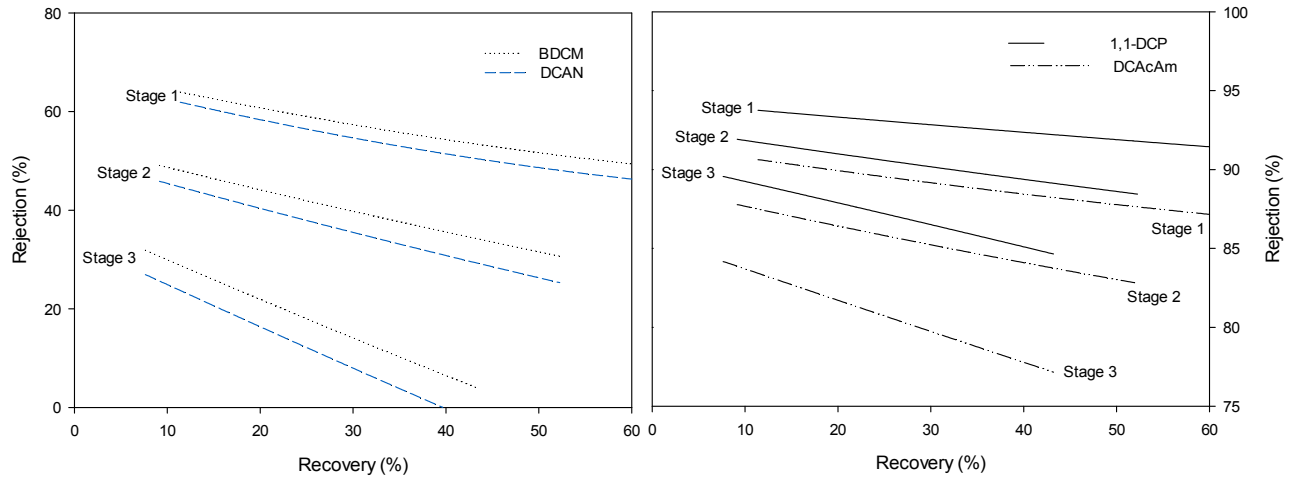


Figure 5.12. Development of BDCM, DCAN, 1,1-DCP, and DCACAm along Stage 1, Stage 2, and Stage 3 with one pressure vessel holding six membrane elements.

With the pressure decrease along each stage, the recovery decreases but also the transmembrane flux decreases, which leads to significantly lower rejections from each stage to the next in the treatment train.

The DBP rejections after the third stage during the filtration process were predicted to be 85% and 92% for 1,1-DCP and 1,1,1-TCP, respectively. THM and DHAN rejection were modeled to be less than 25%, where TCM and DCAN possessed a negative rejection. Figure 5.13 shows the DBP rejections measured at two full-scale AWTPs and the modeled rejection after the third stage. As seen, the modeled rejections for the THMs and DHANs underestimated the rejection measured at full-scale AWTPs. Rejections at both AWTPs ranged between 30 and 50% for the THMs and 10% for DHANs. For comparison, it is important to bear in mind that the modeled rejection is relative to the initial feed concentration at this specific location (or % recovery) and is not referring to the rejection of the combined permeate. To account for the combined permeate at that specific recovery (in this case rejection after the third stage using six membrane modules per pressure vessel) the cumulative rejection is also presented in Figure 5.13.

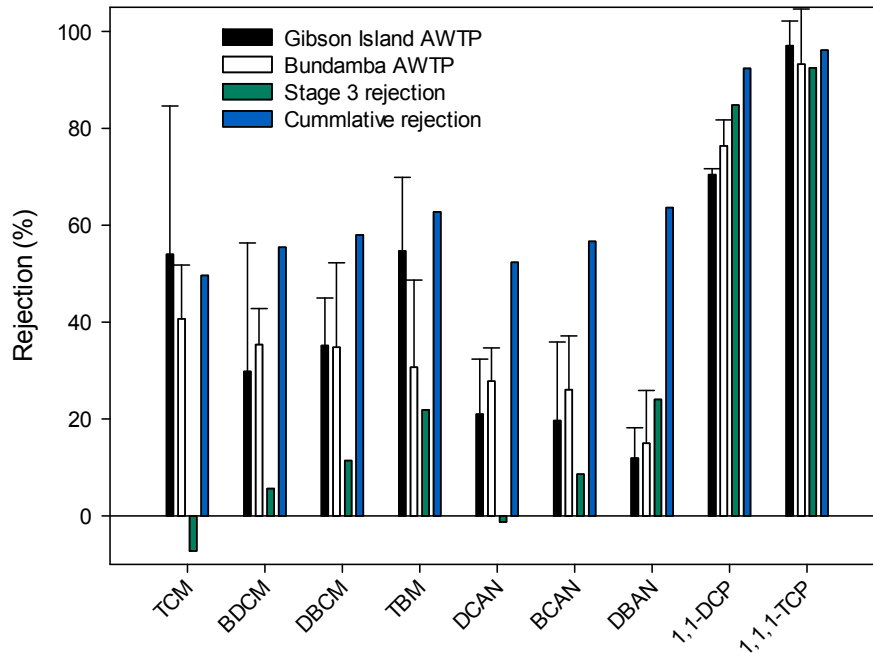


Figure 5.13. DBP rejection during full-scale RO filtration at Gibson Island AWTP (ESPA2), Bundamba AWTP (TFC-HR), modeled DBP rejection after Stage 3 and modeled cumulative rejection after Stage 3.

Notes: Error bars indicate the standard deviation among three sampling events for Gibson Island AWTP and four sampling events for Bundamba AWTP.

The cumulative rejection for the THMs showed a tendency to overestimate the observed rejection at the AWTPs, yet ranged within the variation between the sampling events. The DHANs, on the other hand, were overestimated by the cumulative rejection. In Chapter 4, the DHANs rejection was observed to decrease with decreasing crossflow velocity. Therefore, the loss in crossflow velocity alongside the pressure vessels in each stage may strongly contribute to the lower DHAN rejection seen during the sampling events. This is in accordance with the behavior of the THMs, which were not significantly impacted by changes in crossflow velocity during bench-scale experiments. As a well rejected DBP, 1,1,1-TCP showed good fits with the model, whereas the rejection of 1,1-DCP was already overestimated during the pilot-scale experiments. Here it is important to note that the rejections predicted by the model used experimental data obtained with virgin membranes, whereas the AWTPs treat MF/UF filtered secondary effluent and therefore organic, bio-fouling, and scaling to some degree is inevitable on the membrane surfaces. Subsequently, a higher rejection from fouling-induced pore restriction may occur. On the contrary, the DBPs may be affected to a greater extent by changes in underlying membrane foulant–DBP interactions, which may outweigh the possible gain in rejection because of “effective pore” restriction.

Chapter 6

Conclusions and Perspectives

6.1 Conclusions

Since their discovery, DBPs have been a point of interest in drinking water research for more than 3 decades because of their potential impact on public health. The main objective of this study was to improve the understanding of DBP formation and removal during the treatment of secondary treated wastewater to produce high-quality recycled water using high-pressure membranes. Therefore, 29 DBPs including regulated and so-called emerging DBPs were selected with a wide range of physicochemical properties and with the potential to be formed during these processes. The impact of different operational parameters such as type of disinfectant, pH, and temperature on DBP formation and bromine incorporation was studied in laboratory-scale experiments. Of equal importance was to study the effect of operational parameters on DBP removal by high-pressure membranes. The adaptation of various mathematical models using experimental data at both bench- and pilot-scale allowed for the prediction of DBP removal and analysis of the removal mechanisms involved.

6.1.1 DBP Occurrence in Full-Scale Advanced Water Treatment Plants

Results of several sampling events across two full-scale AWTPs in South East Queensland, Australia, confirmed that DBP formation has to be expected when disinfecting secondary effluent with the aim of limiting biofilm growth on the membrane surface. DBPs including THM4, HANs, HKs, CH, TCNM, and in some cases also DCIM were found at the AWTPs after chloramination of the secondary effluent. Concentrations of all DBPs were generally low, with DCAN and BCAN found close to the regulation limit for recycled water in Queensland, Australia. Overall, lower DBP formation was observed for the AWTP using shorter disinfectant contact times. Also, lower DBP formation was seen when the same AWTP used pre-formed monochloramine instead of inline-formed chloramines as their disinfection strategy.

6.1.2 DBP Formation and Bromine Incorporation

Experiments under controlled conditions at lab-scale varying among three disinfection strategies (chlorination, pre-formed, and inline-formed chloramination), pH (5.5–8.5), temperature (23–35° C) and various reaction times (0.5, 2, 4, 8, 24 hours) confirmed that reaction time and disinfection strategy can impact the bromine incorporation into THMs and DHANs. pH was also identified as an important influencing factor, whereas temperature did not induce changes in bromine incorporation. During the application of pre-formed monochloramine, no bromine incorporation occurred during the first 4 hours, whereas inline-formed chloramines showed incorporation after only half an hour of reaction time. When forming chloramines inline, chlorine is added separately, which, besides reacting with the ammonia, also can react with the bromide present in the water. The reaction of bromide with chlorine is five orders of magnitude faster than with NH_2Cl . In addition to increasing reaction time, low pH conditions exacerbated the degree of bromine incorporation, likely from acid-catalyzed chloramine decomposition.

The investigation of operational parameters such as reaction time, pH, temperature, and disinfection strategy on DBP formation during disinfection of secondary effluent produced results that were similar to drinking water disinfection. The impact of the different parameters was successfully quantified by applying response surface modeling (i.e., 66 models) to all DBP formations during 24 hours of contact time. Depending on the group of DBPs and the disinfection strategy, either pH or reaction time were found to be

the most influential parameters. During chloramination, time was identified to be the major influencing factor for N-DBP formation, whereas pH affected C-DBP formation to a greater extent. It was seen that pH and temperature affected individual DBPs differently depending on degradation by hydrolysis reactions. Elevated temperature and pH led to degradation of the HKs after an initial fast formation, whereas temperature only had a minor positive impact on CH formation during chloramination. For TCNM formation, temperature was of equivalent importance as was pH during chloramination. Similar to the DHANs, TCNM formation did not reach its maximum after 24 hours of contact time. It is interesting that the TCNM levels formed during chloramination approached those formed during chlorination after 24 hours at pH 7, whereas most DBP formation during the first 24 hours of reaction with the different disinfectants followed the order chlorination >> inline-formed monochloramine > pre-formed monochloramine. Secondary effluent is a heterogeneous mixture of NOM that competes for the free chlorine (forming DBPs) and added ammonia (forming chloramines), and more DBPs were formed during inline chloramination. At full-scale treatment plants, applying pre-formed NH_2Cl and short contact times could minimize DBP formation.

6.1.3 The Influence of Molecular Properties on Rejection by Dense Membranes

Once formed, the DBPs were removed to a different extent by the RO membranes in full-scale AWTPs. The bulky trichlorinated DBPs, such as CH, TCAN, and TCNM could be almost completely removed, whereas DHANs and THMs were not well rejected—ranging between 10 and 55%, respectively. The lowest DBP rejections during bench-scale and pilot-scale studies also were observed for the THMs and DHANs. During the bench-scale studies, DBP rejection was investigated with a flat-sheet crossflow cell varying the pH (4.5–8.5), ionic strength (7–70 mM), crossflow velocity (0.04–0.16 m/s), transmembrane flux (3–55 $\text{L}/\text{m}^2\text{h}$ for RO and 3–70 $\text{L}/\text{m}^2\text{h}$ for NF) and temperature (23–36° C). To expand the pool of different molecular properties for further understanding (i.e. hydrophobicity, H-bond acceptors, polarity) I-THMs and HAcAms also were included in the bench-scale investigations, in addition to THMs, HANs, HNMs, HKs, and CH.

DBP rejection by RO and NF could be predicted well using multiple linear regression from data measured with eight RO and five NF membrane coupons for 29 DBPs. Molecular size parameters were identified as good descriptors during NF filtration, whereas during RO filtration results indicated the importance of properties related to the molecule's polarity and solute-membrane interactions in addition to the molecular size.

Polarity interaction promoted the sorption–diffusion process through the membrane, resulting in lower rejection, especially for DBPs that possess the capability to form H-bonds (e.g., HAcAms). Promoted passage by adsorption occurs also by hydrophobic interaction. Significant adsorption for various DBPs on the polyamide layer was demonstrated for the RO and NF membranes. The THMs and I-THMs, which are the most hydrophobic in the suite analyzed, were adsorbed to the greatest extent. Also, greater adsorption was observed for the NF membrane, which led to the conclusion that the larger pore size may facilitate the entry into the pores where more interaction sites were available because of the greater internal surface area.

6.1.4 DBP Rejection—Operational Parameters

Operational parameters and feed solution chemistry are central factors when evaluating DBP removal by RO and NF membranes. After increasing the pH and ionic strength, rejection enhancement was only observed with the NF membrane and for the HAcAms. When increasing pH, the increased concentration of hydroxide ions can interfere with H-bonding between the membrane and the polar HAcAms, leading to an increased rejection. Also, changes in the membrane structure potentially can occur to influence DBP rejection. Similarly, the increased presence of ions dampened the DBP–membrane interaction introduced by their intrinsic polarity and H-bonding capacity, resulting in higher rejection. On the other hand, increasing

temperature led to a significant drop in rejection for all DBPs as was expected because of pore expansion and increased partitioning at higher temperatures. Hydrophobic interaction likely reduced the effect of crossflow velocity for the THMs and I-THMs, whereas only DHAN and DCaAm rejection increased because of reduced concentration polarization during RO filtration. Decreasing transmembrane flux lowered the rejection of all DBPs except TIM by RO and BDIM and TIM by NF probably because of their hydrophobic interactions with the membrane. The greatest change in rejection was observed for DHANs, HNMs, HKs, and HAcAms when modifying transmembrane flux below 18 L/m²h.

When upscaling the DBP rejection from crossflow flat sheet coupons to 4-inch spiral wound RO modules, the effect of temperature, pH, and flux was more pronounced with the spiral wound module. It was hypothesized that the membrane can move more freely in the module and, therefore, is more susceptible to changes in the membrane pore structure induced by variations in pH and temperature.

6.1.5 Prediction of DBP Removal in Bench-, Pilot- and Full-Scale RO Processes

An important difference in full-scale applications is the greater permeate recovery that can influence solute rejection because of increased feed concentrations. In fact, higher rejections of THM, DHAN, and 1,1-DCP were obtained at pilot-scale compared to those measured at two full-scale AWTPs. The decrease in DBP rejections observed at pilot-scale with three 4-inch modules in series resulting in 30% recovery could be described by a mechanistic model approach.

A MLR model for rejection prediction at various operational conditions was developed and validated. The developed model can successfully simulate the rejection by simply using a linear relationship of two common molecular properties—the transmembrane flux and temperature. The group of nitrosamines was not part of this study; however, the developed MLR model was able to successfully predict their rejection at the bench- and pilot-scale. N-nitrosamines are an important group of DBPs to consider in order to provide a comprehensive overview of DBPs at AWTPs. N-nitrosamines compare to the DBPs included in this study by their size—the smallest NDMA similar in size to DCAN. In addition, they are hydrophilic but contain H-bonding sites in their structure like the DHANs and HAcAms. Therefore, polarity is expected to be the major influencing factor with regard to solute–membrane interaction. Because their molecular properties, size, hydrophilicity, and H-bonding capacity are covered by the various DBP groups studied in this report, their rejection can be predicted well with the developed model.

6.1.6 Water Quality Management

As has been shown, DBPs were formed during the disinfection of secondary effluent and not all were rejected well by the membranes. The poor removal of some DBPs suggested that RO and NF membranes cannot be relied on as an efficient barrier, and the disinfection process should aim for minimal formation. Nonetheless, changes in operational parameters at full-scale advanced water treatment plants need to be balanced with the original treatment objectives, that is, to reliably produce water at fit-for-purpose quality at acceptable monetary cost and environmental impact. pH, for example, plays an important role in scaling control. Therefore, increasing pH to minimize DBP formation during chloramination increases the risk of scaling and too little contact time can lead to unwanted biofilm growth on the membrane surfaces. In conclusion, halogenated DBP formation as well as bromine incorporation can be reduced by applying pre-formed chloramination instead of forming chloramine inline, especially at contact times of less than 24 hours.

Because DBP formation cannot be entirely prevented, membrane operation should carefully balance the risks and benefits of meeting the original treatment objectives. For a number of reasons, transmembrane flux can be varied at full-scale installations. The disadvantages of lowering the flux can be a decrease in DBP rejection. When lowering the transmembrane flux, generally TOC removal and salt passage are

monitored to ensure water quality. However, those criteria might not be fully representative for DBP rejection, and lowering the transmembrane flux could result in an unintended increase in DBP passage. Feed water temperature is a parameter difficult to control at full-scale applications but was found to have a strong impact on DBP passage. With temperatures ranging between 20 and 30° C throughout the seasons in southeast Queensland, DBP passage can be expected to increase by 20% to almost double for the initially well-rejected DBPs (>85%).

Besides membrane operation, the design of the treatment plant has to be considered as it is potentially influential on DBP removal. DBP rejection was shown to decline with increasing permeate recovery rate. Full-scale RO and NF treatment systems are generally designed to range in between 50 and 85% recovery. As such, sufficient DBP removal needs to be balanced with an optimal recovery rate.

6.2 Recommendations for Future Research

A number of research questions have arisen from this study that require further investigation. Some of these questions and suggested approaches are discussed in the following:

◆ **Could an advanced oxidation process using UV/H₂O₂ for NDMA removal be another safety barrier for poorly removed DBPs?**

The AOP is installed at the end of the treatment train of the AWTPs in order to ensure sufficient removal of NDMA, as it is poorly rejected by RO membranes. The removal of DBP precursors such as those for THMs and HAAs by this AOP has been widely studied. However, the impact of this process on preexisting DBPs would warrant further investigation. Sampling campaigns in this study indicated a positive influence on the removal of DCIM. It was removed almost completely by the AOP, whereas the RO membrane could only achieve low rejections. The auxiliary effect for DBP removal during the AOP was also observed for DBCM (45%) and DBAN (25%), which also showed a low rejection by the RO membranes. On the other hand, the AOP might enhance the formation potential of specific DBPs by breaking down other material or the hydroxyl radicals providing building blocks for DBPs. CH, for example, was completely removed by the RO membranes and then was formed again after the final chlorination step. In addition, another study showed an increased NDMA formation potential after UV/H₂O₂ treatment of the model compound doxylamine (Farré et al., 2012). This is of concern because the water is again disinfected with chlorine before final release. Therefore, research is needed to shed light on the potential degradation of the DBPs poorly removed by the membranes and also on potential formation of DBPs in the final treated water where AOPs may provide new precursors.

◆ **Does membrane impairment affect DBP rejection?**

The rejection of DBPs by RO and NF membranes was studied at their virgin state. However, during treatment of real water, various types of membrane impairments can occur. Secondary effluent can contain large amounts of organic and inorganic matter that can cause scaling, the formation of organic and colloidal fouling, and a layer of biofouling on the membrane surface (Ning and Troyer, 2007; Xu et al., 2010). Studies have established that the rejection of uncharged organic solutes can be improved or decreased by the different fouling layers (Agenson and Urase, 2007; Xu et al., 2010).

Organic material present in fouling layers can potentially react with disinfectants in the RO feed. Hence, the examination of the fouling layers in terms of their DBP formation potential might lead to interesting results.

Besides the fouling of the membrane, its exposure to disinfectants and chemical cleaning agents can lead to an accelerated ageing of the membrane. Free chlorine can react with the polyamide layer of the RO membrane and lead to changes in the chemical structure (Antony et al., 2010; Kwon and Leckie, 2006). For

example, chlorination replaced hydrogen with chlorine on the amide group of the membrane polymer and caused the loss of hydrogen bonding sites rendering the membrane more hydrophobic) which may have an impact on the DBP rejection. Further research should explore the impact of membrane fouling and chemical ageing to ensure appropriate product water quality.

◆ Do DBP precursors pass through membranes and what is the impact of disinfection strategy on precursor removal?

Every disinfectant forms its own suite of DBPs (Richardson, 1998). Hence, different precursors may be consumed by chlorine compared to chloramine. Therefore, depending on the disinfectant, the membranes are facing different remaining precursors after reaction with either chlorine or chloramines. Those precursors might be retained to a different extent. Research needs to assess which disinfectant leads to lowest DBP formation after filtration in the final treated water. A balance between relevant precursor removal and amount of DBPs formed has to be established. This also has to be seen in the context of their individual toxicity. Bromine- and iodine-containing DBPs have been found to be more toxic than their chlorinated counterparts (Richardson et al., 2007). This is important because NF filtration was shown to increase the Br/DOC ratio (Ates et al., 2009), which, in turn, could lead to a higher bromine level or even iodine incorporation into the DBPs formed on the permeate side. Hence, not only the individual DBPs but also total organic halogen groupings should be evaluated. Also, depending on the disinfectant, few or more bromine- and iodine-containing DBPs will be formed.

An opportunity and necessity for future research involves the understanding of disinfectant-dependent DBP precursor removal and the ability to assess the impact of final disinfection on the DBP concentration and speciation in membrane permeate. Because of the higher DOC rejection compared to the halide ions Br⁻ and I⁻, DBP speciation could potentially shift to the more toxic bromine- and iodine-containing DBPs. This research is of particular interest for NF membranes because of their larger pore size compared to RO membranes.

◆ Is there a simple-to-analyze DBP surrogate?

The literature has suggested boron as a surrogate for NDMA rejection by RO membranes as it can be easily measured using conventional analytical techniques (ion chromatography) or online probes (Tu et al., 2013). As with NDMA, halogenated volatile DBP analysis requires skilled staff and special equipment. Hence, there is a high analytical cost and considerable time involvement to obtain the desired results. A good surrogate should be similar in size, preferably a bit smaller, possess the same charge, and be removed by the same mechanism. Surrogates are of interest for the poorly removed DBPs including THMs, DHANs, and I-THMs. Their removal mechanisms do not solely depend on size exclusion but also on their interaction with the membrane because of their intrinsic hydrophobicity and polar properties. A possible surrogate needs to be small and embrace polar and hydrophobic properties. In addition, it also has to be dependent on operating conditions. However, the three DBP groups react differently to changes in the permeate flux. Therefore, it might be difficult to find a surrogate covering all three groups, and the focus should be on a specific group. Because of their polar properties, the DHANs show a good correlation to the rejection behavior of salt across a range of crossflow velocities (0.04–0.16 m/s), a flux range (3–55 L/m²h), and temperature (23–36° C) (Figure 6.1).

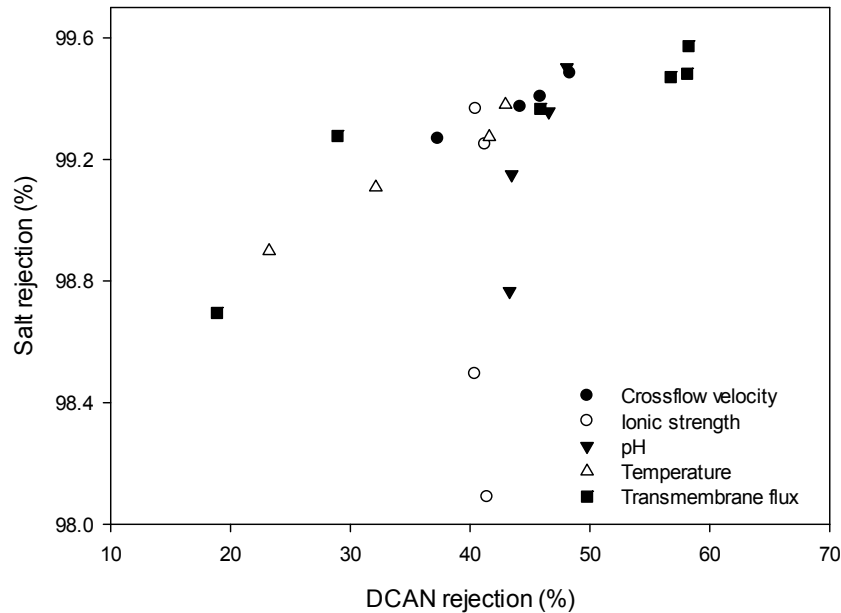


Figure 6.1. DCAN rejection in relation to salt rejection across the RO membrane at varying crossflow velocities (0.04–0.16 m/s), flux range (3–55 L/m²h), temperatures (23–36° C), pH (4.5–8.5), and ionic strength (7–70 mM).

The good correlation may not be widely applicable as those measurements were carried out with membrane coupons in virgin state. Besides operational parameters, salt rejection can also be affected by the age of the membrane surface and most notably by scaling.

DCAN and BDCM themselves appear to be good surrogate measures to monitor RO membrane performance in terms of DBP rejection. Both are not well rejected and have hydrophobicity and polarity properties. In addition, these two DBPs are likely to be found at a sufficiently high concentration in the chloraminated feed and membrane permeate to determine their rejection. For the NF membranes, these DBPs are not applicable as BDCM is not rejected and DCAN only rejected as low as 10%. Therefore, a different set of compounds that have a sufficiently high rejection with similar properties and occurrence need to be identified.

References

- Agenson, K. O.; Urase, T. Change in membrane performance due to organic fouling in nanofiltration (NF)/reverse osmosis (RO) applications. *Sep. Purif. Technol.* **2007**, *55* (2), 147–156.
- Agus, E.; Sedlak, D. L. Formation and fate of chlorination by-products in reverse osmosis desalination systems. *Water Res.* **2010**, *44* (5), 1616–1626.
- Almedeij, J.; Aljarallah, R. Seasonal variation pattern of monthly wastewater influent. *J. Environ. Eng.* **2011**, *137* (5), 332–339.
- Amjad, Z. *Reverse Osmosis: Membrane Technology, Water Chemistry and Industrial Applications*. Van Nostrand Reinhold: New York, 1993.
- Amy, G.; Siddiqui, M.; Zhai, W.; DeBroux, J.; Odem, W. *Survey of bromide in drinking water and impacts on DBP formation*. AWWA Research Foundation and AWWA: Denver, CO, 1994.
- Andrews, J. E.; Nichols, H. P.; Schmid, J. E.; Mole, L. M.; Hunter, E. S.; Klinefelter, G. R. Developmental toxicity of mixtures: The water disinfection by-products dichloro-, dibromo- and bromochloro acetic acid in rat embryo culture. *Reprod. Toxicol.* **2004**, *19* (1), 111–116.
- Antony, A.; Fudianto, R.; Cox, S.; Leslie, G. Assessing the oxidative degradation of polyamide reverse osmosis membrane—Accelerated ageing with hypochlorite exposure. *J. Membr. Sci.* **2010**, *347* (1–2), 159–164.
- APHA. *Standard Methods for the Examination of Waste and Wastewater*, 19th ed.; American Public Health Association: New York, 1999.
- Arsuaga, J. M.; López-Muñoz, M. J.; Aguado, J.; Sotto, A. Temperature, pH and concentration effects on retention and transport of organic pollutants across thin-film composite nanofiltration membranes. *Desalination* **2008**, *221* (1–3), 253–258.
- Ates, N.; Yilmaz, L.; Kitis, M.; Yetis, U. Removal of disinfection by-product precursors by UF and NF membranes in low-SUVA waters. *J. Membr. Sci.* **2009**, *328* (1–2), 104–112.
- Avlonitis, S.; Hanbury, W. T.; Boudinar, M. B. Spiral wound modules performance. An analytical solution, Part I. *Desalination* **1991**, *81* (1–3), 191–208.
- Ayache, C.; Pidou, M.; Gernjak, W.; Poussade, Y.; Croué, J.-P.; Tazi-Pain, A.; Keller, J. Characterization of secondary treated effluents for tertiary membrane filtration and water recycling. *J. Water Reuse and Desalination* **2012**, *2* (2), 74–83.
- Bargeman, G.; Vollenbroek, J. M.; Straatsma, J.; Schroën, C. G. P. H.; Boom, R. M. Nanofiltration of multi-component feeds. Interactions between neutral and charged components and their effect on retention. *J. Membr. Sci.* **2005**, *247* (1–2), 11–20.
- Beckwith, R. C.; Margerum, D. W. Kinetics of hypobromous acid disproportionation. *Inorg. Chem.* **1997**, *36* (17), 3754–3760.
- Bellona, C.; Drewes, J. E.; Xu, P.; Amy, G. Factors affecting the rejection of organic solutes during NF/RO treatment—A literature review. *Water Res.* **2004**, *38*, 2795–2809.
- Bellona, C.; Drewes, J. E. (2005). The role of membrane surface charge and solute physico-chemical properties in the rejection of organic acids by NF membranes. *J. Membr. Sci.* **2005**, *249*, 227–234.
- Ben-David, A.; Basson, S.; Oren, Y.; Freger, V. Mechanism and role of partitioning in removal of organics by RO and NF composite membranes. *Desalination* **2006**, *199*, 49–51.
- Ben Amar, N.; Saidani, H.; Deratani, A.; Palmeri, J. Effect of temperature on the transport of water and neutral solutes across nanofiltration membranes. *Langmuir* **2007**, *23* (6), 2937–2952.

- Brereton, R.G. *Chemometrics: Data Analysis for the Laboratory and Chemical Plant*; John Wiley & Sons: Sussex, UK, **2003**.
- Berg, P.; Hagemeyer, G.; Gimbel, R. Removal of pesticides and other micro-pollutants by nanofiltration. *Desalination* **1997**, *113*, 205–208.
- Bergman, R. *Reverse osmosis and nanofiltration*. American Water Works Association: Denver, CO, 2007.
- Bichsel, Y.; Von Gunten, U. Oxidation of iodide and hypiodous acid in the disinfection of natural waters. *Environ. Sci. Technol.* **1999**, *33* (22), 4040–4045.
- Bichsel, Y.; Von Gunten, U. (2000). Formation of iodo-trihalomethanes during disinfection and oxidation of iodide-containing waters. *Environ. Sci. Technol.* **2000**, *34*, 2784–2791.
- Bieber, T. I.; Trehy, M. L. *Dihaloacetonitriles in chlorinated natural waters*. Ann Arbor Science: Ann Arbor, MI, 1983.
- Bousher, A.; Brimblecombe, P.; Midgley, D. Bromate production in chlorinated waters: Reaction of monochloramine and hypobromite. *Water Res.* **1990**, *24* (10), 1285–1294.
- Braeken, L.; Ramaekers, R.; Zhang, Y.; Maes, G.; Van der Broggen, B.; Vandecasteele, C. Influence of hydrophobicity on retention in nanofiltration of aqueous solutions containing organic compounds. *J. Membr. Sci.* **2005**, *252*, 195–203.
- Cancho, B.; Ventura, F.; Galceran, M.-T. Simultaneous determination of cyanogen chloride and cyanogen bromide in treated water at sub-mg/L levels by a new solid-phase microextraction–gas chromatographic–electron-capture detection method. *J. Chromatogr. A* **2000**, *897* (1–2), 307–315.
- Cantor, K. P.; Villanueva, C. M.; Silverman, D. T.; Figueroa, J. D.; Real, F. X.; Garcia-Closas, M.; Malats N.; Chanock, S.; Yeager, M.; Tardon, A. Polymorphisms in GSTT1, GSTZ1, and CYP2E1, disinfection by-products, and risk of bladder cancer in Spain. *Environ. Health Perspect.* **2010**, *118* (11), 1545–1550.
- Cemeli, E.; Wagner, E. D.; Anderson, D.; Richardson, S. D.; Plewa, M. J. Modulation of the cytotoxicity and genotoxicity of the drinking water disinfection byproduct iodoacetic acid by suppressors of oxidative stress. *Environ. Sci. Technol.* **2006**, *40* (6), 1878–1883.
- Chalatip, R.; Chawalit, R.; Nopawan, R. Removal of haloacetic acids by nanofiltration. *J. Environ. Sci.* **2009**, *21* (1), 96–100.
- Chellam, S.; Taylor, J. S. Simplified analysis of contaminant rejection during ground- and surface water nanofiltration under the information collection rule. *Water Research* **2001**, *35* (10), 2460–2474.
- ChemAxon. *Molecular Properties Modelling* [computer software]. Budapest, Hungary, 2015. Retrieved from <https://www.chemaxon.com/>
- ChemBioUltra3D. *ChemoOffice 15.0* [computer software]. Perkin Elmer: Waltham, MA. Retrieved from <https://www.cambridgesoft.com/software/overview.aspx>
- Chen, B.; Lee, W. Solar photolysis kinetics of disinfection byproducts. *Water Res.* **2010**, *44* (11), 3401–3409
- Chen, C.; Han, B.; Westerhoff, P. K.; Krasner, S. W.; Herckes, P. A new model on the diffusion of small molecule penetrants in dense polymer membranes. *J. Membr. Sci.* **2001**, *187*, 109–118.
- Childress, A. E.; Elimelech, M. Effect of solution chemistry on the surface charge of polymeric reverse osmosis and nanofiltration membranes. *J. Membr. Sci.* **1996**, *199*, 253–268.
- Cimetiere, N.; Dossier-Berne, F.; De Laat, J. Effect of some parameters on the formation of chloroform during chloramination of aqueous solutions of resorcinol. *Water Res.* **2010**, *44* (15), 4497–4504.
- Clifford, J. *Water, a comprehensive treatise*. Plenum Press: New York, 1975.
- Coleman, T. F.; Li, Y. An interior, trust region approach for nonlinear minimization subject to bounds. *SIAM J. Optimiz.* **1996**, *6*, 418–445.

- Cowman, G. A.; Singer, P. C. Effect of bromide ion on haloacetic acid speciation resulting from chlorination and chloramination of aquatic humic substances. *Environ. Sci. Technol.* **1996**, *30* (1), 16–24.
- Croue, J. P.; Reckhow, D. A. Destruction of chlorination byproducts with sulfite. *Environ. Sci. Technol.* **1989**, *23* (11), 1412–1419.
- Dabrowska, A.; Nawrocki, J. Controversies about the occurrence of chloral hydrate in drinking water. *Water Res.* **2009**, *43*, 2201–2208.
- Deborde, M.; von Gunten, U. Reactions of chlorine with inorganic and organic compounds during water treatment—Kinetics and mechanisms: A critical review. *Water Res.* **2008**, *42*, 13–51.
- Déon, S.; Dutournié, P.; Fievet, P.; Limousy, L.; Bourseau, P. Concentration polarization phenomenon during the nanofiltration of multi-ionic solutions: Influence of the filtrated solution and operating conditions. *Water Res.* **2013**, *47* (7), 2260–2272.
- Deshmukh, S. S.; Childress, A. E. Zeta potential of commercial RO membranes: Influence of source water type and chemistry. *Desalination* **2001**, *140*, 87–95.
- Diehl, A. C.; Speitel, J. G. E.; Symons, J. M.; Krasner, S. W.; Hwang, C. J.; Barrett, S. E. DBP formation during chloramination. *J. Amer. Water Works Assoc.* **2000**, *92* (6), 76–90.
- Donose, B. C.; Sukumar, S.; Pidou, M.; Poussade, Y.; Keller, J.; Gernjak, W. Effect of pH on the ageing of reverse osmosis membranes upon exposure to hypochlorite. *Desalination* **2013**, *309* (0), 97–105.
- Dotson, A. D.; Westerhoff, P.; Chen, B.; Lee, W. Organic nitrogen occurrence and characterization. Disinfection by-products in drinking water. *American Chem. Society* **2008**, *995*, 274–288.
- Drewes, J. E.; Bellona, C.; Oedekoven, M.; Xu, Y.; Kim, T.-U.; Amy, G. Rejection of wastewater-derived micropollutants in high-pressure membrane applications leading to indirect potable reuse. *Environ. Prog.* **2005**, *24* (4), 400–407.
- Elimelech, M.; Chen, W. H.; Waypa, J. J. Measuring the zeta (electrokinetic) potential of reverse osmosis membranes by a streaming potential analyzer. *Desalination* **1994**, *95* (3), 269–286.
- Estimation Program Interface (EPI)*, Suite 4.11 [Computer software]. Syracuse Research Corporation: Syracuse, NY, 2012. Retrieved from <http://www.epa.gov/oppt/exposure/pubs/episuite.htm>
- Eriksson, L. *Design of experiments: Principles and applications*. Umetrics AB: Malmö, Sweden, 2008.
- Escoda, A.; Fievet, P.; Lakard, S.; Szymczyk, A.; Déon, S. Influence of salts on the rejection of polyethyleneglycol by an NF organic membrane: Pore swelling and salting-out effects. *J. Membr. Sci.* **2010**, *347* (1–2), 174–182.
- Farré, M. J.; Döderer, K.; Hearn, L.; Poussade, Y.; Keller, J.; Gernjak, W. Understanding the operational parameters affecting NDMA formation at Advanced Water Treatment Plants. *J. Hazard. Mater.* **2011**, *185* (2–3), 1575–1581.
- Farré, M. J.; Radjenovic, J.; Gernjak, W. Assessment of degradation byproducts and NDMA formation potential during UV and UV/H₂O₂ treatment of doxylamine in the presence of monochloramine. *Environ. Sci. Technol.* **2012**, *46* (23), 12904–12912.
- Field, A. *Discovering statistics using SPSS*. Sage: London, UK, 2005.
- Freger, V.; Gilron, J.; Belfer, S. TFC polyamide membranes modified by grafting of hydrophilic polymers: An FT-IR/AFM/TEM study. *J. Membr. Sci.* **2002**, *209* (1), 283–292.
- Fuge, R.; Johnson, C. C. The geochemistry of iodine—A review. *Environ. Geochem. Health* **1986**, *8* (2), 31–54.
- Fujioka, T.; Khan, S. J.; McDonald, J. A.; Roux, A.; Poussade, Y.; Drewes, J. E.; Nghiem, L. D. N-nitrosamine removal by reverse osmosis for indirect potable water reuse—A critical review based on observations from laboratory-, pilot- and full-scale studies. *Sep. Purif. Technol.* **2012a**, *98*, 503–515.

- Fujioka, T.; Nghiem, L. D.; McDonald, J. A.; Roux, A.; Poussade, Y.; Drewes, J. E.; Nghiem, L. D. Effects of feed solution characteristics on the rejection of N-nitrosamines by reverse osmosis membranes. *J.Membr. Sci.* **2012b**, *409–410*, 66–74.
- Fujioka, T.; Khan, S. J.; McDonald, J. A.; Roux, A.; Poussade, Y.; Drewes, J. E.; Nghiem, L. D. N-nitrosamine rejection by nanofiltration and reverse osmosis membranes: The importance of membrane characteristics. *Desalination* **2013a**, *316*, 67–75.
- Fujioka, T.; Khan, S. J.; McDonald, J. A.; Roux, A.; Poussade, Y.; Drewes, J. E.; Nghiem, L. D. N-nitrosamine rejection by reverse osmosis membranes: A full-scale study. *Water Res.* **2013b**, *15* (16), 6141–6148.
- Gardner, T.; Yeates, C.; Shaw, R. *Purified recycled water for drinking water: The technical issues*. Queensland Water Commission: Brisbane, 2008.
- Gazda, M.; Kumar, K.; Margerum, D. W. Non-metal redox kinetics: Oxidation of bromide ion by nitrogen trichloride. *Inorg. Chem.* **1995**, *34*, 3536–3542.
- Gerrity, D.; Mayer, B.; Ryu, H.; Crittenden, J.; Abbaszadegan, M. A comparison of pilot-scale photocatalysis and enhanced coagulation for disinfection byproduct mitigation. *Water Res.* **2009**, *43*, 1597–1610.
- Glezer, V.; Harris, B.; Tal, N.; Iosefzon, B.; Lev, O. Hydrolysis of haloacetonitriles: Linear free energy relationship, kinetics and products. *Water Res.* **1999**, *33* (8), 1938–1948.
- Gould, J. P.; Fitchorn, L. E.; Urheim, E. *Formation of brominated trihalomethanes: Extent and kinetics*. Ann Arbor Science: Ann Arbor, MI, 1983.
- Hair, J. F. J.; Anderson, R. E.; Tatham, R. L.; Black, W. C. *Multivariate data analysis*. MacMillan: New York, 1995.
- Hammer, M. U.; Anderson, T. H.; Chaimovich, A.; Shell, M. S.; Israelachvili, J. The search for the hydrophobic force law. *Faraday Discuss.* **2010**, *146*, 299–308.
- Hu, J.; Song, H.; Karanfil, T. Comparative analysis of halonitromethane and trihalomethane formation and speciation in drinking water: The effects of disinfectants, pH, bromide, and nitrite. *Environ. Sci Technol.* **2010**, *44* (2), 794–799.
- Hua, G.; Reckhow, D. A. Characterisation of disinfection byproduct precursors based on hydrophobicity and molecular size. *Environ. Sci. Technol.* **2007**, *41*, 3309–3315.
- Hua, G.; Reckhow, D. A. DBP formation during chlorination and chloramination: Effect of reaction time, pH, dosage, and temperature. *J. Amer. Water Works Assoc.* **2008**, *100* (8), 82–95.
- Hua, G.; Reckhow, D. A. Evaluation of bromine substitution factors of DBPs during chlorination and chloramination. *Water Res.* **2012**, *46* (13), 4208–4216.
- Hua, G.; Reckhow, D. A.; Kim, J. Effect of bromide and iodide ions on the formation and speciation of disinfection byproducts during chlorination. *Environ. Sci. Technol.* **2006**, *40* (9), 3050–3056.
- Huang, D. M.; Chandler, D. The hydrophobic effect and the influence of solute–solvent attractions. *J. Phys. Chem. B* **2002**, *106* (8), 2047–2053.
- Huang, H.; Wu, Q.-Y.; Chandler, D. Dichloroacetonitrile and dichloroacetamide can form independently during chlorination and chloramination of drinking waters, model organic matters, and wastewater effluents. *Environ. Sci. Tech.* **2012**, *46* (19), 10624–10631.
- Israelachvili, J.; Pashley, R. The hydrophobic interaction is long range, decaying exponentially with distance. *Nature* **1982**, *300*, 341–342.
- Itoh, S.; Gordon, B. A.; Callan, P.; Bartram, J. Regulations and perspectives on disinfection by-products: Importance of estimating overall toxicity. *J. Water Supply Res. T.* **2011**, *60* (5), 261–274.
- Jafvert, C. T.; Valentine, R. L. Reaction scheme for the chlorination of ammoniacal water. *Environ. Sci. Technol.* **1992**, *26* (3), 577–586.

- Jolley, R. L.; Carpenter, J. H. *Aqueous chemistry of chlorine: chemistry, analysis, and environmental fate of reactive oxidant species*. Oak Ridge National Laboratory, Chemical Technology Division: Springfield, VA, 1982.
- Joo, S. H.; Mitch, W. A. Nitrile, aldehyde, and halonitroalkane formation during chlorination/chloramination of primary amines. *Environ. Sci. Technol.* **2007**, *41* (4), 1288–1296.
- Kamide, K.; Iijima, H. *Recent advances in cellulose membranes*. Carl Hanser Verlag: Munich, Germany, 1994.
- Kargalioglu, Y.; McMillan, B. J.; Minear, R. A.; Plewa, M. J. Analysis of the cytotoxicity and mutagenicity of drinking water disinfection by-products in *Salmonella typhimurium*. *Teratogen Carcin. Mut.* **2002**, *22* (2), 113–128.
- Kedem, O.; Katchalsky, A. Permeability of composite membranes. Part 1. Electric current, volume flow and flow of solute through membranes. *T. Faraday Soc.* **1963**, *59* (0), 1918–1930.
- Kim, H. I.; Kim, S. S. Plasma treatment of polypropylene and polysulfone supports for thin film composite reverse osmosis membrane. *J. Membr. Sci.* **2006**, *286*, 193.
- Kim, T.-U.; Drewes, J. E.; Scott Summers, R.; Amy, G. L. Solute transport model for trace organic neutral and charged compounds through nanofiltration and reverse osmosis membranes. *Water Res.* **2007**, *41* (17), 3977–3988.
- Kimura, K.; Amy, G.; Drewes, J. E.; Watanabe, Y. Adsorption of hydrophobic compounds onto NF/RO membranes: An artifact leading to overestimation of rejection. *J. Membr. Sci.* **2003**, *221* (1–2), 89–101
- Kirmeyer, G. J. *Optimizing chloramine treatment*. AWWA Research Foundation: Denver, CO, 2004.
- Kiso, Y. Factors affecting adsorption of organic solutes on cellulose in an aqueous solution system. *Chromatographia* **2001**, *2* (1), 55–58.
- Kiso, Y.; Kitao, T.; Jinno, K.; Miyagi, M. The effects of molecular width on permeation of organic solute through cellulose acetate reverse osmosis membranes. *J. Membr. Sci.* **1992**, *74* (1/2), 95–103.
- Kiso, Y.; Nishimura, Y.; Kitao, T.; Nishimura, K. Rejection properties of non-phenylic pesticides with nanofiltration membranes. *J. Membr. Sci.* **2000**, *171*, 229–237.
- Kiso, Y.; Kon, T.; Kitao, T.; Nishimura, K. Rejection properties of alkyl phthalates with nanofiltration membranes. *J. Membr. Sci.* **2001**, *182*, 205–214.
- Kokkoli, E.; Zukoski, C. F. Interactions between hydrophobic self-assembled monolayers. effect of salt and the chemical potential of water on adhesion. *Langmuir* **1998**, *14*, 1189–1195.
- Košutic, K.; Kaštelan-Kunst, L.; Kunst, B. Porosity of some commercial reverse osmosis and nanofiltration polyamide thin-film composite membranes. *J. Membr. Sci.* **2000**, *168*, 101–108.
- Krasner, S. W.; McGuire, M. J.; Jacangelo, J. G.; Patania, N. L.; Reagan, K. M.; Aieta, E. M. The occurrence of disinfection by-products in U.S. drinking water. *J. Amer. Water Works Assoc.* **1989**, *81* (8), 41–53.
- Krasner, S. W.; Croué, J.-P.; Buffle, J.; Perdue, E. M. Three approaches for characterizing NOM. *J. Am. Water Works Assoc.* **1996**, *88* (6), 66–79.
- Krasner, S. W.; Weinberg, H. S.; Richardson, S. D.; Pastor, S. J.; Chinn, R.; Scilimenti, M. J.; Onstad, G. D.; Thruston, A. D. Occurrence of a new generation of disinfection by-products. *Environ. Sci. Technol.* **2006**, *40* (23), 7175–7185.
- Krasner, S. W.; Westerhoff, P.; Amy, G.; Nam, S.-N.; Chowdhury, Z. K.; Sinha, S.; Rittman, B. E. *Contribution of wastewater to DBP formation*. Water Research Foundation and American Water Works Association: Denver, CO, 2008.

- Krasner, S. W.; Westerhoff, P.; Chen, B.; Rittmann, B. E.; Amy, G. Occurrence of disinfection byproducts in United States wastewater treatment plant effluents. *Environ. Sci. Technol.* **2009a**, *43* (21), 8320–8325.
- Krasner, S. W. The formation and control of emerging disinfection by-products of health concern. *Philos. T. R. Soc. A.* **2009**, *367*, 4077–4095.
- Krasner, S. W.; Westerhoff, P.; Chen, B.; Rittmann, B. E.; Nam, S.; Amy, G. Impact of wastewater treatment processes on organic carbon, organic nitrogen, and DBP precursors in effluent organic matter. *Environ. Sci. Technol.* **2009b**, *43* (8), 2911–2918.
- Krestov, G. A. *Thermodynamics of solvation: Solution and dissolution, ions and solvents, structure and energetics*. Ellis Horwood: New York, 1991.
- Kristiana, I. Disinfection by-products in chlorinated and chloraminated potable water systems: Effects of precursors and environmental factors. Ph.D. Thesis, Curtin University of Technology, Bentley, Perth, Australia, 2007.
- Kumar, K.; Margerum, D. W. Kinetics and mechanism of general-acid-assisted oxidation of bromide by hypochlorite and hypochlorous acid. *Inorg. Chem.* **1987**, *26* (16), 2706–2711.
- Kumar, K.; Day, R. A.; Margerum, D. W. Atom-transfer redox kinetics: General-acid-assisted oxidation of iodide by chloramines and hypochlorite. *Inorg. Chem.* **1986**, *25*, 4344–4350.
- Kwon, Y.-N.; Leckie, J. O. Hypochlorite degradation of crosslinked polyamide membranes: I. Changes in chemical/morphological properties. *J. Membr. Sci.* **2006**, *283* (1–2), 21–26.
- Lee, W.; Westerhoff, P.; Esparza-Soto, M. Occurrence and removal of dissolved organic nitrogen in U.S. water treatment plants. *J. Amer. Water Works Assoc.* **2006**, *98* (10), 102–110.
- Lee, W.; Westerhoff, P.; Croué, J.-P. Dissolved organic nitrogen as a precursor for chloroform, dichloroacetonitrile, N-nitrosodimethylamine, and trichloronitromethane. *Environ. Sci. Tech.* **2007**, *41* (15), 5485–5490.
- Leong, L.Y.C.; Kuo, J.; Tang, C.-C. *Disinfection of wastewater effluent—Comparison of alternative technologies*. Water Environment Research Foundation: Alexandria, VA, **2008**
- Liang, L.; Singer, P. C. Factors influencing the formation and relative distribution of haloacetic acids and trihalomethanes in drinking water. *Environ. Sci. Technol.* **2003**, *37* (13), 2920–2928.
- Libotean, D.; Giralt, J.; Rallo, R.; Cohen, Y.; Giralt, F.; Ridgway, H. F.; Rodriguez, G.; Phipps, D. . Organic compounds passage through RO membranes. *J. Membr. Sci.* **2008**, *313* (1–2), 23–43.
- Linge, K. L.; Blythe, J. W.; Buseti, F.; Blair, P.; Rodriguez, C.; Heitz, A. Formation of halogenated disinfection by-products during microfiltration and reverse osmosis treatment: Implications for water recycling. *Sep. Purif. Technol.* **2013**, *104* (0), 221–228.
- López-Muñoz, M. J.; Sotto, A.; Arsuaga, J. M.; Van der Bruggen, B. Influence of membrane, solute and solution properties on the retention of phenolic compounds in aqueous solution by nanofiltration membranes. *Sep. Purif. Technol.* **2009**, *66* (1), 194–201.
- Luck, W. Contributions to the desalination membrane mechanism by studies of interactions in aqueous solutions and in polymer hydration. *Desalination* **1987**, *62*, 19–35.
- Lundstedt, T.; Seifert, E.; Abramo, L.; Thelin, B.; Nyström, Å.; Pettersen, J.; Bergman, R. Experimental design and optimization. *Chemometr. Intell. Lab.* **1998**, *42* (1–2), 3–40.
- Luong, T.; Peters, C.; Perry, R. Influence of bromide and ammonia upon the formation of trihalomethanes under water-treatment conditions. *Environ. Sci. Technol.* **1982**, *16*, 473–479.
- Mabey, W.; Mill, T. Critical review of hydrolysis of organic compounds in water under environmental conditions. *J. Phys. Chem. Ref. Data* **1978**, *7* (2), 383–416.

- Magazinovic, R. S.; Nicholson, B. C.; Mulcahy, D. E.; Davey, D. E. Bromide levels in natural waters: its relationship to levels of both chloride and total dissolved solids and the implications for water treatment. *Chemosphere* **2004**, *57* (4), 329–335.
- Mane, P. P.; Park, P.-K.; Hyung, H.; Brown, J. C.; Kim, J.-H. Modeling boron rejection in pilot- and full-scale reverse osmosis desalination processes. *J. Membr. Sci.* **2009**, *338* (1–2), 119–127.
- Matsuura, T.; Sourirajan, S. Physicochemical criteria for reverse osmosis separation of alcohols, phenols, and monocarboxylic acid in aqueous solutions using porous cellulose acetate membranes. *J. Appl. Polym. Sci.* **1971**, *15* (12), 2905–2927.
- McDonald, T. A.; Komulainen, H. Carcinogenicity of the chlorination disinfection by-product MX. *J. Environ. Health* **2005**, *23*, 163–241.
- Meares, P. *The physical chemistry of transport and separation by membranes*. Elsevier: Amsterdam, Holland, 1976.
- Merlet, N.; Thibaud, H.; Dore, M. Chloropicrin formation during oxidative treatments in the preparation of drinking water. *Sci. Total Environ.* **1985**, *47*, 223–228.
- Meyer, E. E.; Rosenberg, K. J.; Israelachvili, J. Recent progress in understanding hydrophobic interactions. *Biophysics* **2006**, *103* (43), 15739–15746.
- Michaud, D. S.; Kogevinas, M.; Cantor, K. P.; Villanueva, C. M.; Garcia-Closas, M.; Rothman, N.; Malats, N.; Real, F. X.; Serra, C.; Garcia-Closas, R. Total fluid and water consumption and the joint effect of exposure to disinfection by-products on risk of bladder cancer. *Environ. Health Perspect.* **2007**, *115* (11), 1569–1572.
- Mitch, W. A.; Krasner, S.; Westerhoff, P.; Dotson, A. *Occurrence and formation of nitrogenous disinfection by-products*. Water Research Foundation: Denver, CO, 2009.
- Miyake, Y. Freezing point, osmotic pressure, boiling point and vapor pressure of seawater. *B. Chem. Soc. Jpn.* **1939**, *14*, 58–62.
- Morris, J. C.; Isaac, R. A. *A critical review of kinetic and thermodynamic constants for the aqueous chlorine-ammonia system*. Ann Arbor Science: Ann Arbor, MI, 1983.
- Muellner, M. G.; Wagner, D.; McCalla, K.; Richardson, S. D.; Woo, Y. T.; Plewa, M. J. Haloacetonitriles vs. regulated haloacetic acids: Are nitrogen-containing DBPs more toxic? *Environ. Sci. Technol.* **2007**, *41* (2), 645–651.
- Mulder, M. *Basic principles of membrane technology*. Kluwer Academic: Dordrecht, the Netherlands, 1991.
- Munch, D. J.; Munch, J. W.; Pawlecki, A. M. *Determination of haloacetic acids and dalapon in drinking water by liquid-liquid extraction, derivatization and gas chromatography with electron capture detection*, Method 552.2, EPA/600/R-95-131. Environmental Protection Agency: Washington, DC, 1995.
- Munch, J. W.; Bassett, M. V. *Method development for the analysis of N-nitrosodimethylamine and other N-nitrosamines in drinking water at low nanogram/liter concentrations using solid-phase extraction and gas chromatography with chemical ionization tandem mass spectrometry*, Method 521, EPA/600/R-05/054. Environmental Protection Agency: Washington, DC, 2004.
- Nagy, J. C.; Kumar, K.; Margerum, D. W. Non-metal redox kinetics: Oxidation of iodide by hypochlorous acid and by nitrogen trichloride measured by the pulsed-accelerated-flow method. *Inorg. Chem.* **1988**, *27*, 2773–2780.
- Nakao, S.-I.; Kimura, S. Models of membrane transport phenomena and their applications for ultrafiltration data. *J. Chem. Eng. of Jpn.* **1982**, *15* (3), 200–205.
- Neale, P. A.; Antony, A.; Bartkow, M. E.; Farré, M. J.; Heitz, A.; Kristiana, I.; Tang, J. Y. M.; Escher, B. I. Bioanalytical assessment of the formation of disinfection byproducts in a drinking water treatment plant. *Environ. Sci. Technol.* **2012**, *46* (18), 10317–10325.

- Nghiem, L. D.; Schäfer, A. I. Adsorption and transport of trace contaminant estrone in NF/RO membranes. *Environ. Eng. Sci.* **2002**, *19* (6), 441–451.
- Nghiem, L. D.; Coleman, P. J. NF/RO filtration of the hydrophobic ionogenic compound triclosan: Transport mechanisms and the influence of membrane fouling. *Sep. Purif. Technol.* **2008**, *62*, 709–716.
- Nghiem, L. D.; Schäfer, A. I.; Waite, T. D. Adsorptive interactions between membranes and trace contaminants. *Desalination* **2002**, *147*, 269–274.
- Nghiem, L. D.; Schäfer, A. I.; Elimelech, M. Removal of natural hormones by nanofiltration membranes: Measurement, modeling, and mechanisms. *Environ. Sci. Technol.* **2004**, *38*, 1888–1896.
- Nghiem, L. D.; Schäfer, A. I.; Elimelech, M. Pharmaceutical retention mechanisms by nanofiltration membranes. *Environ. Sci. Technol.* **2005**, *39* (19), 7698–7705.
- Nieuwenhuijsen, M. J.; Toledano, M. B.; Eaton, N. E.; Fawell, J.; Elliott, P. Chlorination disinfection byproducts in water and their association with adverse reproductive outcomes: a review. *Occup. Environ. Med.* **2000**, *57*, 73–85.
- Nikolaou, A. D.; Lekkas, T. D.; Kostopoulou, M. N.; Goufopoulos, S. K. Investigation of the behaviour of haloketones in water samples. *Chemosphere* **2001**, *44* (5), 907–912.
- Nilsson, M.; Trägårdh, G.; Östergren, K. The influence of different kinds of pre-treatment on the performance of a polyamide nanofiltration membrane. *Desalination* **2006**, *195* (1–3), 160–168.
- Ning, R. Y.; Troyer, T. L. Colloidal fouling of RO membranes following MF/UF in the reclamation of municipal wastewater. *Desalination* **2007**, *208* (1–3), 232–237.
- Nunes, S. P.; Peinemann, K. V. *Membrane technology in the chemical industry*. Wiley & Sons: Weinheim, Germany, 2010.
- Obolensky, A.; Singer, P. C. Halogen substitution patterns among disinfection byproducts in the information collection rule database. *Environ. Sci. Technol.* **2005**, *39* (8), 2719–2730.
- Ohanian, E. V.; Mullin, C. S.; Orme, J. Health effects of disinfectants and disinfection by-products: A regulatory perspective. *Water chlorination: Chemistry environmental impact health effects*, Vol. 6, **1989**, 75–86.
- Ohnishi, S.; Yaminsky, V. V.; Christenson, H. K. Measurements of the force between fluorocarbon monolayer surfaces in air and water. *Langmuir* **2000**, *16* (22), 8360–8367.
- Oliver, B. G. Dihaloacetonitriles in drinking water: Algae and fulvic acid as precursors. *Environ. Sci. Technol.* **1983**, *17* (2), 80–83.
- Ong, S. L.; Zhou, W.; Song, L.; Ng, W. J. Evaluation of feed concentration effects on salt/ion transport through RO/NF membranes with the Nernst-Planck-Donnan model. *Environ. Eng. Sci.* **2002**, *19* (6), 429–439.
- Orvik, J. A. Kinetics and mechanism of nitromethane chlorination. A new rate expression. *J. Am. Chem. Soc.* **1980**, *102* (2), 740–743.
- Ozaki, H.; Li, H. Rejection of organic compounds by ultra-low pressure reverse osmosis membrane. *Water Res.* **2002**, *36*, 123–130.
- Pan, Y.; Jackson, R. T. Ethnic difference in the relationship between acute inflammation and serum ferritin in U.S. adult males. *Epidemiol. Infect.* **2008**, *136*, 421–431.
- Peeters, J. M. M.; Boom, J. P.; Mulder, M. H. V.; Strathmann, H. Retention measurements of nanofiltration membranes with electrolyte solutions. *J. Membr. Sci.* **1998**, *145*, 199–209.
- Petersen, R. J. Composite reverse osmosis and nanofiltration membranes. *J. Membr. Sci.* **1993**, *83*, 81–150.
- Pinnekamp, J.; Friedrich, H. (Eds.) *Membrane technology for waste water treatment*. RWTH Aachen University: Aachen, Germany, 2003.

- Plewa, M. J.; Wagner, E. D.; Richardson, S. D.; Thruston, A. D., Jr.; Woo, Y.-T.; McKague, B. Chemical and biological characterization of newly discovered iodoacid drinking water disinfection byproducts. *Environ. Sci. Technol.* **2004**, *38* (18), 4713–4722.
- Plewa, M. J.; Muellner, M. G.; Richardson, S. D.; Fasano, F.; Buettner, K. M.; Woo, Y. T.; McKague, A. B.; Wagner, E. D. Occurrence, synthesis, and mammalian cell cytotoxicity and genotoxicity of haloacetamides: An emerging class of nitrogenous drinking water disinfection byproducts. *Environ. Sci. Technol.* **2008a**, *42* (3), 955–961.
- Plewa, M. J.; Wagner, E. D.; Muellner, M. G.; Kang-Mei Hsu; Richardson, S. D. *Comparative mammalian cell toxicity of N-DBPs and C-DBPs*. Disinfection By-Products in Drinking Water: Occurrence, Formation, Health Effects, and Control. ACS Symposium Series: Washington, DC, 2008b.
- Plumlee, M. H.; Lopez-Mesasa, M.; Heidlberger, A.; Ishida, K. P.; Reinhard, M. N-nitrosodimethylamine (NDMA) removal by reverse osmosis and UV treatment and analysis via LC–MS/MS. *Water Res.* **2008**, *42*, 347–355.
- Public Health Regulation*. Office of the Queensland Parliamentary Counsel: Brisbane, Queensland, Australia, 2005.
- Pusch, W. Performance of RO membranes in correlation with membrane structure, transport mechanisms of matter and module design (fouling). State of the art. *Desalination* **1990**, *77*, 35–54.
- Reckhow, D. A.; Singer, P. C. Mechanisms of organic halide formation during fulvic acid chlorination and implications with respect to pre-ozonation. In *Water chlorination: Environmental impact and health effects*; Lewis Publishers: Chelsea, MI, 1985; Vol. 5, pp 1229–1257.
- Reckhow, D. A.; Platt, T. L.; MacNeill, A. L.; McClellan, J. N. Formation and degradation of dichloroacetonitrile in drinking waters. *J. Water Suppl. Res. Technol.* **2001**, *50*, 1–13.
- Richardson, S. D. Drinking water disinfection by-products. In *Encyclopedia of environmental analysis and remediation*; Meyers, R. A., Ed.; Wiley: New York, NY, 1998; Vol. 3, pp 1398–1421.
- Richardson, S. D. Disinfection by-products and other emerging contaminants in drinking water. *Trends in Anal. Chem.* **2003**, *22* (10), 666–684.
- Richardson, S. D.; Thruston, A. D. J.; Rav-Acha, C.; Groisman, L.; Popilevsky, I.; Juraev, O.; Glezer, V.; McKague, A. B.; Plewa, M. J.; Wagner, E. D. Tribromopyrrole, brominated acids, and other disinfection byproducts produced by disinfection of drinking water rich in bromide. *Environ. Sci. Technol.* **2003**, *37* (17), 3782–3793.
- Richardson, S. D.; Plewa, M. J.; Wagner, E. D.; Schoeny, R.; DeMarini, D. M. Occurrence, genotoxicity, and carcinogenicity of regulated and emerging disinfection by-products in drinking water: A review and roadmap for research. *Mutation Res.* **2007**, *636*, 178–242.
- Richardson, S. D.; Fasano, F.; Ellington, J. J.; Crumley, F. G.; Buettner, K. M.; Evans, J. J.; Blount, B. C.; Silva, L. K.; Waite, T. J.; Luther, G. W. Occurrence and mammalian cell toxicity of iodinated disinfection byproducts in drinking water. *Environ. Sci. Technol.* **2008**, *42* (22), 8330–8338.
- Rodriguez, C.; Van Buynder, P.; Lugg, R.; Blair, P.; Devine, B.; Cook, A.; Weinstein, P. Indirect potable reuse: A sustainable water supply alternative. *Int. J. of Environ. Res. Public Health* **2009**, *6*, 1174–1209.
- Rook, J. J. Formation of haloforms during chlorination of natural water. *Water Treat. Examin.* **1974**, *23*, 234–243.
- Ruckenstein, E.; Churaev, N. A possible hydrodynamic origin of the forces of hydrophobic attraction. *J. Coll. Interface Sci.* **1991**, *147*, 535–538.
- Rudel, R. A.; Attfield, K. R.; Schifano, J. N.; Brody, J. G. Chemicals causing mammary gland tumors in animals signal new directions for epidemiology, chemicals testing and risk assessment for breast cancer prevention. *Cancer* **2007**, *109*, 2635–2666.

- Schäfer, A. I.; Nghiem, L. D.; Waite, T. D. Removal of the natural hormone estrone from aqueous solutions using nanofiltration and reverse osmosis. *Environ. Sci. Technol.* **2003**, *37* (1), 182–188.
- Schäfer, A. I.; Akanyeti, I.; Semião, A. J. C. Micropollutant sorption to membrane polymers: A review of mechanisms for estrogens. *Adv. Colloid Interfac.* **2011**, *164* (1–2), 100–117.
- Sclimenti, M.; Hwang, C. J.; Speitel, G. E.; Diehl, A. C. The simultaneous determination of cyanogen chloride and cyanogen bromide in chloraminated waters by a simplified microextraction GC/ECD technique. In *Proceedings of the AWWA Water Quality Technology Conference*. New York, June 19–23, 1994; AWWA: Denver, CO, 1995.
- Sedlak, D. L.; von Gunten, U. The chlorine dilemma. *Science* **2011**, *7*, 42–43.
- Sekino, M. Performance data analysis for hollow-fiber reverse-osmosis modules in seawater desalination plants. *Kagaku Kougaku Ronbunshu* **1994**, *20*, 574–582.
- Semião, A. J. C.; Schäfer, A. I. Removal of adsorbing estrogenic micropollutants by nanofiltration membranes. Part A—Experimental evidence. *J. Membr. Sci.* **2013**, *431* (0), 244–256.
- Senthilmurugan, S.; Ahluwalia, A.; Gupta, S. K. Modeling of a spiral-wound module and estimation of model parameters using numerical techniques. *Desalination* **2005**, *173* (3), 269–286.
- Shah, A. D.; Mitch, W. A. Halonitroalkanes, halonitriles, haloamides, and n-nitrosamines: A critical review of nitrogenous disinfection by-product formation pathways. *Environ. Sci. Technol.* **2012**, *46* (1), 119–131.
- Shan, J. H.; Hu, J. Y.; Ong, S. L. Adsorption of neutral organic fractions in reclaimed water on RO/NF membrane. *Sep. Purif. Technol.* **2009**, *67*, 1–7.
- Sharma, R. R.; Agrawal, R.; Chellam, S. Temperature effects on sieving characteristics of thin-film composite nanofiltration membranes: Pore size distributions and transport parameters. *J. Membr. Sci.* **2003**, *223* (1–2), 69–87.
- Shon, H. K.; Vigneswaran, S.; Snyder, S. A. Effluent organic matter (EfOM) in wastewater: Constituents, effects, and treatment. *Environ. Sci. Technol.* **2006**, *36* (4), 327–374.
- Singer, P. C. Control of disinfection by-products in drinking water. *J. Environ. Eng.* **1994**, *120*, 727–774.
- Singer, P. C. Humic substances as precursors for potentially harmful disinfection byproducts. *Water Sci. Technol.* **1999**, *40*, 25–30.
- Sirivedhin, T.; Gray, K. A. Comparison of the disinfection by-product formation potentials between a wastewater effluent and surface waters. *Water Res.* **2005**, *39*, 1025–1036.
- Snyder, M. P.; Margerum, D. W. Kinetics of chlorine transfer from chloramine to amines, amino acids, and peptides. *Inorg. Chem.* **1982**, *21* (7), 2545–2550.
- Soltanieh, M.; Gill, W. Review of reverse osmosis membranes and transport models. *Chem. Eng. Commun.* **1981**, *12*, 279–236.
- Song, H.; Addison, J. W.; Hu, J.; Karanfil, T. Halonitromethanes formation in wastewater treatment plant effluents. *Chemosphere* **2010**, *79*, 174–179.
- Spiegler, K. S.; Kedem, O. Thermodynamics of hyperfiltration (reverse osmosis): criteria for efficient membranes. *Desalination* **1996**, *1* (4), 311–326.
- Steinle-Darling, E. Rejection of trace organics—nitrosamines, perfluorochemical, and others—via reverse osmosis and nanofiltration. Ph.D. Dissertation, Stanford University, Department of Civil and Environmental Engineering, Stanford, CA, 2008.
- Steinle-Darling, E.; Zedd, M.; Plumlee, M. H.; Ridgway, H. F.; Reinhard, M. Evaluating the impacts of membrane type, coating, fouling, chemical properties and water chemistry on reverse osmosis rejection of seven nitrosoalkylamines, including NDMA. *Water Res.* **2007**, *41* (17), 3959–3967.
- Steinle-Darling, E.; Litwiller, E.; Reinhard, M. Effects of sorption on the rejection of trace organic contaminants during nanofiltration. *Environ. Sci. Technol.* **2010**, *44*, 2592–2598.

- Stevens, A. A.; Moore, L. A.; Miltner, R. J. Formation and control of non-trihalomethane disinfection by-products. *J. Amer. Water Works Assoc.* **1989**, *81* (8), 54–60.
- Stevens A. A.; Slocum C. J.; Seeger D. R.; Robeck C. B. Measurement of THM and precursor concentration changes. *J. Amer. Water Works Assoc.* **1976**, *68*, 546–554.
- Symons, J. M.; Krasner, S. W.; Simms, L. A.; Scilimenti, M. Measurement of THM and precursor concentrations revisited: The effect of bromide ion. *J. Amer. Water Works Assoc.* **1993**, *85* (1), 51–62.
- Tan, A.; Ziegler, A.; Steinbauer, B.; Seelig, J. Thermodynamics of sodium dodecyl sulfate partitioning into lipid membranes. *Biophys. J.* **2002** *83* (3), 1547–1556.
- Tang, C. Y.; Kwon, Y.-N.; Leckie, J. O. Effect of membrane chemistry and coating layer on physiochemical properties of thin film composite polyamide RO and NF membranes. I. FTIR and XPS characterization of polyamide and coating layer chemistry. *Desalination* **2009**, *242*, 149–167.
- Taniguchi, M.; Kimura, S. Estimation of transport parameters of RO membranes for seawater desalination. *AIChE J.* **2000**, *46* (10), 1967–1973.
- Trehy, M. L.; Bieber, T. I. *Detection, identification, and quantitative analysis of dihaloacetonitriles in chlorinated natural waters*. Ann Arbor Science: Ann Arbor, MI, 1981.
- Trehy, M. L.; Yost, R. A.; Miles, C. J. Chlorination byproducts of amino acids in natural waters. *Environ. Sci. Technol.* **1986**, *20* (11), 1117–1122.
- Trofe, T. W. Kinetics of monochloramine decomposition in the presence of bromide. *Environ. Sci. Technol.* **1980**, *14*, 544–549.
- Tsuru, T.; Ogawa, K.; Kanezashi, M.; Yoshioka, T. Permeation characteristics of electrolytes and neutral solutes through titania nanofiltration membranes at high temperatures. *Langmuir* **2010**, *26* (13), 10897–10905.
- Tu, K. L.; Nghiem, L. D.; Chivas, A. R. Coupling effects of feed solution pH and ionic strength on the rejection of boron by NF/RO membranes. *Chem. Eng. J.* **2011**, *168* (2), 700–706.
- Tu, K. L.; Fujioka, T.; Khan, S. J.; Poussade, Y.; Roux, A.; Drewes, J. E.; Chivas, A. R.; Nghiem, L. D. Boron as a surrogate for N-nitrosodimethylamine rejection by reverse osmosis membranes in potable water reuse applications. *Environ. Sci. Technol.* **2013**, *47* (12), 6425–6430.
- U.S. EPA. National Primary Drinking Water Regulations: Stage 2 Disinfectants and Disinfection Byproducts Rule, *Fed Reg.* **2006**, *71*, 387–493.
- Uyak, V.; Koyuncu, I.; Oktem, I.; Cakmakci, M.; Toroz, I. Removal of trihalomethanes from drinking water by nanofiltration membranes. *J. Hazard. Mater.* **2008**, *152* (2), 789–794.
- Valentine, R. L. Bromochloramine oxidation of N,N-diethyl-p-phenylenediamine in the presence of monochloramine. *Environ. Sci. Technol.* **1986**, *20* (2), 166–170.
- Valentine, R. L.; Brandt, K. I.; Jafvert, C. T. A spectrophotometric study of the formation of an unidentified monochloramine decomposition product. *Water Res.* **1986**, *20* (8), 1067–1074.
- Van der Bruggen, B.; Vandecasteele, C. Modelling of the retention of uncharged molecules with nanofiltration. *Water Res.* **2002**, *36*, 1360–1368.
- Van der Bruggen, B.; Schaep, J.; Maes, W.; Wilms, D.; Vandecasteele, C. Nanofiltration as a treatment method for the removal of pesticides from ground waters. *Desalination* **1998**, *117*, 139–147.
- Van der Bruggen, B.; Schaep, J.; Wilms, D.; Vandecasteele, C. Influence of molecular size, polarity and charge on the retention of organic molecules by nanofiltration. *J. Membr. Sci.* **1999**, *156*, 29–41.
- Van der Bruggen, B.; Wilms, D.; Vandecasteele, C. Application of nanofiltration for removal of pesticides, nitrate and hardness from ground water: Rejection properties and economic evaluation. *J. Membr. Sci.* **2001**, *193* (2), 239–248.

- Van der Bruggen, B.; Braeken, L.; Vandecasteele, C. Evaluation of parameters describing flux decline in nanofiltration of aqueous solutions containing organic compounds. *Desalination* **2002**, *147* (1–3), 281–288.
- Van der Bruggen, B.; Mänttäri, M.; Nystrom, M. Drawbacks of applying nanofiltration and how to avoid them: A review. *Sep. Purif. Technol.* **2008**, *63* (2), 251–263.
- Verliefde, A. Rejection of organic micropollutants by high-pressure membranes (NF/RO). Ph.D. Dissertation, Delft University of Technology: Delft, The Netherlands, 2008.
- Verliefde, A. R. D.; Cornelissen, E. R.; Heijman, S. G. J.; Hoek, E. M. V.; Amy, G. L.; Van der Bruggen, B.; van Dijk, J. C. Influence of solute–membrane affinity on rejection of uncharged organic solutes by nanofiltration membranes. *Environ. Sci. Technol.* **2009a**, *43* (7), 2400–2406.
- Verliefde, A. R. D.; Cornelissen, E. R.; Heijman, S. G. J.; Verberk, J. Q. J. C.; Amy, G. L.; Van der Bruggen, B.; van Dijk, J. C. Construction and validation of a full-scale model for rejection of organic micropollutants by NF membranes. *J. Membr. Sci.* **2009b**, *339*, 10–20.
- Vikesland, P. J.; Ozekin, K.; Valentine, R. L. Monochloramine decay in model and distribution system waters. *Water Res.* **2001**, *35* (7), 1766–1776.
- Villanueva, C. M.; Cantor, P. K.; Grimalt, J. O.; Malats, N.; Silverman, D.; Tardon, A.; Garcia-Closas, R.; Serra, C.; Carrato, A.; Kogevinas, M. Bladder cancer and exposure to water disinfection by-products through ingestion, bathing, showering and swimming in pools. *Am. J. Epidemiol.* **2006**, *165* (2), 148–156.
- Wajon, J. E.; Morris, J. C. *Bromamination chemistry: Rates of formation of NH₂Br and some N-bromamino acids*. Ann Arbor Science Publishers: Ann Arbor, MI, 1980.
- Wang, K. Y.; Chung, T.-S. The characterization of flat composite nanofiltration membranes and their applications in the separation of Cephalexin. *J. Membr. Sci.* **2005**, *247* (1–2), 37–50.
- Wang, X.-L.; Tsuru, T.; Nakao, S.; Kimura, S. The electrostatic and steric-hindrance model for the transport of charged solutes through nanofiltration membranes. *J. Membr. Sci.* **1997**, *135* (1), 19–32.
- Waniek, A.; Bodzek, M.; Konieczny, K. Trihalomethane removal from water using membrane processes. *Polish J. Environ. Studies* **2002**, *11* (2), 171–178.
- Weinberg, H. S.; Krasner, S. W.; Richardson, S. D.; Thruston, A. D. J. *The occurrence of disinfection byproducts (DBPs) of health concern in drinking water: Results of a nationwide DBP occurrence study*. Environmental Protection Agency: Athens, GA, 2002.
- Westerhoff, P.; Mash, H. Dissolved organic nitrogen in drinking water supplies: A review. *J. Water Supply: Res. Technol.* **2002**, *51* (8), 415–448.
- Westerhoff, P.; Chao, P.; Mash, H. Reactivity of natural organic matter with aqueous chlorine and bromine. *Water Res.* **2004**, *38* (6), 1502–1513.
- White, G. C. *Handbook of chlorination and alternative disinfectants*. John Wiley & Sons: Hoboken, NJ, 2011.
- Wijmans, J. G.; Baker, R. W. The solution-diffusion model: A review. *J. of Membr. Sci.* **1995**, *107* (1–2), 1–21.
- Wilf, M. *The guidebook to membrane technology for wastewater reclamation*. Balaban Desalination Publications: LAquila, Italy, 2010.
- Williams, D. T.; Hestekin, J. A.; Smothers, C. N.; Bhattacharyya, D. Separation of organic pollutants by reverse osmosis and nanofiltration membranes: Mathematical models and experimental verification. *I&EC Res.* **1999**, *38*, 3683–3695.

- Williams, M. E. *A Review of reverse osmosis theory*. EET Corporation and Williams Engineering Services Company: Harriman, TN, 2003. http://www.eetcorp.com/heepm/RO_TheoryE.pdf (accessed December 22, 2014).
- Winograd, Y.; Solan, A.; Toren, M. Mass transfer in narrow channels in the presence of turbulence promoters. *Desalination* **1973**, *13*, 171–186.
- Xu, P.; Drewes, J. E.; Bellona, C.; Amy, G.; Kim, T.-U.; Adam, M.; Heberer, T. Rejection of emerging organic micropollutants in nanofiltration–reverse osmosis membrane applications. *Water Environ. Res.* **2005**, *77* (1), 40–48.
- Xu, P., Bellona, C.; Drewes, J. E. Fouling of nanofiltration and reverse osmosis membranes during municipal wastewater reclamation: Membrane autopsy results from pilot-scale investigations. *J. Membr. Sci.* **2010**, *53* (1–2), 111–121.
- Xu, Y.; Lebrun, R. E. Investigation of the solute separation by charged nanofiltration membrane: Effect of pH, ionic strength and solute type. *J. Membr. Sci.* **1999**, *158* (1–2), 93–104.
- Xu, Y.; Drewes, J. E.; Kim, T.-U.; Bellona, C.; Amy, G. Effect of membrane fouling on transport of organic contaminants in NF/RO membrane applications. *J. Membr. Sci.* **2006**, *279* (1–2), 165–175.
- Yang, X.; Shanga, C.; Westerhoff, P. Factors affecting formation of haloacetonitriles, haloketones, chloropicrin and cyanogen halides during chloramination. *Water Res.* **2007**, *41* (6), 1193–1200.
- Yang, X.; Fan, C.; Zhao, Q. Nitrogenous disinfection byproducts formation and nitrogen origin exploration during chloramination of nitrogenous organic compounds. *Water Res.* **2010**, *44*, 2691–2702.
- Yang, X.; Shen, Q.; Guo, W.; Peng, J.; Liang, Y. Precursors and nitrogen origins of trichloronitromethane and dichloroacetonitrile during chlorination/chloramination. *Chemosphere* **2012**, *88* (1), 25–32.
- Zhang, Y.-L.; Zhou, L.-L.; Zeng, G.; Song, Z.-G.; Li, G.-B. Factors affecting the formation of trihalomethanes in the presence of bromide during chloramination. *J. Zhejiang University* **2010**, *11* (8), 606–612.
- Zularisam, A. W.; Ismail, A. F.; Salim, R. Behaviours of natural organic matter in membrane filtration for surface water treatment—A review. *Desalination* **2006**, *194*, 211–231.

Appendix A

Appendix A contains the formation kinetics at 23° C and pH 5.5, 7, 8.5 during the different disinfection strategies, including chlorination, pre- and inline-formed chloramination for TCM, BDCM, DBCM, TBM, TCAN, DCAN, BCAN, DBAN, 1,1-DCP, 1,1,1-TCP, TCNM, and CH. In addition, the normalized linear, quadratic, and interaction regression coefficients during chlorination and pre-formed chloramination are presented.

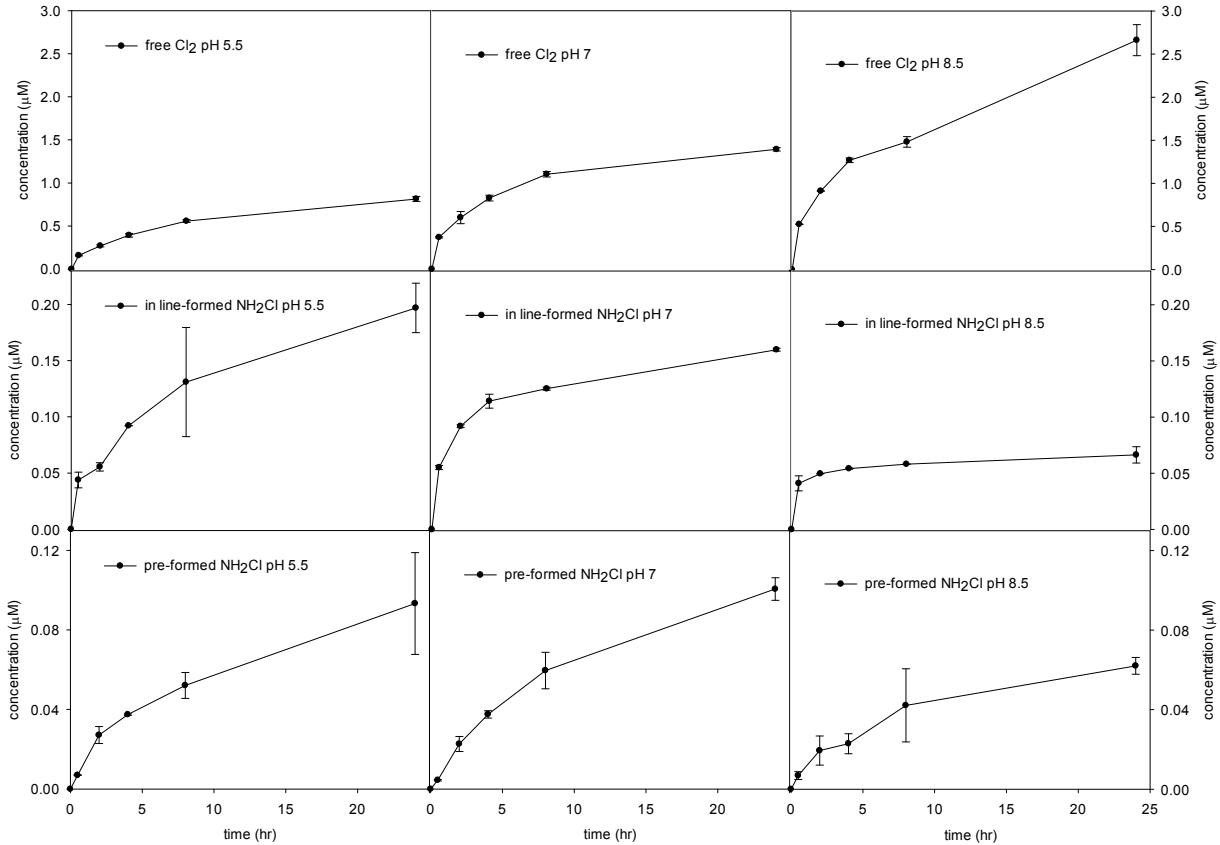


Figure A.1. Chloroform formation kinetics during chlorination, inline-formed chloramination and pre-formed chloramination (25 mg/L Cl₂) at 23° C and pH 5.5, 7, and 8.5.

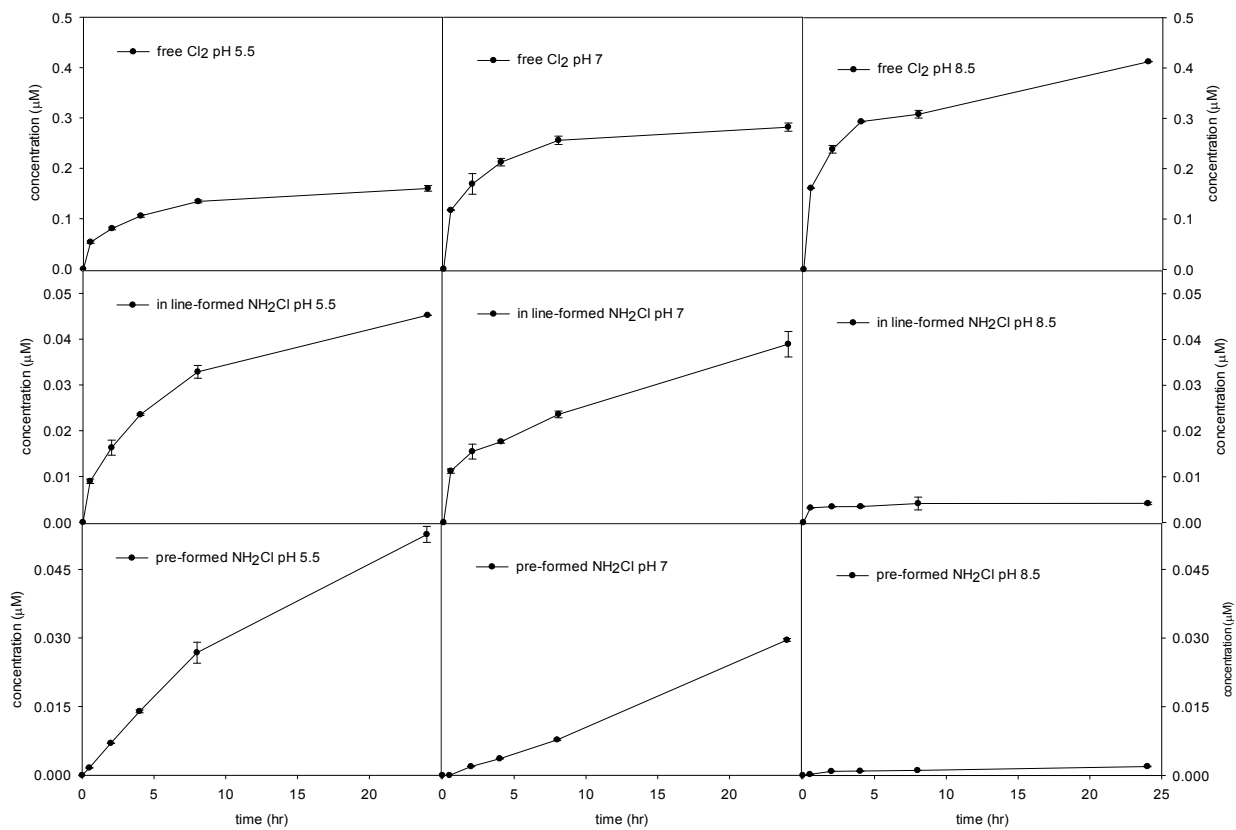


Figure A.2. Bromodichloromethane formation kinetics during chlorination, inline-formed chloramination, and pre-formed chloramination (25 mg/L Cl₂) at 23° C and pH 5.5, 7, and 8.5.

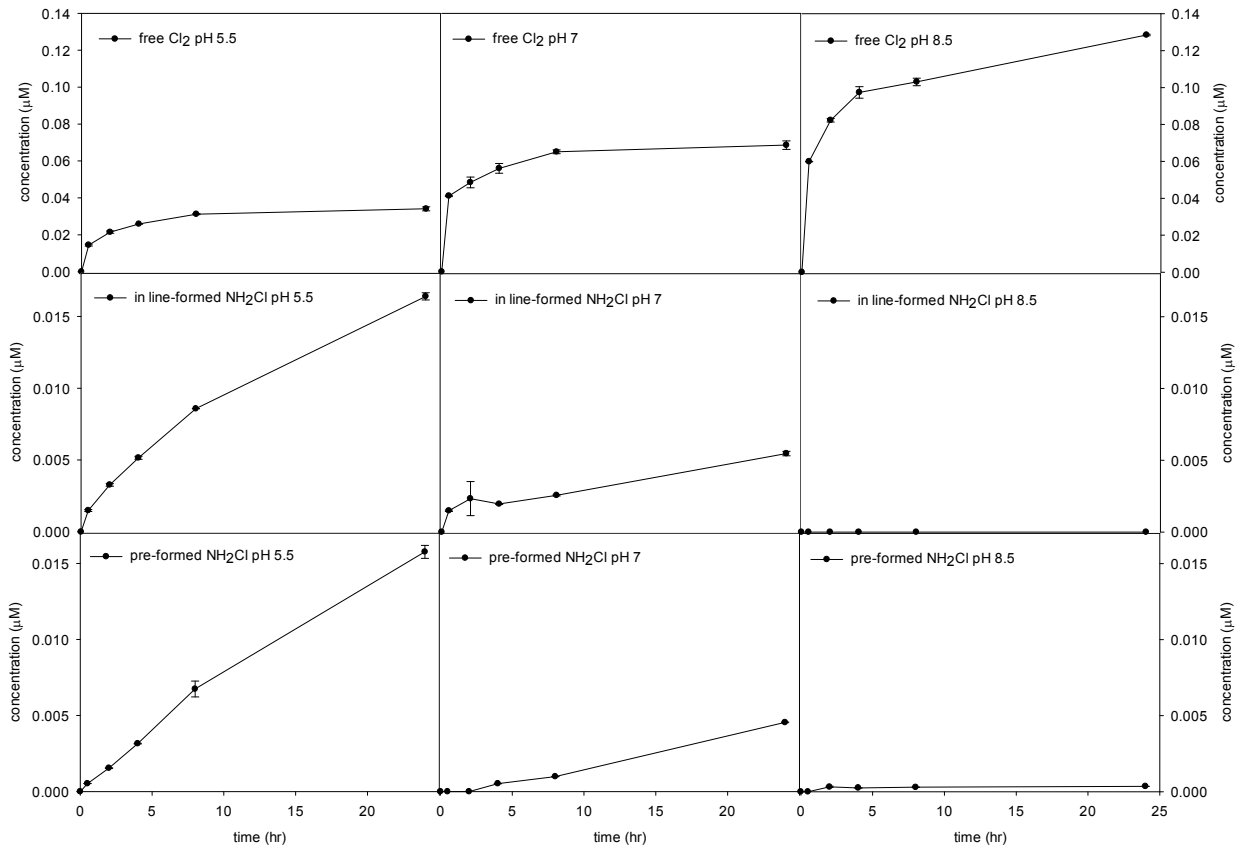


Figure A.3. Dibromochloromethane formation kinetics during chlorination, inline-formed chloramination, and pre-formed chloramination (25 mg/L Cl₂) at 23° C and pH 5.5, 7, and 8.5.

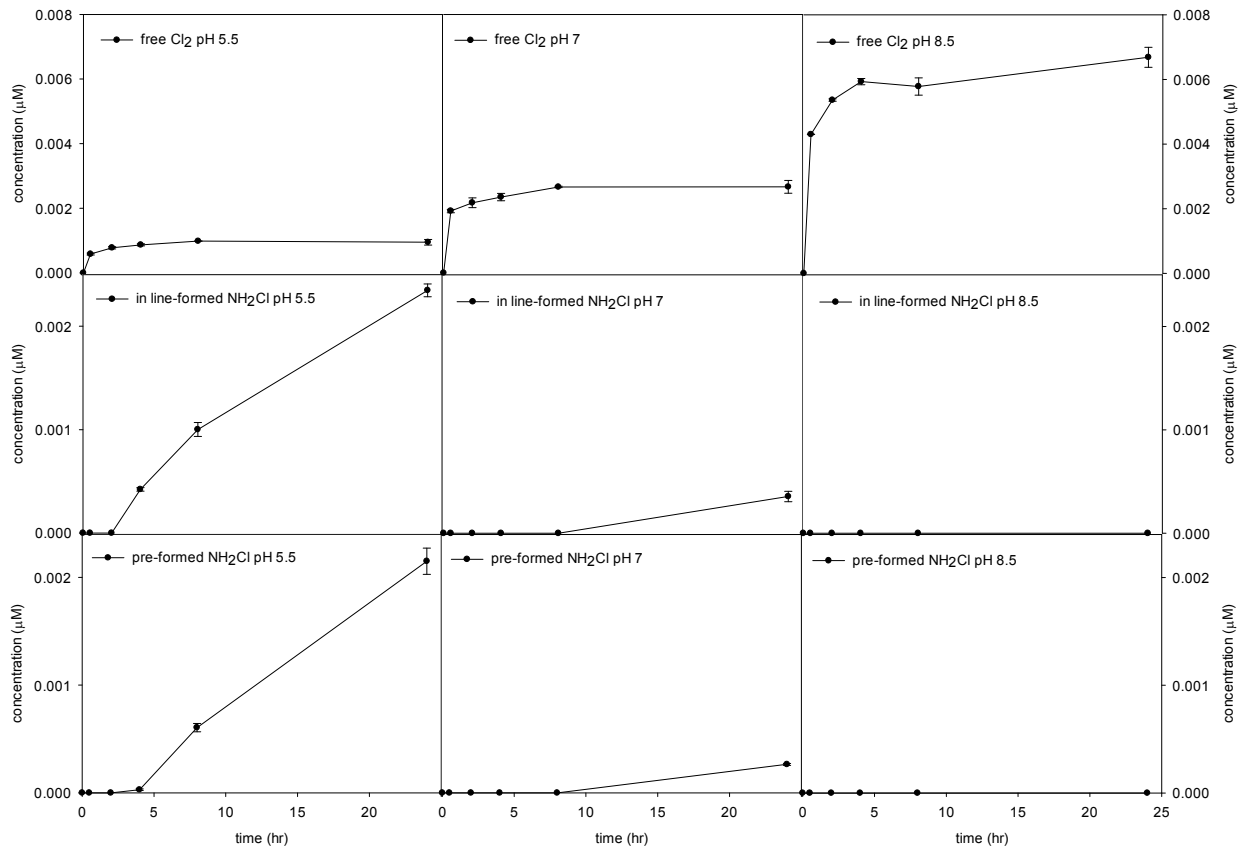


Figure A.4. Tribromomethane formation kinetics during chlorination, inline-formed chloramination, and pre-formed chloramination (25 mg/L Cl_2) at 23° C and pH 5.5, 7, and 8.5.

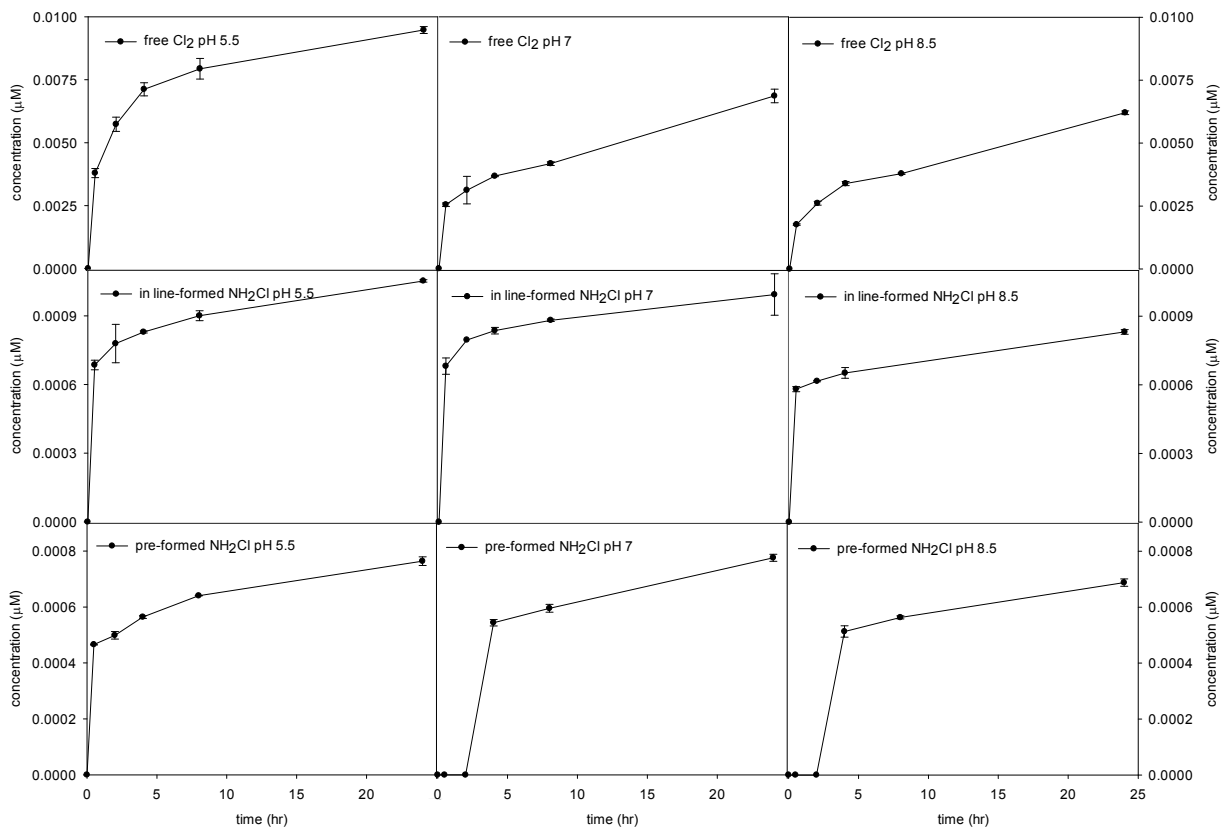


Figure A.5. Trichloroacetonitrile formation kinetics during chlorination, inline-formed chloramination, and pre-formed chloramination (25 mg/L Cl₂) at 23° C and pH 5.5, 7, and 8.5.

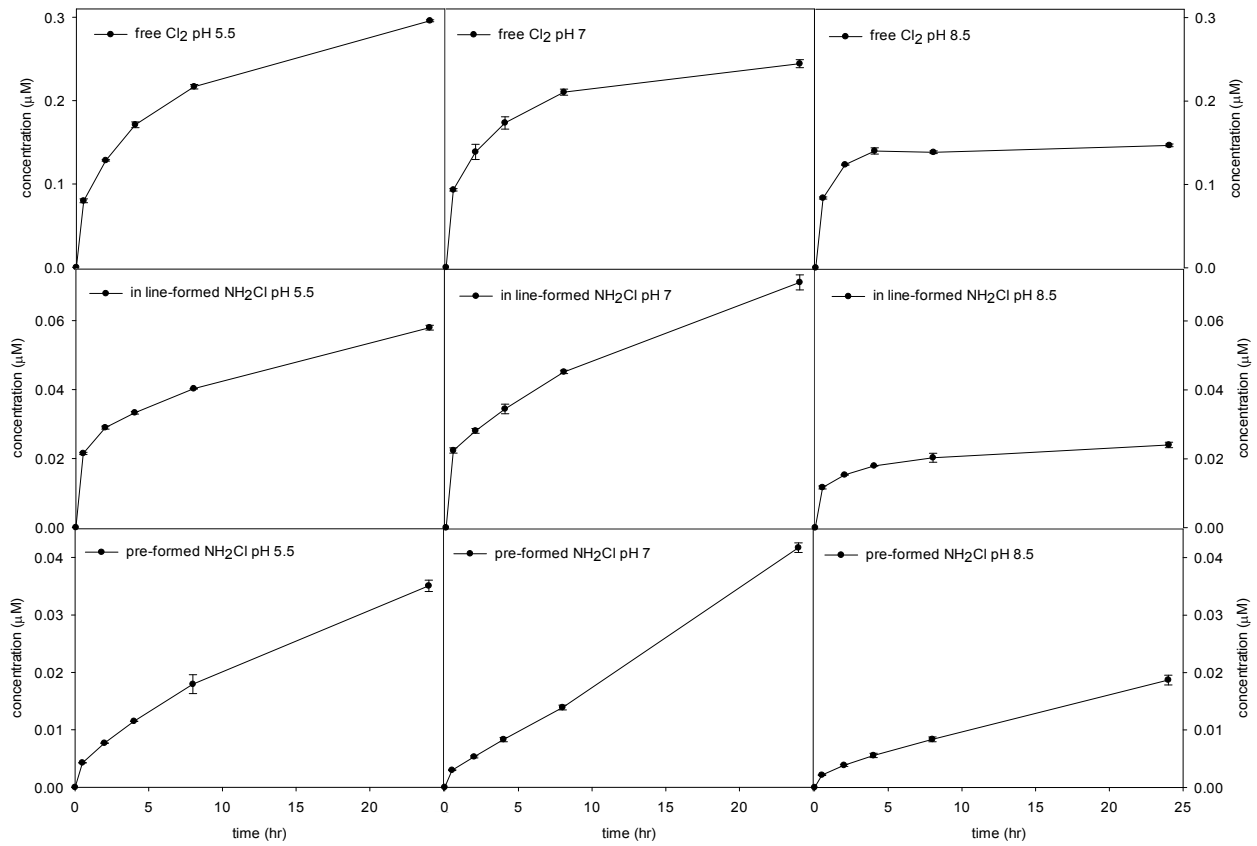


Figure A.6. Dichloroacetonitrile formation kinetics during chlorination, inline-formed chloramination, and pre-formed chloramination (25 mg/L Cl₂) at 23° C and pH 5.5, 7, and 8.5.

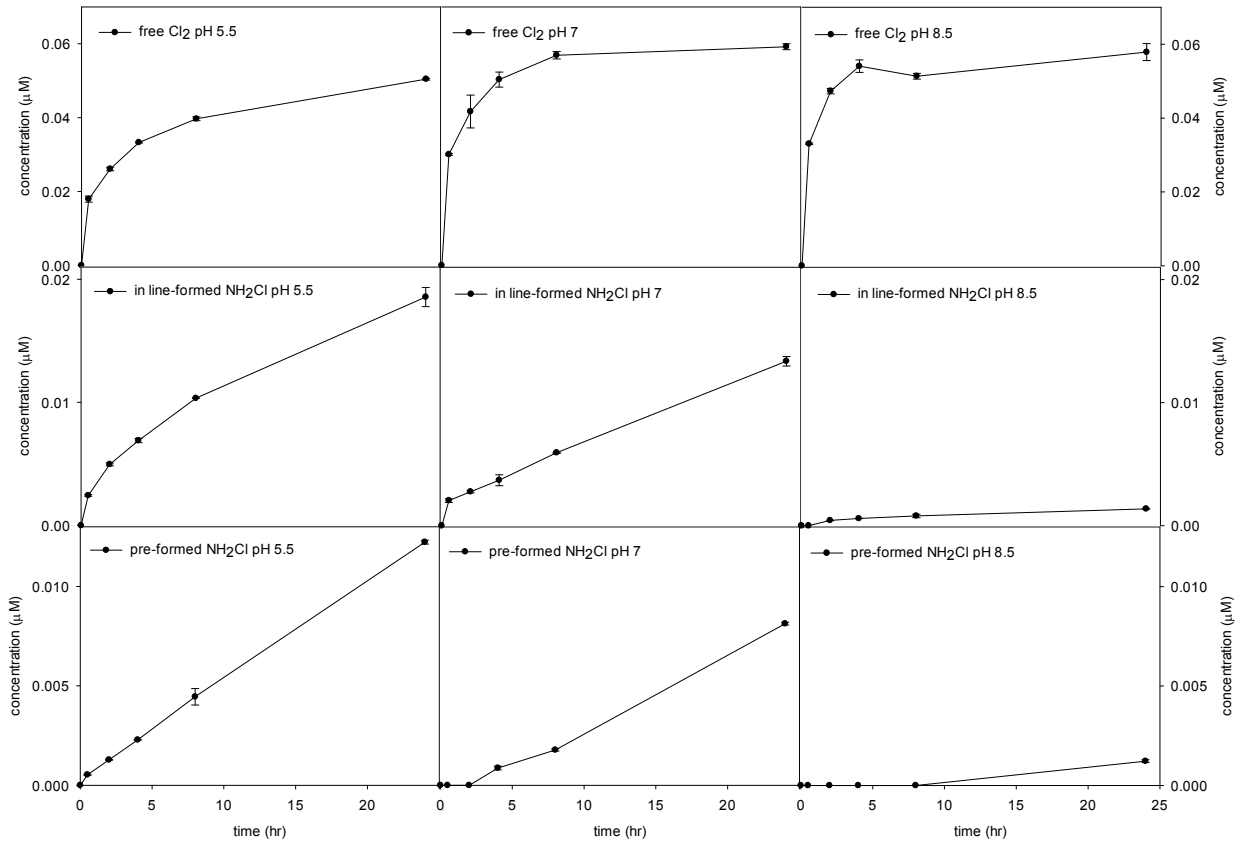


Figure A.7. Bromochloroacetonitrile formation kinetics during chlorination, inline-formed chloramination, and pre-formed chloramination (25 mg/L Cl₂) at 23° C and pH 5.5, 7, and 8.5.

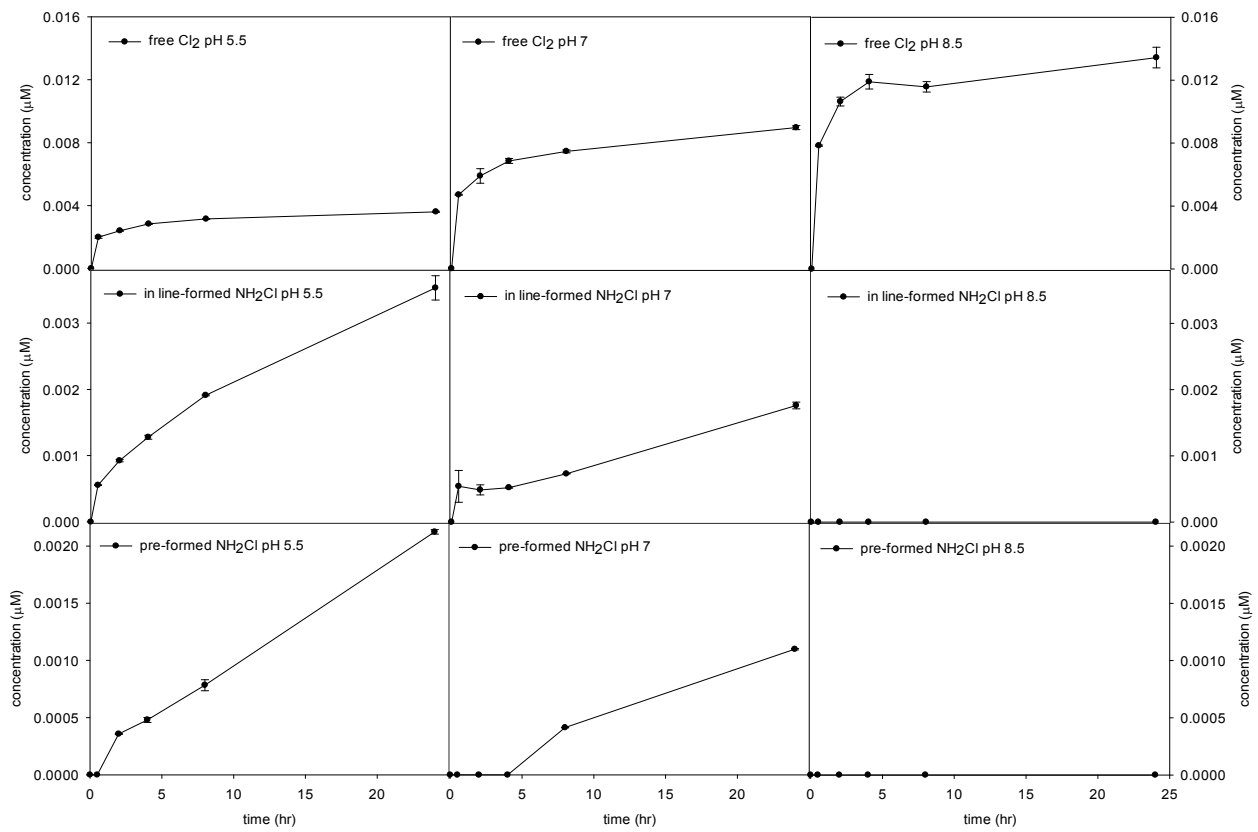


Figure A.8. Dibromoacetonitrile formation kinetics during chlorination, inline-formed chloramination, and pre-formed chloramination (25 mg/L Cl_2) at 23° C and pH 5.5, 7, and 8.5.

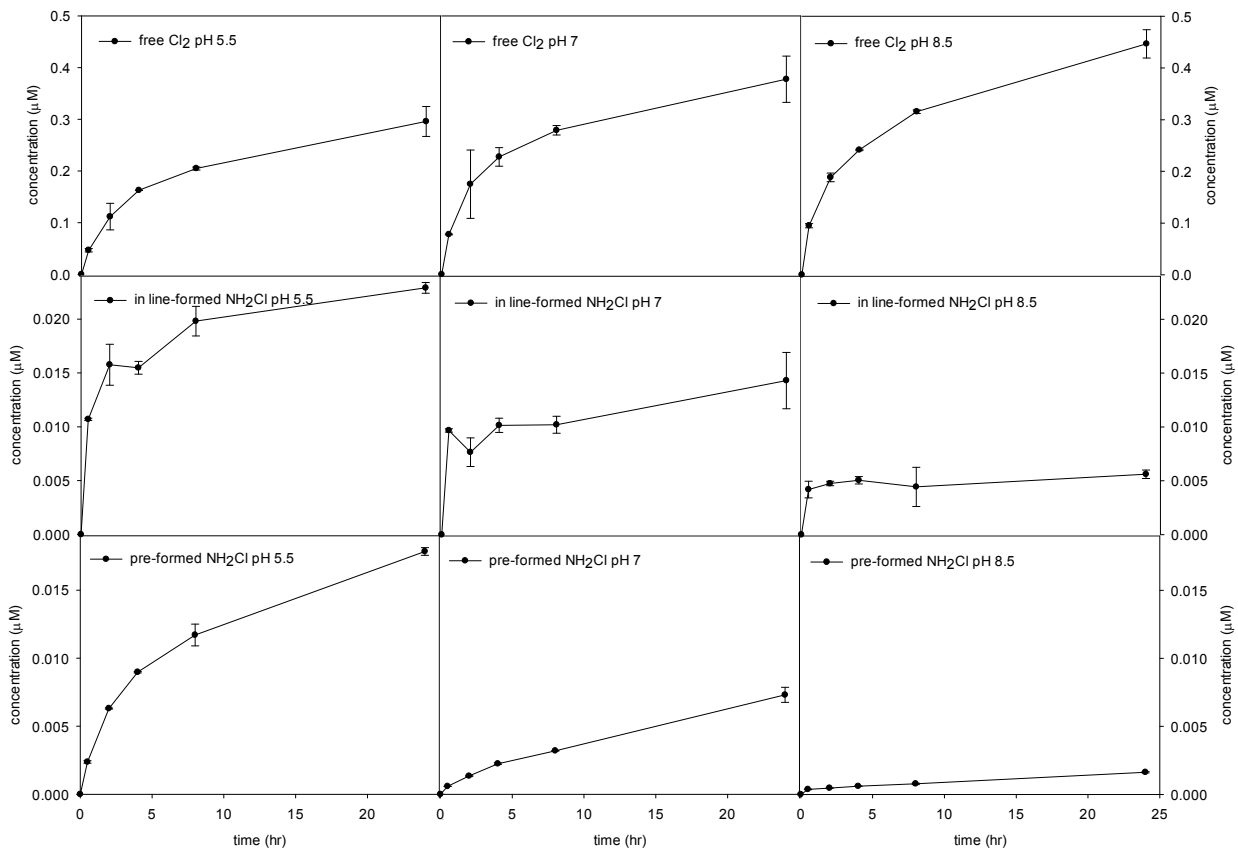


Figure A.9. Chloral hydrate formation kinetics during chlorination, inline-formed chloramination, and pre-formed chloramination (25 mg/L Cl₂) at 23° C and pH 5.5, 7, and 8.5.

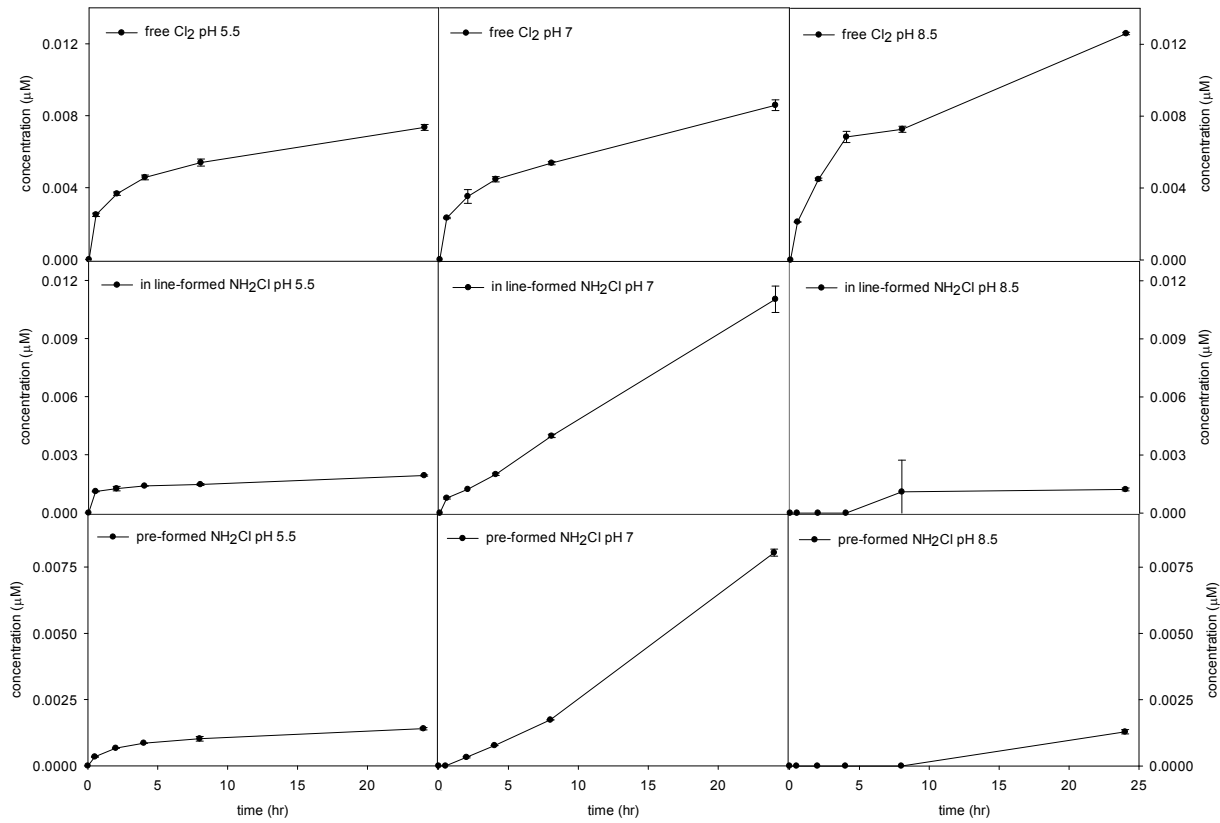


Figure A.10. Trichloronitromethane formation kinetics during chlorination, in-line-formed chloramination, and pre-formed chloramination (25 mg/L Cl₂) at 23 °C and pH 5.5, 7, and 8.5.

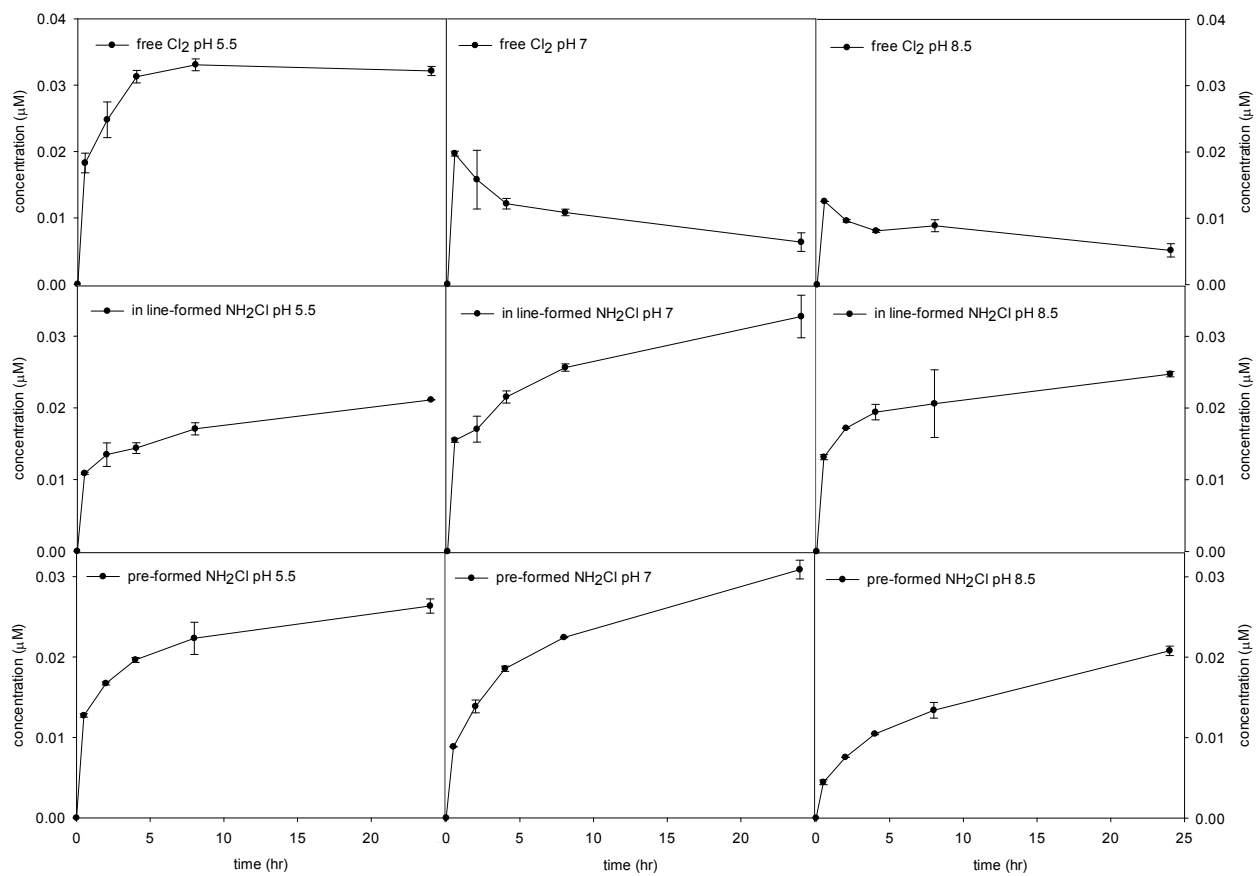


Figure A.11. 1,1-Dichloropropanone formation kinetics during chlorination, in-line-formed chloramination, and pre-formed chloramination (25 mg/L Cl₂) at 23° C and pH 5.5, 7, and 8.5.

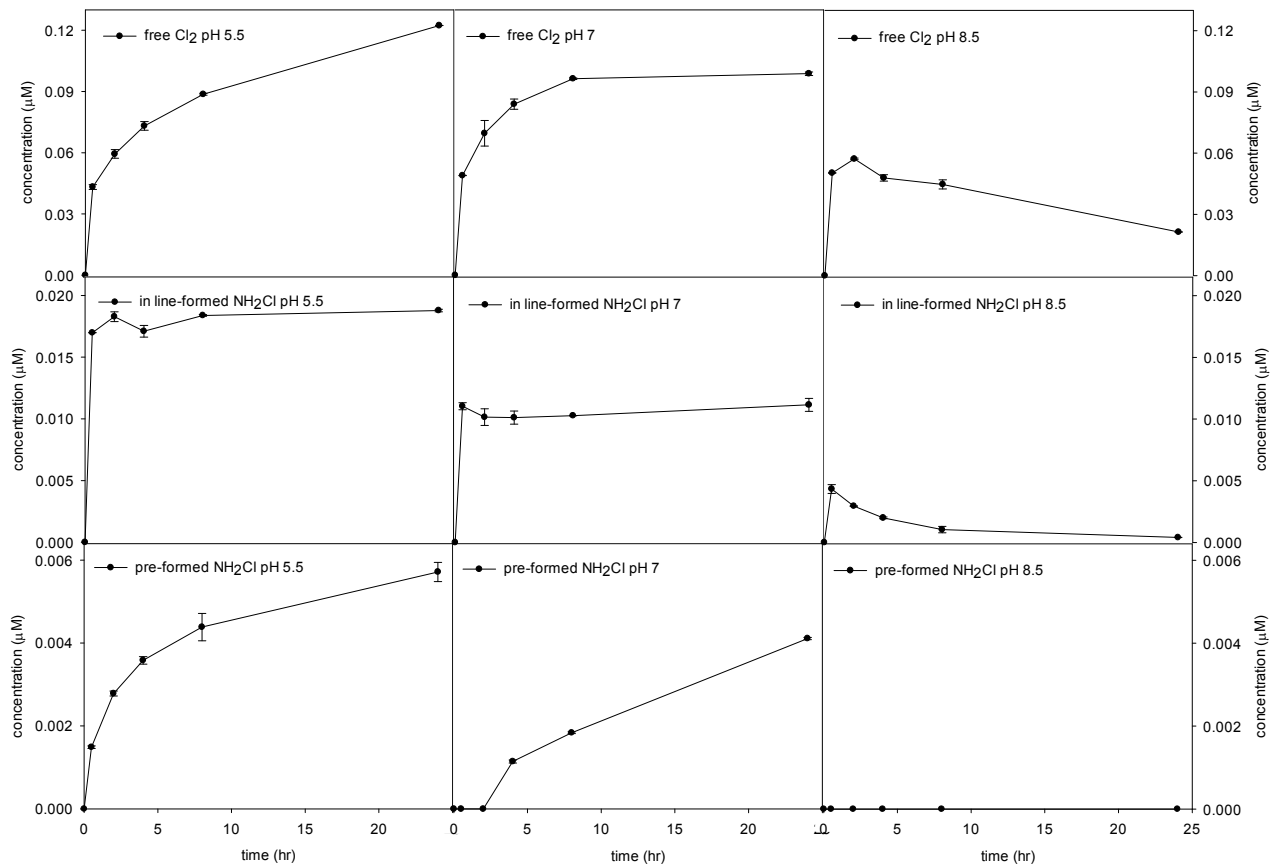


Figure A.12. 1,1,1-Trichloropropanone formation kinetics during chlorination, inline-formed chloramination, and pre-formed chloramination (25 mg/L Cl₂) at 23° C and pH 5.5, 7, and 8.5.

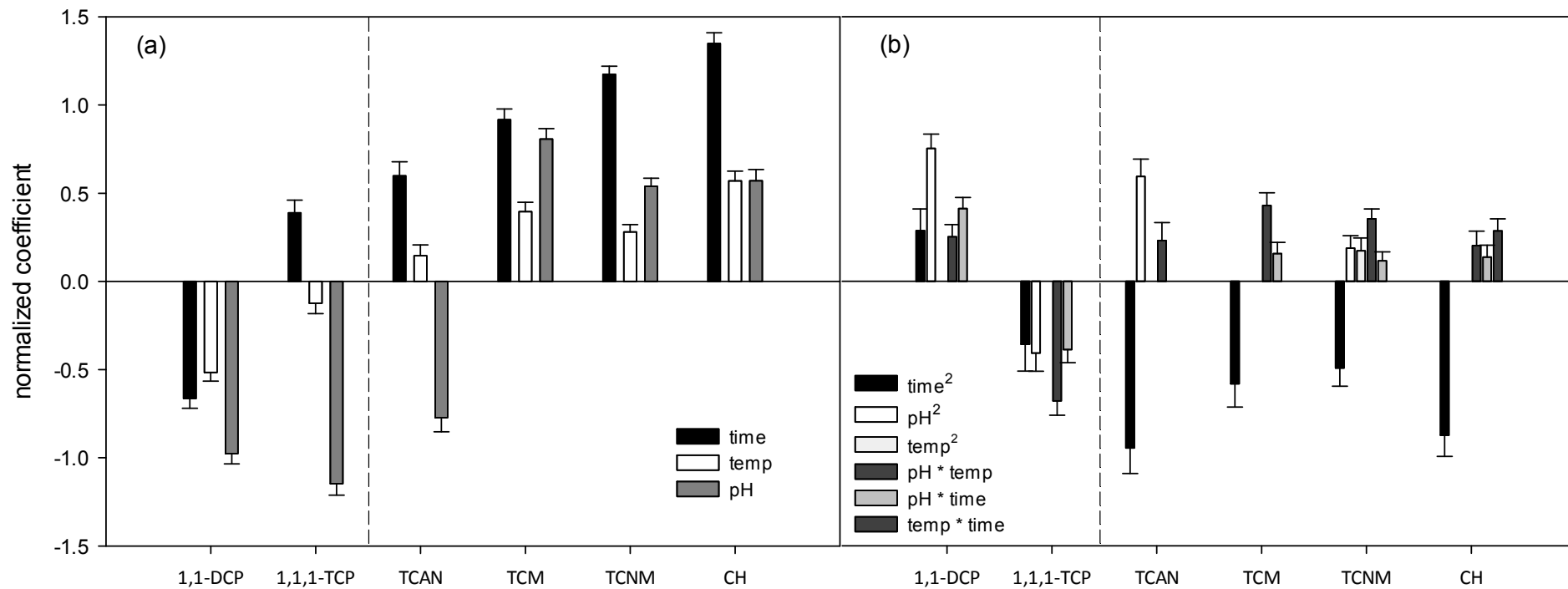


Figure A.13. Comparison of normalized (a) linear, (b) quadratic and interaction regression coefficients during chlorination of only chlorine-containing DBPs.

Note: Error bars correspond to the standard error that is due to the model.

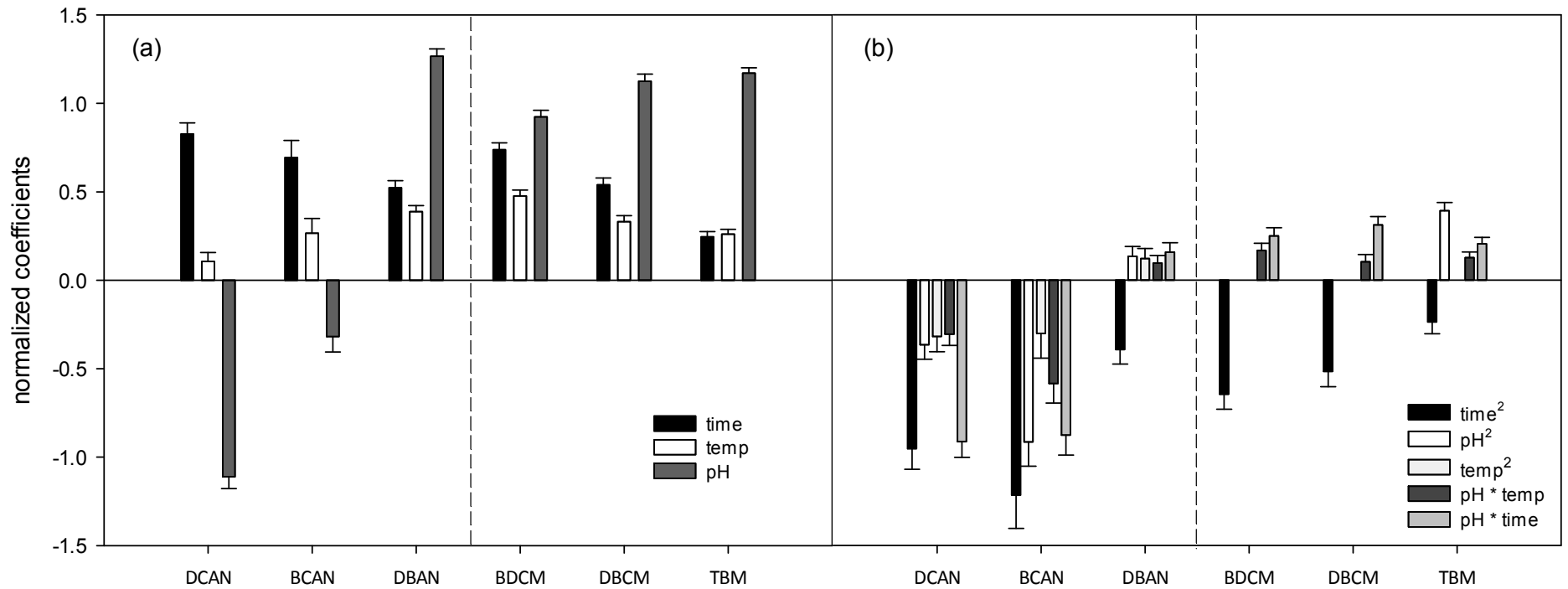


Figure A.14. Comparison of normalized (a) linear, (b) quadratic and interaction regression coefficients during chlorination, including DHANs and bromide containing THMs.

Note: Error bars correspond to the standard error that is due to the model.

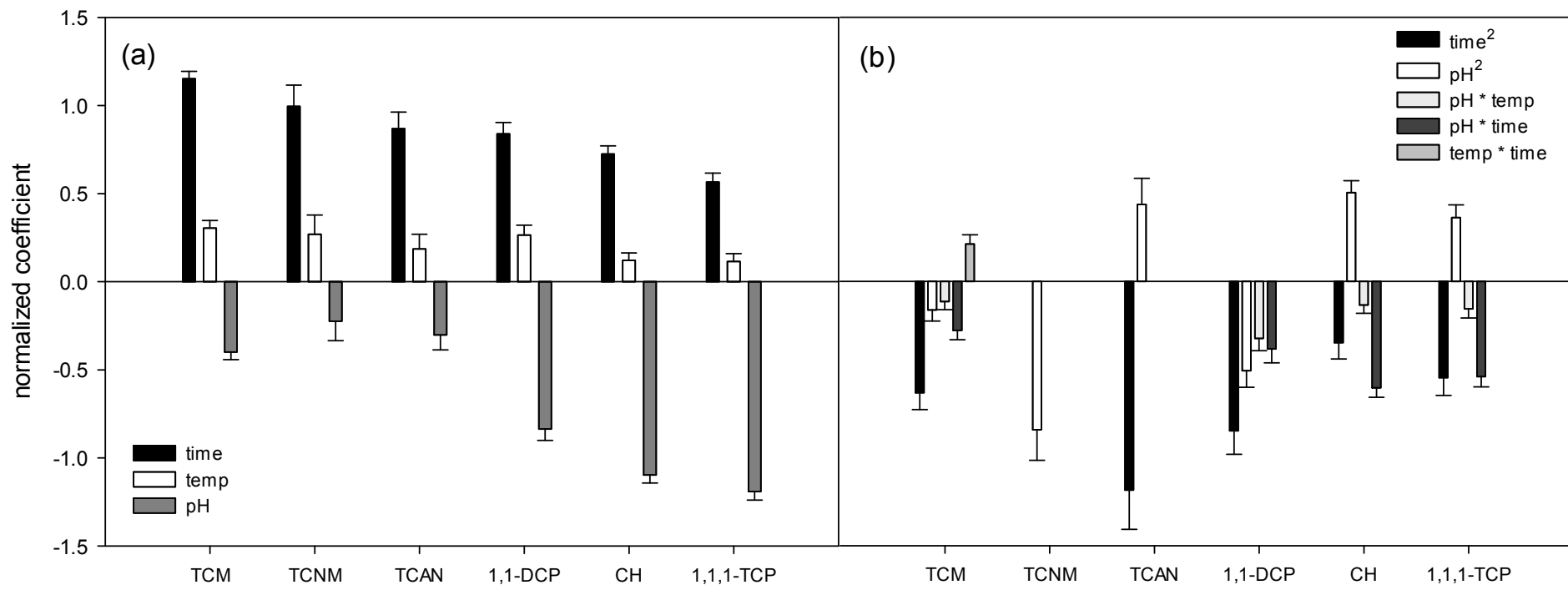


Figure A.15. Comparison of normalized (a) linear, (b) quadratic and interaction regression coefficients during pre-formed chloramination of only chlorine containing DBPs.

Note: Error bars correspond to the standard error that is due to the model.

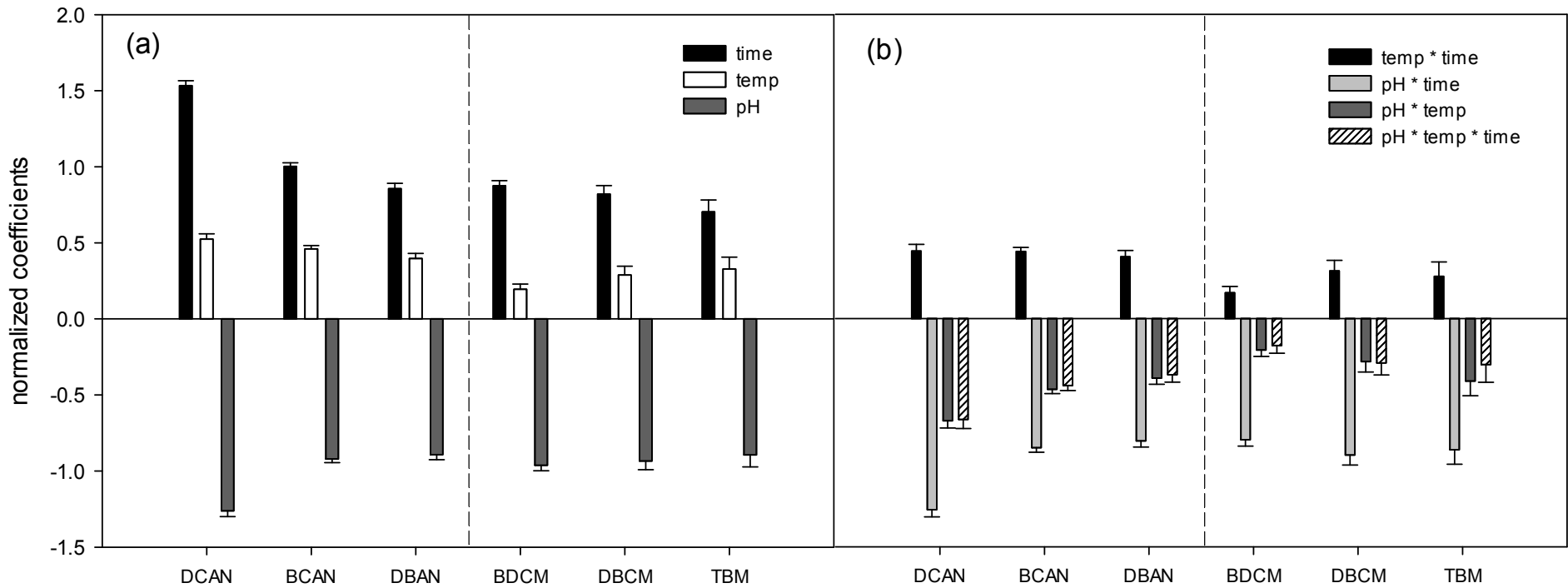


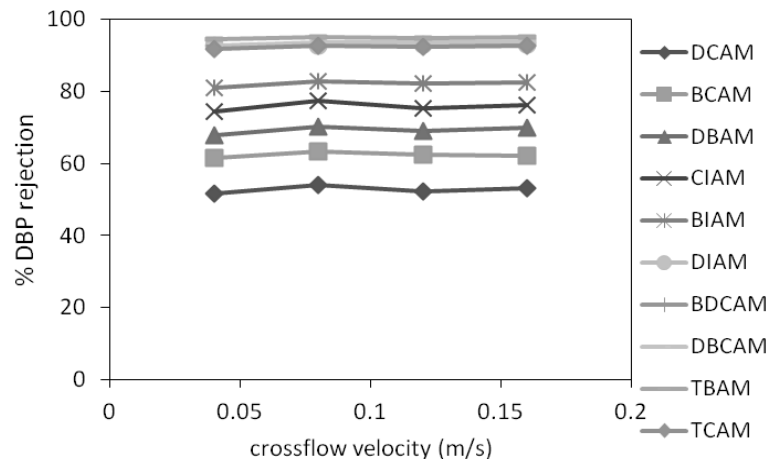
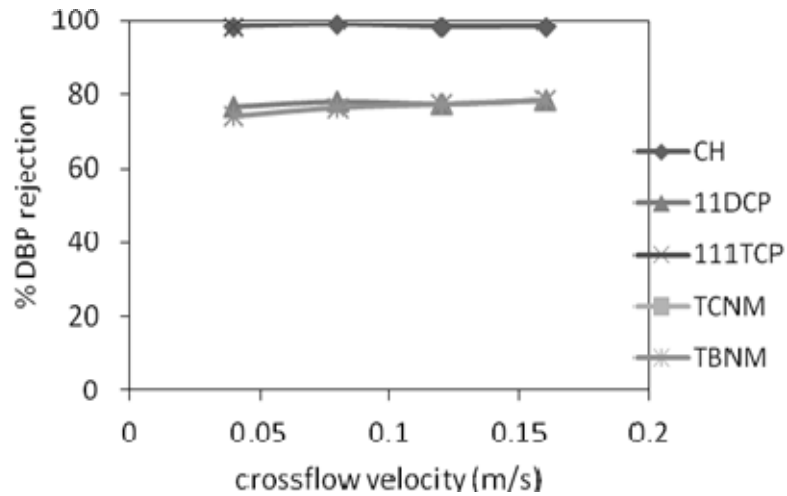
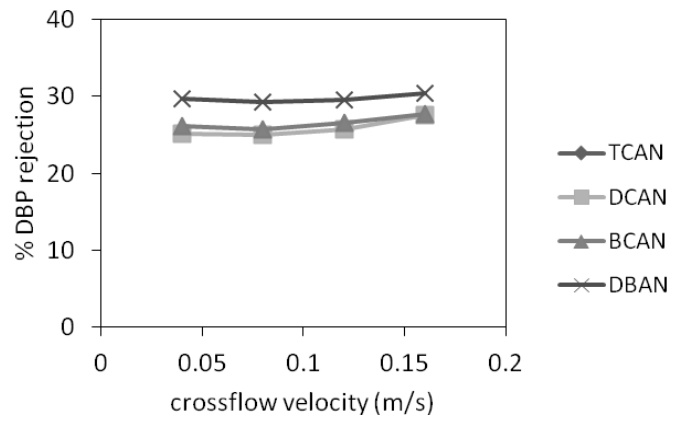
Figure A.16. Comparison of normalized (a) linear, (b) quadratic and interaction regression coefficients during pre-formed chloramination, including DHANs and bromide containing THMs.

Note: Error bars correspond to the standard error that is due to the model.

Appendix B

Appendix B contains the impact of operational parameters and feed solution chemistry with the RO and NF membrane and on all the DBPs studied. TCAN, CH, and TCNM could not be measured for every experiment because of losses in the experimental setup. TBNM and TCACAm could only be included in the experiments with the RO membrane after obtaining the commercially available standards, including the experiments of crossflow velocity and transmembrane flux. The data for the transmembrane flux is shown in Chapter 5 and is, therefore, not listed in this Appendix.

Figure B.8 shows a higher rejection at pH 8.5 for TCM. TCM is a degradation product of other DBPs present in solution, for example, 1,1,1-TCP (Nikolalou et al., 2001). Therefore, it is suspected that the steady state was not reached because of the continuous degradation of the other DBPs, leading to a higher concentration in the feed and that lead to an overestimation of the rejection



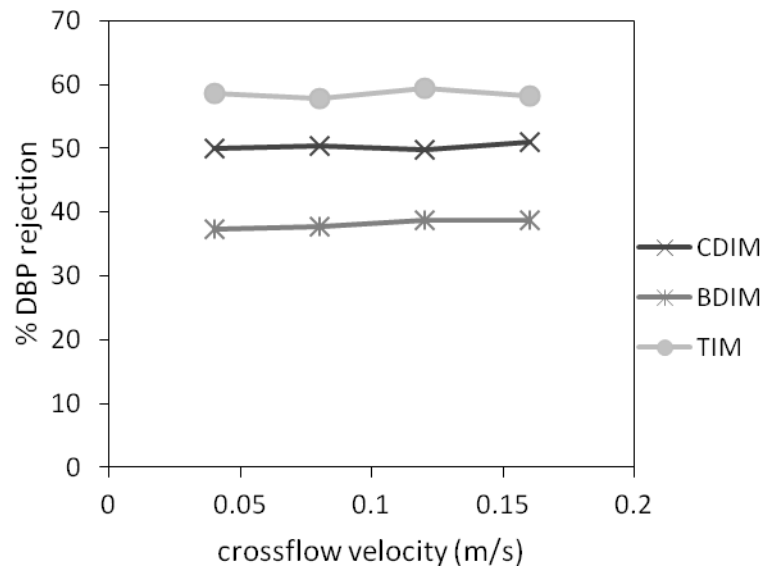


Figure B.1. Impact of crossflow velocity on DBP rejection by NF.

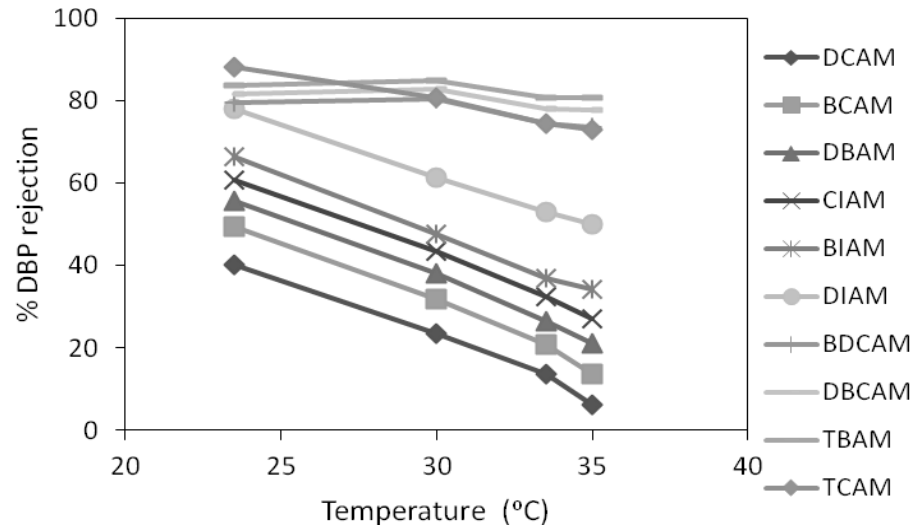
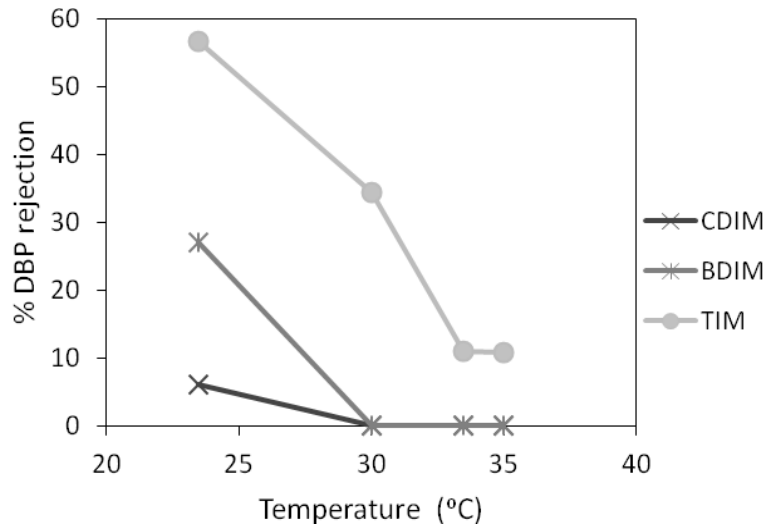
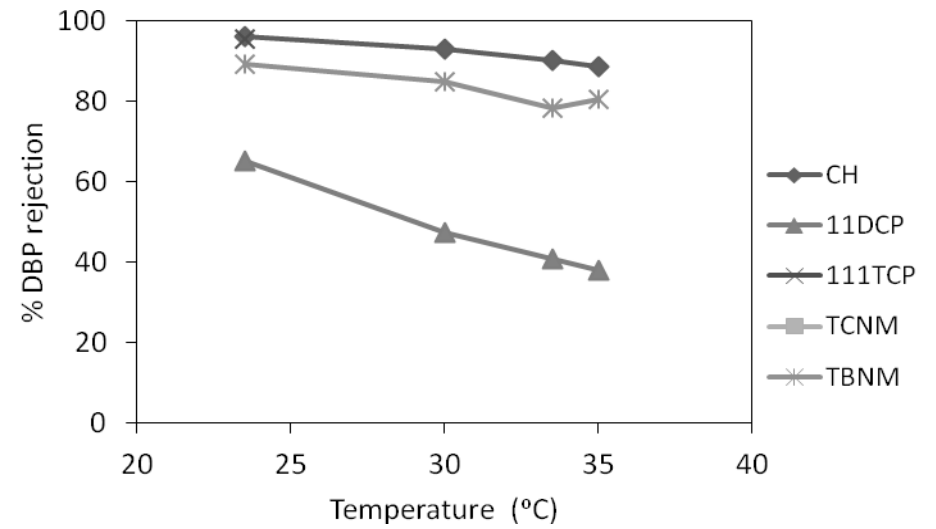
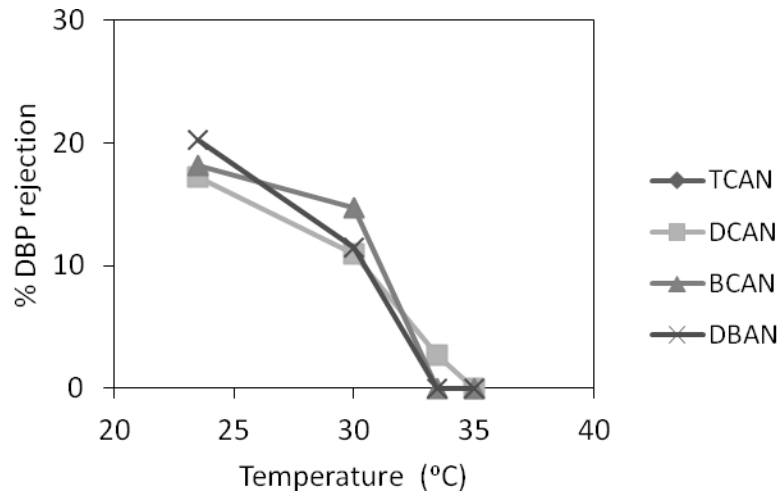


Figure B.2. Impact of feed solution temperature on DBP rejection by NF.

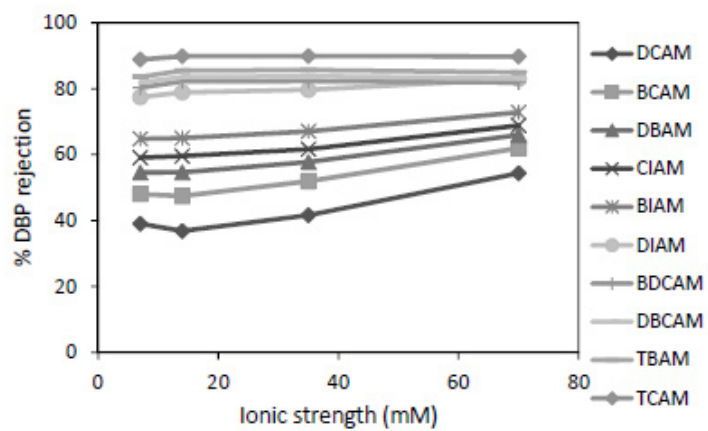
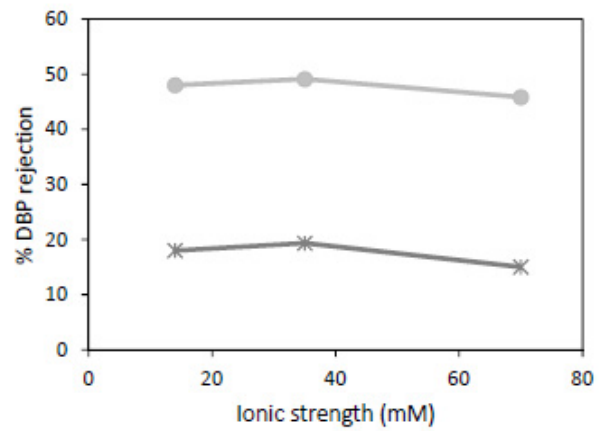
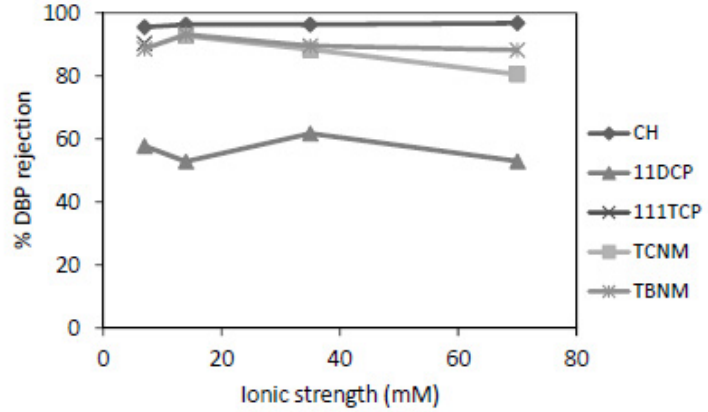
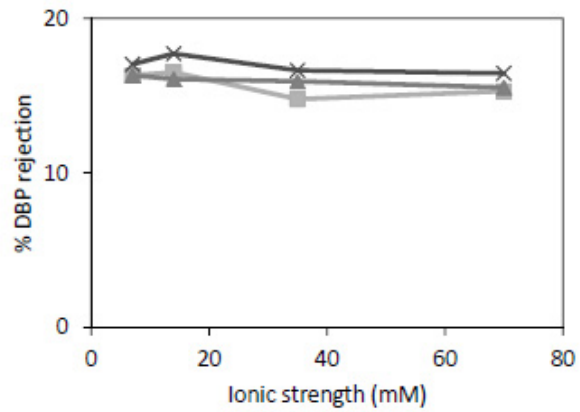


Figure B.3. Impact of feed solution ionic strength on DBP rejection by NF.

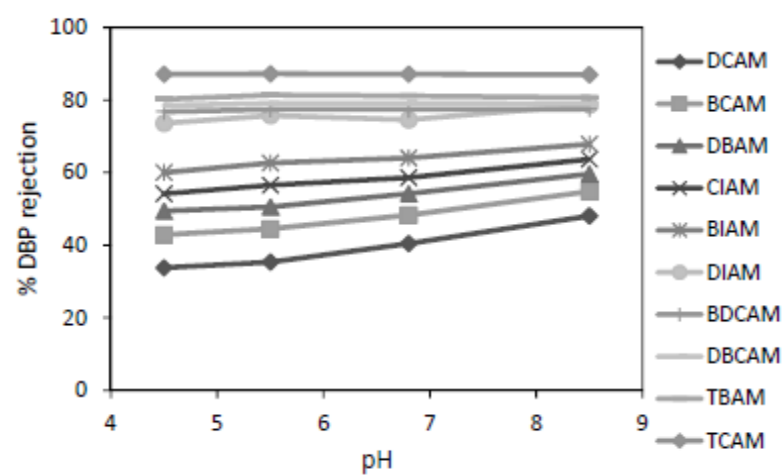
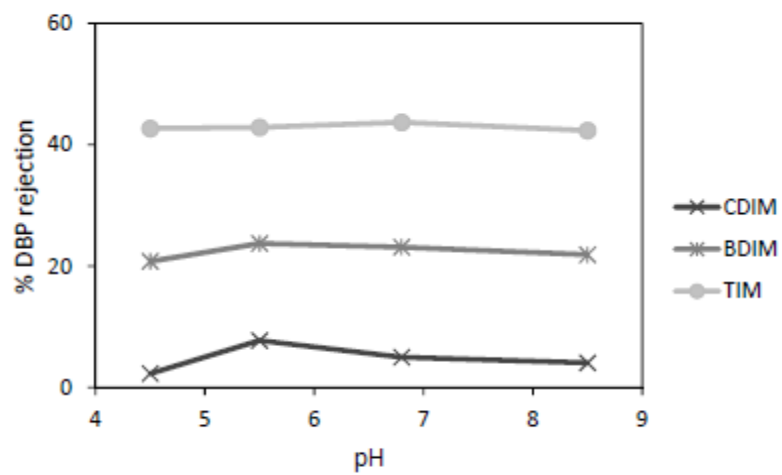
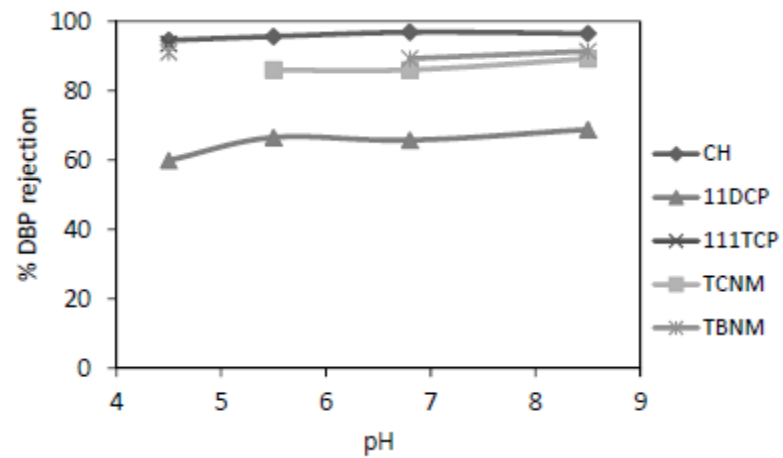
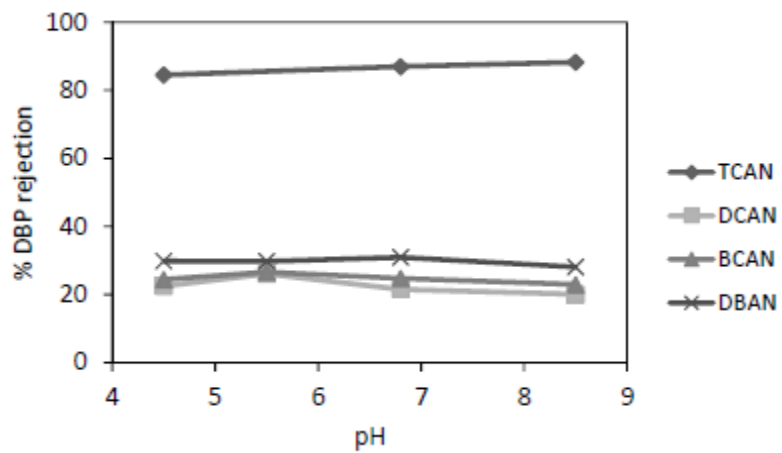


Figure B.4. Impact of feed solution pH on DBP rejection by NF.

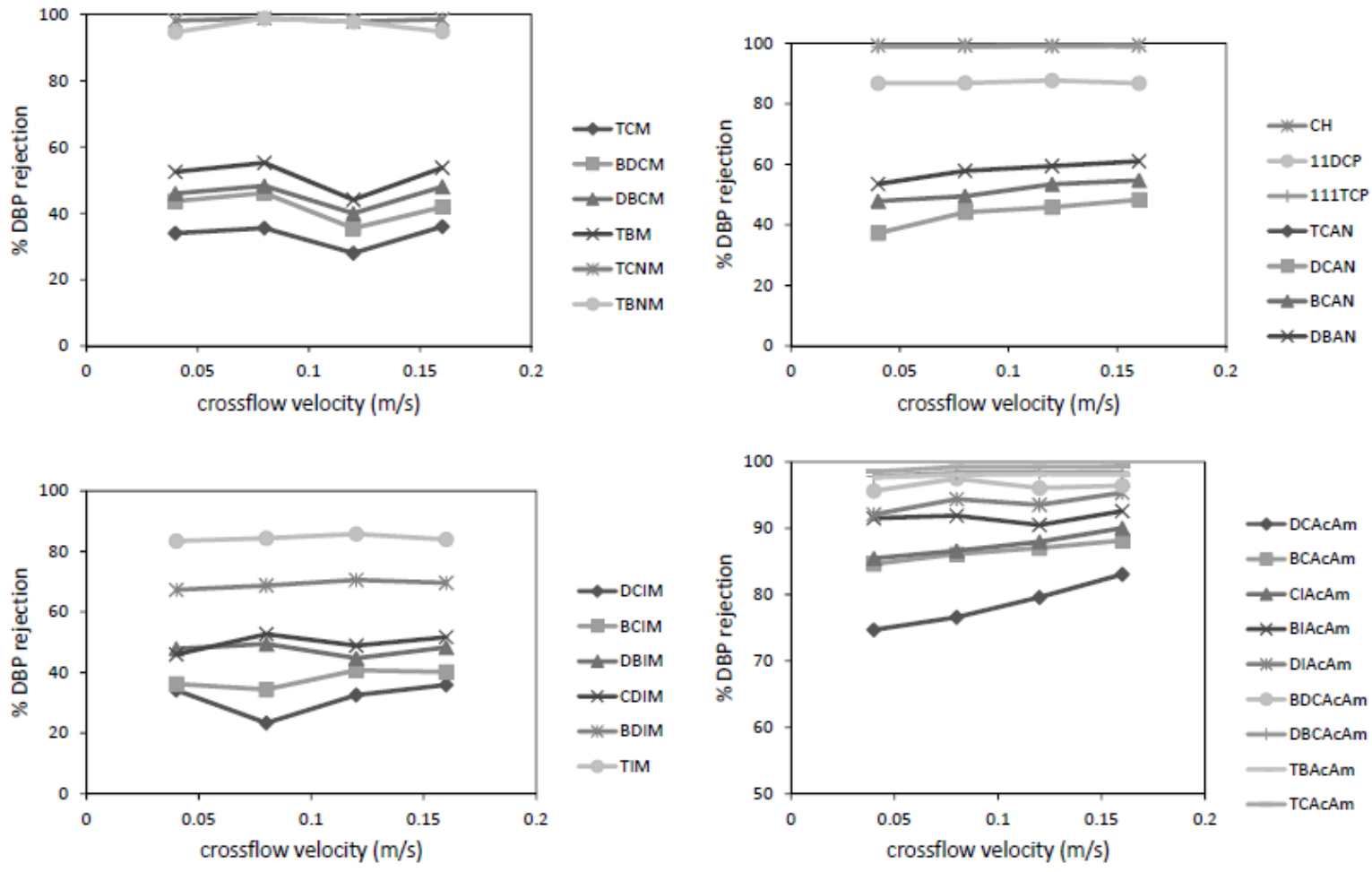


Figure B.5. Impact of crossflow velocity on DBP rejection by RO.

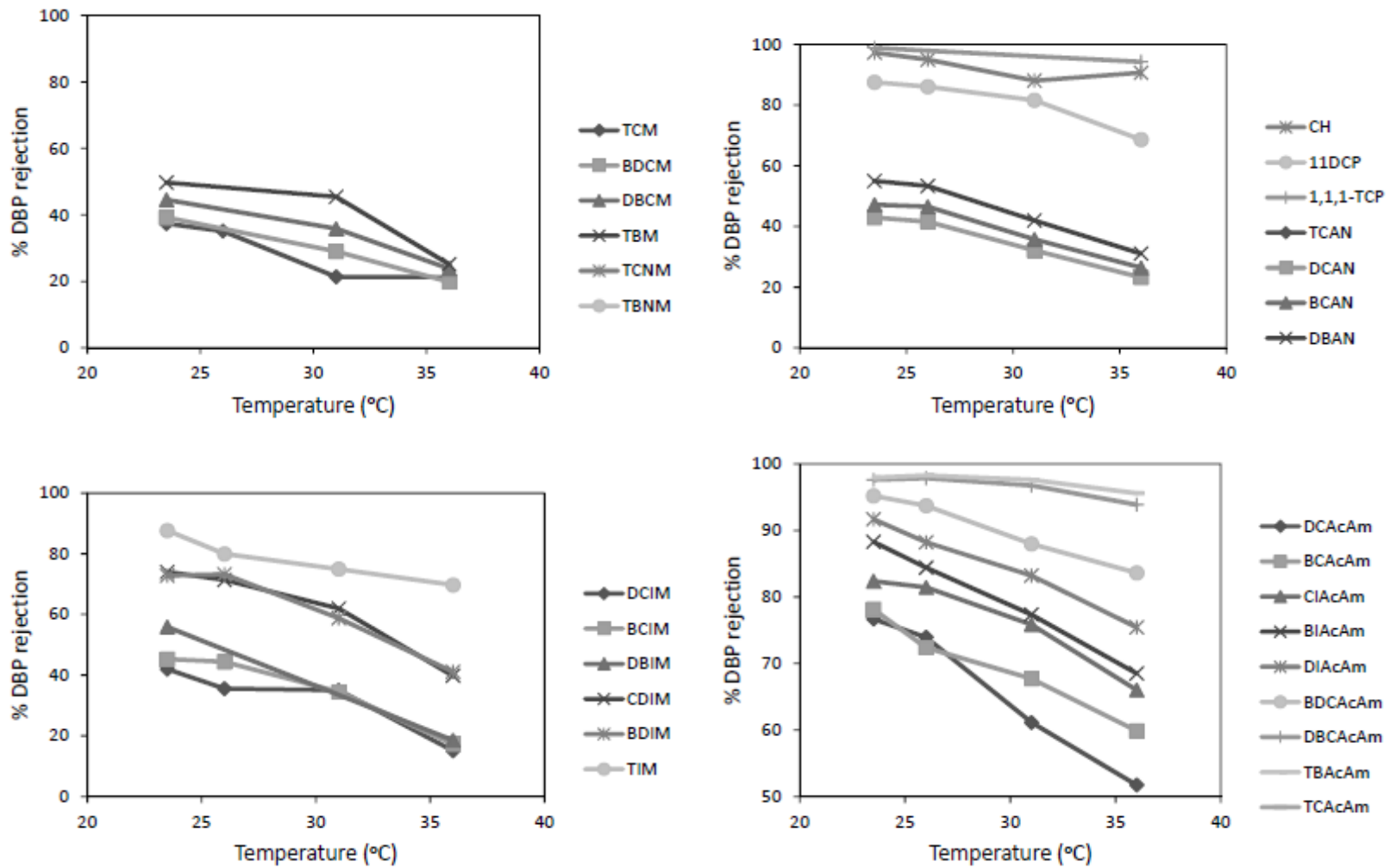


Figure B.6. Impact of feed solution temperature on DBP rejection by RO.

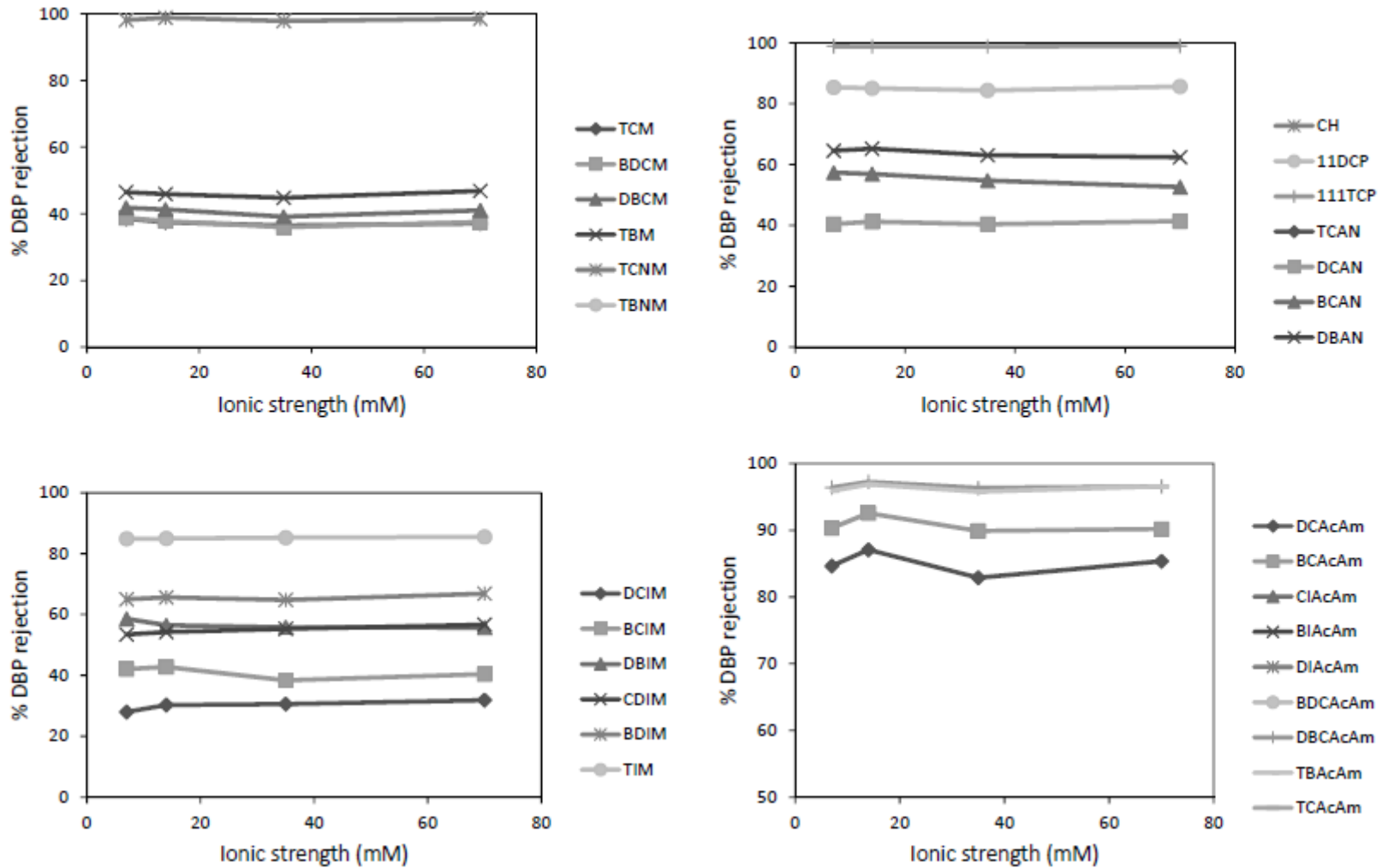


Figure B.7. Impact of feed solution ionic strength on DBP rejection by RO.

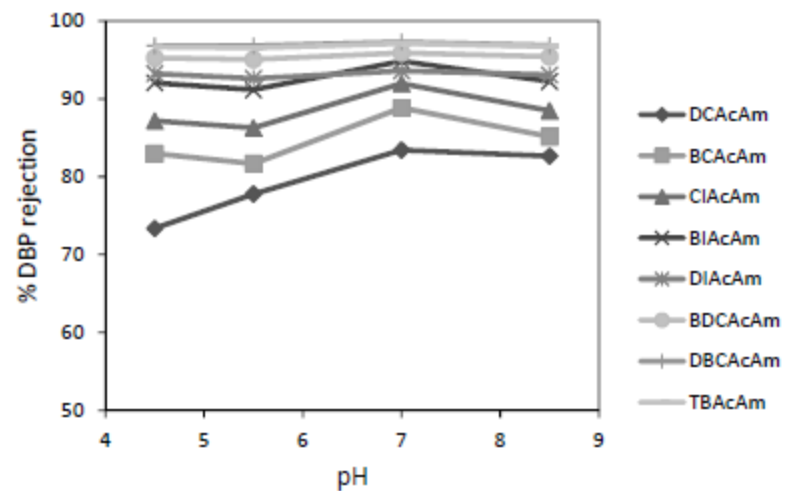
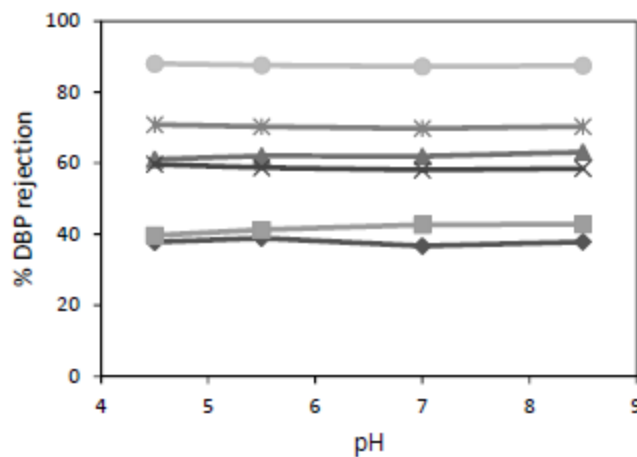
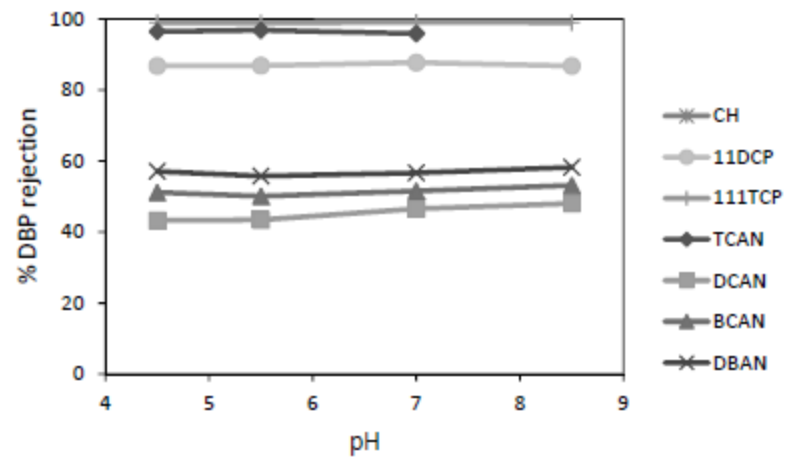
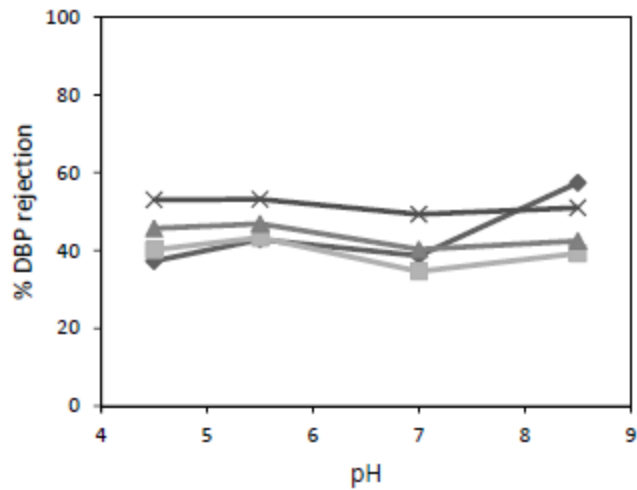


Figure B.8. Impact of feed solution pH on DBP rejection by RO.

Appendix C

Appendix C shows the data for DBP rejection by RO and NF membranes obtained at UNC. Figures C.1. and C.2. present the results under baseline conditions. Figure C.3. shows the impact of transmembrane flux, Figure C.4. the effect of temperature, and Figure C.5. the effect of pH.

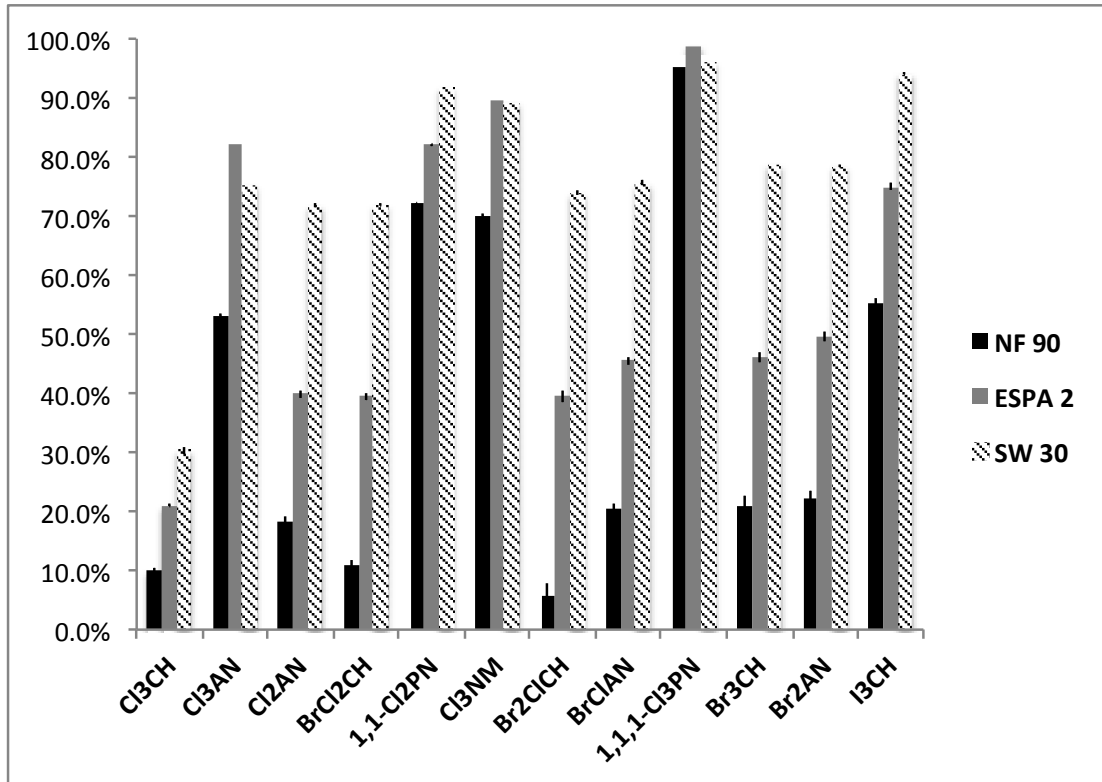


Figure C.1. Rejection of THMs, HANs, HKs, and Cl₃NM by NF 90, ESPA 2, and SW 30 under baseline conditions.

Notes: Error bars indicate the standard error among four rejection values. (feed pH 7, crossflow velocity 0.12 m/s, 7 mM NaCl, 1 mM KH₂PO₄, flux 18 L/m²hr, temperature 21° C).

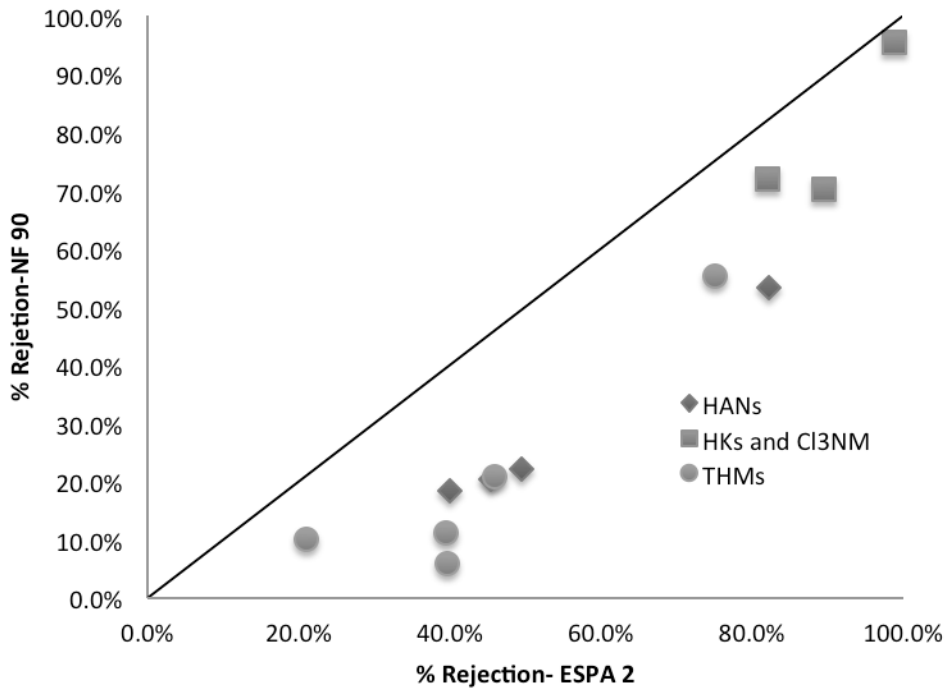


Figure C.2. Rejection of THMs, HANs, HKs, and Cl₃NM by NF 90 (NF) versus ESPA 2 (RO) under baseline conditions.

Note: Error bars indicate the standard error between four rejection values.

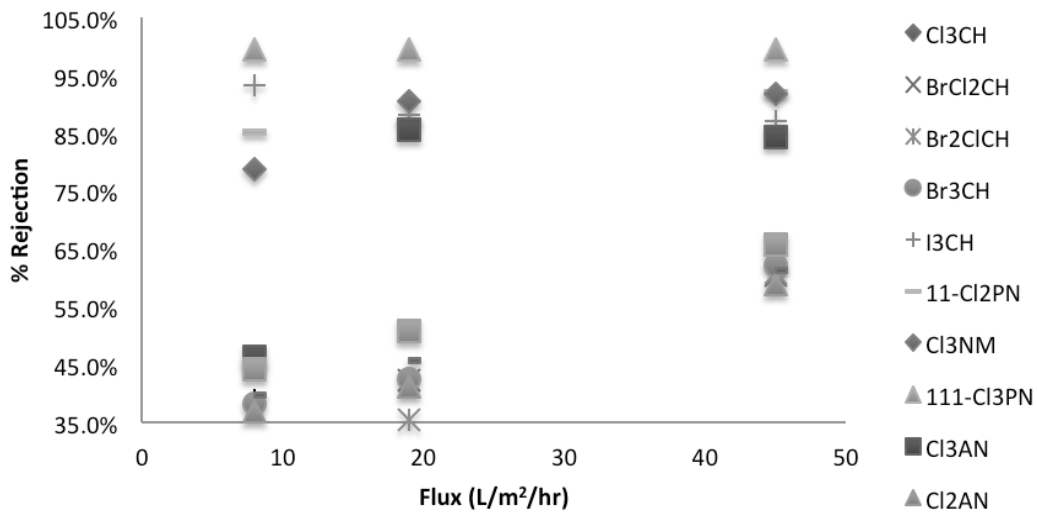


Figure C.3. THM, HAN, HK, and Cl₃NM rejection by ESPA2 as a function of transmembrane flux.

Notes: Error bars indicate the standard error among four rejection values. (feed pH 7, crossflow velocity 0.12 m/s, 7 mM NaCl, 1 mM KH₂PO₄, feed temperature 21° C).

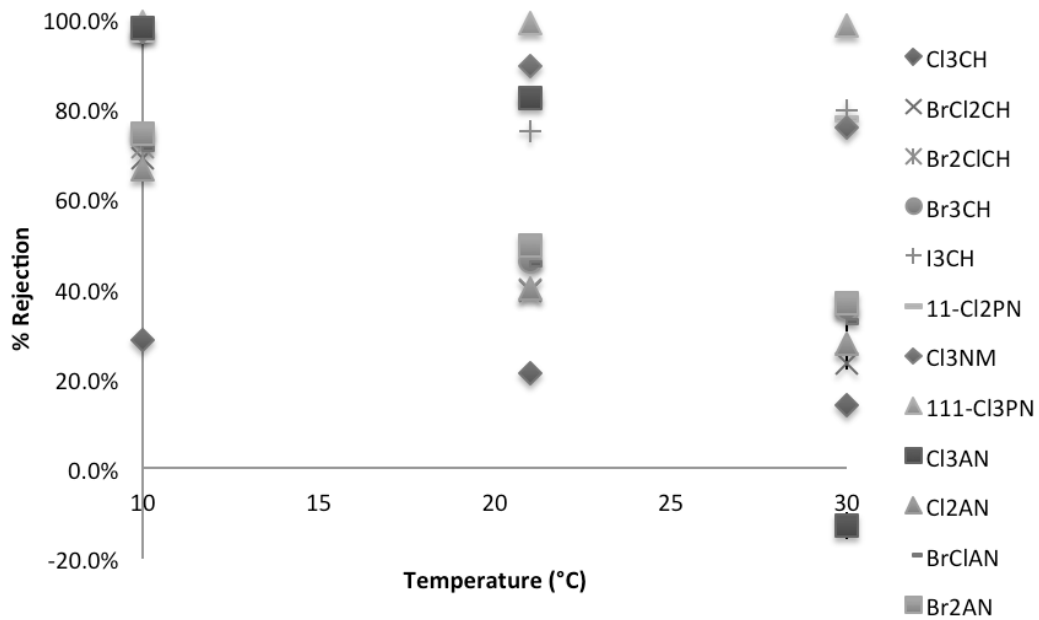


Figure C.4. THM, HAN, HK, and Cl₃NM rejection by ESPA2 as a function of temperature.

Notes: Error bars indicate the standard error between four rejection values. (feed pH 7, crossflow velocity 0.12 m/s, 7 mM NaCl, 1 mM KH₂PO₄, flux 18 L/m²hr).

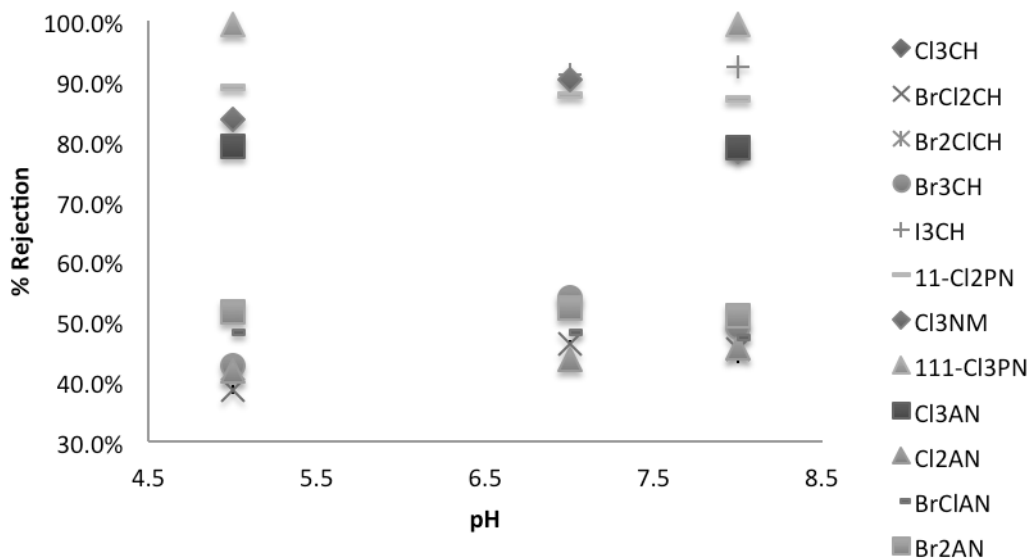


Figure C.5. THM, HAN, HK, and Cl₃NM rejection by ESPA2 as a function of pH.

Notes: Error bars indicate the standard error between four rejection values. (crossflow velocity 0.12 m/s, 7 mM NaCl, 1 mM KH₂PO₄, flux 18 L/m²hr, feed temperature 21° C).



WATERREUSE

1199 North Fairfax Street, Suite 410

Alexandria, VA 22314 USA

703.548.0880

703,548.5085 (fax)

foundation@watereuse.org

www.WateReuse.org